Development and Application of Nickel Stable Isotopes as a New Geochemical Tracer

Louise Gall

Thesis submitted to the University of Oxford
for the degree of
Doctor of Philosophy in Earth Sciences

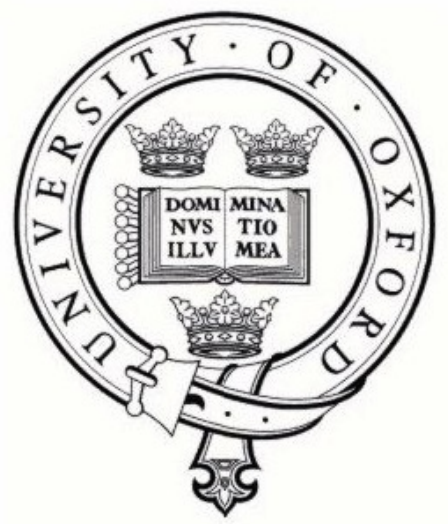

Department of Earth Sciences
and Linacre College,
University of Oxford
2011

DECLARATION

The contents of this thesis are all my own work, except where otherwise stated. The views and opinions expressed herein are mine and not necessarily those of any other person or body unless so attributed.

Abstract

In this thesis, I have developed a new methodology for the accurate determination of mass-dependent variations in nickel (Ni) isotope compositions. Nickel is initially separated in a three-column ion-exchange procedure, and the purified solutions are analysed by multi-collector inductively coupled plasma mass spectrometry (MC-ICPMS) using a double-spike technique. Using this methodology, I have measured the first Ni isotope ratios for a wide variety of natural geological samples. Significant Ni isotope variations were observed, with an overall spread in δ^{60}Ni-values of -0.9 to 2.5‰. In igneous rocks Ni isotopes appear to be largely homogeneous, with only small variations (∼0.2‰) between different rock types. Weathering of silicate rocks does on the other hand appear to cause significant fractionation of Ni isotopes, probably producing an isotopically heavy riverine input to the ocean. A heavy isotope signature is also visible in hydrogenetic ferromanganese crusts, with surface scrapings from globally distributed crusts show an average δ^{60}Ni-value of 1.65‰. However, the variation in these samples is over 1.5‰, likely reflecting local sources or biological processes, or alternatively indicating a heterogeneous Ni isotopic composition of the ocean. Organic-rich sediments also show heavy isotopic compositions, which are possibly transferred to the crude oils originating in these types of sediments. The only significant reservoir of light Ni isotopes found during this project are sulphides from magmatic systems. Overall, this thesis demonstrates the potential of this system as a powerful new tracer for a variety of geochemical processes.

CONTENTS

Extended Abstract **8**

List of Tables **12**

List of Figures **15**

1 Introduction **24**

1.1 Introduction 25

1.1.1 Geochemistry of nickel 25

1.1.2 Biochemistry of nickel 27

1.1.3 Motivation for this study 28

1.2 Nickel isotope geochemistry 29

1.2.1 Stable isotope fractionation 29

1.2.1.1 Fractionation processes 31

1.2.2 Mixing of isotope reservoirs 34

1.2.3 Stable isotopes of nickel 35

1.3 Previous work on nickel isotopes 37

1.3.1 Nickel isotopes in cosmochemistry 37

1.3.2 Nickel isotopes in terrestrial samples 41
1.4 Outline of this thesis 43

2 New preparation technique for quantitative separation of nickel from a geological sample matrix 45

2.1 Introduction 46
2.2 Sample digestion 48
2.2.1 Reagents 48
2.2.2 Wet digestion 49
2.2.3 Microwave-assisted digestion 50
2.3 Ion Exchange Chromatography 51
2.3.1 Nickel-specific resin 60
2.3.2 Procedure for separating Ni from a geological matrix 61
2.3.3 Procedural Blank 64
2.3.4 Nickel Yields 66
2.4 Conclusions 67

3 Determination of the nickel isotopic composition in geological samples using Multi-Collector ICPMS 68

3.1 Introduction 69
3.1.1 Principles of MC-ICPMS 69
3.1.1.1 Introduction system 69
3.1.1.2 Plasma source 71
3.1.1.3 Ion separation 72
3.1.1.4 Detectors 73
3.1.2 Instrument resolution 75

3.2 Isobaric Interferences 76
3.3 Instrumental mass fractionation corrections 79
3.3.1 Sample-Standard-Bracketing 80
3.3.2 External correction by element doping 81
3.3.3 Internal correction by double-spiking 85
3.3.3.1 Choice of Spike Composition 85
3.3.3.2 Spike calibration 92
3.4 Analytical protocol 95
3.4.1 Measurement details 95
3.4.2 Isobaric interference corrections 95
3.4.3 Fractionation associated with the chemical separation 98
3.4.4 Fractionation associated with matrix effects 99
3.5 Reproducibility and accuracy of measurements 101
3.6 Conclusions 104

4 Nickel isotope variations in the silicate Earth 105

4.1 Introduction 106
4.1.1 Nickel behaviour in silicates 106
4.2 The Mantle 108
4.2.1 Peridotites 108
4.2.2 Komatiites 109
4.3 The Oceanic Crust 111
4.3.1 Isotopic fractionation with melt formation 111
4.3.2 Isotopic source signature? 115
4.4 The Continental Crust 117

4.4.1 Fractionation with igneous differentiation 117
4.4.2 Source inherited composition? 118
4.5 Alteration of silicate rocks 121
4.5.1 Alteration of the oceanic crust 122
4.5.2 Alteration of a peridotite protolith 125
4.5.3 Primary conclusions for silicate alteration 127
4.6 The primitive Earth 128
4.6.1 The Bulk Silicate Earth 128
4.6.2 Nickel isotopic composition of meteorites 128
4.6.3 Fractionation of Ni isotopes during core formation? 132
4.7 Conclusions 136

5 Variations in ni isotope compositions of ferromanganese crusts 138
5.1 Introduction 139
5.1.1 Nickel in seawater 139
5.1.2 Biological utilisation of Ni in seawater 140
5.2 Sources and sinks of Ni in the ocean 143
5.2.1 Nickel sources 144
5.2.1.1 Freshwater flux 145
5.2.1.2 Atmospheric flux 146
5.2.1.3 Hydrothermal flux 147
5.2.1.4 Other input sources 148
5.2.2 Nickel sinks 149
5.2.2.1 Pelagic sediments 149
5.2.2.2 Ferromanganese crusts 150

5.2.2.3 Other output sinks . . . 150
5.2.3 Oceanic residence time of Ni . . . 152
5.3 Ferromanganese oxide crusts . . . 152
5.3.1 Nickel adsorption to FeMn crusts . . . 154
5.4 Experimental study on Ni–MnO adsorption . . . 155
5.4.1 Experimental procedure . . . 156
5.4.2 Preliminary results . . . 159
5.5 Isotopic composition of surface scrapings . . . 162
5.5.1 Sample selection . . . 162
5.5.2 Results: isotopic variations in hydrogenetic crusts . . . 164
5.5.3 Results: isotopic composition of hydrothermal crusts . . . 164
5.5.4 Discussion . . . 165
5.5.4.1 Crustal growth location . . . 166
5.5.4.2 Crustal growth depth . . . 168
5.5.4.3 Crustal Ni concentration . . . 168
5.5.4.4 Seawater composition . . . 170
5.5.4.5 Biological input . . . 172
5.6 Depth profile through a hydrogenetic crust . . . 174
5.6.1 Sampling and analytical procedures . . . 174
5.6.2 Results . . . 176
5.6.3 Discussion . . . 177
5.6.3.1 Crustal mineralogy . . . 177
5.6.3.2 Comparison with Fe isotope ratios . . . 181
5.6.3.3 Isotopic signature due to environmental change? . . . 182
5.7 Conclusions . . . 183

6 Applications of nickel isotopes as a tracer in economic geology 185

6.1 Introduction 186

6.2 Nickel in petroleum geochemistry 186

6.2.1 Metal speciation 187

6.2.2 Origin of metals 188

6.2.3 Previous isotope studies on petroleum 190

6.2.4 Nickel isotopic composition of crude oil 191

6.3 Nickel in ore deposit geochemistry 196

6.3.1 Introduction 196

6.3.2 Chemistry of Ni sulphides 196

6.3.3 Nickel ore deposits associated with komatiies 197

6.3.4 The Sudbury Igneous Complex 198

6.3.5 Nickel isotopic composition of sulphides 200

6.4 Conclusions 205

7 Conclusions and outlook 206

7.1 Conclusions of thesis project 207

7.2 Future work on nickel isotope geochemistry 210

7.2.1 The role of Ni in biogeochemical reactions 210

7.2.2 Decline of Ni before oxygenation of the atmosphere? 211

7.2.3 Chemical evolution of the mantle 212

Bibliography 213

APPENDIX 237

A Double-spike calculations: Mathematical descriptions **237**

A.1 The angle (θ) in between two planes 238

A.2 Optimal spike by geometrical projection 240

A.3 Optimal spike by algebraic inversion 243

Acknowledgements **244**

Extended Abstract

Isotopic variations in the first row transition metals are of particular interest due to the abundance of these elements in a wide variety of rock types and their utilisation in many biological processes. However, in contrast to many other transition metal isotope systems such as iron and molybdenum, few studies have addressed mass-dependent variations in nickel (Ni) isotopes, largely due to the difficulty of separating pure Ni from geological samples. The principal aim of this thesis is to develop and apply a new methodology for the accurate determination of mass-dependent variations in Ni isotope compositions in a range of geological materials.

Chapter 1 introduces nickel and its isotope system. Nickel (Z = 28) has five stable isotopes, ^{58}Ni, ^{60}Ni, ^{61}Ni, ^{62}Ni, and ^{64}Ni, with respective natural abundances of 68.08%, 26.22%, 1.14%, 3.63%, and 0.93%. It is the seventh most abundant transition metal in the Earth's crust, and is present in most geological reservoirs. It also plays a key role in several enzymes important in the carbon cycle, including methane production and uptake of nitrogen during primary productivity. Although Ni can possess a range of different oxidation states (from 0 to +IV) it is essentially only present in the +II state in natural samples. The lack of change in oxidation state with redox reactions renders Ni distinct from most other first row transition metals. Instead, Ni isotope fractionation may be caused by changes in speciation or coordination, making it an interesting addition to the established field of non-traditional stable isotopes.

Chapter 2 outlines a new chemical separation procedure which successfully isolates Ni from most geological matrices. Such separation has long proved challenging due to similarities in chemical behaviour between Ni and geologically more

abundant elements such as Na, Mg, and Ca. Tests demonstrated that previous methods suggested for extracting Ni from geological samples are unsuitable for high precision analysis of mass-dependent Ni isotopes. The new procedure developed here involves three steps of column chromatography. The first two columns exploit Ni's strong affinity for forming complexes with both ammonia (NH_3) and the organic chelator dimethylglyoxime (DMG), and a final column removes any remaining Fe, an isobar of Ni. The Ni separation procedure is independent of sample pH and works even for samples with large matrix-to-analyte ratios. Processed Ni solutions are totally free of matrix elements and the yield is normally 85–95%. Any isotopic fractionation effects due to incomplete yield are compensated by addition of a double-spike before chromatography.

Chapter 3 lays out the instrumental procedure used to determine $^{60}Ni/^{58}Ni$, $^{61}Ni/^{58}Ni$, and $^{62}Ni/^{58}Ni$ ratios of the purified Ni solutions. Samples were analysed on a Nu Instruments Nu Plasma-HR, a multi-collector inductively coupled plasma mass spectrometer (MC-ICPMS), and were bracketed by analyses of NIST SRM 986 (pure Ni metal) at the same concentration. A double-spike technique was used to correct for instrumental mass fractionation during mass spectrometry analysis. The optimal double-spike composition was established as a mixture of 25% ^{61}Ni and 75% ^{62}Ni and the optimal sample/spike ratio shown to be approximately 0.4. Tests performed on both mixtures of synthetic and natural terrestrial standards demonstrate that the method is accurate, with no interferences or matrix effects. Replicate measurements of USGS reference materials (peridotite PCC-1, basalt BHVO-2, and shale SCo-1) yield a long-term external reproducibility (2 s.d.) of typically ±0.07‰, ±0.1‰, and ±0.14‰ for $^{60}Ni/^{58}Ni$, $^{61}Ni/^{58}Ni$, and $^{62}Ni/^{58}Ni$ respectively, and typical measurement errors are as low as 0.04‰ (2 s.d.).

Chapter 4 focuses on variations of Ni isotope ratios (δ^{60}Ni) in igneous silicate rocks. Analyses of samples spanning the whole silicate spectra (from ultramafics to granites) demonstrate that igneous rocks are largely homogeneous in Ni isotopic composition, with only small variations ($\sim$0.2‰) between different rock types. The average isotopic composition of the mantle was estimated from analyses of mantle xenoliths and tertiary komatiites. This first set of data also reveals an isotopic difference between Mid-Ocean Ridge Basalts (MORB) and intraplate basalts, with MORB being slightly lighter than intraplate basalts and mantle rocks. This suggests that their respective source regions may be of different Ni isotopic composition, although additional analyses of basalts from different sources are needed to confirm this. Finally, the estimated Ni isotopic composition of the silicate Earth was compared to analyses of differentiated and undifferentiated meteorites. Results suggest that core formation was accompanied by a small amount of isotopic fractionation with the heavier Ni isotopes entering the Earth's core.

Chapter 5 investigates Ni isotopic variations in the ocean. The yearly inputs and outputs of Ni in the ocean were estimated and a new, shorter, residence time of $\sim$3,500 years was calculated. This is not long enough time to ensure complete isotopic mixing in the ocean, implying that the Ni isotopic composition of deep water may be heterogeneous. In Chapter 4 it was concluded that weathering of silicate rocks causes significant Ni isotope fractionation, resulting in an isotopically heavy riverine input to the ocean. Hydrogenetic ferromanganese (FeMn) crusts show a global average δ^{60}Ni-value of 1.65‰, with large regional variations (0.9-2.5‰), supporting the idea of an isotopically heavy ocean. Additionally, a depth profile through one hydrogenetic FeMn crust shows that the Ni isotopic composition may have varied as a result of changes in seawater chemistry, possibly due to differences

in the uptake of Ni onto MnO during these periods. Preliminary analyses of sorption experiments also demonstrate that a possible cause for isotopic fractionation between seawater and FeMn crusts is Ni incorporation into vacancies in the vernadite lattice structure, resulting in a fractionation of at least 0.5‰ between these phases. As manganese oxides are a major sink of Ni in the ocean, this fractionation could potentially have a major impact on deep water Ni isotopic composition.

Chapter 6 demonstrates that Ni isotopes can be successfully applied as a tracer for research in economic geology. Analyses of crude oils show that their Ni isotopic composition may be a remnant of their source rocks, as organic-rich shales exhibit similar δ^{60}Ni-values. These results indicate that the heavy Ni isotopes (compared to igneous rocks) correlate with the organic matter in sedimentary rocks, implying either that the Ni taken up during primary productivity is originally heavy (hinting that the ocean may also be isotopically heavy), or that Ni is fractionated towards heavier isotopic composition during biological uptake. Meanwhile, analyses of Ni-rich ore deposits show that the partitioning of Ni into magmatic sulphides during silicate-sulphate melt segregation fractionates Ni isotopes towards lighter isotopic compositions. The only exception found here is pentlandite from the Sudbury Igneous Complex, a world class Ni ore deposit generated by a large meteorite impact. One possibility is that the heavy Ni isotopic composition of this sample is a signature from the impacting meteorite, although further analyses of other Ni-sulphides samples would help confirm or reject this hypothesis.

Chapter 7 summarises the natural variations in Ni isotopic compositions established in this thesis, and presents an outlook on the future potential for this new system as a tracer for geochemical processes.

LIST OF TABLES

1.1 *Isotope ratios of NIST SRM986, as determined by Gramlish et al. (1989a).* . . . 37

2.1 *Full chromatography procedure for separating Ni from a geological matrix* 66

3.1 ***a)*** *the normal detector array of a Nu Plasma,* ***b)*** *the modified detector array of the Nu Plasma-HR at the department of Earth Sciences in Oxford. The top line of numbers refer to the Faraday cups available for the difference array configurations. The masses below the cups refer to the position of each ion beam during analysis. IC shows the position of the ion counters for the different detection configurations.* 74

3.2 *Possible elemental and molecular isobaric interferences on the masses of interest. The number in brackets next to each interference is the resolution required for this interference to be resolved from the Ni isotope peak of interest.* 77

3.3 *Results of the* ^{61}*Ni-*^{62}*Ni double-spike and Ni standard (NIST SRM 986) calibration.* 94

3.4 *Normal instrument settings during Ni isotope ratio analysis on the Nu Plasma-HR.* 95

4.1 *Summary of mantle rock samples analysed for Ni isotope composition.* 110

4.2 *Summary of basalt samples analysed for their Ni isotope composition. The results of the two USGS reference materials BHVO-2 and BCR-2 and MORB analyses of the East Pacific Rise agree well (within error) with published analyses from Cameron et al. (2009).* 113

4.3 *Summary of continental rocks analysed for their Ni isotopic composition.* 120

4.4 *Summary of hydrothermally altered oceanic crust samples from ODP hole 504B.* . . 123

4.5 *Summary of the isotopic compositions of samples from the Cerro Matoso Ni-laterite mine, Colombia, and the Lizard complex, UK, analysed for this section on alteration.* 126

4.6 *Summary of the Ni isotopic compositions in all meteorites analysed for this thesis.* 131

5.1 *Estimated fluxes of inputs and outputs of mol Ni to the ocean over one year.* ***References:*** *a) MBARI (2011), b) Li & Schoonmaker (2003); Gaillardet et al. (2003), c) Zektser & Loaiciga (1993), d) Rauch & Pacyna (2009) (and references therein), e) Rehkämper & Nielsen (2004) (and references therein), f) Nriagu (1989), g) Galindo et al. (1998), h) Elderfield & Schultz (1996), i) Kraemer & Schornick (1974) ; (1) Based on that only 0.47% of the Ni attached to aerosol particles is soluble in seawater (Duce et al., 1991) ; (2) Area for pelagic accumulation was estimated to 300 × 10^6 km^2 ; (3) higher total value includes the ferromanganese crusts.* 151

5.2 *Preliminary Ni isotope data for the experiments on Ni adsorption onto synthetic hexagonal birnessite. Errors on each sample measurement (2 s.e.) was 0.02-0.03 ‰.* 161

5.3 *Summary of crust samples and results of Ni isotope analyses of the surface scrapings. The samples were provided by the US Geological Survey (Jim Hein), Menlo Park, USA; Scripps Inst. Oceanography, UC San Diego, USA; University Rhode Island, USA; National History Museum and British Museum, London, UK; Bundesanstalt für Geowissenschaften und Rohstoffe, Germany; and Universität Kiel, Germany.* 163

5.4 *Intervals (mm from top of crust) sampled and analysed for a Ni isotope ratio depth profile through ferromanganese crust CD29-2, from north central Pacific Ocean. Every sample aliquot was analysed three times, the errors given are 2 s.e. of these measurements.* 175

6.1 *Summary of all crude oils and organic rich shales analysed for their Ni isotopic composition.* 192

6.2 *Structural and chemical information on Ni-sulphides (pentlandite and millerite) and important Ni-containing Fe and Cu sulphides (pyrrhotite, pyrite and chalcopyrite). Data from Makovicky (2006) and Anthony et al. (2011).* 198

6.3 *Summary of all sulphides analysed for their Ni isotopic composition. Pent = pentlandite, pyrr = pyrrhotite, cpy = chalcopyrite. All samples were provided by the Natural History Museum, London.* 201

LIST OF FIGURES

1.1 *Comparison of the equilibrium versus kinetic mass-dependent fractionation lines. Plotted are also typical error bars (2 s.e.) of a measurement to illustrate the difficulty in using this approach to separate the two fractionation processes for the Ni isotope system, due to the relatively small isotopic range and current precision available.* 33

1.2 *Published data of Ni isotope compositions in whole rock meteorite samples, from Cameron et al. (2009), Moynier et al. (2007) and Cook et al. (2007). Error bars are 2 s.d.* 40

1.3 *Published Ni isotope ratios of abiotic terrestrial samples, data from Cameron et al. (2009), Steele et al. (2011), and Tanimizu & Hirata (2006).* 42

2.1 *Separation experiment of a synthetic calibration solution containing equal concentrations of the elements plotted. The experiment was performed using 2 mL columns filled with cation resin (AG50W-X4). After preconditioning the resin and loading the calibration solution, the column was washed with 5 mL each of first 1M HF followed by 0.1M HF–1M HNO while collecting the elute.* 54

2.2 *Separation experiment of a synthetic calibration solution containing equal concentrations of the elements plotted. The experiment was performed using 2 mL columns filled with cation resin (AG50W-X4). After preconditioning the resin and loading the calibration solution, the column was washed with 5 mL each of first 1M H_2SO_4 followed by 3M HCl while collecting the elute.* 54

2.3 *Separation experiments of a synthetic calibration solution containing equal concentrations of the elements plotted. The experiments were performed using 2 mL columns filled with anion resin (AG1-X8). After preconditioning the resin and loading the calibration solution, the column was washed with 5 mL each of 0.05M Oxalic acid–0.2M HCl followed by 0.25M Oxalic acid–1M HCl while collecting the elutes separately.* 56

2.4 *Separation experiments of a synthetic calibration solution containing equal concentrations of the elements plotted. The experiments were performed using 2 mL columns filled with cation resin (AG50W-X4). After preconditioning the resin and loading the calibration solution, the column was washed with 5 mL each of 0.05M Oxalic acid–0.2M HCl followed by 3M HCl while collecting the elutes separately.* . 56

2.5 *Separation experiments of a synthetic calibration solution containing equal concentrations of the elements plotted. The experiments were performed using 2 mL columns filled with cation resin (AG50W-X4). After preconditioning the resin and loading the calibration solution, the column was washed with 5 mL each of 0.5M HCl in 90% acetone followed by 0.5M HCl in 95% acetone while collecting the elutes separately.* 57

2.6 *Separation experiments of a synthetic calibration solution containing equal concentrations of the elements plotted. The experiments were performed using 2 mL columns filled with cation resin (AG50W-X4). After washing off matrix elements from the column with HCl-acetone mixtures as described above, Ni was eluted as a DMG complex by adding DMG dissolved in an acetone-HCl-solution. The HCl-cut shows the DMG-complex directly added on another cation column and rinsed from DMG before elution with 3M HCl.* 57

2.7 *Schematic illustration of complexation of Ni^{2+} by di-methylglyoxime* 58

2.8 *Separation experiments of a synthetic calibration solution containing equal concentrations of the elements plotted. The experiments were performed using 2 mL columns filled with cation resin (AG50W-X4). After preconditioning the resin and loading the calibration solution, the column was washed with 5 mL each of 0.1M di-ammonium-citrate (dAC) in 3M ammonium solution (NH_4OH) followed by 3M HCl while collecting the elutes separately.* 59

2.9 *Separation experiment using the Ni-specific resin from Eichrom Inc. Here only the Ni-eluting cut (3M HNO_3 used as eluting agent) has been plotted in the figure. The results show that only Cu and minor amounts of Fe, Co, Zn, Mg, Ca, and Al are let through together with the Ni.* 59

2.10 *Column calibration of step 1 and 2 in the Ni separation procedure, using a synthetic calibration solution containing a matrix elements-to-Ni ratio similar to silicate rocks.* 65

3.1 *Schematic overview of the Nu Plasma-HR (figure from Nu Instruments manual).* 73

3.2 *Demonstration of low (left) and high (right) pseudo-resolution. This technique never truly separates the two ion beams (analyte and interference), but allows the low mass side of the peak to be measured without contribution from the overlapping interference. Many authors have used this technique to separate ^{58}Ni from the potential interference of $^{40}Ar^{18}O^{+}$. If this interference had an impact on the ion beam at mass 58 the two species could be separated.* 76

3.3 *Flat topped peaks of ion beams on masses 58, 60, and 62 in low-resolution mode (left), medium-resolution mode (middle), and high-resolution mode (right). As can be seen in the medium and high resolution figures, there are no resolvable interferences on the displayed Ni isotope beams in either resolution mode.* 78

3.4 *Measurements of an untreated Ni-standard solution over several months. The data shows that a combination of Cu-doping and sample-standard-bracketing provides excellent precision and reproducibility, giving an average value of $\delta^{60}Ni$ = 0.000065 ± 0.074‰ (2 s.d., n = 390). Error bars are 2 s.e. of the individual measurements.* 83

3.5 *Uncorrected data from two different measurement sessions, plotted as the natural logarithm of the measured ratios (M) divided by the true ratios (T) for isotope pairs of Cu and Ni. If the instrumental fractionation factor (f) is the same for both Cu and Ni then, according to the exponential fractionation law, the data should plot on a line of slope = 1. As shown above, this is not the case for these two elements, but as $f_{Cu} \propto f_{Ni}$ and constant for a whole session, the relationship $f_{Cu} = f_{Ni}$ can still be used as long as all ratio measurements are made relative to a standard.* . 84

3.6 ***a)** (left) Sketch showing the relationship between the points N, M, and S, the line N-M-S, and the angle, θ in three-isotope-space – these parameters can be used for calculating the optimal double-spike following Galer (1999). **b)** (right) Similar sketch of three-isotope-space showing the relationship between the instrumental fractionation, β, the natural fractionation, α, the plane 'z' defined by the sample, standard, and the spike compositions – these parameters are all used for calculating the optimal double-spike composition following Siebert et al. (2001).* 87

3.7 *Optimal double-spike composition calculations for a ^{61}Ni-^{62}Ni double-spike, calculated following the mathematical procedure from Siebert et al. (2001). The two figures displays the proportion of ^{61}Ni in the double-spike together with the proportion double-spike in the spike-sample mixture, plotted against the error in α (i.e. error on the measured natural sample) for each combination. The optimal double-spike combination and spike-sample mixture would have the lowest error. The results show there is relatively little difference in the errors between proportional mixtures of ratios ^{61}Ni:^{62}Ni = 25:75 – 65:45 respectively.* 89

3.8 *Optimal double-spike composition calculations for different combinations of each isotope in a ^{61}Ni-^{62}Ni double-spike, calculated using 'The double spike toolbox' (Rudge et al., 2009). Similarly to the previous figure, displaying the proportion of ^{61}Ni in the double-spike together with the proportion double-spike in the spike-sample mixture, plotted against the error in α or each combination. The results from these calculations are in accordance with previous calculations, giving the optimal double-spike composition as approximately 50% each of ^{61}Ni and ^{62}Ni.* . 90

3.9 *Optimal spike compositions for the Ni isotope system, calculated using 'The double spike toolbox' (Rudge et al., 2009) for different sets of double-spike components.* . 91

3.10 *Data collected for mixtures of the Ni reference standard (SRM 986) and the ^{61}Ni-^{62}Ni double-spike solution for a range of sample/spike ratios. The measured values for the Ni standard of all ratios are within the long-term external error (± 0.07‰, 2 s.d.).* 94

3.11 *Analyses of a Ni standard solution doped with different amount of Fe. The black circles are the measurements without correcting for the ^{58}Fe interference on ^{58}Ni, and the white circles are the same measurements after applying the correction. As can been seen in the figure, any Fe present in the sample can be corrected for by our correction scheme.* 96

3.12 *Scans of mass spectra (45-70 amu) of a chemically processed silicate sample (USGS rock standard BHVO-2) and a blank solution (2% 0.3M HNO_3) showing how the purified Ni solution is clean from interferences other than small amounts of Cu and Zn. However, this sample spectrum also shows why correcting for instrumental mass fractionation by Cu-doping alone does not produce correct Ni isotope ratios, as there is still Cu left in the original purified sample solution.* 97

3.13 *Measurements of the Ni standard NIST SRM 986 to test chemical separation procedure. Open symbols are a mixture of SRM 986 and the artificial calibration solution (plasma standards, Alfa Aesar, see text for more information) put through the separation procedure. Closed symbols are the SRM 986 on its own put through the separation procedure. Error bars are 2 s.e. of individual measurement. Dotted lines are ±2 s.d. of all SRM 986 measurements.* 99

3.14 *Analyses of a Ni standard solution doped with different elements in varying concentration ratios to Ni. The error bars are 2 s.e. of the measurement. The dotted lines show the 2 s.d. error on all (un-doped) Ni standard solution analyses during the measurement session.* 102

3.15 *Long term instrument reproducibility tested by measurements of a Ni-oxide solution (NiO powder, Sigma Aldrich) analysed during several measurement sessions over one year. The overall average value for the NiO solution was* $\delta^{60}Ni$ *= -0.159 ± 0.034‰ (2 s.d.). Error bars in the figure are 2 s.e. of the individual measurements.* 103

3.16 *Long term external reproducibility tested by measurements of three USGS rock standards of different silicates, processed and analysed during several measurement sessions over one year. Each data point is a complete chemical replicate of the three silicate sample, showing that the precision for Ni isotope analysis is excellent. By these analyses, the external* $\delta^{60}Ni$ *sample reproducibility is typically ± 0.07‰ (2 s.d.) for silicate samples.* 103

4.1 *Summary of all mantle derived samples analysed for Ni isotopic composition. The dotted lines show the estimated average mantle isotopic composition (*$\delta^{60}Ni_{Mantle}$ *= 0.19 ± 0.13 ‰). The figure shows how ultramafic rocks are clustered within a very narrow range in Ni isotopic composition. Plotted in the figure are also different mantle derived melts (komatiites and basalts), showing that some parts of the mantle may be of different Ni isotopic composition.* 114

4.2 *Plot of* $\delta^{60}Ni$*-values of all basalts against degree of melt extraction in the form of the samples' Mg-numbers (MgO/(MgO+FeO). Symbols represent the same samples as in Fig. 4.1. Major element data from Gannoun et al. (2007).* 116

4.3 *Granites and Granitiod rocks analysed for their Ni isotopic composition. As displayed in the figure, there is no significant difference in $\delta^{60}Ni$ either between rocks of different SiO_2 composition (where andesite < granodiorite < granite) or between granites composed of material from different origins (I- or S-type). Also plotted are samples of sediments generally regarded to be the source material of the S-granites, although these are of lighter Ni isotopic composition then the analysed granites. The dotted lines shows the estimated average mantle isotopic composition ($\delta^{60}Ni_{Mantle} = 0.19 \pm 0.13$ ‰) as a reference.* 121

4.4 *Plot displaying the Ni isotopic composition of both fresh and hydrothermally altered oceanic crust. The dotted lines shows the estimated average mantle isotopic composition ($\delta^{60}Ni_{Mantle} = 0.19 \pm 0.13$ ‰) as a reference.* 124

4.5 *Probability density plot made using isoplot showing that there is a significant difference in Ni isotopic composition between the fresh and the altered oceanic crust samples.* 124

4.6 *Plot displaying the Ni isotopic composition of the weathered samples form Cerro Matoso laterite mine, showing how both Ni-oxides and Ni-clays contain a lighter Ni isotope composition than the underlying peridotite. This indicates that the heavier Ni isotopes must have been leached from the protolith and, ultimately, deposited in the ocean.* 127

4.7 *Figure showing the Ni isotopic compositions in all meteorites analysed for this study (top), compared to all published data (from Cook et al. (2007); Moynier et al. (2007); Cameron et al. (2009) and Steele et al. (2011)), showing that the new data agree well with published data. The dotted lines shows the estimated isotopic composition for the silicate Earth as a reference.* 133

5.1 *Seawater concentration of Ni with depth in the Atlantic, Southern, Indian, and Pacific Ocean, showing how the dissolved Ni concentration varies between different ocean basins. In the top figures – black triangles are data NE Atlantic (British Isles, Jickells (1988)), white triangles data from NW Atlantic (Sargasso Sea, Saager et al. (1997)), and grey triangles data from the Southern Ocean (Atlantic side, Löscher (1999)). In the bottom figures – black triangles are data from NW Pacific Ocean (Southern China Sea, Norisuye et al. (2007)), white triangles data from NE Pacific Ocean (California–Hawaii, NE Pacific Bruland (1980)), and grey triangle data from the Indian Ocean (west of India, Saager et al. (1997)).* . 141

5.2 *Seawater concentration (nmol/kg) of micro-nutrients Cd (grey triangles), Zn (white triangles), and Ni (black diamonds) with depth (NE Pacific data from Bruland (1980)), plotted in both linear and logarithmic scale to clarify the difference in surface water concentrations. The figure shows that surface waters contain significantly higher concentrations of Ni than of Cd and Zn, but all elements show the same concentration pattern below 1000 m depth.* 144

5.3 *Isotope data from the adsorption experiments plotted together with model fractionation curves. The low pH experiments (left) fit well with Rayleigh fractionation curves, while pH 7 experiments (right) seem to follow a constant, equilibrium, fractionation.* 160

5.4 *Preliminary results showing Ni isotope fractionations (expressed as* $\Delta^{60/58}Ni$*) between* $Ni_{solution}$ – $Ni_{adsorbed}$ *(pH 1.5, 2, and 3) and* $Ni_{adsorbed}$ – $Ni_{incorporated}$ *(pH >7).* 161

5.5 *Samples and results for all ferromanganese crust surface scrapings analysed for their Ni isotope composition plotted according to their location of growth. Also plotted is the location for the crust selected for an isotope depth profile study (CD29-2).* 165

5.6 *Nickel isotope compositions of surface scrapings gathered by ocean basin of origin (Atlantic, Indian, Southern, and Pacific Ocean). No clear variation between the different ocean basins can be seen, although there is a hint of generally lighter* $\delta^{60}Ni$*-values in the Atlantic than in the Pacific. Error bars are 2 s.d. of all measurements performed.* 167

5.7 *Probability density plot comparing the Ni isotopic composition (including individual sample errors) of FeMn crust samples from the Atlantic, Indian, and Pacific Ocean. Although the curves are overlapping the mean of their respective curve are offset from each other, implying a statistical difference in the isotopic composition of FeMn crusts of the three ocean basins.* 167

5.8 *Nickel isotope ratios of ferromanganese crusts plotted against the sample depth of growth. The samples are grouped by ocean basin for clarification (white squares = Atlantic; black diamonds = Indian; grey triangles = Pacific; black triangles = South China Sea; white triangles = Southern Ocean).* 169

5.9 *Nickel isotope ratios of ferromanganese crusts plotted against the sample Ni concentrations. The samples are grouped by ocean basin for clarification (white squares = Atlantic; black diamonds = Indian; grey triangles = Pacific; black triangles = South China Sea; white triangles = Southern Ocean). The figure shows how the crust Ni concentration seem to increase from the Atlantic to the Pacific Ocean (except for one Atlantic outlier), but the same trend is not seen for Ni isotopic composition.* 169

5.10 *Variation in Ni isotope composition of the ferromanganese crusts plotted against the distance from the closest continental shelf to the crust's place of growth. The samples are grouped by ocean basin for clarification (white squares = Atlantic; black diamonds = Indian; grey triangles = Pacific; black triangles = S. China Sea; white triangles = Southern Ocean). The figure shows how the heaviest Ni isotope compositions are found in crusts growing very close to a continental shelf.* 173

5.11 *Plot of the Ni isotope composition versus the sample Fe isotopic composition (data from Levasseur et al. (2004)). Legend for samples of the different ocean basins are the same as in Fig. 5.6.* 173

5.12 *Photograph of the crust CD29-2 sampled for this depth profile isotope study.* . . . 175

5.13 *Nickel isotopic depth profile through the crust CD29-2 from the north central Pacific Ocean. Section δ^{60}Ni-values are plotted according to their position in the crust, measured in mm from the most recent growth surface. The error bars shown are 2 s.e.* 176

5.14 *Correlation between the concentrations of Mn and Ni in crust CD29-2. The regression shows how the relationship between the elements can be described by the exponential growth equation given in the figure, where a = 35.3, and b = 3.14.* . 178

5.15 *Major element data profiles through CD29-2 analysed by electron microprobe byFrank et al. (1999) (the full dataset is yet unpublished). The data profiles shows that the concentrations of selected element pairs (Fe–Ti, Mn–Ni, and Ca–P) are related.* . 179

5.16 *δ^{60}Ni-values plotted against the concentration of major elements in crust CD29-2: Fe, Ca, Mn, and Ni. As no correlations with Ni isotope ratios are visible, the controlling factor for isotopic fractionation is probably not the crust's mineralogy.* 180

5.17 *Profiles of Ni isotope and Fe isotope ($\delta^{57/54}$Fe) data from CD29-2 plotted according to their position within the crust (mm from the top). The ratios were analysed on the same sample solutions. Iron isotope analyses were performed by Helen Williams (pers. com.).* 181

5.18 *Nickel isotope compositions of the depth profile through the crust CD29-2 plotted according to the sample model age (by Nielsen et al. (2009) based on Klemm et al. (2005)).* 182

6.1 *Comparison of two common Ni-porphyrins and there probable precursor molecules. Top row shows a 'Chlorophyll a' (left) which during diagenesis could be transformed into a 'deoxophylloerythroetioporphyrin' (right), while the bottom row shows a 'Haeme' molecule (left) which breaks down to an 'etioporphyrin' (right) (figure adapted from Treibs, 1934; Czernuszewicz, 2000; Keely, 2006).* 189

6.2 *Plot showing the Ni isotopic compositions of the five crude oil samples (NIST RM 8505, and Amostra 1-4) together with analysed isotopic compositions of two organic rich shales (USGS reference materials SDO-1 and SGR-1). The dotted lines show the estimated average isotopic composition of the mantle (see Chapter 4) as a reference.* 193

6.3 *Plot showing the Ni isotopic compositions of all analysed sulphide samples. Also plotted are the two sulphide samples analysed by Tanimizu & Hirata (2006), which agrees well with the samples analysed here. The dotted lines show the estimated average isotopic composition of the mantle (see Chapter 4) as a reference.* 204

7.1 *Summary of the Ni isotope compositions of all samples discussed in this thesis.* . 209

A.1 *Figures describing the notations used in the geometrical calculations. Top – illustration of the line N-M-S and angle θ; Bottom – illustration of the plane (z), line (z), and intersection point of the line on the plane (X, Y, Z) for finding β and α* 242

A.2 *From Rudge et al. (2009)* 243

CHAPTER

ONE

INTRODUCTION

1.1 Introduction

Advances in multi-collector inductively coupled plasma mass spectrometry (MC-ICPMS) over the last couple of decades has made it possible to investigate the stable isotope systems of "heavy" elements (> 24 a.m.u.), so called "non-traditional" stable isotopes (Johnson et al., 2004). Amongst the new elements currently being studied with isotopic research, the first row transition metals are of particular interest due to their potential to provide constraints on geological processes as well as their key roles in biology. Relatively few studies have addressed mass-dependent variations in nickel (Ni) isotopes, in contrast to other transition metal isotope systems, such as iron (Fe) and molybdenum (Mo) (e.g. Beard et al., 1999; Anbar et al., 2007). The large relative mass differences of the five isotopes (approximately 10%, 7%, and 3.5% between ^{64}Ni, ^{62}Ni, ^{60}Ni and ^{58}Ni, respectively), together with the small measurement errors expected for isotopes of this mass range (< 0.2 ‰), are likely to result in measurable isotopic variations. The applicability of this system to geological questions requires definition of the isotopic compositions of its principal reservoirs and identification of the geochemical (and biological) processes responsible for fractionation.

1.1.1 Geochemistry of nickel

Geochemically, Ni displays siderophile, chalcophile, and lithophile behaviour. Nickel is a common component in the iron alloys of differentiated iron meteorites, which

can contain up to 20 wt% Ni (Haack & McCoy, 2003), suggesting that at high pressures and reducing conditions Ni preferentially partitions into iron phases. High-pressure experiments have further shown that the Earth's core is likely to consist of a similar Fe-Ni alloy, containing over 90% of the Ni present on Earth (McDonough & Sun, 1998). The remaining ∼10% is mainly bound in silicates in the mantle (average concentration of ∼2000 μg/g, (McDonough, 2003)), preferably situated in olivine but also in pyroxenes and spinel. In normal silicate melts Ni acts as a highly compatible element, with the result that the available Ni is largely contained within the mantle. Mantle rocks therefore contain significantly higher concentrations of Ni than the oceanic crust, which in turn contain more Ni than continental crustal rocks (average concentrations of 150 μg/g and 50 μg/g respectively, (Rauch & Pacyna, 2009)). However, in sulphur saturated melts, Ni will behave differently. Both natural and experimental samples have shown how Ni preferentially enters the sulphide melt during sulphide-silicate segregation (Peach et al., 1990), sometimes producing a highly enriched Ni-sulphide cumulate.

The Ni concentration in seawater is low, on average 8.2 nmol/kg (MBARI, 2011), and the element's residence time has been estimated to 10,000 years (Sclater et al., 1976). In the ocean water column Ni correlate with nutrients such as, Si and N, showing depletion in the top layers and gradual increase in concentration down to around 1000 m depth and thereafter constant, or slightly decreasing, concentration (Sclater et al., 1976). This indicate that Ni, like other first row transition metals, is a bioactive metal. The most likely speciation of Ni in seawater

is as a complex with carbonate (e.g. $NiCO_3^0$), or possibly chlorine (e.g. $NiCl^+$) (Glasby & Schulz, 1999). However, there are studies indicating that Ni may also be complexed by a variety of organic molecules (van den Berg et al., 1991; Xue et al., 2001; Turner & Martino, 2006), especially in fresh water, estuaries and costal seawater.

1.1.2 Biochemistry of nickel

Nickel is also important in biological reactions, as research during the last two decades have shown that Ni is a bio-essential metal and a key element in several key enzymes for the carbon cycle (Siegel et al., 2006). Although, theoretically, enzymes should not be consumed during the reaction they catalyse this does happen in the nature, resulting in a net uptake of Ni by the organism. This makes several biological environments dependent on a continuous supply of Ni for life-sustaining reactions to take place.

Many eucaryotic and procaryotic cells can use the waste product urea as a source of nitrogen. The Ni-enzyme *urease* is used for hydrolysing urea to ammonia and carbonic acid ($(NH_2)_2CO + 2H_2O \rightleftharpoons 2NH_3 + H_2CO_3$). Urease is found in many plants, algae and bacteria, and is therefore a critical enzyme for primary productivity. The Ni-enzymes *CO-dehydrogenase* and *hydrogenase* allow microbes to use carbon monoxide and hydrogen as their sole source of carbon and energy, by aiding the oxidation of CO to CO_2 and thereby freeing protons and electrons for energy transportation within the organism ($CO + H_2O \rightleftharpoons 2H^+ + CO_2 + 2e^-$ and

$H_2 \rightleftharpoons 2H^+ + 2e^-$). These enzymes are crucial for the functioning of e.g. aerobic nitrogen-fixing bacteria, sulphate-reducing bacteria, acetogenic bacteria and methanogens. In nature *acetyl-Coenzyme-A (CoA) synthase* appears to be found in a complex with CO-dehydrogenase, as both enzymes utilize CO and catalyse carbon-fixation reactions. However, *acetyl-CoA synthase* can also use CO_2 in place of carbon monoxide ($CO + CH_3 \cdot CFeS\text{-}Protein + CoA^- \rightleftharpoons acetyl\text{-}CoA + CFeS\text{-}Protein$). The last of the most important Ni-enzymes is *methyl-coenzyme-M reductase* (or *MCR*), an enzyme necessary for methanogens (archaea) to complete their trophic cycle and the production of CH_4. Here the Ni-containing cofactor F_{430} catalyses the last reaction in the carbon-reduction ($CH_3 \cdot S \cdot C_2H_4SO_3^- + 2H^+ + 2e^+ \rightleftharpoons HS \cdot C_2H_4SO_3^- + CH_4$) from which methanogens gain their energy.

1.1.3 Motivation for this study

The primary aim for this project has been to set up a method for analysing the stable isotope ratios of Ni and to use this to acquire data for common geological standards and materials, thereby establishing the general framework for the range of fractionation in terrestrial samples. Although isotopic fractionation in transition metal systems have become an important part of stable isotope geochemistry during the last decade, we still have very poor knowledge about the isotope geochemistry of Ni. Due to being a biologically important and geologically ubiquitous element Ni isotopes have the potential to shed light on important geochemical processes, especially in low-temperature environments, but also in high temperature

silicate, sulphide and hydrothermal systems.

1.2 Nickel isotope geochemistry

1.2.1 Stable isotope fractionation

Isotopes are atoms of the same element but of different masses, containing the same number of protons and electrons but differing numbers of neutrons. Isotopes that do not change their atomic properties by radioactive decay are considered stable. The relative proportions of the stable isotopes of an element can be different between different phases. Although all isotopes of the element take part in the same reaction, as the isotopes have different masses they may react at different rates. This results in a change in atomic abundance of isotopes in the different phases, called isotopic fractionation. This is the measurable effect of a physical, chemical, or biological, process – such as oxidation, phase changes, and change in bonding environment – affecting an element with stable isotopes.

Sample stable isotope ratios are usually expressed in the delta notation (δ), calculated as permil ($‰$) deviation from the ratios of an isotopic standard (std).

$$\delta^{i/j}E = \frac{R({}^{i}E/{}^{j}E)_{sample} - R({}^{i}E/{}^{j}E)_{std}}{R({}^{i}E/{}^{j}E)_{std}} \tag{1.1}$$

Where R is the ratio for the isotopes i and j of element E (Coplen, 2011). When comparing isotopic reservoirs the difference between reservoir a and b are calcu-

lated as the difference of R_a/R_b expressed as the fractionation factor, α_b^a:

$$\alpha_b^a \;=\; \frac{R_a}{R_b} \;=\; \frac{\delta_a + 10^3}{\delta_b + 10^3} \tag{1.2}$$

From this expression the exact difference between the two reservoirs can be calculated to be equal to $10^3 ln\ \alpha_b^a$ in the following way:

$$\alpha_b^a - 1 \;=\; \frac{R_a - R_b}{R_b} \;=\; \frac{\delta_a - \delta_b}{\delta_b + 10^3} \;\approx\; \frac{\delta_a - \delta_b}{10^3} \qquad (as\ \ 10^3 >> \delta_b) \tag{1.3}$$

$$\Rightarrow \quad (\alpha_b^a - 1) \times 10^3 \;=\; 10^3 ln\ \alpha_b^a \tag{1.4}$$

Which is approximately the difference between the δ-values for reservoirs a and b:

$$\Rightarrow \quad 10^3 ln\ \alpha_b^a \;\approx\; \delta_a - \delta_b \;=\; \Delta_{a-b} \tag{1.5}$$

Stable isotopes of an element, of an originally homogeneous reservoir, will under normal circumstances show *mass-dependent* fractionation. If m_i, m_j, and m_k are the masses of isotopes i, j, and k respectively, the isotope ratios of element A are related as follows:

$$^{k/j}A \;=\; (^{i/j}A)^z \qquad \left(where\ \ z = \frac{m_i/m_k}{m_k - m_j/m_i - m_j} \right) \tag{1.6}$$

Over small ranges in isotopic composition, this can be approximated as follows:

$$\Rightarrow \quad \delta^k A \approx \left(\frac{m_k - m_j}{m_i - m_j}\right) \delta^i A \tag{1.7}$$

This results in that the difference between isotope ratios of an element are only dependent on the mass differences between the isotopes, as long as both ratios are expressed using the same denominator. This relation produces a straight line in a three-isotope plot (e.g. $\delta^{62/58}$Ni vs. $\delta^{60/58}$Ni), known as a mass-dependent fractionation line. A sample exhibiting mass-dependent fractionation of a single homogeneous reservoir, e.g. all terrestrial samples, should plot along this line.

1.2.1.1 Fractionation processes

There are two main types of isotope fractionation: *equilibrium* fractionation and *kinetic* fractionation. Equilibrium fractionation requires that isotopic equilibrium is reached and maintained during the reaction. To accomplish this, the reactants and products need to remain in contact until reaction is completed and chemical and isotopic equilibrium has been reached. The theory behind this type of fractionation is based on the physical properties of isotopes. As quantum mechanics has shown that heavier isotopes prefer the bonding phase in the lower energy state (Valley & Cole, 2001), isotopic equilibrium will result in a concentration of the isotopically "heavy" species in such bonding sites, which are usually typified by high "force-constant" (short and stiff) bonds, where the element of interest is either in a

higher oxidation state or lower coordination state relative to "low" force-constant bonding environments.

Kinetic fractionation on the other hand is the result of reactions where the substances do not have the chance to reach equilibrium (e.g. diffusion, biological reactions, or evaporation). This could be because the reaction is proceeding too quickly for equilibrium to be reached, or because one of the substances has been removed from a system before the reaction is in equilibrium. Kinetic fractionation mainly favours the lighter isotopes of an element as these can move more quickly.

The resulting isotopic variations of the two fractionation processes follow slightly different mass fractionation rules (Young et al., 2002). These can be expressed by differences in the slope of the mass fractionation line, where β_E and β_K are the slopes for the equilibrium and kinetic fractionation lines respectively:

$$\beta_E = \frac{\left(\frac{1}{m_k} - \frac{1}{m_j}\right)}{\left(\frac{1}{m_k} - \frac{1}{m_i}\right)} \qquad \beta_K = \frac{ln\left(\frac{m_k}{m_j}\right)}{ln\left(\frac{m_k}{m_i}\right)} \tag{1.8}$$

For Ni these slopes would be $\beta_E = 2.06779$ and $\beta_K = 2.03279$, (if plotting $\delta^{62/58}$Ni vs. $\delta^{60/58}$Ni, Fig. 1.1). With such a small difference between these slopes it is unfortunately impossible to make a real distinction between the two fractionation types given the limited isotopic variability and current precision available for the Ni isotope system. Therefore, the use of a mass fractionation line has in this thesis instead only been used as a quality indicator for mass-dependent isotope data, as any delta values deviating from this line indicates either incorrectly measured

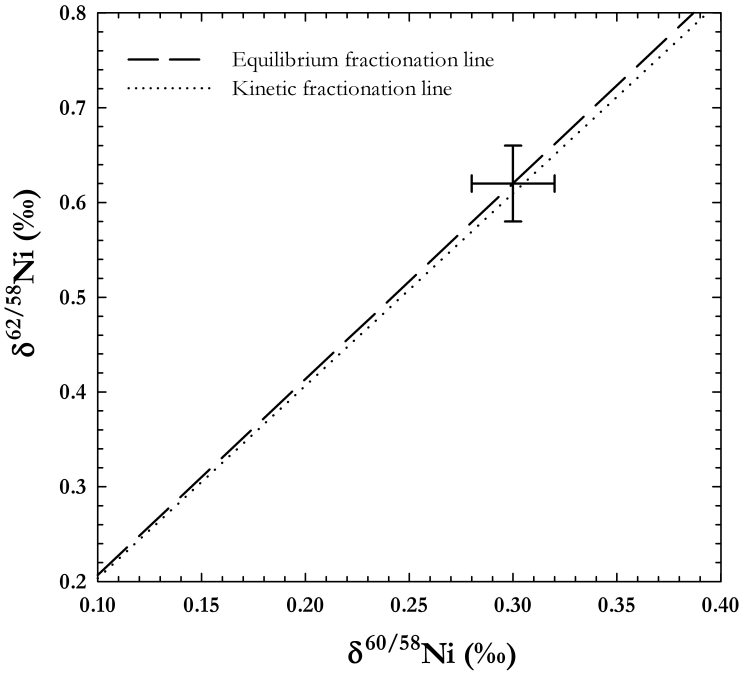

Figure 1.1: *Comparison of the equilibrium versus kinetic mass-dependent fractionation lines. Plotted are also typical error bars (2 s.e.) of a measurement to illustrate the difficulty in using this approach to separate the two fractionation processes for the Ni isotope system, due to the relatively small isotopic range and current precision available.*

isotope ratios, or that the fractionation process responsible for the samples isotopic variations is independent of mass. Mass-independent fractionation effects do occur in nature, but the processes causing such effects are considered to be different from described above and are not relevant to the processes fractionating Ni as discussed in this thesis.

1.2.2 Mixing of isotope reservoirs

If two isotope reservoirs are mixed together the contribution of each reservoir (isotope source a and b) to the isotope ratio of the mixture (mix) can be calculated:

$$\left(\frac{^iE}{^jE}\right)_{mix} = \frac{^iE_a + {}^iE_b}{^jE_a + {}^jE_b} = \frac{\left(\frac{^iE}{^jE}\right)_a {}^jE_a + \left(\frac{^iE}{^jE}\right)_b {}^jE_b}{^jE_a + {}^jE_b} \tag{1.9}$$

Which can be simplified to the following expression if substituting in f and 1-f:

$$^{i/j}R_{mix} = {}^{i/j}R_a f + {}^{i/j}R_b(1-f) \tag{1.10}$$

$$\frac{^jE_a}{^jE_a + {}^jE_b} = f \qquad \frac{^jE_b}{^jE_a + {}^jE_b} = 1-f \tag{1.11}$$

Expressed in the δ-notation, where f is the fraction of isotope source a:

$$\delta^iE_{mix} = \delta^iE_a \cdot f + \delta^iE_b \cdot (1-f) \tag{1.12}$$

Or, alternatively, with weighting of a and b by their respective concentrations:

$$\delta^iE_{mix} = \delta^iE_a \cdot f \cdot \frac{[E]_a}{[E]_{mix}} + \delta^iE_b \cdot (1-f) \cdot \frac{[E]_b}{[E]_{mix}} \tag{1.13}$$

These mixing equations are also valid for calculating the initial isotope ratio, by substituting R_{mix} for R^0, in the cases where the two fractionated isotope reservoirs are in contact with each other. However, if the different isotope reservoirs are separated after fractionation the *Rayleigh law* should instead be used to accurately

calculate the initial isotope ratio (R^0 or δ^0):

$$R_a \;=\; R^0\; f^{\alpha-1} \qquad\qquad R_b \;=\; R^0\alpha\; f^{\alpha-1} \tag{1.14}$$

Or expressed in the δ-notation, where f is the fraction of isotope reservoir a:

$$\delta_a \;=\; (\delta^0 + 10^3)\; f^{\alpha-1} - 10^3 \qquad\qquad \delta_b \;=\; (\delta^0 + 10^3)\; \frac{1-f^{\alpha}}{1-f} - 10^3 \tag{1.15}$$

1.2.3 Stable isotopes of nickel

Nickel ($Z = 28$) has five stable isotopes, ^{58}Ni, ^{60}Ni, ^{61}Ni, ^{62}Ni, and ^{64}Ni, with respective natural abundances of 68.08%, 26.22%, 1.14%, 3.63%, and 0.93% (Gramlish et al., 1989a). The basic physical properties of nickel isotopes, their weights, natural abundances and isotope ratios, were studied in detail by Aston (1935); Dempster (1936); Lub (1939); Ewald (1944) and White & Cameron (1948). Potential variations in the isotope ratios were first investigated a couple of decades later by Shima (1965) and Suzuki & Matsuo (1967). For these studies, both authors used mass spectrometry, but applied different introduction and ionization techniques to compare the isotope ratios in terrestrial silicate samples with meteorites. Shima (1965) used surface ionization and Suzuki & Matsuo (1967) gas-source by converting the samples to a highly toxic volatile Ni carbonyl gas complex ($Ni(CO)_4$), a process mainly used to purify Ni-ores. However, the results of neither study showed

a difference between crustal sample and meteorites, due to large errors on the measured isotope ratios (>1 ‰). Since then, Ni isotope ratios have been measured using thermal ionization mass spectrometry, TIMS, (e.g. Shimamura & Lugmair, 1983; Morand & Albarède, 1983), secondary ion mass spectrometry, SIMS, (e.g. Mostefaoui et al., 2005; Tachibana et al., 2006), and in recently also by MC-ICPMS (e.g. Cook et al., 2006; Quitte et al., 2006). All these studies mainly focussed on the difference between terrestrial samples and meteorites and concerned tracing radiogenic effects and nucleosynthetic variations. Hardly any attempt has been made to investigate mass dependent stable isotope variations.

As for other stable isotope systems, Ni isotope ratios are presented in the δ-notation, where isotope ratios (^{n}Ni/^{58}Ni, where n = 60, 61, or 62) are calculated pas the deviation from a pure Ni standard, expressed in ‰.

$$\delta^{n/58}Ni = \frac{(^{n}Ni/^{58}Ni)_{sample}}{(^{n}Ni/^{58}Ni)_{SRM986}} - 1 \tag{1.16}$$

The isotopic reference material used is a pure Ni metal from NIST (SRM 986), for which the isotope ratios were determined by Gramlish et al. (1989a) by TIMS analysis and calculated using ^{60}Ni in the denominator (Table 1.1). As ^{58}Ni is both the most abundant isotope and has the lowest mass of the Ni isotopes, the isotope ratios in this thesis are instead expressed using ^{58}Ni as the denominator, using the ratios from Gramlish et al. (1989a) recalculated to this denominator.

Physiochemical processes likely to cause Ni isotopic fractionation are alterations in bonding environment – e.g. changes in coordination or speciation – or

Ratio	determined values (± 2 s.d.)	Ratio	recalculated values (± 2 s.d.)
$^{58}Ni/^{60}Ni$	2.596061 ± 0.000728	$^{60}Ni/^{58}Ni$	0.385199 ± 0.000216
$^{61}Ni/^{60}Ni$	0.043469 ± 0.000015	$^{61}Ni/^{58}Ni$	0.016744 ± 0.000021
$^{62}Ni/^{60}Ni$	0.138600 ± 0.000045	$^{62}Ni/^{58}Ni$	0.053389 ± 0.000065
$^{64}Ni/^{60}Ni$	0.035295 ± 0.000024	$^{64}Ni/^{58}Ni$	0.013596 ± 0.000026

Table 1.1: *Isotope ratios of NIST SRM986, as determined by Gramlish et al. (1989a).*

biologically mediated processes, and probably not redox processes. Nickel has the electron configuration [Ar] $3d^8 4s^2$, resulting in Ni normally being present in either the 0 or +II oxidation state. The +I and +III oxidation states can theoretically exist under certain conditions, but are not stable in aqueous solutions. Therefore, redox reactions are not directly of importance for Ni isotopic fractionation in nature. This lack of participation in redox reactions also separates Ni from most other first row transition metals, which makes the study of Ni isotope geochemistry an interesting addition to other, already established, elements in the field of non-traditional stable isotopes, such as Fe and Mo.

1.3 Previous work on nickel isotopes

1.3.1 Nickel isotopes in cosmochemistry

Previous research into Ni isotope geochemistry has almost exclusively focused on extraterrestrial samples, searching for isotopic anomalies on some, or all, of the heavier Ni isotopes. Isotope anomalies are enrichments or depletions compared to a terrestrial standard that are mass-independent. If found they could potentially

provide information about what type of nucleosynthetic processes (*s*-, *r*-, or *p*-processes) were active over the period leading up to the time our solar system formed (Birck, 2004). Nickel is especially interesting in cosmochemistry because excess ^{60}Ni may be the in-situ decay product of the extinct short-lived radionuclide ^{60}Fe, which decays to ^{60}Ni by β^--decay and a half life of 1.49 Myrs. Many studies have been published over the years searching for evidence of extinct ^{60}Fe (measured as isotopic excess abundance on ^{60}Ni), as the relatively short half-life (1.49 Myrs) of this radionuclide makes it potentially useful as a fine scale chronometer for dating early processes, such as differentiation (or crystallisation) of planetary material. The presence of extinct ^{60}Fe in extraterrestrial materials has also been studied as a way to investigate the degree of element heterogeneity in the protoplanetary disk.

The first publications to focus on isotopic anomalies in Ni were Morand & Albarède (1983) and Shimamura & Lugmair (1983), but due to large analytical errors no conclusions could then be made concerning the possible existence of such anomalies. The first indications of traces from ^{60}Fe were found in calcium-aluminium inclusions (CAI) in the carbonaceous chondrite Allende a few years later, by Birck & Lugmair (1988). Since then several studies have identified similar ^{60}Ni-anomalies in a variety of meteorites and CAIs (e.g. Mostefaoui et al., 2005; Quitte et al., 2007; Guan et al., 2007; Regelous et al., 2008), while others report not finding any ^{60}Ni-anomalies with current analytical precision (e.g. Cook et al., 2006; Moynier et al., 2007; Chen et al., 2009), indicating that all Ni in the solar system must have come from a single Ni-isotope reservoir.

At present, there are few published studies concerning mass-dependent Ni isotope fractionation in extraterrestrial materials. Cook et al. (2007) and Moynier et al. (2007) measured the Ni isotopic composition in the metal fraction from different classes of meteorites (e.g. chondrites, mesosiderites, pallasites, and iron meteorites). Both studies found mass fractionations of up to ∼0.4 ‰ per mass unit, for all types of meteorites. However, as these analyses are difficult to interpret without knowing the fractionation in the whole rock samples only data for the iron meteorite samples from these studies have been taken into account here.

The only studies to have measured mass-dependent Ni isotope variations in whole rock samples of different type of meteorites are Cameron et al. (2009) and Steele et al. (2011). Here, one sample each for a range of different meteorites (ordinary chondrites, carbonaceous chondrites, enstatite chondrites, and different iron meteorites) were analysed with results showing even less variation between the different meteorite classes, only varying 0.08 ‰ per mass unit (Fig. 1.2). As no systematic variation between meteorite classes could be found both studies concluded that all Ni isotopes must have fractionated from a single reservoir.

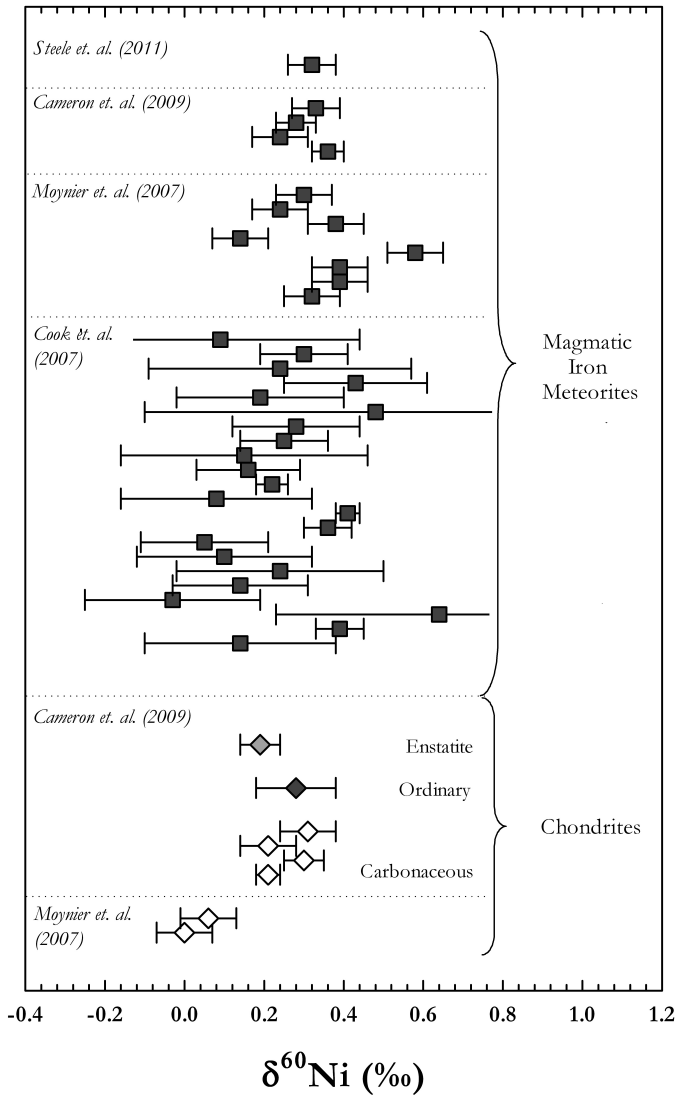

Figure 1.2: *Published data of Ni isotope compositions in whole rock meteorite samples, from Cameron et al. (2009), Moynier et al. (2007) and Cook et al. (2007). Error bars are 2 s.d.*

1.3.2 Nickel isotopes in terrestrial samples

The work presented in this thesis focuses on mass-dependent fractionation of Ni isotopes in terrestrial samples. At the start of this project the range of potential isotopic variations in terrestrial reservoirs was essentially unknown. The only published study concerning any type of terrestrial samples was Tanimizu & Hirata (2006), where the isotopic variation in a variety of commercial Ni-metals and in two Ni-sulphides was measured with the aim of establishing the true atomic weight of Ni and the adequacy of NIST-SRM 986 as a representative terrestrial standard.

The first study on Ni isotopes in a variety of terrestrial geological samples was published in 2009. In this publication Cameron et al. (2009) presented data for a range of whole rock standard samples representing the mantle and crust (Fig. 1.3) with the aim to establish the variation in Ni isotopic composition occurring in abiotic terrestrial samples. Their results showed that the range of Ni isotope fractionation in these geological samples were limited to only a few tenths of a permil, with no significant different between mantle and crust materials, with an average of $\delta^{60}\text{Ni} = 0.15 \pm 0.24$ ‰ (2 s.d.).

Also plotted in Fig. 1.3 are analyses of peridotites, from Steele et al. (2011), and sulphides, from Tanimizu & Hirata (2006). The two peridotites agree well with the main body of silicate rocks from Cameron et al. (2009), although the one peridotite analysed in this study display a significantly heavier δ^{60}Ni-value. The sulphides show large variations compared to igneous rocks. However, the two samples show opposite values, with the pentlandite ($(Fe,Ni)_9S_8$, from Sudbury,

Canada) displaying a very heavy value, while the millerite (NiS, from Manitoba, Canada) shows a very light value. This is possibly due to the different lattice structure in the two sulphides, which would lead to different Ni coordination numbers and could thus cause fractionation. These sulphide data show the possibility for inorganic mass-dependent fractionation of Ni in terrestrial samples.

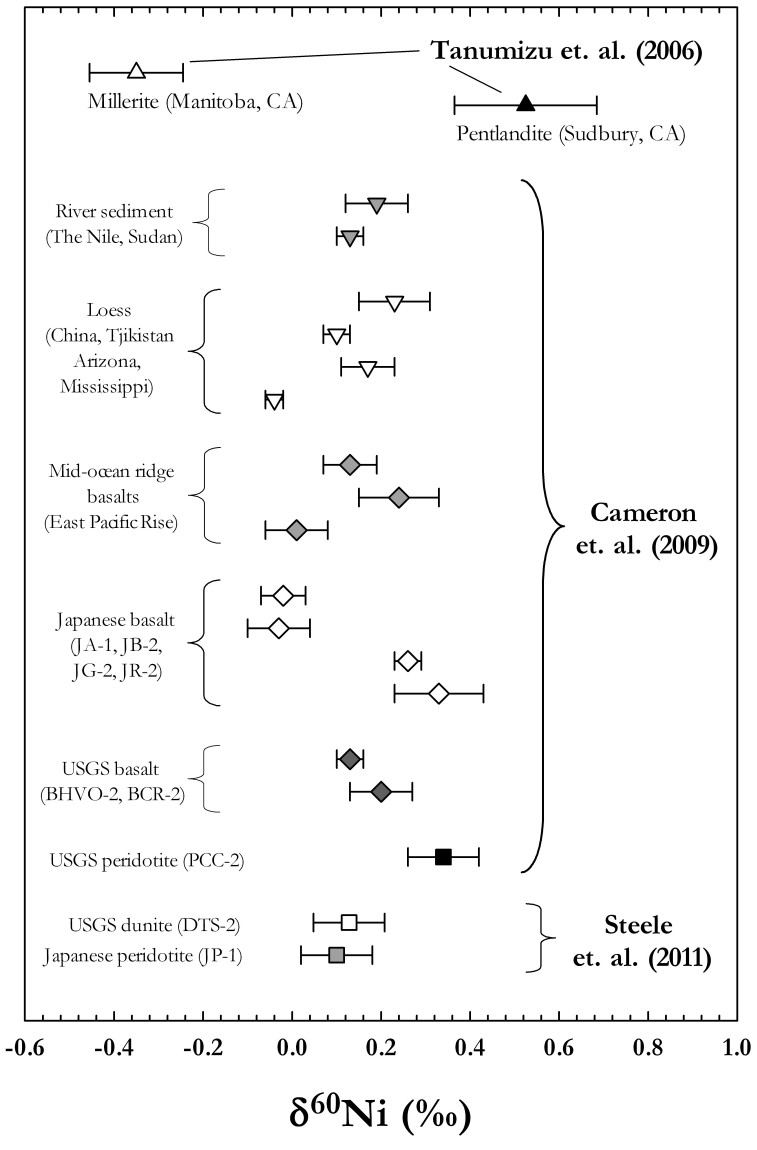

Figure 1.3: *Published Ni isotope ratios of abiotic terrestrial samples, data from Cameron et al. (2009), Steele et al. (2011), and Tanimizu & Hirata (2006).*

Cameron et al. (2009) also investigated if methanogens fractionate Ni isotopes. Four species of Archea (three methanogens and one heterotrophic Archea) were grown under controlled conditions and the Ni isotopic composition of the original growth solution, the residual media and the cultured cells were measured. The results showed that the methanogens in this experiment clearly fractionate the Ni isotopes toward lighter δ-values, unlike the non-methanogenic Archea which essentially showed no fractionation. This demonstrates potential for isotopic fractionation to take place in specific environments mediated by specific organisms.

1.4 Outline of this thesis

Separating Ni from a geological matrix and establishing an analytical protocol to accurately and precisely determine the Ni isotope composition has been a challenging task, requiring a significant amount of time during my D.Phil. project. In chapters two and three, I present a method for Ni separation from geological matrices and isotopic analysis of mass-dependent Ni isotope variations by multi-collector inductively coupled plasma mass spectrometer (MC-ICPMS), employing the double-spike method to correct for instrumental mass bias. Chapter four evaluates possible fractionation of Ni in high temperature environments, e.g. the mantle and crust. Here I show preliminary Ni isotope data for a range of silicate rock samples and discuss their variation in the light of which processes that possibly could cause fractionation. In this chapter is also an estimated value of the Ni isotopic composition of the bulk silicate Earth compared to Ni isotope data from a range of

meteorites to determine if core-mantle differentiation could have caused mass fractionation of the total terrestrial Ni pool. To complete the inventory of the range of Ni isotope variations, chapter five is completely focussed on low temperature Ni isotope geochemistry. Here I discuss the varying Ni isotopic composition in surface scrapings of globally distributed hydrogenetic ferromanganese crusts. Finally, as Ni is a commonly used metal as well as being regularly used as a tracer in the oil industry my last chapter, number six, is focussed on the possibility of using Ni isotopes for understanding the formation of Ni ore deposits and for tracing crude oil reservoirs.

CHAPTER

TWO

NEW PREPARATION TECHNIQUE FOR QUANTITATIVE SEPARATION OF NICKEL FROM A GEOLOGICAL SAMPLE MATRIX

(This chapter is published as: ***Determination of mass-dependent variations in nickel isotope compositions using double spiking and MC-ICPMS***, *L. Gall, H.M. Williams, C. Siebert, and A.N. Halliday, J. Anal. At. Spect., 2012, 27, 137-145*)

2.1 Introduction

When measuring stable isotopic compositions using MC-ICPMS, sample purification prior to measurements is crucial for data quality. Separating the element of interest from the sample matrix removes the possibility for molecular and isobaric interferences during, or induce other artefacts such as changing the instrumental mass discrimination.

As discussed in the previous chapter, other studies on Ni isotopes have predominately focused on mass-independent effects in iron meteorites (e.g. Quitte et al., 2006; Cook et al., 2006; Chen et al., 2009), from which separation of Ni is relatively straightforward, mainly comprising of anion-exchange chemistry in HCl media. As the aim of these previous studies mainly was to investigate the occurrence of isotopic anomalies in extra-terrestrial materials, quantitative yields of Ni were not required, as any isotopic fractionation during chemical processing is corrected for by internal normalisation. Only a few studies address purification of Ni from more complex matrices, such as silicates rocks.

A very limited amount of work has been published on methods for investigating mass-dependent isotope effects. These studies employed a range of methods for the extraction of Ni, but all are mainly based on the Ni-complexing ability of dimethylglyoxime (from here on DMG), an organic chelator highly selective for Ni under alkaline conditions. Quitte & Oberli (2006) proposed a solvent extraction method using a solution of DMG-in-ethanol together with chloroform as the organic extraction phase. Regelous et al. (2008) developed a three column set-up

using a DMG-in-acetone mixture, originally based on Victor (1986). Cameron et al. (2009) used the commercially available Nickel-Specific Resin, by Eichrom Inc., also suggested by Quitte & Oberli (2006), which binds Ni to DMG in the resin polymer.

The solvent extraction method suggested by Quitte & Oberli (2006) does not give as high a yield as column chromatography and may also cause mass-independent fractionation, as shown for Zn by Fujii et al. (2010), which is why this method was discarded as unsuitable at an early stage. The DMG-in-acetone column procedure (Regelous et al., 2008) requires significant volumes of DMG per sample in order to fully separate Ni from Na, Mg and Ca, which display similar chemical behaviour to Ni. Such large quantities of DMG are potentially problematic, as DMG is an organic molecule which must be completely broken down and decomposed prior to mass spectrometry. Methods of Ni purification employing Ni-specific resin (Cameron et al., 2009; Quitte & Oberli, 2006) also involve large quantities of DMG, although in this case DMG is bound to the resin beads. In this technique, Ni is eluted in a mixture of DMG and resin polymer, and it is very difficult to fully destroy the organics in the sample post-chromatography. Another disadvantage of the Ni-specific resin is that the sample need to be adjusted to a particular pH (8.0-8.5) before loading on the resin, which in turn determines the success of the Ni extraction procedure.

In the studies mentioned above, the purification protocols developed were either designed for very specific sample matrices or the procedure requires a very long

time to be completed due to difficulties with breaking down the organics used in the chromatography. Therefore, the first part of this project aims to develop a new, quicker, Ni separation protocol that could consistently produce quantitative yields of Ni from a wide range of geological samples. The chromatography procedures investigated during the process establishing this new separation procedure, as well as the final protocol itself, is described in detail in the following sections.

2.2 Sample digestion

2.2.1 Reagents

All chemical work during sample preparation was performed under clean laboratory conditions at the Department of Earth Sciences in Oxford. All acids (HCl, HNO_3, HF) used in the procedure were purified by in-house sub-boiling distillation. Solutions of dimethylglyoxime (DMG), ammonium-citrate ($(NH_4)_2C_6H_6O_7$) and sodium hydroxide (NaOH) were prepared from crystalline commercial reagents, ammonia solution (NH_3 or NH_4OH), acetone and ethanol were reagent grade solutions, and dichloromethane (DCM) used for solvent extraction was of trace element grade – all from Fischer Scientific. Any water added during chemistry was 18.2 MΩ-grade taken from a Milli-Q Element water purification system.

2.2.2 Wet digestion

Silicate samples were dissolved by conventional digestion methods, using concentrated HF-HNO_3 mixtures, in a volume ratio of 5:1, in pre-cleaned Savillex teflon beakers left on a hotplate at 130^{o}C overnight. The sample solution was evaporated to dryness and the residue dissolved in small amounts (0.2 mL) of concentrated HNO_3 and left to evaporate. This procedure was repeated three times to completely drive off fluorides formed during the first digestion step. The last stage of digestion comprised refluxing the sample in approximately 5 mL 6M HCl. This step was repeated twice if complete dissolution was not achieved in the first reflux cycle. During the whole digestion procedure the sample was treated several times in an ultrasonic bath for 15 minutes at a time. Oxide samples were treated similar to silicates, although without addition of HF to the digestion acids.

After complete digestion the sample was dried down, converted to nitrate form by adding a drop of concentrated HNO_3, taken up in 2% HNO_3 and analysed for Ni concentration using a quadrupole ICP-MS. This procedure was necessary for any samples for which the Ni concentrations was not already known. To each sample was then added a specific volume of double-spike solution (in 2% HNO_3) to achieve a sample-to-spike ratio of 0.4 (see chapter 3 for details on double-spike calibration). The mixture was then fluxed on a hotplate for at least 24 hours to ensure complete equilibration between sample and spike solution.

2.2.3 Microwave-assisted digestion

Silicate samples with high organic carbon content (e.g. shales and sediments) were digested in an Anton Paar Multiwave 3000 microwave. Approximately 0.1g of sample was added to a pre-cleaned teflon XF-100 vessel, to which were added concentrated acids as follows: 4 mL HF, 2 mL HCl, and 2 mL HNO_3. The samples were digested for 1 h at 800 W, during which time the maximum pressure and temperature reached was 60 bar and 220^{o}C respectively. After full digestion the samples were transferred to pre-cleaned Savillex teflon beakers and treated with multiple cycles of HNO_3 and ultimately 6M HCl, in a similar manner to other silicate samples, as described above.

Crude oils were digested using a CEM MARS microwave. To account for sample heterogeneities (mainly due to large differences in density between small and large carbon chain/complexes) samples of each crude oil were dissolved in trace metal grade dichloromethane (DCM) and then transferred to clean microwave teflon vessels. The DCM was then completely removed by evaporation over night on a hotplate at 70^{o}C. Each crude oil sample was first subjected to two back-to-back microwave digestions. For these two runs, the microwave was programmed to increase power linearly (ramp) up to 220^{o}C over a 25 minutes period at a maximum power of 1600 W with a maximum pressure of 80 bars. This temperature was then held for 25 minutes. After these digestions were completion 2 mL of hydrogen peroxide (30% wt. concentration) was added to each vessel for a third microwave run. For this last run the microwave was programmed to ramp to 235^{o}C over a 25

min period at a maximum power of 1600 W with a maximum pressure of 80 bars.

After completed microwave digestion the sample solutions were transferred to cleaned Savillex beakers and evaporated to complete dryness. To remove any last remains of organic material the sample was boiled in aqua regia (1:3 of HNO_3:HCl) and then in equal amounts of concentrated distilled HNO_3 and H_2O_2 on a hotplate (130^oC). This procedure was repeated several times until the solution was clear.

2.3 Ion Exchange Chromatography

To compare the efficiency of different separation methods, calibration solutions of geologically important matrix elements (e.g. Mg, Al, Ca, Fe, Ti, Mn) and elements of possible isobars (e.g. Cu, Zn, Cd, Sn) were made up of elemental plasma standards (Alfa Aesar). Both a solution containing equal concentrations of the elements as well as a solution mixed to represent matrix-to-analyte ratios found in nature (e.g. 1000 ppm Mg : 1 ppm Ni) were used. The final separation procedure was tested on a variety of different natural matrices, mainly USGS rock standards.

Cation exchange chromatography is based on the principle that positive ions, or molecules, in a solution will be retained on the resin due to coulombic interactions with the negatively charged functional groups in the resin polymer. How strongly the ions are retained on the resin depends on the ionic strength of the solution (i.e. concentration of solutes/acid) together with the complex-binding abilities of the solution (i.e. type of solutes/acid). Anion exchange chromatography is based

on the opposite principals to cation exchange chromatography. Here the resin polymer instead contains positively charged functional groups, which will bind to anions in the solution. For separation of cations on an anion resin this means that the controlling factor, i.e. whether an element is retained by the resin or not, is the affinity for cations to form complexes with anions in the acid of choice.

Quantitative separation and purification of Ni from geological matrices is particularly challenging due to the similarity in chemical behaviour of Ni to a number of other elements that are abundant in geological samples, especially the alkali and alkaline earth metals (e.g. Na, Mg, and Ca), but also the trivalent cations of Cr, Ti and Al. This difficulty is further exacerbated by the abundance of these elements in geological samples relative to Ni, which is most often present in trace quantities. To methodically investigate the properties of Ni during ion exchange chromatography, the synthetic calibration solutions were tested using a range of different acids and solvents. All separation experiments were at first hand performed on 2 mL Bio-Rad polypropylene columns, as these are non-expensive and disposable. All procedures were then scaled down to either 1 mL or 0.2 mL teflon columns to reduce the overall blank for each sample before fine tuning the column calibrations.

Hydrochloric acid: In hydrochloric media Ni has a very small distribution coefficient over all acid molarities when put over an anionic exchange resin. Fe, Cu, and Zn (together with V, Co, Ga, Ge, Zr, Mo, Ru, Pd, Cd, Sn, Sb, Te, Hf, W, Os, Pt, Au, Hg, Tl, Bi, and U) are on the other hand retained by the resin at higher acid

concentrations (> 4M HCl, Saito (1984)). An anion exchange column (resin AG1-8X or AGMP-1M) can therefore be used to separate Ni from the most important interfering element, Fe. As ^{58}Fe is virtually impossible to resolve from ^{58}Ni in the mass spectrometer, a complete separation of the two elements is necessary. Tests performed during my calibration experiments showed that a 6M HCl solution containing small amounts (0.05%) of hydrogen peroxide (H_2O_2) provides the best purification results. The Ni distribution coefficient for a cation resin in HCl media varies strongly with acid concentration. At low HCl concentrations (< 0.2M) Ni will stick to the resin, but higher concentrations (> 3M) will make the element elute completely (Saito, 1984; Strelow, 1960). This feature was useful for the cation exchange chromatography experiments discussed below as 3M HCl always could be used as an eluting agent after the matrix separation tests were performed.

Hydrofluoric acid: Weak solutions of hydrofluoric acid can be used to separate Ni from elements that display high affinity to form negative fluoride complexes (e.g. Al and Ti) (Fritz et al., 1961; Saito, 1984). As Ni itself does not tend to form fluoride complexes, it will be strongly retained on a cation resin while Al, Ti, Cr, Fe, etc. will elute as complexes. When this method was tested using a synthetic calibration solution, the results showed that some of the fluoride complexed elements were still retained on the resin (Fig. 2.1, black staples). A combination of weak solutions of HF and HNO_3 provided better results, tailoring the separation further (Fig. 2.1, grey staples) by also eluting the alkali metals and Al, but the tests revealed that small amounts of Ni (∼10%) were also eluted.

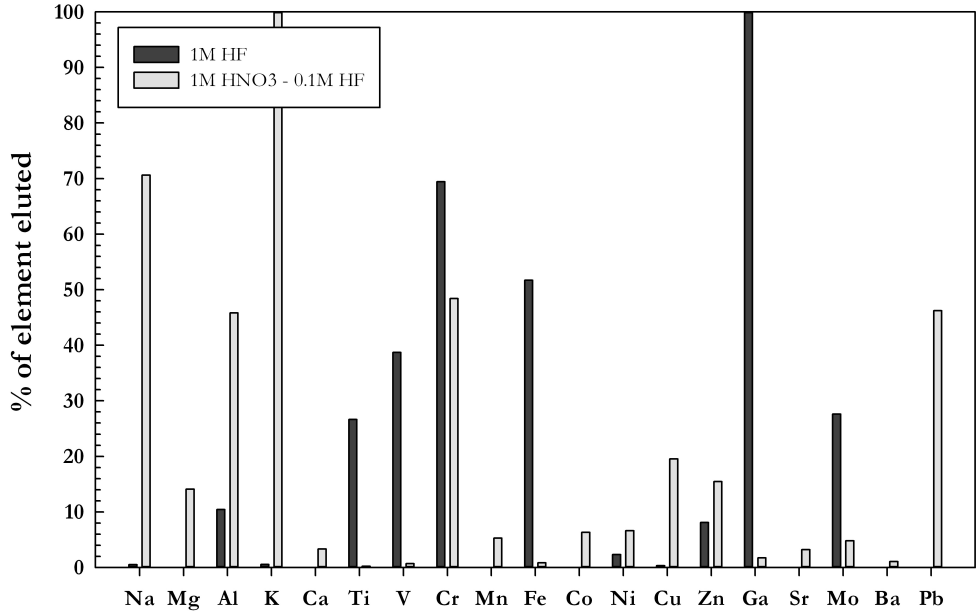

Figure 2.1: *Separation experiment of a synthetic calibration solution containing equal concentrations of the elements plotted. The experiment was performed using 2 mL columns filled with cation resin (AG50W-X4). After preconditioning the resin and loading the calibration solution, the column was washed with 5 mL each of first 1M HF followed by 0.1M HF–1M HNO while collecting the elute.*

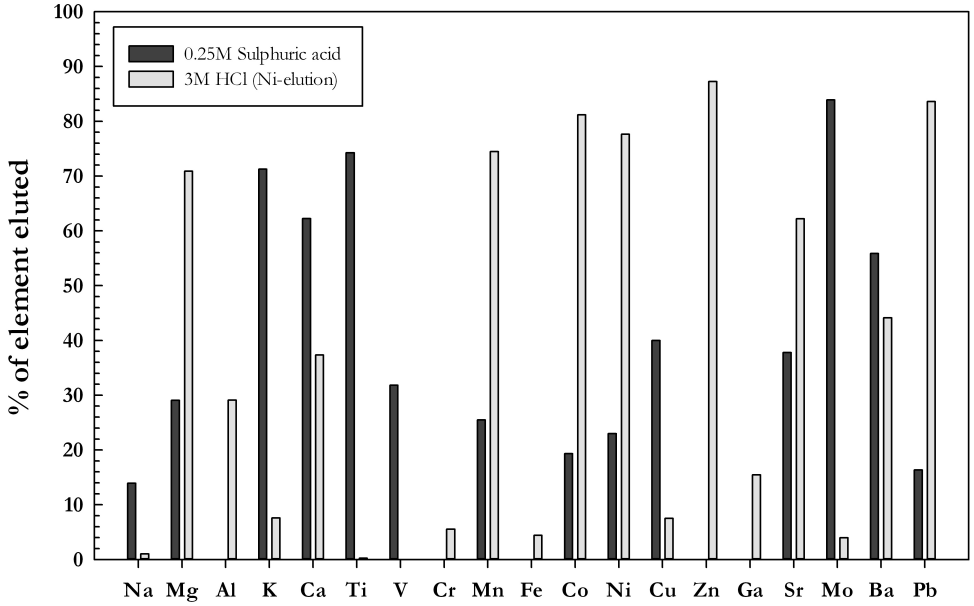

Figure 2.2: *Separation experiment of a synthetic calibration solution containing equal concentrations of the elements plotted. The experiment was performed using 2 mL columns filled with cation resin (AG50W-X4). After preconditioning the resin and loading the calibration solution, the column was washed with 5 mL each of first 1M H_2SO_4 followed by 3M HCl while collecting the elute.*

Sulphuric acid: Strelow et al. (1965) and Strelow & Bothma (1967) showed that weak solutions of sulphuric acid (H_2SO_4) on a cation resin can be used to separate Ni from Cr and Ti. When tested the results showed that matrix elements were satisfactorily eluted using 0.25M H_2SO_4, but so was a significant fraction ($\sim$ 20%) of the Ni in the solution (Fig. 2.2).

Hydrochloric–Oxalic acid: A mixture of weak solutions of oxalic acid and HCl should according to the distributions coefficients published in Strelow et al. (1972) be successful in separating Ni from several geological important elements. Tests using anion resin showed that different oxalic acid–HCl mixture indeed are very effective of separating Ni from Al, V, Ti, and partly from Cr, as these elements stick on the resin as negative oxalic complexes while Ni is eluted (Fig. 2.3). To avoid the difficulty of breaking down any remaining organics in the Ni-cut, the same procedure was also tested using cation resin instead, where, theoretically, Ni should be retained on the resin while elements forming oxalic complexes are eluted to waste. Afterwards, the Ni could then be eluted using 3M HCl (Fig. 2.4).

Hydrochloric–Acetone: The combination of HCl and acetone has been investigated for column chromatoraphy in several studies (e.g. Fritz & Rettig, 1962; Strelow & Victor, 1972). Distribution coefficients calculated by these studies shows that Ni is strongly retained on the resin, This makes HCl-acetone mixtures very effective for separating Ni from most other transition metals. It does not, however, separate Ni from any alkali or alkaline earth metals (Fig. 2.5).

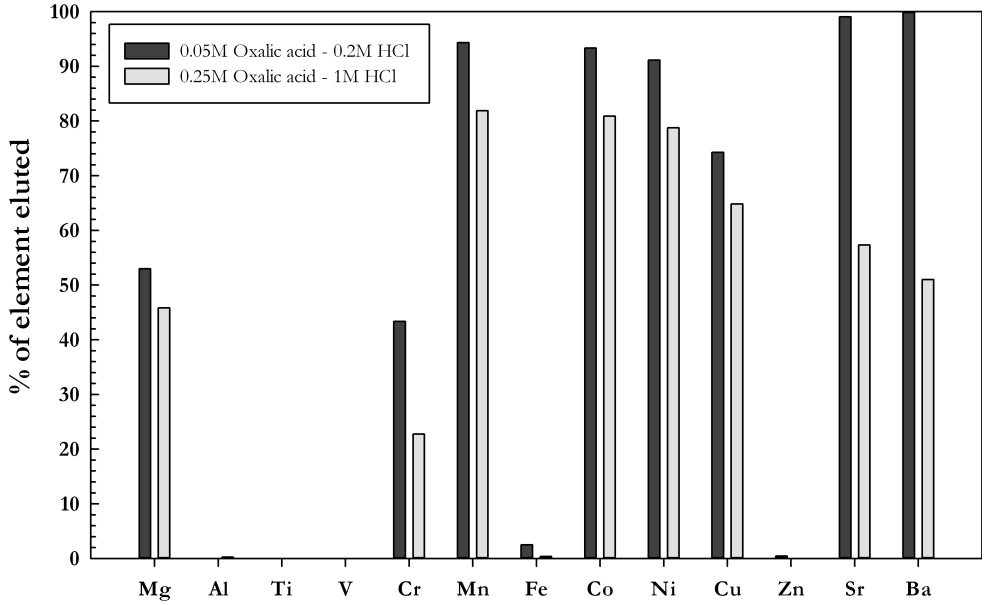

Figure 2.3: *Separation experiments of a synthetic calibration solution containing equal concentrations of the elements plotted. The experiments were performed using 2 mL columns filled with anion resin (AG1-X8). After preconditioning the resin and loading the calibration solution, the column was washed with 5 mL each of 0.05M Oxalic acid–0.2M HCl followed by 0.25M Oxalic acid–1M HCl while collecting the elutes separately.*

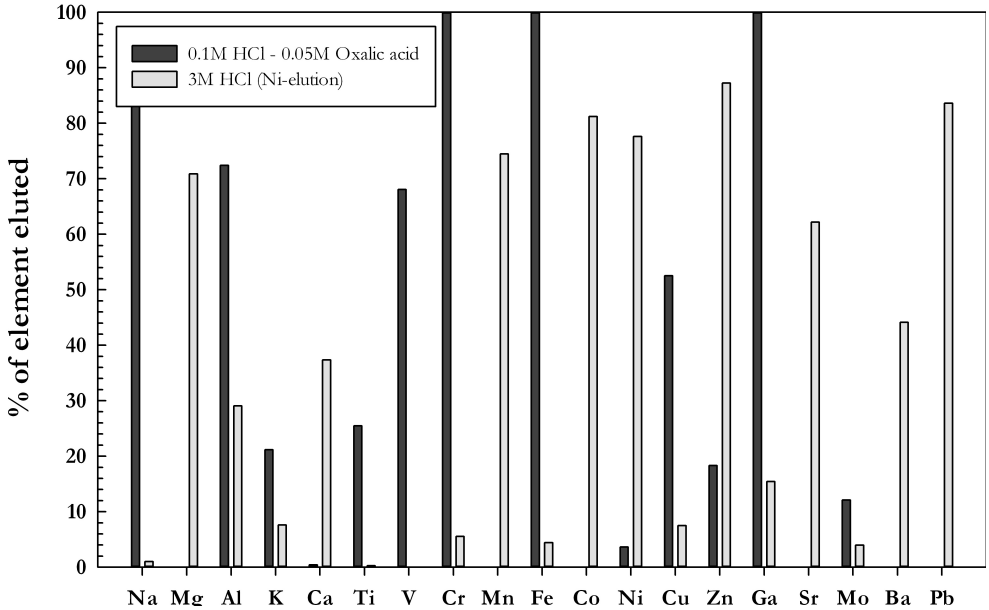

Figure 2.4: *Separation experiments of a synthetic calibration solution containing equal concentrations of the elements plotted. The experiments were performed using 2 mL columns filled with cation resin (AG50W-X4). After preconditioning the resin and loading the calibration solution, the column was washed with 5 mL each of 0.05M Oxalic acid–0.2M HCl followed by 3M HCl while collecting the elutes separately.*

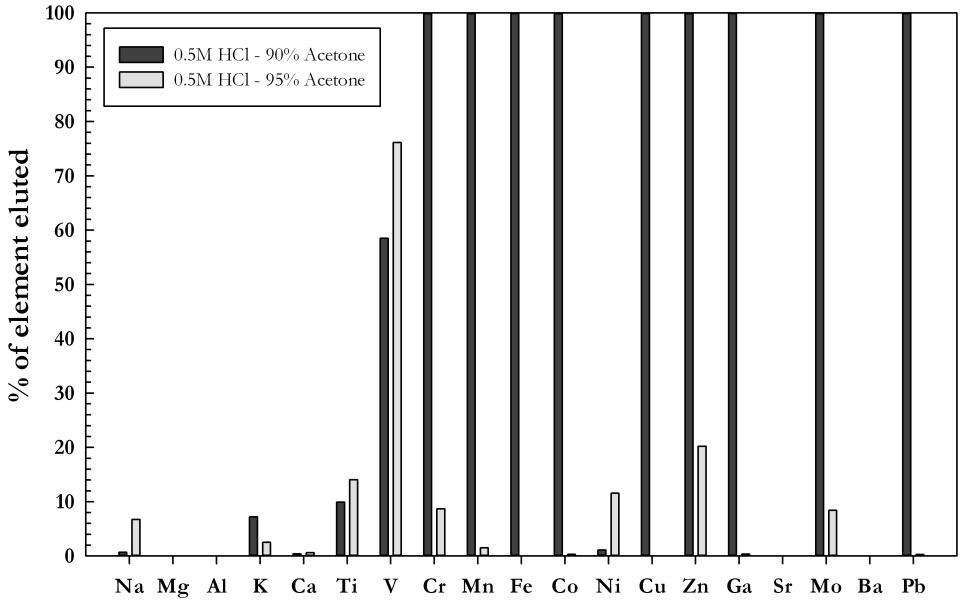

Figure 2.5: *Separation experiments of a synthetic calibration solution containing equal concentrations of the elements plotted. The experiments were performed using 2 mL columns filled with cation resin (AG50W-X4). After preconditioning the resin and loading the calibration solution, the column was washed with 5 mL each of 0.5M HCl in 90% acetone followed by 0.5M HCl in 95% acetone while collecting the elutes separately.*

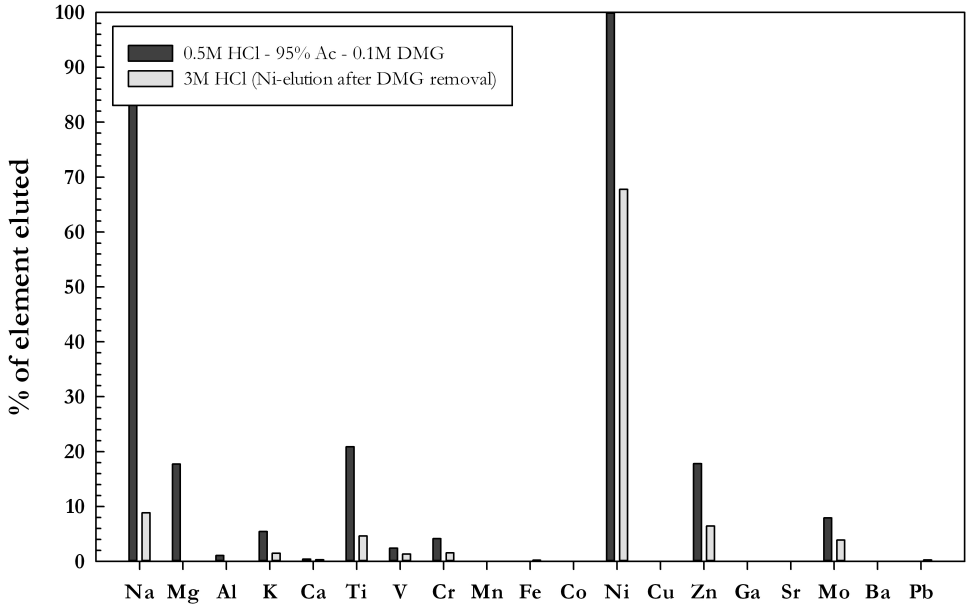

Figure 2.6: *Separation experiments of a synthetic calibration solution containing equal concentrations of the elements plotted. The experiments were performed using 2 mL columns filled with cation resin (AG50W-X4). After washing off matrix elements from the column with HCl-acetone mixtures as described above, Ni was eluted as a DMG complex by adding DMG dissolved in an acetone-HCl-solution. The HCl-cut shows the DMG-complex directly added on another cation column and rinsed from DMG before elution with 3M HCl.*

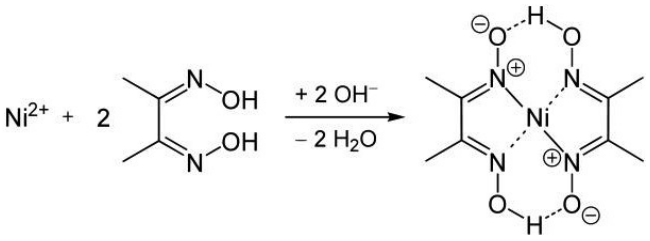

Figure 2.7: *Schematic illustration of complexation of Ni^{2+} by di-methylglyoxime .*

Hydrochloric–Acetone–DMG: In chemistry, the most widely used method for determining the of presence Ni is based on Victor (1986), who used a combination of the high distribution coefficient for Ni in a mixture of HCl and acetone with the specific affinity of the organic chelator di-methylglyoxime (DMG) to complex Ni under alkaline conditions (Fig. 2.7). The experiments performed here showed the DMG-complexation to be very selective and only small amounts of Cr, Ti, V and Fe accompany Ni in the eluted solution (Fig. 2.6). However, the Ni-DMG-complex is difficult to completely break down and the remnants thereof can interfere with subsequent sample chemistry.

Ammonium citrate–Ammonium hydroxide solution: Strelow (1990) report that a weak solution of ammonium citrate in combination with excess ammonia can be used for separating Ni from the other s-block elements. The basis for this separation is that free ammonia bind strongly to the more electronegative divalent ions present in the sample (e.g. Ni and Cu), while other divalent elements (e.g. Mg and Ca) prefer to bind as citrate complexes in this solution. As Ni forms a cationic complex with ammonia ($Ni(NH_3)_n^+$) this is retained on a cation resin, while the neutral citrate complexes are eluted.

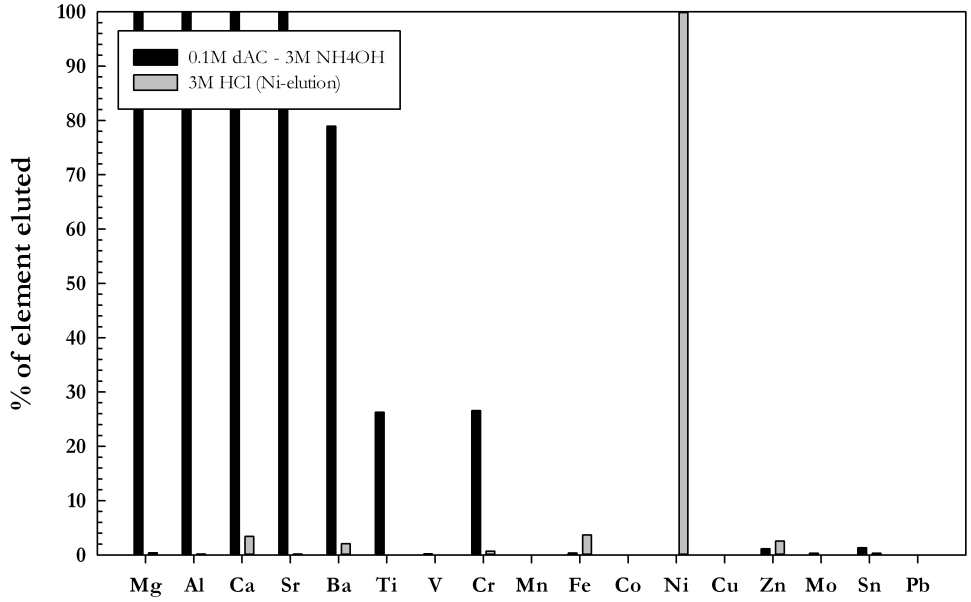

Figure 2.8: *Separation experiments of a synthetic calibration solution containing equal concentrations of the elements plotted. The experiments were performed using 2 mL columns filled with cation resin (AG50W-X4). After preconditioning the resin and loading the calibration solution, the column was washed with 5 mL each of 0.1M di-ammonium-citrate (dAC) in 3M ammonium solution (NH_4OH) followed by 3M HCl while collecting the elutes separately.*

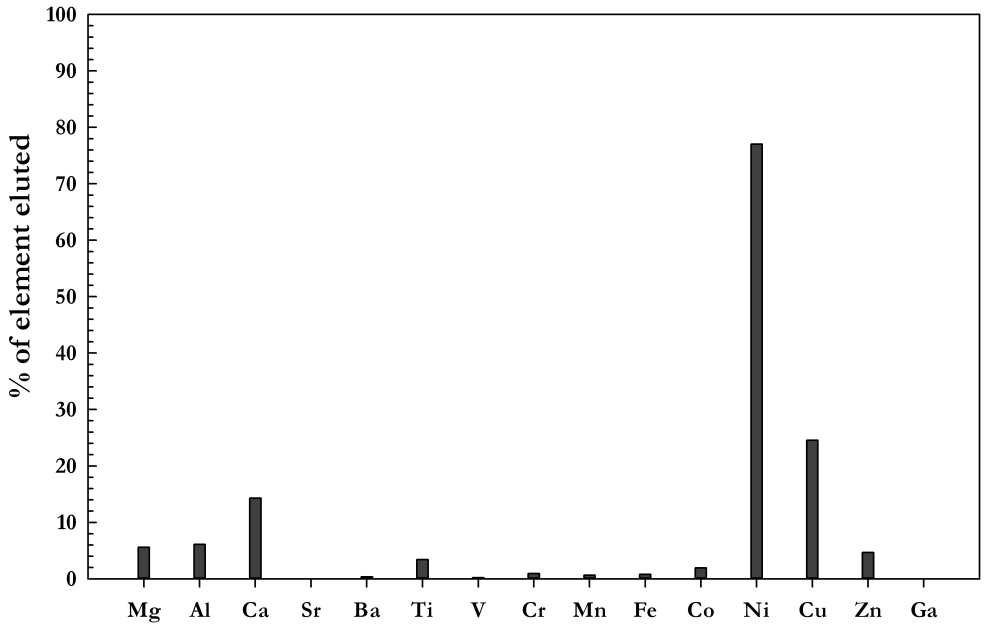

Figure 2.9: *Separation experiment using the Ni-specific resin from Eichrom Inc. Here only the Ni-eluting cut (3M HNO_3 used as eluting agent) has been plotted in the figure. The results show that only Cu and minor amounts of Fe, Co, Zn, Mg, Ca, and Al are let through together with the Ni.*

After complete elution of matrix elements the Ni-complex can be eluted by 3M HCl. As is shown in Fig. 2.8 this method successfully separates Ni from most other matrix elements. However, as Ni is eluted as an ammonia-complex the ammonium ions (NH_4^+) need to be removed before isotope analysis of the purified solution is possible.

2.3.1 Nickel-specific resin

An alternative for separating Ni from a geological matrix is to use the 'Nickel specific resin' from Eichrom Technologies Inc. (as used by Cameron et al. (2009)). This resin holds DMG in the pore space of an inert polymer and in this way also make use of the complex-forming properties of DMG. The sample, dissolved in ammonium citrate, is passed through a column where Ni is adsorbed within the resin while most other matrix elements are washed through, after which Ni can be collected using 3M HNO_3. The resin should effectively separate Ni from all other elements of importance in a geological matrix. Although the method appears simple there are some major disadvantages. The resin is strongly pH-dependant and will only function properly if the sample and wash solution are held between pH 8 and 8.5. If the pH is outside of this narrow range, any Ni present in the sample will be washed of the column and is impossible to retrieve from the ammonium citrate solution. If Ni is retained on the column the second major difficulty consists of breaking down the organics present after drying down the subsequent elute. Due to the resin polymer contained in the elute the end product

is a large mass of organic material that is extremely difficult to break down, which is necessary for further chromatographic treatment and isotope analysis.

2.3.2 Procedure for separating Ni from a geological matrix

Using the results and experience gained from testing of the procedures described above an effective and quantitative procedure for separating Ni form a variety of geological matrices has been developed. The total procedure for Ni purification involves three steps of column chromatography. The new method also minimises the volumes of DMG to simplify the post-purification treatment of the sample. The first step involves separation of Ni from the s-block elements (e.g. Na, K, Mg, and Ca), and other geologically important cations (e.g. Al and Ti) by using weak solutions of di-ammonium citrate ($(NH_4)_2C_6H_6O_7$) in combination with excess NH_4OH. The chemical basis for this extraction method is that the excess ammonia binds to the more electronegative divalent ions present in the sample (e.g. Ni, Cu, Zn) by forming an ammonia-complex (such as $(NH_3)_n{}^+$), which is strongly bound to the resin. Other elements (e.g. Mg, Al, Fe) preferentially form citrate complexes, which do not attach to the resin under these conditions and are thus eluted (Strelow, 1990). The second step of the separation procedure is adapted from Victor (1986) and Strelow et al. (1972) and employs firstly oxalic acid-HCl solutions which separate elements with valencies $>$ +II (e.g. Fe, Al, Cr, and Ti) which elute as oxalic complexes, and subsequently HCl-acetone mixtures which elute divalent elements (e.g. Mn, Cu, Zn, Cd, Sn). Nickel is finally eluted as

a Ni-DMG complex in HCl-acetone media. The final chromatography step is a miniature clean up anion-exchange column, which completely separates Fe from Ni using HCl-H_2O_2 mixtures. These procedures are described in detail below.

Nickel Purification: Step 1 Dissolved and spiked (see Chapter 3) samples were evaporated and converted to chloride form, then redissolved in 2 mL 0.5 HCl, to which 0.3 mL 1M di-ammonium-citrate and 0.6 mL concentrated NH_4OH were added, creating a solution of approximately 3M NH_4OH in 0.1M di-ammonium-citrate. The sample solutions were subsequently loaded onto an ion exchange columns filled with approximately 0.8 mL of cation resin (AG50W-4X, chloride form, 200-400 mesh; 1 mL teflon columns) preconditioned with 3M NH_4OH–0.1M di-ammonium-citrate. When the loading fraction had passed through the resin a final 1 mL of the same ammonia-solution was loaded on the column to elute remaining unwanted elements. The resin was subsequently cleaned of ammonia by loading an additional 1 mL of 0.4M HCl, which was eluted to waste. The Ni-ammonia-complex was subsequently eluted in 3 mL 3M HCl. The collected Ni fractions were then evaporated on a hotplate (130^{o}C) to near dryness. Ten drops of concentrated HNO_3 were added to break the Ni-ammonium complex, after which the solution was evaporated and converted to chloride from by addition of 1 drop 6M HCl, and again evaporated to dryness. As can be seen in Fig. 2.10a most alkaline earth metals, as well as geologically common elements such as Al, Ti, Fe, and Cr are washed out with the first phase, and the only elements that elute together with Ni are Cu and Zn.

Nickel Purification: Step 2 The ammonia complexation employed above is an extremely effective mean of separating Ni from the bulk of matrix elements, and the $Ni(NH_3)_n^+$ complex can easily be broken using concentrated HNO_3 after the elute has been dried down. However, this procedure results in the presence of residual ammonium salts in the Ni fraction which require removal. In order to remove the ammonium salts and divalent elements such as Cu and Zn, which are not separated in the first step, a second column chemistry step is used, adapted from Victor (1986) and Strelow et al. (1972), which is tailored to remove remaining Mg, Ca, NH_4, Na, Al, Ti, and Cr as well as other divalent elements. Nickel fractions from the first step are redissolved in 0.1 mL 1M HCl, to which 0.8 mL 18.2 MΩ H_2O and 0.1 mL 0.5M Oxalic acid are added, creating a solution of 0.1M HCl in 0.05M Oxalic acid. The sample solution is loaded onto an ion exchange column filled with approximately 0.2 mL of preconditioned cation exchange resin (same resin as Step 1; 0.3 mL teflon columns). The loading fraction is eluted to waste, following which an additional 2 mL of the same Oxalic-HCl solution is loaded on the column to elute elements with valencies > +II (e.g. Fe, Al, Cr, and Ti) as oxalic complexes. The elution reagent is then switched to 0.5M HCl in 95% acetone, which extracts most divalent elements apart from Ni (e.g. Mn, Cu, Zn, Cd, Sn). The Ni is then eluted in 1 mL of 0.5M HCl in 95% acetone + 0.1M DMG. The eluted solution is evaporated to complete dryness on a hotplate at 90^oC, after which five drops of concentrated HNO_3 are added to each sample – to break the Ni-DMG complex – and the sample is left to evaporate again. As only small volumes of DMG are

used in this column any remaining organics are easily broken down by treating the sample with ten drops of concentrated HNO_3 on a hotplate (160^{o}C) overnight. After evaporation the sample is converted to chloride form by addition of 1 drop 6M HCl, and again evaporated to dryness. This method effectively separates Ni from Fe, Al, Cr, Ti and divalent elements such as Mn, Cu, Zn, Cd, Sn (Fig. 2.10b).

Nickel Purification: Step 3 As ^{58}Fe is a non-resolvable interference on ^{58}Ni a final clean-up column is needed in order to ensure complete separation of sample Ni from Fe. Nickel fractions are dissolved in 0.2 mL 6M HCl containing 0.05% H_2O_2. The anion exchange resin (0.1 mL AG1-X8, chloride form, 200-400 mesh; 0.15 mL teflon columns) is preconditioned with the same reagent before the sample is loaded onto the resin bed. While Fe is retained on the resin bed at this HCl molarity, Ni immediately elutes and the loading volume is collected in addition to a further 0.2 mL of 6M HCl + 0.05% H_2O_2 required for complete elution of Ni. After evaporation the Ni fractions are converted to nitride form by addition of a drop of concentrated HNO_3, allowed to evaporate to dryness, and then dissolved in 2% HNO_3 ready for mass spectrometric analysis.

2.3.3 Procedural Blank

To quantify the full procedural blank of the dissolution and chemical separation, a blank sample was processed together with every batch of geological samples. The total blank ranged from 0.5 to 2.5 ng Ni, which is negligible relative to the amounts of Ni processed for each sample (usually 5-10 μg).

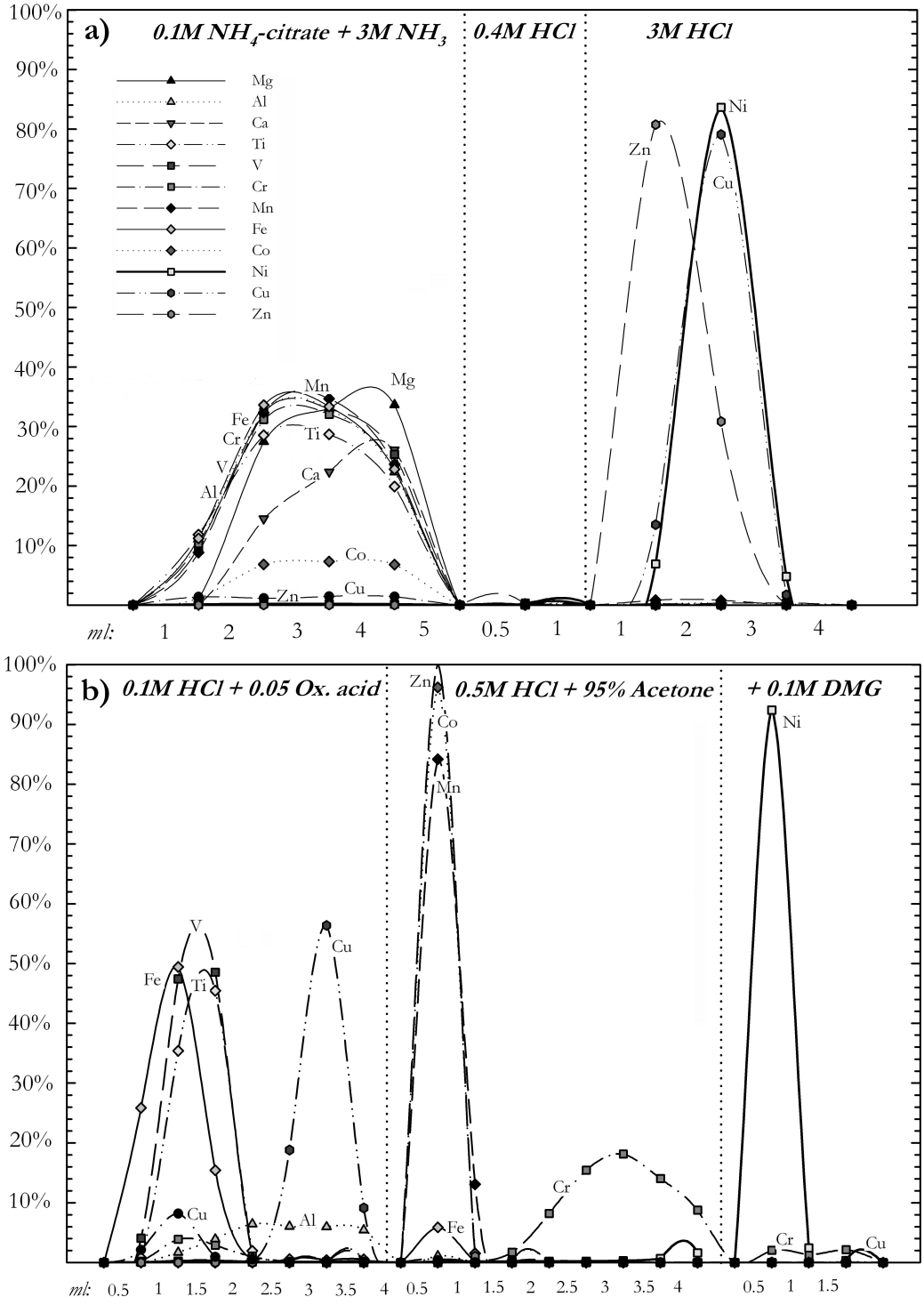

Figure 2.10: *Column calibration of step 1 and 2 in the Ni separation procedure, using a synthetic calibration solution containing a matrix elements-to-Ni ratio similar to silicate rocks.*

1) AG50W-X4, 1 mL resin bed	**solution & concentration**	**mL**
Column preconditioning:	0.1M NH_4-citrate + 3M NH_4OH	2
Sample loading:	0.1M NH_4-citrate + 3M NH_4OH	3
Cleaning step 1:	0.1M NH_4-citrate + 3M NH_4OH	3
Cleaning step 2:	0.4M HCl	0.5
Elution of Ni:	3M HCl	2
2) AG50W-X4, 0.2 mL resin bed		
Column preconditioning:	0.1M HCl + 0.05M Oxalic acid	1
Sample loading:	0.1M HCl + 0.05M Oxalic acid	1
Cleaning step 1:	0.1M HCl + 0.05M Oxalic acid	2
Cleaning step 2:	0.5M HCl + 95% acetone	2
Elution of Ni:	0.5M HCl + 95% acetone + 0.1M DMG	1
3) AG1-X8, 0.1 mL resin bed		
Column preconditioning:	6M HCl + 0.5% H_2O_2	0.4
Sample loading:	6M HCl + 0.5% H_2O_2	0.2
Elution of Ni:	6M HCl + 0.5% H_2O_2	0.2

Table 2.1: *Full chromatography procedure for separating Ni from a geological matrix*

2.3.4 Nickel Yields

Total yield of Ni for samples using the full separation procedure varies due to sample matrix. A sample with a low matrix-to-Ni ratio generally shows complete yield (95-100%), but a sample with a high matrix-to-Ni ratio gives a slightly lower yield (normally 85-95%). For example, a peridotite sample containing relatively high Ni concentrations (approximately 2000 ppm) will show close to 100% yield,

but a basalt or shale sample containing only small amounts of Ni (approximately 10-30 ppm) will rather produce a yield of only 85%. Therefore, a double-spike approach, where a calibrated ^{61}Ni–^{62}Ni spike is added to the samples prior to Ni purification, is used to correct for any isotopic fractionation that may relate to incomplete Ni yields during chemistry (see chapter 3).

2.4 Conclusions

This chapter describes the development of an effective new, low blank, separation procedure, producing clean Ni solutions from most geological samples. The method involves an ion-exchange procedure comprising three columns and utilising the ability of Ni to form strong complexes with both ammonia and dimethylglyoxime. The separation procedure is independent of sample pH and works even for samples with large matrix to analyte ratios due to the different complexes strong affinity for the resins. Another big advantage of this new separation protocol is that the full procedure only takes three days to perform (one day per column step), which is less than half the time the separation procedure published by Cameron et al. (2009) take, thereby significantly improving sample throughput. The purified solution is of high yield and containing no interfering matrix elements, making it suitable for isotope analysis by MC-ICP-MS.

CHAPTER

THREE

DETERMINATION OF THE NICKEL ISOTOPIC COMPOSITION IN GEOLOGICAL SAMPLES USING MULTI-COLLECTOR ICPMS

(This chapter is published as: ***Determination of mass-dependent variations in nickel isotope compositions using double spiking and MC-ICPMS***, *L. Gall, H.M. Williams, C. Siebert, and A.N. Halliday, J. Anal. At. Spect., 2012, 27, 137-145*)

3.1 Introduction

To be able to measure Ni isotopic compositions accurately and precisely using multi-collector inductively-coupled-plasma mass spectrometry (MC-ICPMS) considerable analytical development has been required in addition to that of the separation chemistry. This chapter is a summary of the work undertaken for the development of a rigorous measurement protocol for analysing Ni isotopes on the *Nu Plasma-HR* (Nu Instruments, Wrexham, UK) at the Department of Earth Sciences, Oxford. This chapter also demonstrates how different correction methods for instrumental mass bias may influence the analyses, and how variation of sample matrix affect the data quality and reproducibility.

3.1.1 Principles of MC-ICPMS

3.1.1.1 Introduction system

There are several sample introduction systems available for application with ICPMS, of which mainly two methods have been used in this thesis. The first one is by direct aspiration of the sample solution into the plasma. The solution is taken up by a self-aspirating micro-flow PFA nebuliser (Elemental Scientific Inc.) at a speed of 50-75 μL min^{-1}, by which it is converted into a fine aerosol and sprayed into an externally cooled cyclonic spray-chamber. The form of the spray-chamber makes it only possible for the smaller aerosol droplets to pass directly into the plasma, whereas the rest of the solution condenses on the spray-chamber walls. This in-

troduction system is very reliable and generally produces a stable ion beam, but the transfer efficiency is very low, with only very small amounts of the solution actually reaching the plasma, necessitating the use of high concentration solutions to achieve quality isotope ratio measurements. Another problem is the formation of oxides, hydrides, and nitrides from the acid solution (usually 2% HNO_3) that is sprayed into the plasma together with the analyte, which can cause significant interferences on the first row transition metals masses.

The second introduction system used in this thesis is a desolvating system, mainly the DSN-100 made by Nu Instruments. Here the solution is instead aspirated into a heated spray-chamber, where the aerosol solvent evaporates, which reduces the droplet size even further. The heated droplets are then transferred into a heated hydrophobic PTFE Teflon membrane, where the analyte is separated from the solvent by a hot counter flowing Ar gas. The dry analyte is then transferred directly into the plasma for ionization. By separating the analyte from the solvent the desolvating process reduce the amount of solvent transferred into the plasma by up to 99%. This drastically improves the sensitivity of the mass spectrometer for a given analyte, making it possible to analyse smaller samples, as well as reducing the amount of isobaric interferences derived from solvent molecules (e.g. argon oxides and nitrides). The drawback of this introduction system is the potential mass fractionation of the sample in the membrane during the desolvating process.

3.1.1.2 Plasma source

The inductively coupled plasma utilizes Ar that is ionized by collisions generated from motion in a high frequency electromagnetic field. The Ar gas flows (∼15 L min^{-1}) through a quartz torch, which is surrounded by a copper load coil at the end. The high frequency (27 MHz) is provided by a rf-generator operating at a power of around 1300 W, driving a current through the load coil, which produces a electromagnetic field. Argon gas flowing through this field is ignited by a high-voltage spark producing free electrons stripped from Ar atoms. The electrons are accelerated within the rf-field and in turn initiate a chain reaction by colliding with other Ar atoms, which produces more electrons. The collisions cause the plasma to heat up to gas temperatures of about 5000-8000 K, providing sufficient energy to ionize most elements in the periodic table. The plasma can be sustained as long as the gas and energy supply are constant.

The sample is transferred to the plasma by the nebuliser gas (Ar gas, ∼1.0 L min^{-1}) flowing through the centre of the quartz torch leading the analyte directly into the plasma. In the plasma the sample aerosol goes through different physical phase changes before finally the sample atoms are ionised. The ions created in the plasma are then extracted into the interface region, consisting of two nickel cones (sampler and skimmer cone) with holes of different sizes which allows for a pressure difference to build up between the plasma (atmospheric pressure) and the mass spectrometer (very low pressure). The ions are accelerated through the interface region by potential differences and guided by sets of optical lenses,

steering and focusing the ion beam in to the mass-analyser. The first acceleration potential in the Nu Plasma as used in this study is 6 kV. Although the interface ion transfer process is relatively straightforward, a significant instrumental mass fractionation effect originates from this region. As all ions created are positive, charge repulsion in the space around the cones (so called 'space-charge' effects) will cause preferential throughput of heavier ions and give rise to an instrumental mass bias.

3.1.1.3 Ion separation

The Nu Plasma-HR uses a static ion separation method in the form of a double-focussing magnetic sector. The ions are here separated both with respect to their mass (or mass/charge, m/z, ratio) and to their kinetic energy. This is necessary as a plasma source operating at high voltage produces ion beams with very large energy spreads. Here a magnetic field alone would not be able to separate the ions efficiently, as ions of the same m/z ratio can have very different velocities. This would cause them to take different trajectories through the mass analyser and get separated into two ion beams instead of one. In MC-ICPMS a combination of a magnetic field and an electric sector analyser (ESA) is used instead. Here the ions first enter the ESA and are separated with respect to their kinetic energy and focused into a beam of ions of sorted velocities before entering the magnetic sector and the actual mass separation procedure.

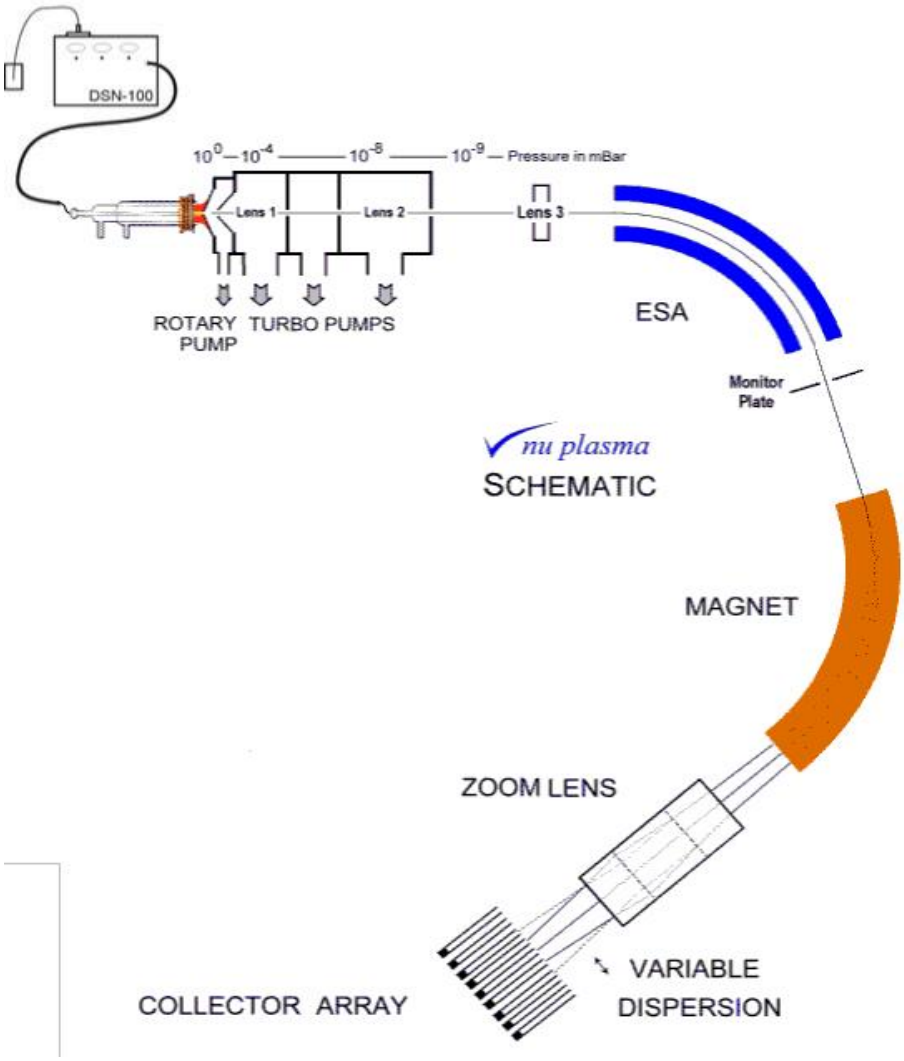

Figure 3.1: *Schematic overview of the Nu Plasma-HR (figure from Nu Instruments manual).*

3.1.1.4 Detectors

The Nu Plasma is normally equipped with 12 Faraday cups and some number of secondary electron multipliers each with ion counting enabling a large dynamic range of ion beams to be measured. The detectors are configured in a fixed array with a set off zoom lenses focusing the ion beams into the individual detectors. For this thesis, only the Faraday cups have been utilised for measurements. This is a

a)	0	–	1	–	2	3	4	5	6	7	8	IC	9	IC	10	IC	11
	-	-	62	-	-	61	-	-	60	-	-	(*59*)	-	-	58	-	-

b)	0	–	1	2	3	–	4	–	5	6	7	–	8	IC	9	10	11
	62	-	-	61	-	-	60	-	-	(*59*)	-	-	58	-	-	57	-

Table 3.1: ***a)*** *the normal detector array of a Nu Plasma,* ***b)*** *the modified detector array of the Nu Plasma-HR at the department of Earth Sciences in Oxford. The top line of numbers refer to the Faraday cups available for the difference array configurations. The masses below the cups refer to the position of each ion beam during analysis. IC shows the position of the ion counters for the different detection configurations.*

small graphite lined metal bucket where the incoming positive ion beam induces an equal flow of electrons, which flow through a large resistor as an electrical current. The resistor in a Nu Plasma Faraday detector is usually $10^{11}\Omega$, which enables a current of 10^{-11}A to be registered as an ion beam of 1V. This regular resistor set-up can measure currents up to 10^{-10}A (or an ion beam of 10V). Changing the resistor of a Faraday cup would change the range of current that could be measured for the ion beam focused into this detector. The use of multiple collectors in a detector array enables the measurement of several ion beams simultaneously. This is essential for precise isotopic studies as beam fluctuations due to e.g. plasma flicker are cancelled out, enabling a more exact ratio measurement.

The mass spectrometer used for isotope analyses during this project has a modified detector array of 12 Faraday cups to facilitate the analyses of transition metal isotope ratios, making it possible to simultaneously measure the ion beams of 6 isotopes while maintaining a 0.33 spacing (i.e. an ion beam placed in every

third Faraday collector). This modified detector array is vital for the analysis of Ni isotope ratios as a normal detector array on a Nu Plasma-HR does not permit the necessary monitoring of ^{57}Fe during analysis of Ni isotope ratios. Table 3.1 below shows both the normal and modified detector array on the Nu Plasma-HR. The numbers *0-11* show the places for the 12 available Faraday collectors and *IC* show the placements and number of ion counters. The atomic masses marked out are the positions of each ion beam during analysis.

As the aim for this project was to investigate mass-dependent fractionation of Ni isotopes, the focus was foremost on performing precise measurements of the three stable isotope ratios needed: ^{60}Ni/^{58}Ni, ^{61}Ni/^{58}Ni, and ^{62}Ni/^{58}Ni. Because of this, the ratio ^{64}Ni/^{58}Ni was not measured for any samples. As ^{64}Ni is very small (only 0.9% natural abundance) it is hard to measure accurately and precisely due to the large isobaric interference of ^{64}Zn (64% natural abundance).

3.1.2 Instrument resolution

The Nu Plasma-HR can be operated at three different resolution modes – low, medium, and high resolution. The lowest resolution is $R_{LR} = m/\Delta m \approx 400$, which is achieved keeping the the adjustable source and alpha slits fully open. The higher resolution modes ($R_{MR} = m/\Delta m \approx 4000$ and $R_{HR} = m/\Delta m \approx 8000$ respectively) are achieved by reducing the width of the source slit and choosing an intermediate value for the alpha restrictor slits located in front of the electrostatic analyser, and thereby cutting of the sides of the ion beam. As the ion beam is cut

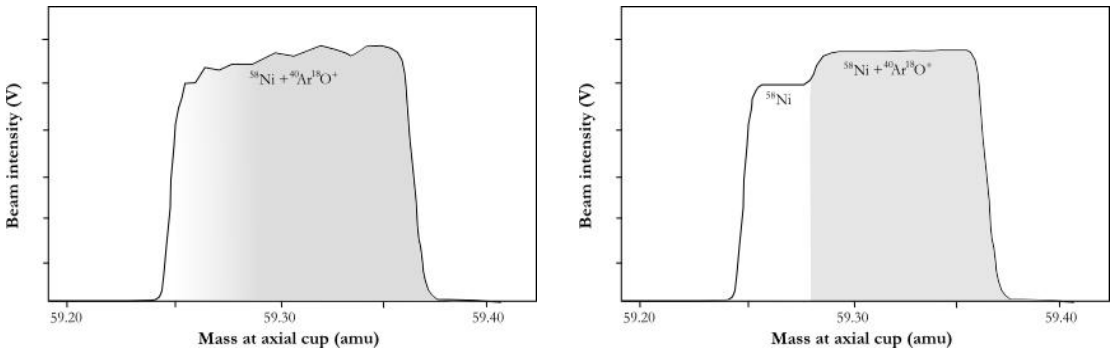

Figure 3.2: *Demonstration of low (left) and high (right) pseudo-resolution. This technique never truly separates the two ion beams (analyte and interference), but allows the low mass side of the peak to be measured without contribution from the overlapping interference. Many authors have used this technique to separate ^{58}Ni from the potential interference of $^{40}Ar^{18}O^+$. If this interference had an impact on the ion beam at mass 58 the two species could be separated.*

with increased resolution the transmission is simultaneously decreased. The effect is that if a low resolution mode allows 100% transmission, only ∼5% of the beam is left at high resolution. This loss in sensitivity demands higher concentration solutions to be run, which makes increased sample size necessary. The achieved peak separation is sometimes called *pseudo* high-resolution, as it does not truly separate the two ion beams. Instead they are displayed as one peak where one side is free of interferences and can be measured correctly (Fig. 3.2).

3.2 Isobaric Interferences

There are several possible isobaric interferences on Ni isotopes that need to be addressed, the most critical of which is the overlap of ^{58}Fe with ^{58}Ni, as ^{58}Ni is the denominator isotope in all ratios. To fully resolve ^{58}Fe from ^{58}Ni a resolution of ∼28,000 would be needed, which is not possible with current analytical instruments (similarly it would take a resolution of ∼55,000 to separate ^{64}Ni from

	^{58}Ni	^{60}Ni	^{61}Ni	^{62}Ni
Elemental:	$^{58}Fe^{+}_{(28,000)}$			
Double-charged:	$^{116}Cd^{++}_{(3,400)}$	$^{120}Te^{++}_{(2,800)}$	$^{122}Te^{++}_{(3,000)}$	$^{124}Te^{++}_{(2,700)}$
	$^{116}Sn^{++}_{(3,700)}$	$^{120}Sn^{++}_{(2,900)}$	$^{122}Sn^{++}_{(2,900)}$	$^{124}Sn^{++}_{(2,500)}$
Argides:	$^{40}Ar^{18}O^{+}_{(2,200)}$	$^{24}Mg^{36}Ar^{+}_{(2,700)}$	$^{25}Mg^{36}Ar^{+}_{(2,700)}$	$^{24}Mg^{38}Ar^{+}_{(3,200)}$
	$^{22}Ne^{36}Ar^{+}_{(2,500)}$	$^{20}Ne^{40}Ar^{+}_{(2,500)}$	$^{21}Ne^{40}Ar^{+}_{(2,500)}$	$^{26}Mg^{36}Ar^{+}_{(2,800)}$
	$^{20}Ne^{38}Ar^{+}_{(2,900)}$	$^{22}Ne^{38}Ar^{+}_{(2,600)}$		$^{22}Ne^{40}Ar^{+}_{(2,500)}$
Oxides:	$^{40}Ca^{18}O^{+}_{(2,200)}$	$^{42}Ca^{18}O^{+}_{(2,200)}$	$^{43}Ca^{18}O^{+}_{(2,200)}$	$^{44}Ca^{18}O^{+}_{(2,400)}$
	$^{42}Ca^{16}O^{+}_{(3,200)}$	$^{44}Ca^{16}O^{+}_{(3,100)}$		$^{46}Ti^{16}O^{+}_{(3,200)}$

Table 3.2: *Possible elemental and molecular isobaric interferences on the masses of interest. The number in brackets next to each interference is the resolution required for this interference to be resolved from the Ni isotope peak of interest.*

^{64}Zn). Therefore, an accurate and reliable correction procedure must be adapted to the analytical protocol to resolve any addition of ^{58}Fe. In addition to Fe, other potential elemental interferences on Ni isotopes are double-charged ions of Cd, Sn, and Te. Production of double-charged ions cannot be completely avoided, which makes efficient sample purification procedures and careful assessment of mass spectra quality necessary to exclude any interferences from these elements.

The most important polyatomic interference for Ni isotope measurements is $^{40}Ar^{18}O^{+}$, potentially present on the high mass end of ^{58}Ni. Previous studies on Ni isotopes have used high-resolution settings on instruments (Quitte & Oberli, 2006; Regelous et al., 2008), alternatively utilized a hexapole collision cell (Cook et al.,

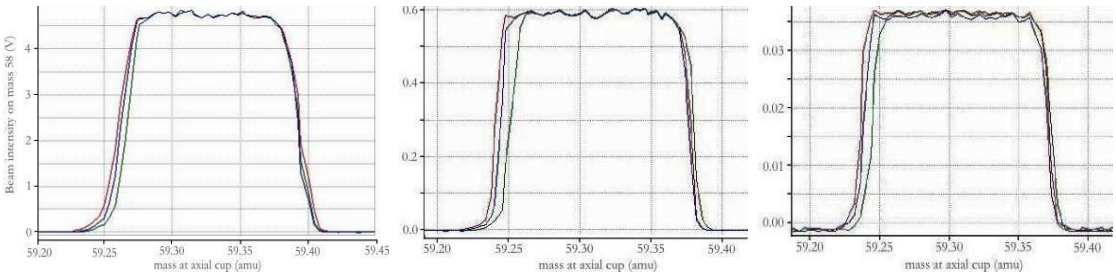

Figure 3.3: *Flat topped peaks of ion beams on masses 58, 60, and 62 in low-resolution mode (left), medium-resolution mode (middle), and high-resolution mode (right). As can be seen in the medium and high resolution figures, there are no resolvable interferences on the displayed Ni isotope beams in either resolution mode.*

2006), to resolve this argon oxide interference from ^{58}Ni. There is also a chance that remaining matrix elements in the sample (if chemical separation is incomplete) can form molecules and cause an isobaric interferences (see Table 3.2). Because of this it is highly important to completely separate Ni from the elements Mg, Ti, and Ca, or to otherwise ensure that these interferences are completely resolved. After careful investigation of possible interferences on the Ni masses of interest at a medium- and high-resolution we did not reveal the presence of any detectable peaks that could correspond to either $^{40}Ar^{18}O^{+}$ or any of the possible NeAr-species that could theoretically interfere on the masses of interest (Fig. 3.3). Therefore, the measurements of Ni isotope ratios presented in this thesis were mainly made in low resolution mode. However, when performing an analysis in low-resolution mode while only aspirating 0.3M HNO_3 a measurable background in the range of 0.5-5mV on all Ni masses does show. This small signal was interpreted as the instrumental blank originating from the cones, as ICPMS sampler and skimmer cones typically are made of Ni. Tests using aluminium skimmer and sampler cones showed that Ni cones account for ∼50% of this background (*H. Williams, pers.*

com.). The remaining background presumably originates from other stainless steel components of the mass spectrometer. This Ni background is, however, constant and does not seem to affect the measurements as no bias was detected between analyses involving an on-peak-zero background measurement in blank acid and analyses where the background was measured by only ESA deflection.

3.3 Instrumental mass fractionation corrections

The mass discrimination observed in the ICP source can generally be described as a larger throughput of heavier ions over lighter ions compared to the natural isotope ratios. This is mainly caused by the preferential deflection of lighter ions from the centre of the ion beam in the expansion chamber, and is thought to depend on so called space-charge effects, or Coulomb repulsion, of charged ions in the interface region (Becker, 2007). As this effect is a time independent function of mass, this can be corrected for by adapting different techniques and mathematical treatment of collected data.

To calculate the instrumental fractionation factor, f, in each standard/sample measurement and correct for the mass bias in the measurement, a mathematical fractionation law is applied. Different versions of this fractionation law have been used over time, but for ICPMS mainly the *power law* (left equation) and the *exponential law* (right equation) are used.

$$\frac{R^{\,true}}{R^{\,meas}} = (1+f)^{\Delta m} \qquad \frac{R^{\,true}}{R^{\,meas}} = \left(\frac{m_1}{m_2}\right)^{f} \tag{3.1}$$

Where R denotes the *true* (or corrected) and *measured* isotope ratio of interest, Δm the mass difference between the two isotopes of masses m_1 and m_2. The exponential fractionation law was first described by Russell et al. (1978), who showed that this expression is especially preferred at high resolution studies, by describing the instrumental mass fractionation factor, f, as solely dependent of the absolute masses of the isotopes measured and not just on the mass difference between the isotopes. Therefore, the exponential fractionation law should provide a better description, and thereby more accurate data correction, of the instrumental mass fractionation occurring during isotope ratio measurements of Ni on the MC-ICPMS. Especially for higher resolution studies.

3.3.1 Sample-Standard-Bracketing

There are several ways to correct for this instrumental mass bias. The simplest, and most used, form of correction is the sample-standard-bracketing technique. By bracketing every sample analysis with a standard analysis on each side the mass bias (as well as any drift that occurs during the analysis) can be corrected for. This method assumes that the mass bias is the same for both standard and sample. This requires that all the standard and sample have the exact same matrix, or that all matrix elements are quantitatively removed during the chemical separation. If this is not the case, or if the chemical separation is suspected to be incomplete, this method for instrumental fractionation correction is not reliable. An alternative for compensating for isotope fractionation that has taken place during chemical

separation is to treat the bracketing standard in the same way as the sample, on the assumption that the exact same fractionation will occur for the standard as for the sample regardless of no matrix elements being present.

3.3.2 External correction by element doping

The instrumental mass fractionation can also be externally corrected for by adding a known amount of an element of similar mass to the sample and standard, as it is generally assumed that elements of similar mass experience the same fractionation in the mass spectrometer. For Ni, Cu is theoretically the best choice as Cu has two naturally occurring isotopes – ^{65}Cu and ^{63}Cu – which are close to Ni in mass yet do not interfere with the Ni isotopes masses. To examine if this mass bias correction method is valid for Ni isotope analysis a Cu-solution (plasma standard, Alfa Aesar) was added to a solution of pure Ni (also plasma standard, Alfa Aesar) in a Ni:Cu ratio of approximately 2:1 (e.g. 2 ppm Ni mixed with 1 ppm Cu). By analysing the mixed solution and calculating f for each element, we tested the assumption that these two elements should behave similarly in the mass spectrometer. Fig. 3.5 show the results of two measuring sessions from different months where the Ni-Cu mixed solution was analysed over several days. In the figures these series of measurements are plotted expressed as the natural logarithm of the measured ratios divided by the natural ratios (here used as our standard values). Which, following the exponential fractionation law in equation 2.1, gives us:

$$ln\left(\frac{R_{Cu}^{meas}/R_{Cu}^{true}}{R_{Ni}^{meas}/R_{Ni}^{true}}\right) = \frac{f_{Cu}}{f_{Ni}} \cdot ln\left(\frac{m_{65}/m_{63}}{m_{60}/m_{58}}\right) \quad (3.2)$$

In Fig. 3.5 uncorrected measured ratios are plotted in form of $\ln(^{60}\text{Ni}/^{58}\text{Ni})$ vs. $\ln(^{65}\text{Cu}/^{63}\text{Cu})$, showing that $f_{Ni} \neq f_{Cu}$, as the slope for the plotted measurements have changed significantly in between sessions. This makes it unsuitable to use Cu-doping for calculating the absolute Ni isotope ratios of a sample. On the other hand, the figure also show that during the exact same operating conditions (i.e. measurements take place during the same day and with the same settings) then the ratio f_{Ni}/f_{Cu} is constant. This makes it possible to use the correction method, if all isotope ratios are measured relative to a standard reference material – which also is analysed during the same session, under the exact same operating conditions, and with the exact same Cu-doping procedure – as the relative ratios then are valid. As δ-values always are expressed relative to an isotope standard this external correction method still can be used for Ni isotope analysis. Assuming that $f_{Ni} \approx f_{Cu}$ and using the exponential fractionation law, the measured Ni isotope ratios can be corrected for instrumental mass fractionation by:

$$R_{Ni}^{corr} = R_{Ni}^{meas} \cdot \left(\frac{m_{60}}{m_{58}}\right)^{f_{Ni}} \qquad \Leftrightarrow \qquad f_{Ni} \approx \ f_{Cu} = \frac{ln\left(R_{Cu}^{nat}/R_{Cu}^{meas}\right)}{ln\left(m_{65}/m_{63}\right)} \quad (3.3)$$

Fig. 3.4 displays measurements performed over a period of nine months expressed in the δ-notation, showing that the combination of Cu-doping and sample-standard-bracketing provides excellent precision and reproducibility, giving an av-

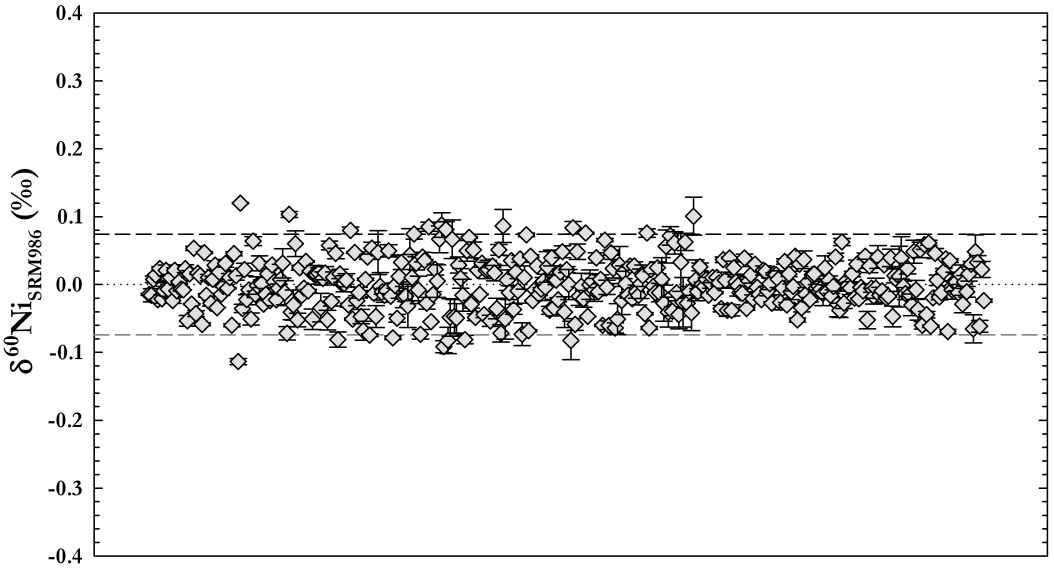

Figure 3.4: *Measurements of an untreated Ni-standard solution over several months. The data shows that a combination of Cu-doping and sample-standard-bracketing provides excellent precision and reproducibility, giving an average value of $\delta^{60}Ni$ = 0.000065 ± 0.074‰ (2 s.d., n = 390). Error bars are 2 s.e. of the individual measurements.*

erage value for all the measurements of δ^{60}Ni = 0.000065 ± 0.074‰ (2 s.d., n = 390). All measurements were done using a larger resistor ($10^{-10}\Omega$ instead of the normal $10^{-11}\Omega$ resistor) on the Faraday cup assigned to mass 58. This is to allow a larger ion beam to be measured with this cup, thereby making it possible to increase the concentration of the sample solution, achieving better counting statistics for the ion beams on masses 61 and 62, which are isotopes with very low natural abundance (1.14% and 3.63% respectively). When this method was tested using USGS reference rock standards the results showed that this does not always give accurate relative isotope ratios for natural samples. The cause for this is probably incomplete separation of Cu originally present in the sample. This does unfortunately make it unreliable to use Cu-doping for analyses Ni isotope ratios in natural samples.

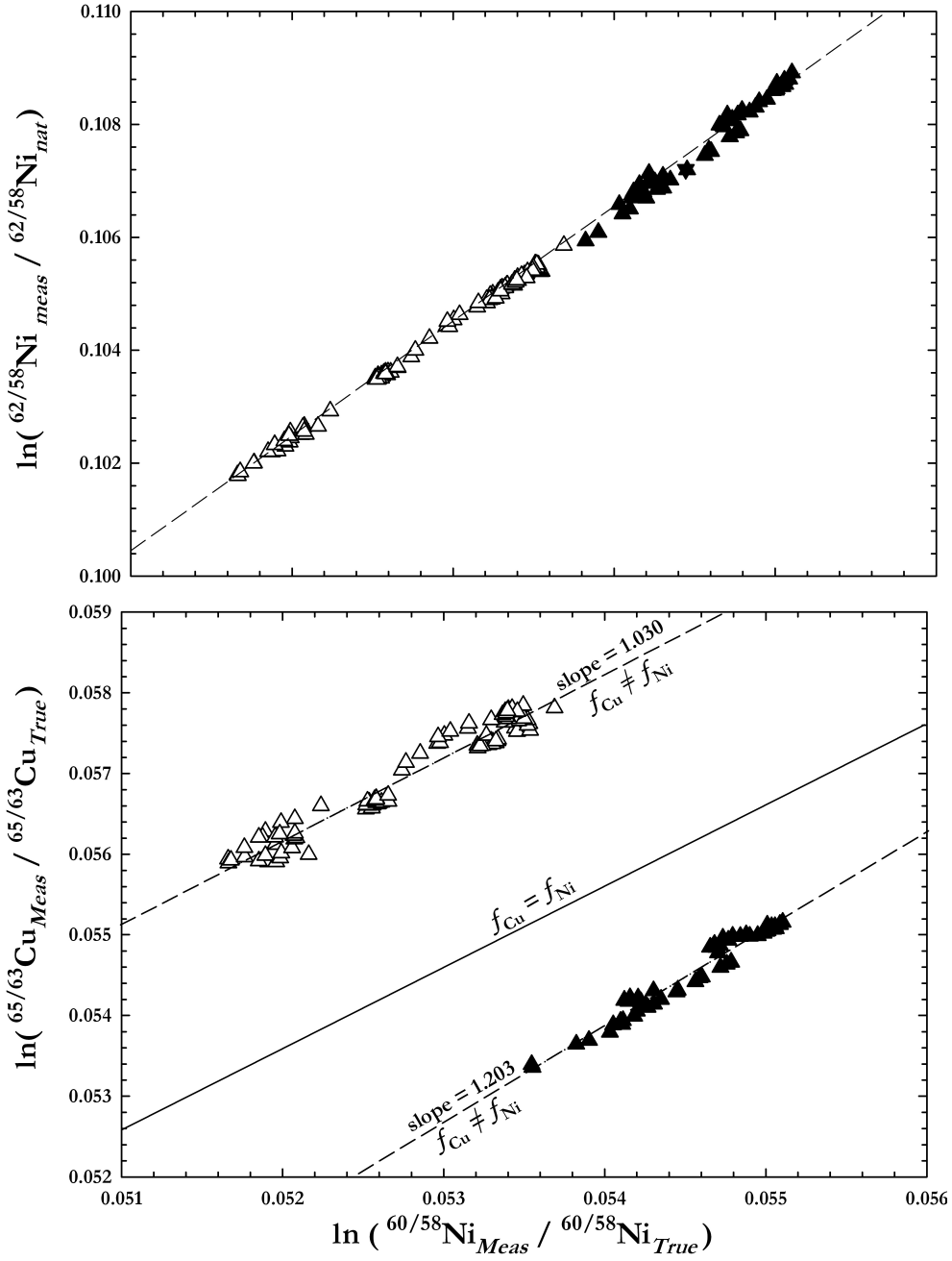

Figure 3.5: *Uncorrected data from two different measurement sessions, plotted as the natural logarithm of the measured ratios (M) divided by the true ratios (T) for isotope pairs of Cu and Ni. If the instrumental fractionation factor (f) is the same for both Cu and Ni then, according to the exponential fractionation law, the data should plot on a line of slope = 1. As shown above, this is not the case for these two elements, but as $f_{Cu} \propto f_{Ni}$ and constant for a whole session, the relationship $f_{Cu} = f_{Ni}$ can still be used as long as all ratio measurements are made relative to a standard.*

3.3.3 Internal correction by double-spiking

A more robust instrumental fractionation correction method is to spike the standard and sample with a solution containing two of the element's own isotopes of a known composition. This way the uncertainty of the assumption that two elements behave exactly the same in the mass spectrometer is circumvented. The technique has been proven as a highly robust and accurate means of correcting for instrumental mass fractionation (e.g. Galer, 1999; Johnson & Beard, 1999; Dodson, 1970). The double-spike method also has the advantage that, if added to the sample before chemical separation any isotope fractionation during chemical processing is automatically corrected for during data reduction. The method can be used for any isotope system where the element has at least four naturally occurring isotopes, as three isotope ratios are needed for data reduction.

3.3.3.1 Choice of Spike Composition

To obtain high-precision isotopic measurements it is crucial to optimise the isotopic composition of the double spike (and the isotopic compositions of the spike-sample mixtures), because different combinations of isotopes will result in dramatically differences in measurement quality. To produce the optimal Ni double-spike two methods of calculations have been compared both theoretically and experimentally.

The first method uses the geometrical relationships between the double-spike, the standard, and the mixture of the two in a three dimensional isotope space. Here these form three points lying on the unique line *N*-*M*-*S*, where *S* is the

double-spike, N is the natural standard, and M is the spike-standard mixture. As explained in (e.g. Hofmann, 1971; Galer, 1999; Siebert et al., 2001), the optimal double-spike composition usually generates a large angle between the planes n and m (see Fig. 3.6a for further explanation). The best double-spike composition is given by the spike combination producing a large θ, as the angle is a measure of how well the planes can be resolved from each other. A larger θ should therefore give a more exact determination of the *N-M-S* line and consequently give a low error on the calculation of N_{true} (Galer, 1999). When calculating θ for the a set double-spike the results showed that the value of the angle is only dependent on the sample/spike ratio, as all proportions of the spike isotopes gave approximately the same angle at a set sample/spike ratio. Because of this we only used the value of θ a guide line for which double-spike combinations and sample/spike ratios that could be of interest while performing our calculations.

Using the mathematical description from Siebert et al. (2001) the optimal double-spike composition was modelled, with respect to the angle θ and the error (s.d.) on the natural fractionation. In these calculations ^{61}Ni and ^{62}Ni were chosen as the double-spike components. The choice of isotopes was based on their natural abundances – as ^{61}Ni and ^{62}Ni are the smallest isotopes of Ni (disregarding ^{64}Ni) they naturally also produce the smallest ion beams during mass spectrometry analysis, and will therefore have the highest errors associated with their measurement. Choosing these isotopes as the components in our double-spike will increase the proportion of these isotopes in our solution, producing beams of approximately

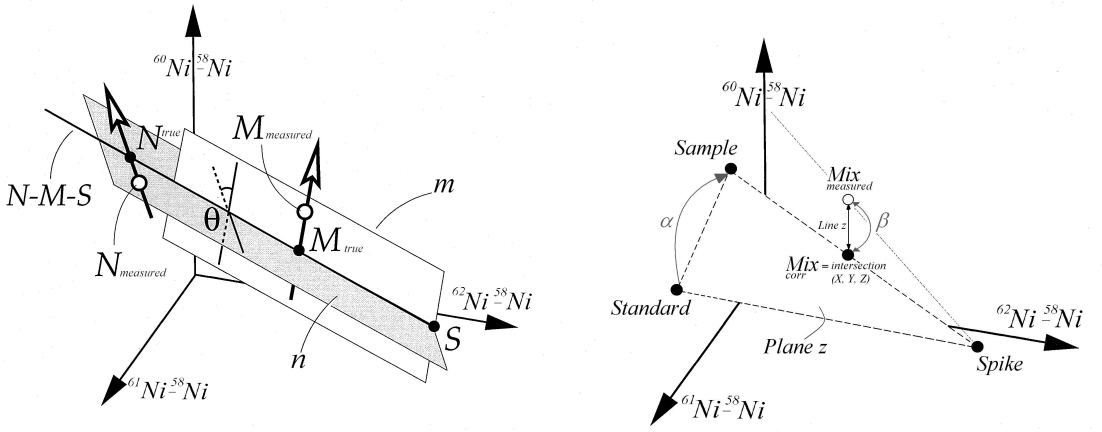

Figure 3.6: ***a)*** *(left) Sketch showing the relationship between the points N, M, and S, the line N-M-S, and the angle, θ in three-isotope-space – these parameters can be used for calculating the optimal double-spike following Galer (1999).* ***b)*** *(right) Similar sketch of three-isotope-space showing the relationship between the instrumental fractionation, β, the natural fractionation, α, the plane 'z' defined by the sample, standard, and the spike compositions – these parameters are all used for calculating the optimal double-spike composition following Siebert et al. (2001).*

equal size to ^{60}Ni and ^{58}Ni. This would greatly improve counting statistics and therefore produce an overall better isotope ratio measurement.

In order to theoretically evaluate the impact of different combinations of double-spike mixtures and sample/spike ratios on measurement precision, we used a model based on real Ni isotope analysis data (non-spiked), adapted for the different spike additions and spike-sample ratios. The aim was to find a double-spike composition that resulted in high-precision measurements which were not highly sensitive to the spike-sample ratio. In the calculations, the certified composition of the Ni isotope standard NIST SRM 986 (Gramlish et al., 1989a) was used as the true standard values and the Ni isotope composition of the enriched ^{61}Ni and ^{62}Ni spikes – 99.44% ^{61}Ni and 96.46% ^{62}Ni, metal form (provided by Oak Ridge National Laboratory) – as the original spike components.

Further was also assumed that Ni follows the exponential fractionation law during instrumental fractionation, as well as that the instrumental fractionation – β – has a value of 2 (as the instrumental fractionation factor for elements of similar masses to Ni have been observed to be around 2) and that the sample is a fractionated standard with a natural fractionation – α – of 0.2‰. These calculations gave the optimal double-spike composition to be a mixture of 50% each of ^{61}Ni and ^{62}Ni and the optimal sample/spike ratio to be approximately 0.4 (i.e. 70% of the Ni should come from the double-spike). Full results of these calculations are shown in Fig. 3.7.

As can be seen in the latter of these figures, there is relatively little difference in the errors expected between proportional mixtures of ratios in the range ^{61}Ni:^{62}Ni = 25:75 – 65:45 respectively. The double-spike composition was chosen to be ^{61}Ni:^{62}Ni of 25:75%, which is close to the isotopes natural ratio.

Another approach for finding the optimal double-spike is to calculate the composition by setting up equations describing the system and inverting these to find the optimal solution (e.g. Dodson, 1963, 1970; Cumming, 1973). A recent development of this way of optimising the double-spike composition was recently proposed by Rudge et al. (2009), where the authors adapted calculations for MATLAB, using inversion calculations. Their program – named 'The double spike toolbox' – aims to find the double-spike combination and sample-spike ratio with minimal error on the natural fractionation factor (α), and therefore the lowest error on the calculated sample delta value. When using this program and the same choice of

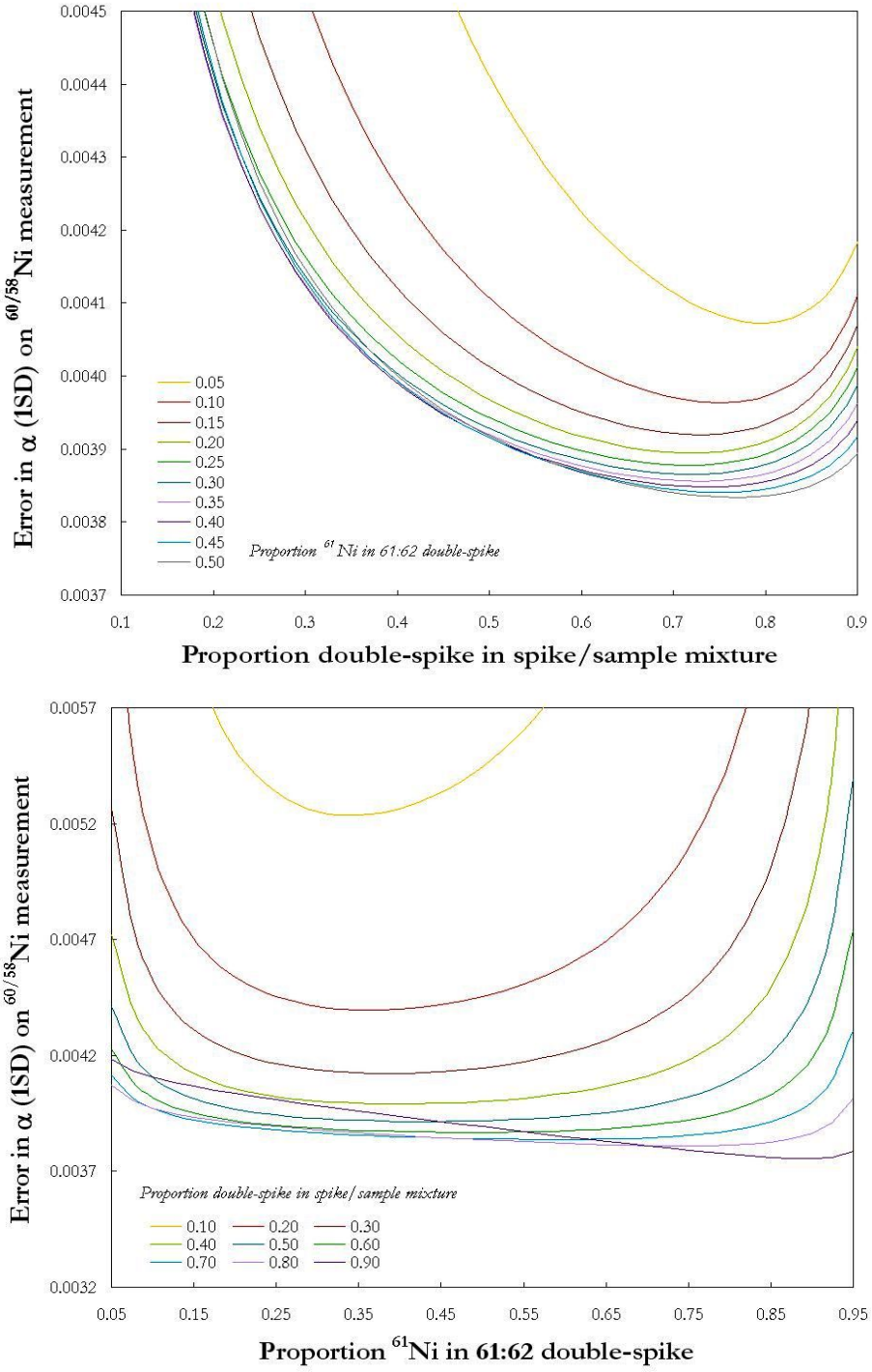

Figure 3.7: *Optimal double-spike composition calculations for a ^{61}Ni-^{62}Ni double-spike, calculated following the mathematical procedure from Siebert et al. (2001). The two figures displays the proportion of ^{61}Ni in the double-spike together with the proportion double-spike in the spike-sample mixture, plotted against the error in α (i.e. error on the measured natural sample) for each combination. The optimal double-spike combination and spike-sample mixture would have the lowest error. The results show there is relatively little difference in the errors between proportional mixtures of ratios ^{61}Ni:^{62}Ni = 25:75 – 65:45 respectively.*

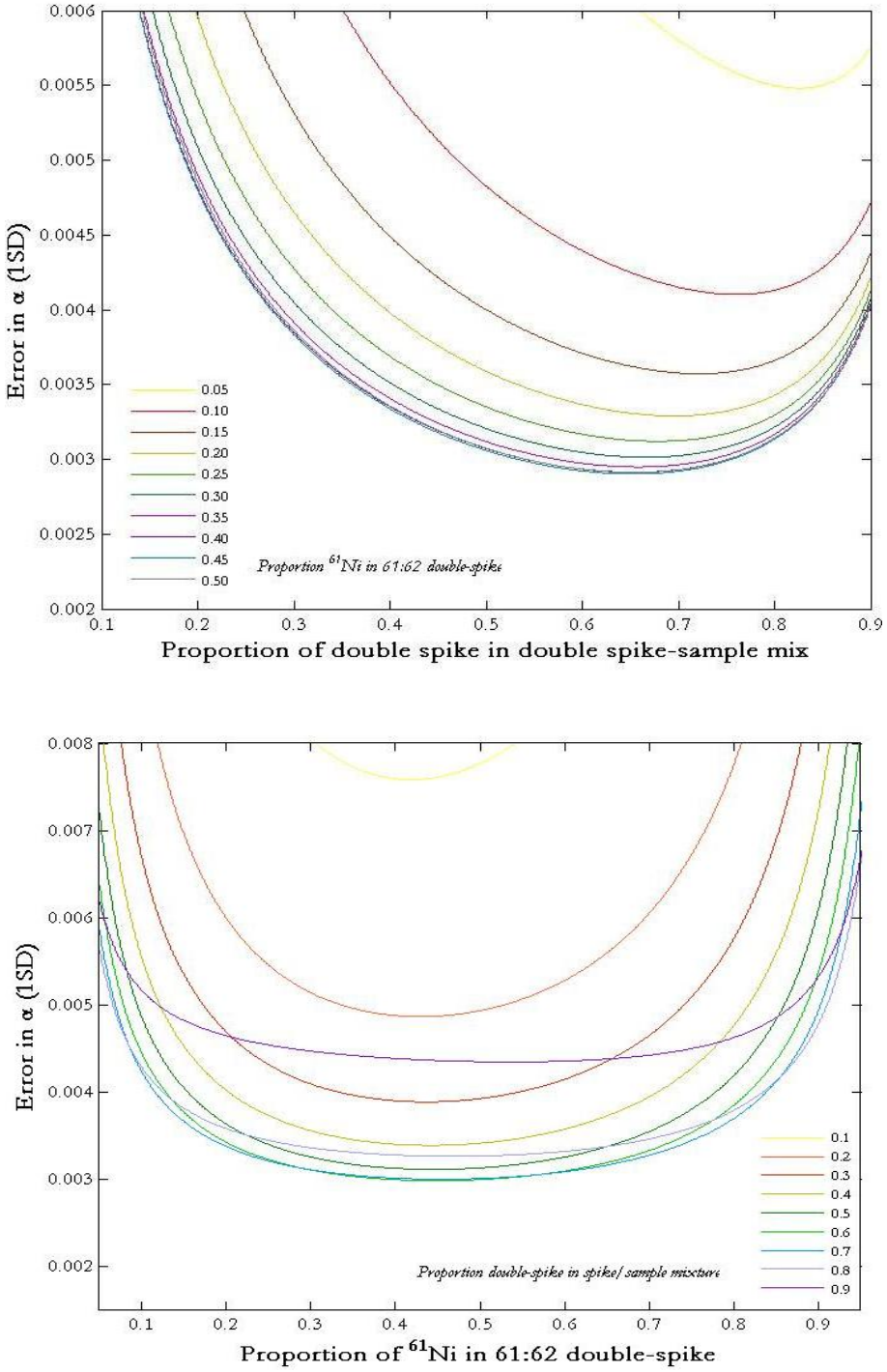

Figure 3.8: *Optimal double-spike composition calculations for different combinations of each isotope in a ^{61}Ni-^{62}Ni double-spike, calculated using 'The double spike toolbox' (Rudge et al., 2009). Similarly to the previous figure, displaying the proportion of ^{61}Ni in the double-spike together with the proportion double-spike in the spike-sample mixture, plotted against the error in α or each combination. The results from these calculations are in accordance with previous calculations, giving the optimal double-spike composition as approximately 50% each of ^{61}Ni and ^{62}Ni.*

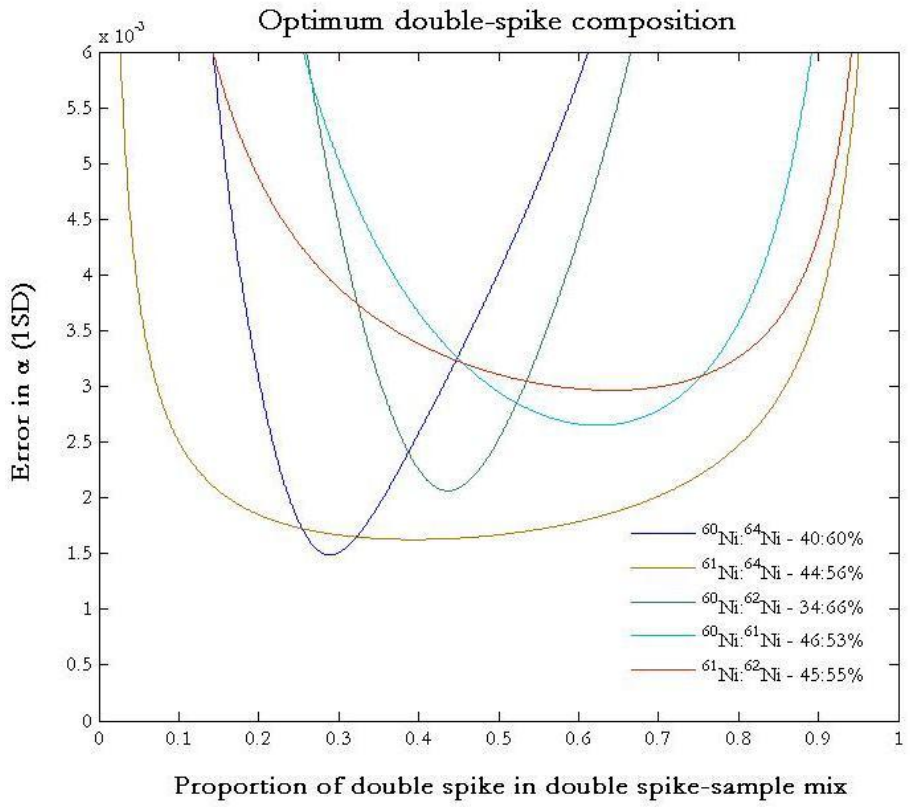

Figure 3.9: *Optimal spike compositions for the Ni isotope system, calculated using 'The double spike toolbox' (Rudge et al., 2009) for different sets of double-spike components.*

isotopes in previous calculations the optimal composition is given as 45% ^{61}Ni and 55% ^{62}Ni and a sample/spike ratio of 0.56 (Fig. 3.8).

When comparing the two model's results graphically (Fig. 3.7 and 3.8) the differences mainly seem to concern solutions at extreme spike compositions. This probably depends on the fact that the geometrical model uses simple weighting of measured, un-spiked, Ni isotope ratios, while the MATLAB program assumes the isotopes to interact with each other, especially at extreme values, and automatically corrects for these deviations from the model (Rudge, pers. comm.). Both results are therefore likely to be valid and the difference between the models should not interfere with the calculated optimal double-spike compositions.

According to the program there are several other isotope combinations that theoretically produce lower errors in the natural fractionation calculations. If excluding ^{58}Ni from the calculations – as this isotope is used as the denominator – then a double-spike composition of ^{60}Ni-^{64}Ni or ^{61}Ni-^{64}Ni seem to give the lowest errors of all possible isotope combinations (Fig. 3.9). But as these double-spike combinations contain ^{64}Ni – an isotope difficult to measure accurately due to a large interference from ^{64}Zn – they are not practical choices. Of the remaining optimal combinations both ^{60}Ni-^{62}Ni and ^{60}Ni-^{61}Ni theoretically give lower errors on α than a double-spike consisting of ^{61}Ni-^{62}Ni. But as the error curves for the former combinations are much steeper than the one for our chosen double-spike isotopes (^{61}Ni-^{62}Ni) a set-up using ^{60}Ni-^{62}Ni or ^{60}Ni-^{61}Ni will require a very precise knowledge about the sample Ni concentration as a specific sample/spike ratio has to be obtained. This is not practical as it sometimes can be difficult to know the exact concentration of your sample. Due to this, a double-spike composed by ^{61}Ni-^{62}Ni is still preferred for the Ni isotope system.

3.3.3.2 Spike calibration

To accurately make up a double-spike solution of the composition determined above, the two isotope enriched metal powders were weighed to the fifth decimal in pre-cleaned and pre-weighed PEF-bottles. The weighing was repeated three times, after which each spike powder was dissolved in Teflon distilled 50% HNO_3 and diluted with the same acid to achieve a solution of 200 ppm ^{61}Ni and 800ppm

^{62}Ni each. These two isotope spike solutions were then added together in the right proportions to make up the required double-spike solution – 25% ^{61}Ni and 75% ^{62}Ni – with total Ni-concentration of 100 ppm and final acid molarity of approximately 10% (∼1.5 M) HNO_3. In order to account for any impurities in the solutions and provide real exact isotope ratios, both the reference standard and the double-spike solution was calibrated for all isotope ratios used in the data reduction ($^{60/58}$Ni, $^{61/58}$Ni, and $^{62/58}$Ni) using external normalisation to Cu to correct for instrumental mass bias assuming the exponential fractionation law (e.g. Archer & Vance, 2004; Maréchal et al., 1999). To correct for the instrumental mass fractionation during calibration the Cu-doping method described above was used, as this method is valid for non-treated standard solutions if all measurements take place under the exact same conditions and relative to a standard. As the calibration of the double-spike is relative to the calibration of the standard used, this correction method gives accurate calibration results, even if the absolute isotopic composition of NIST SRM 986 is not precisely determined. The calibration was done using a larger resistor ($10^{10}\Omega$ instead of the normal $10^{11}\Omega$ resistor) on the Faraday cup assigned to mass 58, making it possible to analyse solutions of higher Ni concentration, thereby achieving better counting statistics for the smaller ion beams on mass 61 and 62. The calibrations of both solutions were performed using a wet-plasma set-up using an external peltier cooled spray chamber from Elemental Scientific (PC^3– SSI), which reduces oxide formation and enhances sensitivity without creating a mass bias fractionation as often seen in membrane desolvators.

	$^{60/58}$**Ni**	(± 2 s.d.)	$^{61/58}$**Ni**	(± 2 s.d.)	$^{62/58}$**Ni**	(± 2 s.d.)
NIST SRM 986:	0.38414	(± 2.4·E^{-5})	0.01668	(± 2.8·E^{-6})	0.05311	(± 6.8·E^{-6})
Double-spike:	0.72048	(± 2.0·E^{-5})	18.80495	(± 1.3·E^{-3})	49.36995	(± 3.8·E^{-3})

Table 3.3: *Results of the ^{61}Ni-^{62}Ni double-spike and Ni standard (NIST SRM 986) calibration.*

Five analyses of both solutions were measured in the same session and the averages of these analyses assumed as the isotope ratios of each solution relative to each other. No modification of the calibrated isotope ratios was necessary. The mathematical treatment of raw data follows Siebert et al. (2001), assuming Ni follows the experimental fractionation law and calculating the isotope ratios by iteration of the instrumental and natural fractionation factors.

In order to test whether our given sample/spike ratio of 0.4 is suitable, solutions of NIST SRM 986 doped with the double-spike solution in different sample/spike ratios were analysed. The results of these analyses are plotted in Fig. 3.10, which shows how most measured sample/spike ratios (0.3 – 2.0) would give accurate results, although a low ratio (0.4 – 0.6) is preferred due to lower errors.

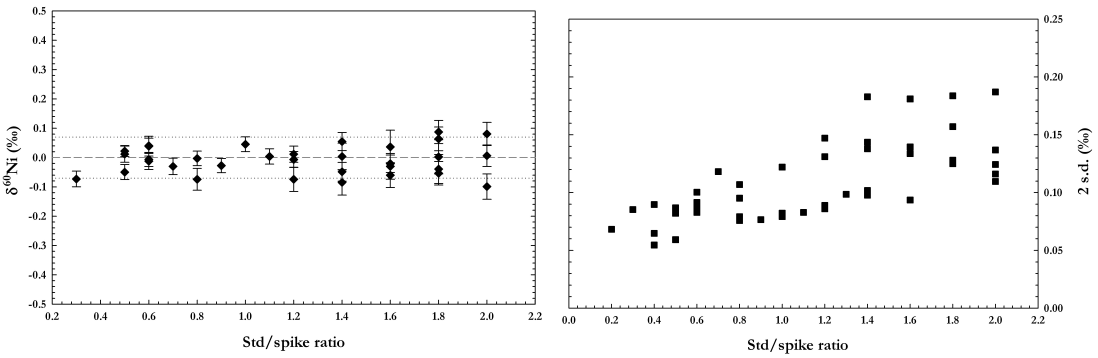

Figure 3.10: *Data collected for mixtures of the Ni reference standard (SRM 986) and the ^{61}Ni-^{62}Ni double-spike solution for a range of sample/spike ratios. The measured values for the Ni standard of all ratios are within the long-term external error (± 0.07‰, 2 s.d.).*

Instrument parameter settings		Ar gas flow rate (min^{-1})		Analysis time (sec.)	
RF power	1300 W	Coolant	13 L	Sample uptake	60
Accel. voltage	5.85 kV	Auxililary	0.8-1.0 L	Background	20
Sampler cone	B-type,	Nebuliser	25-30 psi	Washout	300
(Nu Instruments)	1.0 mm ∅	Membrane	3.40-4.20 psi	Cycle integration	10
Skimmer cone	WA-type,	Hot gas	0.15-0.30 psi		
(Nu Instruments)	0.7 mm ∅	Uptake rate	50-75 μL	Number of cycles	40

Table 3.4: *Normal instrument settings during Ni isotope ratio analysis on the Nu Plasma-HR.*

3.4 Analytical protocol

3.4.1 Measurement details

Samples were usually run at a concentration of 100-200 ppb introduced to the plasma via a microconcentric PFA nebulizer (ESI Scientific; 50-75μl/minute) coupled to a desolvator (Nu Instruments, DSN-100) in order to enhance sensitivity and minimise oxide formation. The desolvating system was washed by aspirating 2% (0.3M) HNO_3 for 5 minutes between analyses. All isotopes were measured simultaneously in static collection mode. Each measurement consisted of a sequence of 40 cycles of 10s integrations of the ion beam intensity. Electronic background noise was measured by ESA-deflection for 20s prior to analysis. All samples were diluted to the same intensity (± 10%) as standard and measured bracketed by analyses of NIST SRM 986 to allow for drift correction.

3.4.2 Isobaric interference corrections

When using a double-spike approach to correct for mass bias, the data reduction procedure assumes the sample to be a mass-dependently fractionated standard.

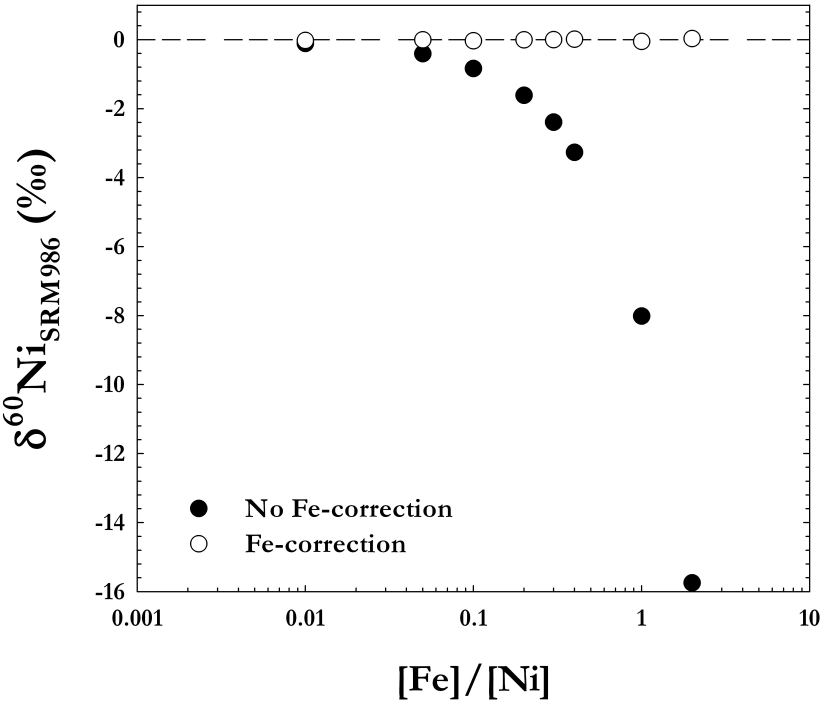

Figure 3.11: *Analyses of a Ni standard solution doped with different amount of Fe. The black circles are the measurements without correcting for the ^{58}Fe interference on ^{58}Ni, and the white circles are the same measurements after applying the correction. As can been seen in the figure, any Fe present in the sample can be corrected for by our correction scheme.*

This approach will therefore only work for pure mass-dependent fractionation if there are no isobaric interferences present, as any interferences on the Ni isotope masses potentially could compromise the analysis, resulting in apparent mass-independent isotope fractionation.

We corrected for any background Fe in the desolvator or mass spectrometer by monitoring the ^{57}Fe ion beam and calculating the theoretical contribution of ^{58}Fe, assuming that Fe isotopes were fractionated to the same extent as Ni isotopes, following the exponential fractionation law and using the fractionation factor found through the double-spike approach.

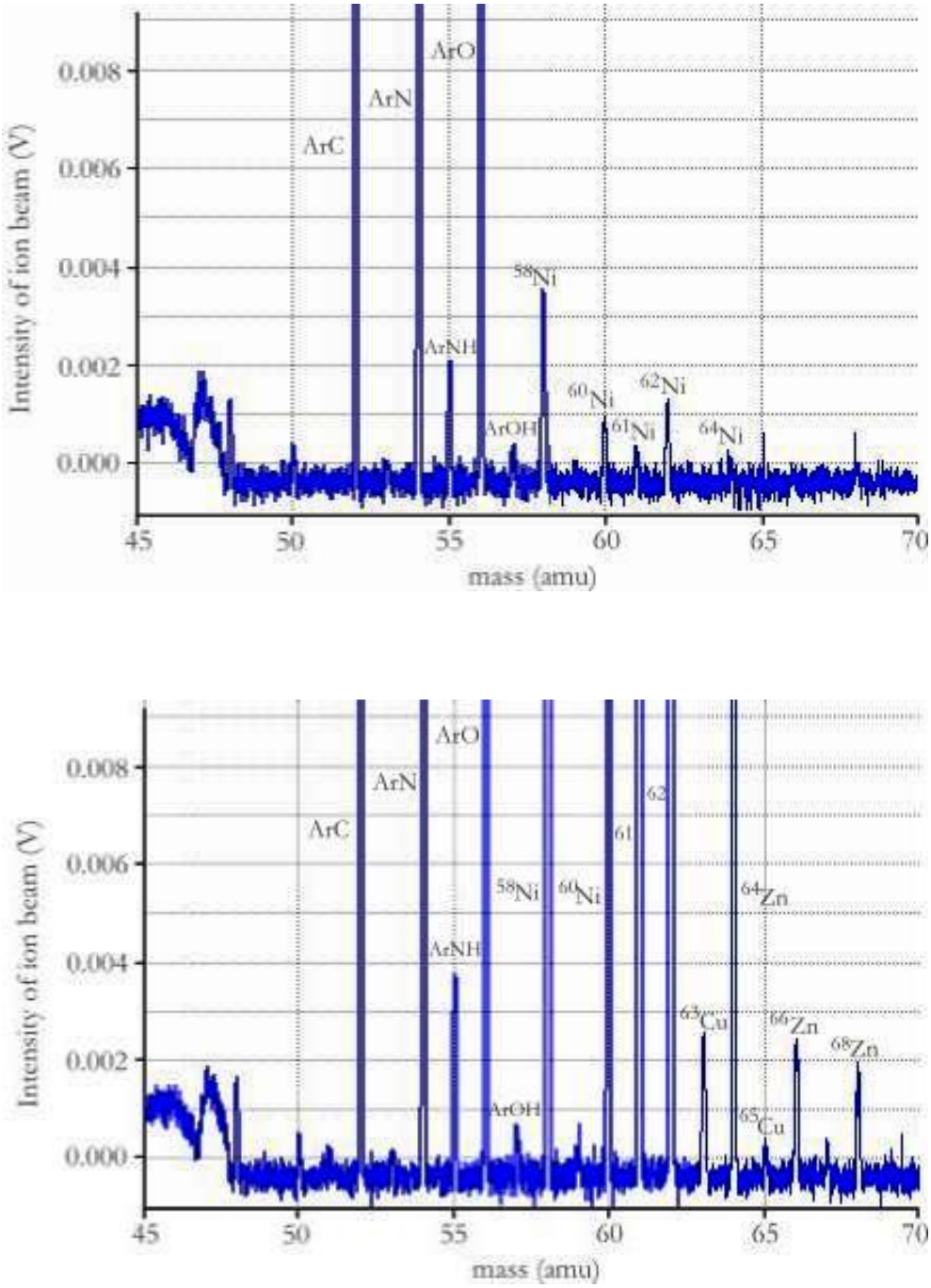

Figure 3.12: *Scans of mass spectra (45-70 amu) of a chemically processed silicate sample (USGS rock standard BHVO-2) and a blank solution (2% 0.3M HNO_3) showing how the purified Ni solution is clean from interferences other than small amounts of Cu and Zn. However, this sample spectrum also shows why correcting for instrumental mass fractionation by Cu-doping alone does not produce correct Ni isotope ratios, as there is still Cu left in the original purified sample solution.*

In Fig. 3.11 measurements of a standard Ni solution doped with different amounts of Fe are plotted both with and without the applied correction for the ^{58}Fe contribution on ^{58}Ni. These results demonstrate that the Ni isotope composition of a solution can be measured correctly regardless of the Fe concentration left in the sample if using this correction protocol.

In addition to Fe, other potential elemental interferences on Ni isotopes are double-charged ions of Cd, Sn, and Te. Production of double-charged ions cannot be completely avoided, which makes efficient sample purification procedures, and following control of mass spectra, necessary to exclude any interferences from these elements. As the chemical separation effectively removes all these elements present in the samples their signals were not detected when searching their mass range (Fig. 3.12). Mass 59 detected was also monitored, as the presence of a detectable 59 beams reflects $^{118}Cd^{++}$ or $^{118}Sn^{++}$. However, no 59 beams above detection limits were observed for any samples or standards measured, and double-charged ions of Cd and Sn were therefore considered insignificant in our Ni isotope measurements.

3.4.3 Fractionation associated with the chemical separation

In order to fully investigate the capability of our chemical separation procedure we performed matrix tests, employing mixtures of plasma standards (from Alfa Aesar) of geologically important matrix elements such as Mg, Al, Ca, Fe, Ti, V, Cr, Mn, Co, Cu, Zn, Mo, Cd, Sn, and Pb mixed together with the Ni standard solution to yield element abundances in similar proportions to silicate rocks. After process-

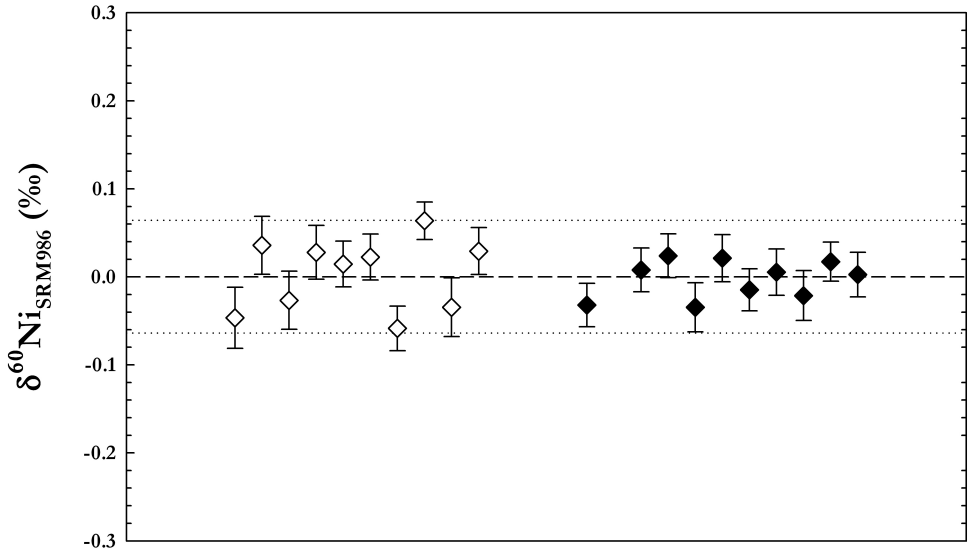

Figure 3.13: *Measurements of the Ni standard NIST SRM 986 to test chemical separation procedure. Open symbols are a mixture of SRM 986 and the artificial calibration solution (plasma standards, Alfa Aesar, see text for more information) put through the separation procedure. Closed symbols are the SRM 986 on its own put through the separation procedure. Error bars are 2 s.e. of individual measurement. Dotted lines are ±2 s.d. of all SRM 986 measurements.*

ing the standard mixture through our column chemistry procedure the purified Ni solutions were analysed, and yielded isotopic compositions identical with the untreated standard reference solution within error (Fig. 3.13), demonstrating that the chemical separation does not generate any instrumental matrix effects from introduction of additional elements into the plasma. Fig. 3.13 also demonstrates how well the double-spike technique corrects for possible mass fractionation during column chromatography if the samples are spiked prior to separation.

3.4.4 Fractionation associated with matrix effects

If the chemical separation of Ni is inefficient this can significantly affect the measurement, as the presence of these elements may depress the ionization and

throughput of Ni in the plasma and interface region of the mass spectrometer. Although our chemical protocol effectively separates Ni from matrix elements, we carried out tests to evaluate the effects of residual matrix elements in sample solutions on isotopic ratio measurements. Nickel standard solutions were doped with a chosen set of individual elements (Ca, Cr, Fe, Mg, Na, Ti, and Zn) at different element-to-Ni ratios. These elements were chosen as they are either of similar mass range (Fe, Zn), difficult to separate from Ni by ion-exchange chromatography (Ti, Cr), or ubiquitous in geological samples (Na, Ca, Mg).

The results of these tests are shown in Fig. 3.14 where all measurements are plotted against their concentration ratio. To some extent the effect the elements may have on the measurement is corrected for by the double-spike technique, at least for most single elements and at relatively low concentration, but careful chemical separation of Ni from matrix elements is still required for high-precision isotopic ratio determinations.

Some remaining matrix elements may also form argide or oxide molecules in the plasma and cause interferences on the masses of interest. For example $^{24}Mg^{36}Ar^{+}$ interferes on ^{60}Ni, and $^{44}Ca^{16}O^{+}$ and $^{46}Ti^{16}O^{+}$ on ^{62}Ni (see Table 3.2). Therefore it is particularly important to fully separate Ni from Mg, Ti, and Ca. However, as can be seen in Fig. 3.14, doping a Ni solution with Mg seems to affect neither the accuracy nor the precision of the measurement, as argides are not formed in the plasma to the same extent as oxides (Becker, 1996). On the other hand, the addition of Ca or Ti significantly offsets the measurement accuracy. Adding Ca

to the solution pushes the measurement towards higher delta values, while Ti in the solution has the opposite effect, producing lighter delta values than the undoped Ni standard (Fig. 3.14). This is because the most abundant Ca isotope (^{40}Ca, natural abundance 96.9%) can form $^{40}Ca^{18}O^{+}$ which interferes with ^{58}Ni, denominator in all isotope ratios measured, pushing the ratios higher. On the other hand only ^{46}Ti can form an oxide possible of interfering on any of the Ni masses analysed, $^{46}Ti^{16}O^{+}$. This molecule would interfere with ^{62}Ni, an isotope used in the double-spike, and thus interfere with the double-spike data reduction procedure.

3.5 Reproducibility and accuracy of measurements

In order to determine the long-term reproducibility of Ni isotope ratio measurements we have taken two different approaches. Instrument reproducibility was tested by measurements of a pure NiO powder (from Sigma Aldrich, 98% Ni), which had been dissolved and spiked, but not treated thought the chemical separation procedure. The NiO solution was analysed during several measurement sessions over one year, giving an overall average value of δ^{60}Ni = -0.159 ± 0.034‰ (2 s.d., n = 310) (Fig. 3.15). Typically, 10 pure Ni standards were analysed per sample measurement session. For actual samples however, the long-term reproducibility is expected to be larger than the one given by the instrument as the chemical separation also may affect analytical reproducibility.

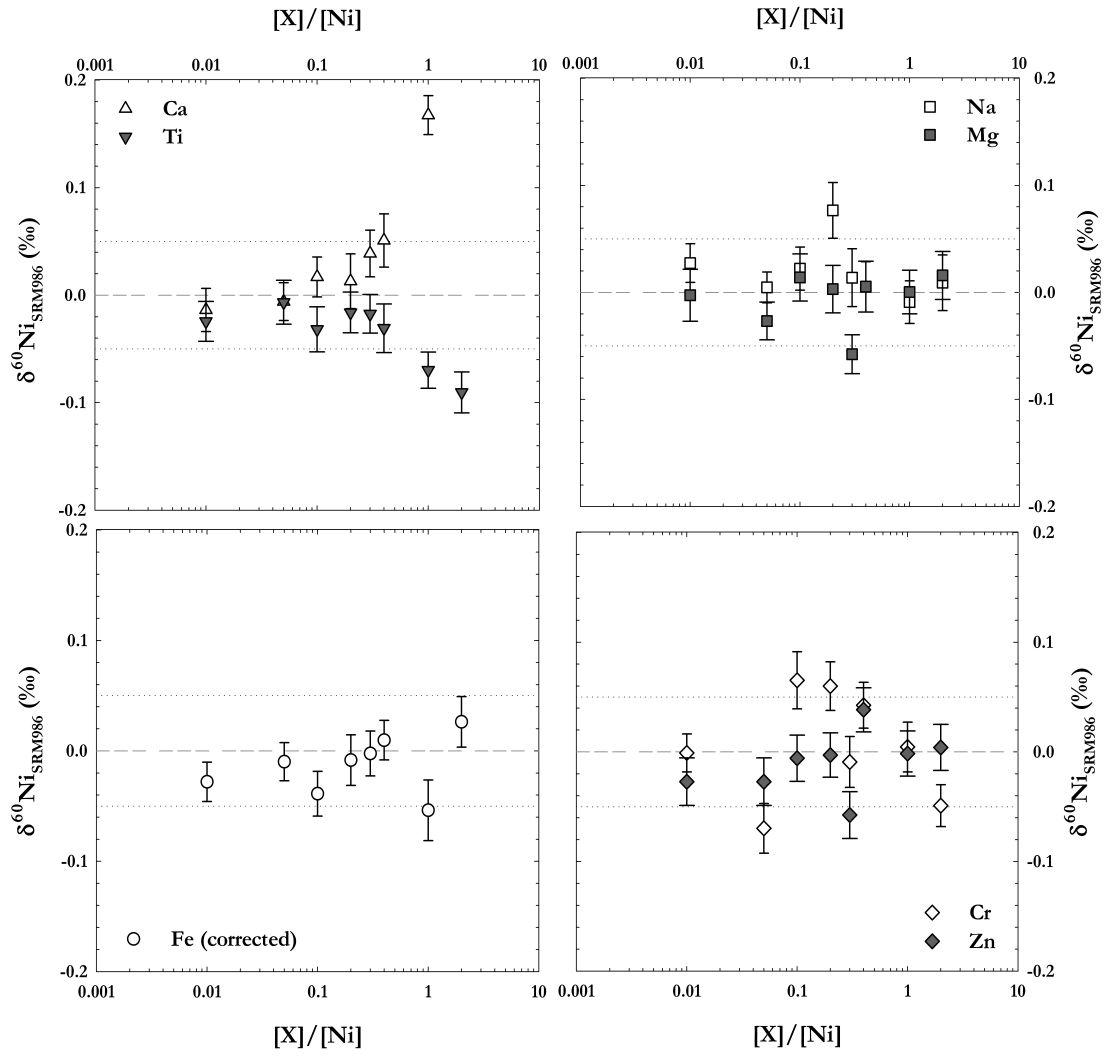

Figure 3.14: *Analyses of a Ni standard solution doped with different elements in varying concentration ratios to Ni. The error bars are 2 s.e. of the measurement. The dotted lines show the 2 s.d. error on all (un-doped) Ni standard solution analyses during the measurement session.*

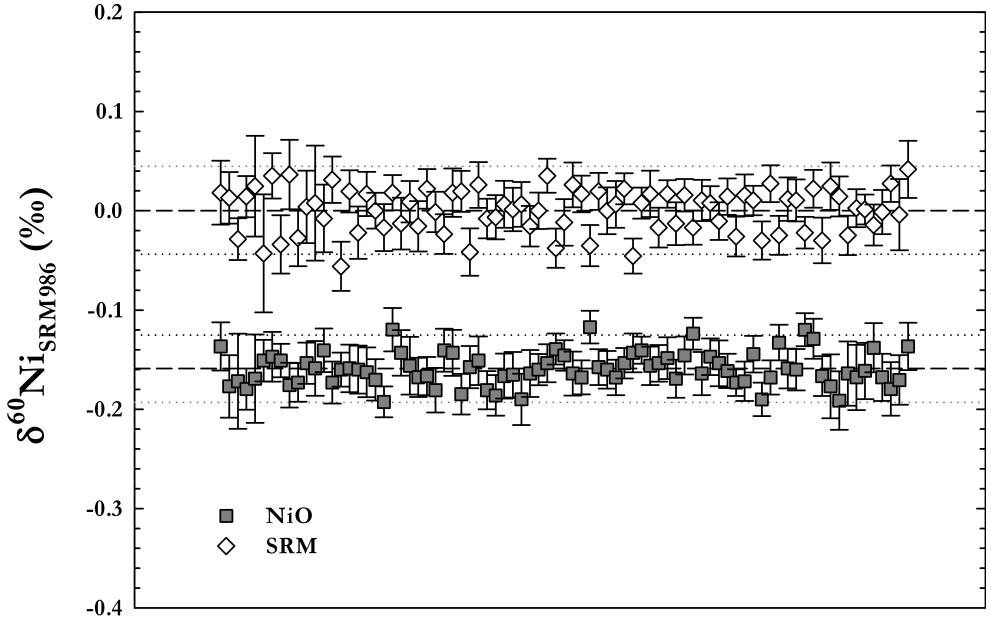

Figure 3.15: *Long term instrument reproducibility tested by measurements of a Ni-oxide solution (NiO powder, Sigma Aldrich) analysed during several measurement sessions over one year. The overall average value for the NiO solution was $\delta^{60}Ni$ = -0.159 ± 0.034‰ (2 s.d.). Error bars in the figure are 2 s.e. of the individual measurements.*

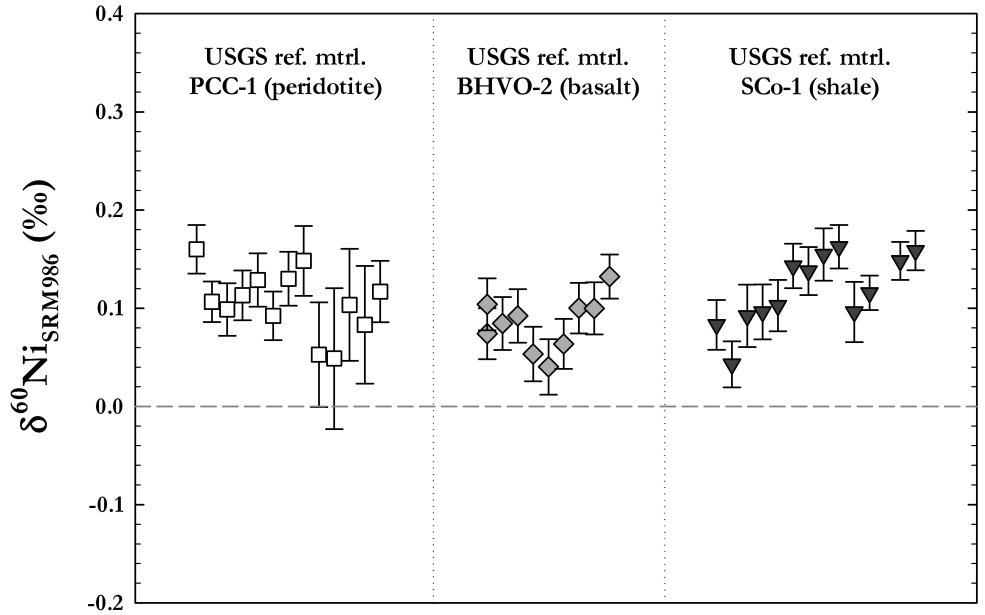

Figure 3.16: *Long term external reproducibility tested by measurements of three USGS rock standards of different silicates, processed and analysed during several measurement sessions over one year. Each data point is a complete chemical replicate of the three silicate sample, showing that the precision for Ni isotope analysis is excellent. By these analyses, the external $\delta^{60}Ni$ sample reproducibility is typically ± 0.07‰ (2 s.d.) for silicate samples.*

This was tested by measurements of three USGS rock standards of different silicates, processed and analysed during several measurement sessions over one year. The results of these analyses are shown in Fig. 3.16, where full replicates (each data point is a separately digested and chemically processed sample) of the three silicate samples are displayed. These analyses show that the precision for Ni isotope analysis is excellent and that the long-term external δ^{60}Ni sample reproducibility for silicate samples is typically ± 0.07‰ (2 s.d.). Small differences were noted between samples of different analyte-to-matrix ratios, as samples with higher ratios (e.g. ferromanganese nodules) show a long term reproducibility as low as ± 0.05‰. Because of this, matrix matching with available rock standards is advisable to get best results for unknown samples.

3.6 Conclusions

This chapter describes the development of an MC-ICPMS analysis method for the accurate and precise measurement of Ni isotope ratios. To correct for instrumental fractionation effects, as well as for correcting possible isotope fractionation during the chemical separation procedure, a double-spike method was used. Tests performed on both mixtures of synthetic and natural terrestrial standards demonstrates that the method is accurate. Replicate measurements of USGS rock standards yield a long-term external reproducibility (2 s.d.) of ± 0.07‰, ± 0.1‰, and ± 0.14‰ for ^{60}Ni/^{58}Ni, ^{61}Ni/^{58}Ni, and ^{62}Ni/^{58}Ni respectively. This method will allow further investigation of Ni isotope variation in terrestrial samples.

CHAPTER

FOUR

NICKEL ISOTOPE VARIATIONS IN THE SILICATE EARTH

4.1 Introduction

The first task when studying a new isotope system is to determine the main range of fractionation in the silicate earth. This chapter aims to present precise Ni isotope analyses of a range of silicate rocks of different origins and chemical composition, and to discuss the possible causes for isotope fractionation between these different silicate reservoirs. To accomplish this, rock samples spanning the whole silicate spectra, from ultramafics to granites, have been analysed for their Ni isotopic composition using methods described in chapter 2 and 3. Additionally, an estimate of the Ni isotopic composition of the bulk silicate Earth was calculated based on the analyses of terrestrial silicate rocks samples. This value was then compared with Ni isotope analyses of meteorites of different classes to determine if core formation processes could have caused isotopic fractionation of the total terrestrial Ni reservoir.

4.1.1 Nickel behaviour in silicates

In the mantle Ni is usually situated in olivine ($(Mg,Fe)_2SiO_4$), a mineral making up over 50% of the upper mantle. Nickel-bearing olivine is usually Mg-dominant, as is common in ultramafic rocks, and contains on average ∼3000 μg/g Ni incorporated into its lattice structure in the place of Mg (e.g. Saito, 1977; Sobolev et al., 2005), with octahedral (6-fold) coordination. Apart form olivine spinel (MgAl2O4) can also accommodate large quantities of Ni, where it substitutes for olivine in the tetrahedral site under certain conditions. The Ni concentration is ∼4000 μg/g

Ni in mantle spinels from normal peridodites (Deer et al., 1982). However, as spinel is thought to make up only approximately 2% of the upper mantle, which is significantly less than that of olivine, the total amount of Ni situated in spinel is very low. Orthopyroxene is the second most common mineral in the upper mantle and can also hold minor amounts of Ni (< 1000 μg/g), substituting for Mg or Fe in the lattice structure in octahedral coordination.

Nickel can also be found in garnet and clinopyroxene minerals, but for these mineral Ni is generally only present in trace amounts (< 100 μg/g) (Deer et al., 1982). Thus, if there is an equilibrium fractionation of Ni isotopes between the different mantle minerals during crystallisation, preferential extraction, of e.g. orthopyroxene over olivine, during partial melting of the mantle could result in fractionation of Ni isotopes between the solid and melt. The magnitude of this fractionation is, however, likely to be small as Ni is in very similar bonding environments in both olivine and orthopyroxene. Analysis of separated minerals would be required to confirm the presence of equilibrium isotope fractionation between these phases.

The igneous continental crust consists of SiO_2-rich rocks, with chemical compositions ranging from intermediate diorites and andesites (52–63% SiO_2) to felsic granites and rhyolites ($\geq$69% SiO_2). In mantle-derived melts, e.g. basalts, the small amount of Ni present will mainly be situated in olivine minerals. During igneous differentiation of such mafic materials Ni will behave as a compatible element, with only very small quantities going into the melt (e.g. for basalt-melt and

dacite-melt systems $D_{Ni}^{ol} \gg 10$ and $D_{Ni}^{opx} > 1$, GERM (2011)). Therefore dioritic and andesitic rocks will contain a significantly smaller amount of Ni than basalts, with granodiorites and granites in their turn containing even less. As a result of this Ni-depletion during igneous differentiation, the igneous continental crust only contains trace amounts of Ni ($\ll 100$ μg/g).

4.2 The Mantle

The mantle is the Earth's largest reservoir for silicate bound Ni. The average Ni concentration for mantle rocks is 1960 μg/g making the mantle contain approximately 7.9×10^{21} kg Ni, or 99.97% of the total silicate bound Ni on Earth (McDonough, 2003). To estimate the isotopic composition of the mantle different types of ultramafic rock samples were analysed for this thesis, including 2 dunites, 2 sp lherzolites, 3 gt lherzolites, and 6 samples of a Tertiary komatiite suite.

4.2.1 Peridotites

Peridotites are considered to be the residues of partial melting in the upper mantle, of which dunites are thought to have experienced the highest degree of melt extraction and lherzolites the lowest. A difference in isotopic composition between these two rock types could therefore indicate if melt extraction is accompanied by fractionation of Ni isotopes. Seven peridotites of different tectonic settings were analysed in an attempt to estimate the variation in Ni isotopic composition in the upper mantle.

Of these samples two were the USGS reference materials DTS-1 and PCC-1, both depleted intrusive peridoites from the Western US. Two samples were provided by the Natural History Museum, London, of which one orogenic peridotite from the Appalachians (Stueber, 1969), and one kimberlite xenolith from the Kaapvaal craton (Carswell & Dawson, 1970), with the remaining three being volcanic xenoliths from the East African Rift (Dawson et al., 1970; Cohen et al., 1984; Rudnick et al., 1992; Dawson et al., 1997; Burton et al., 2000)

Analyses showed that dunites exhibit slightly lighter δ^{60}Ni-values compared to lherzolites. However, the values are within error of the other peridotite samples the dunites are not statistically different for this sample set. Also the peridotite PCC-1 show a slightly lighter δ-value, which could possibly be due to alteration if this sample has been affected by the widespread metasomatism of the ultramafic massif the sample originates from. As the peridotite samples are spread over > 0.1 ‰ there is no clear signal of fractionation with degree of melt extraction in mantle peridotites (Table 4.1). Therefore, if peridotites are representative for Ni in the upper mantle, these samples indicate that, with current analytical precision, the mantle could be considered to be of homogeneous Ni isotopic composition with an average of δ^{60}Ni-value of 0.17 ± 0.16 ‰ (2 s.d.).

4.2.2 Komatiites

Komatiites are ultramafic volcanic rocks of extremely high magnesium contents (MgO $> 18\%$). The conditions necessary for creating such melts are very high

Sample	*Type*	Location	*Description*	δ^{60}Ni (‰)	± 2 s.d.
Peridotites					
DTS-1	*Dunite*	Washington	*intrusive peridotite*	0.05	0.03
NHM01	*Dunite*	NW Carolina	*orogenic peridotite*	0.16	0.07
PCC-1	*Spinel lherzolite*	California	*intrusive peridotite*	0.12	0.03
NHM02	*Garnet lherzolite*	South Africa	*kimberlite xenolith*	0.22	0.06
BD730	*Garnet lherzolite*	N Tanzania	*rift volcanic xenolith*	0.22	0.06
BD774	*Garnet lherzolite*	N Tanzania	*rift volcanic xenolith*	0.29	0.05
BD822	*Chromite lherzolite*	N Tanzania	*rift volcanic xenolith*	0.16	0.02
			Peridotites avg:	**0.17**	**± 0.16 ‰**
Tertiary komatiites – Gorgona Island					
GOR 94-32	*picrite*	Colombia		0.22	0.02
GOR 94-3	*komatiite*	Colombia	main flow	0.22	0.02
GOR 94-19	*komatiite*	Colombia	main flow	0.26	0.04
GOR 94-43	*komatiite*	Colombia	main flow	0.25	0.04
GOR 94-17	*komatiite*	Colombia	olivine cumulate	0.16	0.03
GOR 94-44	*komatiite*	Colombia	olivine cumulate	0.20	0.01
			Komatiites avg:	**0.22**	**± 0.08 ‰**

Table 4.1: *Summary of mantle rock samples analysed for Ni isotope composition.*

emplacement temperatures (200-300^o higher than for basalts) and very large degrees of partial melting ($\geq$50%) (Huppert et al., 1984; Arndt et al., 1998). This makes komatiites especially useful for studying the mantle, as the high temperature should reduce any isotopic fractionation that may take place during melt formation. Additionally, due to their unusually high degree of partial melting, the isotopic composition of komatiites should be very similar to that of the initial source (Dauphas et al., 2010). Most komatiite occurrences are of Archean or Early Proterozoic age, possibly indicating that the thermal conditions of the early Earth mantle were very different from today. The only documented example of post-

Proterozoic komatiite occurrence are the komatiites on Gorgona Island, located approxiamtely 50 km off the coast of Colombia (e.g. Echeverria, 1980; Aitkem & Echeverria, 1984). These komatiites have been dated at ∼90 Ma (Walker et al., 1999) and are texturally the least altered samples of this rock type available (e.g. Kerr, 2005).

Six whole rock samples from this Tertiary komatiite suite (main komatiite body, cumulate zone, and related picrite) have been analysed, giving an average isotope composition of 0.22 ± 0.08 ‰ (Table 4.1). As komatiites geochemically represent the melts extracted from the residual peridotite samples, a comparison between these two rock types should show if significant isotopic fractionation takes place during partial melting of the mantle. However, the average δ^{60}Ni-values for these two sample groups overlap, confirming that no isotopic fractionation has taken place between mantle rocks and komatiites. This results in a final estimate of the Ni isotopic composition for the mantle of $\delta^{60}Ni_{mantle} = 0.19 \pm 0.13$ ‰ (2 s.d.).

4.3 The Oceanic Crust

4.3.1 Isotopic fractionation with melt formation

To investigate whether fractionation of Ni isotopes occurs during basalt formation (10-20% partial melting), different types of basalts was analysed. Partial melting has previously been suggested to cause isotope fractionation of Fe stable isotopes due to preferential extraction of heavy isotopes (in the form of ferric iron) from

the solid phase (Williams et al., 2005; Weyer & Ionov, 2007; Schoenberg & Blanckenburg, von, 2006). For the Ni isotope system fractionation due to oxidation is not of importance, as the oxidation state of Ni (+II) does not change between different mineral phases and most likely does not change between solid and melt phases. However, fractionation might occur due to changes in bonding environments, making it theoretically possible for equilibrium fractionation to take place between solid and melt due to polymerisation, or between different mantle minerals due to differences in bond strengths or coordination for the metal ion in the minerals available. Alternatively, disequilibrum (kinetic) processes, relating to the faster transport of the lighter isotope into the melt, could also also generate stable isotope fractionation between melts and residues. In this case we would expect the smallest degree partial melts to be the lightest isotopically, because as the degree of partial melt increases, mass balance dictates that the isotopic composition of the melts will approach that of their source region.

To determine if melting of mantle material does cause a fractionation in Ni isotopes 8 MORB glasses (outermost crust of pillows) from different localities were analysed for their isotopic composition. Of the 8 samples 2 were from the Mid-Atlantic Ridge, 3 from the Indian Ocean Ridge, and 3 from the East Pacific Rise. All samples were from different geographical locations. As the spreading rate of a ridge determines the rate of melt formation, which in turn could have an effect on the Ni isotopic composition, samples of different spreading rates were analysed. There is a hint in the MORB data of a relationship between δ^{60}Ni-values and the

local rate of ridge spreading (and by implication, the rate of melt formation). The three samples from the faster-spreading East Pacific Rise are heavier on average than those from the slower Mid-Atlantic and Indian Ocean Ridges, although all are isotopically light relative to peridotites and komatiites. However, as there are overlap in the these data more analyses are needed are to confirm whether or not correlations are present. Overall, the eight MORB samples have an average δ^{60}Ni-value of -0.09 ± 0.15 ‰ (2 s.d.), which is significantly lighter than the estimated δ^{60}Ni-value for the mantle (0.19 ± 0.13 ‰). This suggests that partial melting of the upper mantle does cause fractionation of Ni isotopes, with the lighter isotopes being preferably extracted into the melt.

Sample	*Type*	Location	*Description*	δ^{60}Ni (‰)	± 2 s.d.
Mid-Ocean Ridge Basalts			*Spreading rate*		
APR74, 11-18	*basalt glass*	N Mid-Atlantic Ridge	*2.0 mm/yr*	-0.11	0.02
EW93-09, 15D	*basalt glass*	S Mid-Atlantic Ridge	*3.2 mm/yr*	-0.14	0.04
MD34, D4	*basalt glass*	SW Indian Ridge	*1.4 mm/yr*	-0.22	0.07
MD57, D13-7	*basalt glass*	Central Indian Ridge	*2.7 mm/yr*	-0.07	0.05
MD57, 10-1	*basalt glass*	Central Indian Ridge	*3.2 mm/yr*	0.04	0.06
CYP78, 18-65	*basalt glass*	N East Pacific Rise	*6.7 mm/yr*	-0.05	0.03
CY82, 27-1	*basalt glass*	N East Pacific Rise	*9.9 mm/yr*	-0.03	0.06
Naudur, ND51	*basalt glass*	S East Pacific Rise	*15.3 mm/yr*	-0.01	0.05
			MORB glasses:	**-0.09**	**± 0.15 ‰**
Intraplate basalts of mantle plume source					
BHVO-2	*OIB*	Hawaii	*USGS ref. mtrl.*	0.07	0.09
BIR-1a	*OIB*	Iceland	*USGS ref. mtrl.*	0.13	0.11
BCR-2	*Flood basalt*	Oregon	*USGS ref. mtrl.*	0.20	0.05
			Plume basalts:	**0.13**	**± 0.14 ‰**

Table 4.2: *Summary of basalt samples analysed for their Ni isotope composition. The results of the two USGS reference materials BHVO-2 and BCR-2 and MORB analyses of the East Pacific Rise agree well (within error) with published analyses from Cameron et al. (2009).*

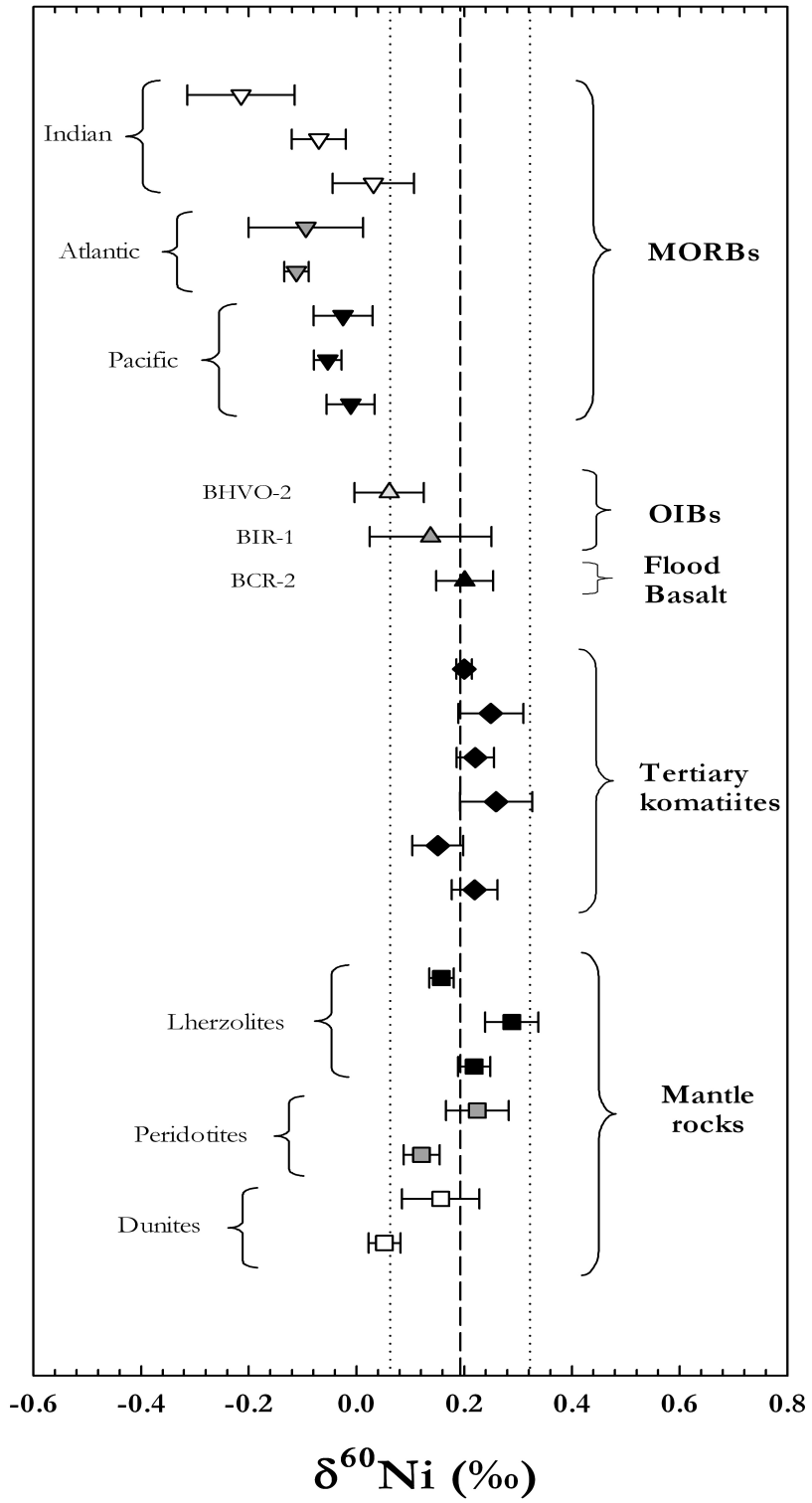

Figure 4.1: *Summary of all mantle derived samples analysed for Ni isotopic composition. The dotted lines show the estimated average mantle isotopic composition ($\delta^{60}Ni_{Mantle}$ = 0.19 ± 0.13 ‰). The figure shows how ultramafic rocks are clustered within a very narrow range in Ni isotopic composition. Plotted in the figure are also different mantle derived melts (komatiites and basalts), showing that some parts of the mantle may be of different Ni isotopic composition.*

4.3.2 Isotopic source signature?

Isotopic compositions of basalts should reflect their respective source melt region (Hofmann, 1997). Basaltic melts brought up by mantle plumes (Ocean Island Basalts, OIB) are considered to originate in the garnet stability field, while basalts formed at spreading centres (Mid-Ocean Ridge Basalts, MORB) are sourced from higher up in the mantle, in the spinel stability field (Turner et al., 2000). The uppermost part of the mantle is generally considered to be depleted in incompatible elements due to continuous melt formation. Comparative analyses of OIB and MORB basalt types would therefore indicate whether the depleted upper mantle is of different Ni isotopic composition than the lower mantle, in line with some other inferred chemical, isotopic and mineralogical differences.

As a comparison with the MORB glasses, three additional basalt samples of different origin have been measured for their Ni isotopic composition. These are the USGS reference materials BIR-1, BHVO-2, and BCR-2, all intraplate basalts. The melts forming these samples are all characterised as originating from a mantle plume with an enriched, "primitive", source. Two of the samples (BIR-1 from Iceland and BHVO-2 from Hawaii) are of typical OIB type, while the third, BCR-2, is a Miocene continental flood basalt and part of a large igneous province in Western North America. Analyses of the basalt reference materials give very different δ^{60}Ni-values for the three samples. Of the OIBs, the Hawaiian basalt is lighter than the Icelandic basalt (0.06 ± 0.07 ‰ and 0.13 ± 0.11 ‰ respectively), while the flood basalt sample is heavier than both the OIBs (0.20 ± 0.05 ‰). However,

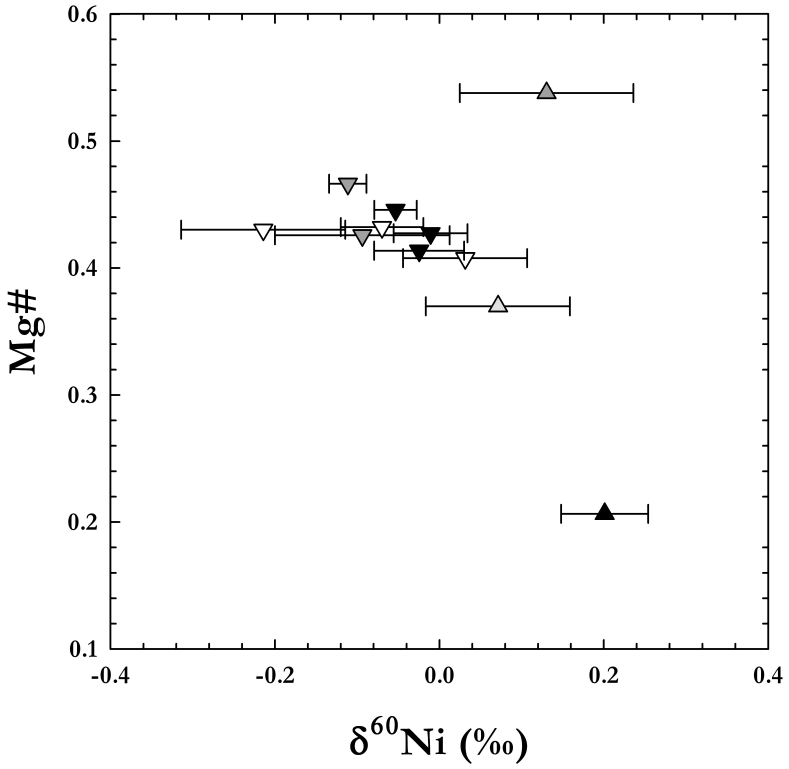

Figure 4.2: *Plot of δ^{60}Ni-values of all basalts against degree of melt extraction in the form of the samples' Mg-numbers (MgO/(MgO+FeO). Symbols represent the same samples as in Fig. 4.1. Major element data from Gannoun et al. (2007).*

as these values are within error of the estimated δ^{60}Ni-value for the mantle (0.19 ± 0.13 ‰), these samples indicate that there is essentially no isotopic fractionation between mantle rocks and intraplate basalts. This confirms the conclusions from the section on komatiites, showing that for mantle plume material the degree of partial melting does not have a large effect on the Ni isotopic composition.

These results suggest that basalts may have small differences in their Ni isotopic composition depending on their origin, with MORBs appearing lighter than intraplate basalts. Whether this is because of differences in degree of partial melting or in original chemical composition is difficult to say without further analyses.

If isotopic fractionation was caused by partial melting there should be a correlation between δ^{60}Ni and the amount of melt, which could be supported by the correlation between the samples Ni isotope ratios and Mg-numbers in Fig. 4.2. However, as this correlation shows an overall trend where the smallest amount of melt (lowest Mg-number) corresponds to the highest δ^{60}Ni-value, kinetic fractionation during partial melting is unlikely to be the reason for the differences between different basalts. However, if the process of partial melting is causing equilibrium fractionation between solid and melt in the mantle resulting in the melt (basalt) being slightly lighter than the residual solid (e.g. upper mantle peridotite), then the deep undepleted mantle (i.e. the source area for mantle plume basalts) may contain a reservoir of heavier δ^{60}Ni. This reservoir would then significantly alter the average δ^{60}Ni for the mantle, although the amount of this shift is impossible to quantify. Therefore, the preliminary conclusion is that the variation in Ni isotopic composition between MORBs and intraplate basalts may instead be caused by differences in isotopic composition between their respective source regions.

4.4 The Continental Crust

4.4.1 Fractionation with igneous differentiation

To investigate whether igneous differentiation causes fractionation of Ni isotopes, one andesite, one granodiorite and two granites (of igneous source) have been

analysed for their Ni isotopic composition. The results give an average δ^{60}Ni-value for granites of 0.18 ± 0.17 ‰, which agrees well within error with the isotopic compositions of both the granodiorite (0.02 ± 0.09 ‰) and andesite (0.14 ± 0.17 ‰) samples. These preliminary data suggest that there is no significant variation in isotopic composition with SiO_2-content, implying that Ni does not fractionate during the differentiation of continental igneous rocks, although more samples would be needed to confirm these findings.

4.4.2 Source inherited composition?

Granites are often subdivided into I-type granites, which are considered to originate from meta-igneous middle- to lower-crustal melts, and S-type granites, which are inferred to derive from the melting of supracrustal sedimentary source rocks (e.g. Chappell & Simpson, 1984). Given the earlier result that Ni isotopes do not fractionate during continental melting, a comparison of δ^{60}Ni values for these two granite types could establish whether there are differences in Ni isotopic composition between the lower/middle crust (represented by I-type granites) and the upper crust (represented by S-type granites). To address this question Ni isotope analyses were made of 2 I-type and 3 S-type granite samples from the Lachlan Fold Belt in Southeastern Australia, considered the type locality for defining I- and S-type granites (Chappell & Simpson, 1984).

The Lachlan Fold Belt was constructed during stepwise deformation and metamorphism in the late Ordovician to early Carboniferous. A period of extensive

volcanism in the Silurian and Devonian led to massive bodies of granitoid plutons intruding the area, including both I- and S-type examples (Foster & Gray, 2000). Lachlan Fold Belt granites and sediments have previously been analysed for the isotopic composition of Li (Teng et al., 2004), Mg (Li et al., 2010), Cu (Li et al., 2009), Si (Savage et al., 2010), and Mo (Jie Yang, *pers. com.*). To evaluate if Ni isotope ratios could be used to distinguish between I-type and S-type granites, samples of the two granite types were analysed for their Ni isotopic composition. However, of the few samples measured the Ni isotopic data shows no significant differences between the average δ^{60}Ni values for S-type and I-type granites (0.18 ± 0.17 ‰ and 0.16 ± 0.07 ‰, respectively) (Fig. 4.3). Though preliminary, these data suggest that there is essentially no difference in Ni isotopic composition between granites sourced from igneous rocks and those sourced from sedimentary rocks.

An unresolved question regarding the S-type granites in the Lachlan Fold Belt area concerns what material constituted their original source rock. Several publications have concluded that the source may be local Ordovician sedimentary rocks, generally interpreted as turbidite layers (Chappell et al., 2000; Glen et al., 1998). To evaluate if Ni isotope ratios could be used for determining if these sediments truly are the source rock of the area's S-type granites 4 samples of these sedimentary units were analysed for their Ni isotopic composition. The samples comprised of one clay-rich shale, one quartz-rich graywacke, and two intermediate samples (Table 4.3). When comparing the Ni isotopic compositions of the shales

Sample	*Sample location*	Rock type	δ^{60}Ni (‰)	± 2 s.d.
USGS reference materials				
AGV-2	*Guano Valley, Oregon*	Andesite	0.14	0.17
GSP-2	*Silver Plume, Colorado*	Granodiorite	0.02	0.09
Lachlan Fold Belt, SE Australia – Granites				
AB-82	*Bega Batholith*	I-type Granite	0.12	0.14
AB-195	*Bega Batholith*	I-type Granite	0.24	0.01
		I-type avg:	**0.18**	**± 0.17 ‰**
BB-09	*Berridale Batholith*	S-type Granite	0.12	0.03
BB-12	*Berridale Batholith*	S-type Granite	0.20	0.02
BB-53	*Berridale Batholith*	S-type Granite	0.17	0.07
		S-type avg:	**0.16**	**± 0.07 ‰**
Lachlan Fold Belt, SE Australia – Sediments				
OS31	*Ordivician sediment*	Shale/greywacke	0.05	0.05
OS32	*Ordivician sediment*	Greywacke	0.11	0.05
OS35	*Ordivician sediment*	Shale	0.01	0.09
OS39	*Ordivician sediment*	Shale/greywacke	0.11	0.09
		LFB shales avg:	**0.07**	**± 0.10 ‰**

Table 4.3: *Summary of continental rocks analysed for their Ni isotopic composition.*

and greywackes with the S-type granites analysed, the sediments give on average a slightly lighter δ^{60}Ni-value (0.07 ± 0.10 ‰). As previously shown in this chapter, there is no clear indication that Ni isotopes fractionate during melting processes, implying either that the analysed sediments may not be the material source of the S-granites, or that the amount of these sediments mixed into the granitoid melt may have been less than previously thought. This conclusion is also supported by analyses of Si and Mo isotope ratios of the same sample suite (P. Savage & J. Yang, *pers. com.*).

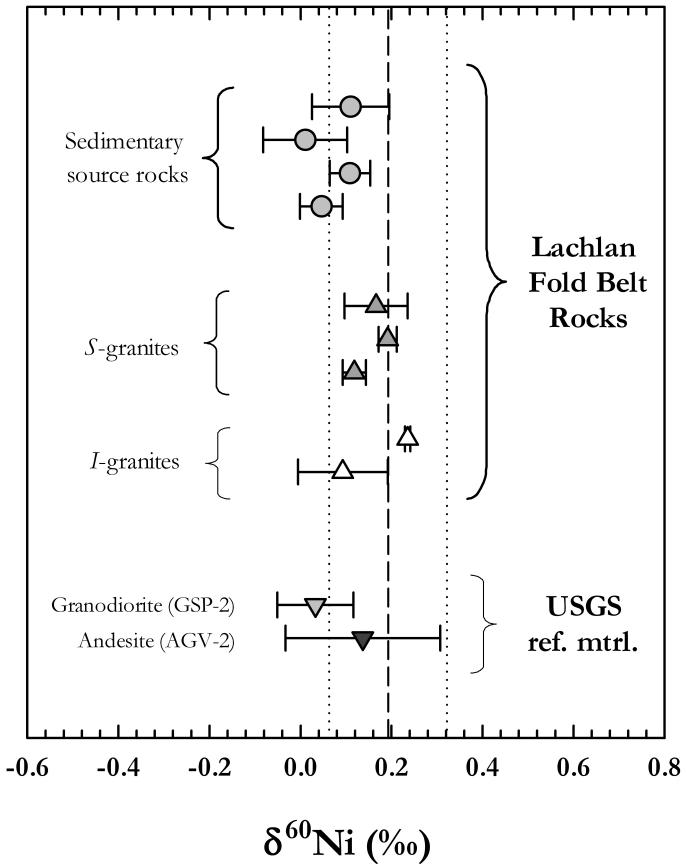

Figure 4.3: *Granites and Granitiod rocks analysed for their Ni isotopic composition. As displayed in the figure, there is no significant difference in $\delta^{60}Ni$ either between rocks of different SiO_2 composition (where andesite < granodiorite < granite) or between granites composed of material from different origins (I- or S-type). Also plotted are samples of sediments generally regarded to be the source material of the S-granites, although these are of lighter Ni isotopic composition then the analysed granites. The dotted lines shows the estimated average mantle isotopic composition ($\delta^{60}Ni_{Mantle} = 0.19 \pm 0.13$ ‰) as a reference.*

4.5 Alteration of silicate rocks

Up until now this chapter has focused on whether high-temperature processes affecting silicate rocks can possibly cause isotopic fractionation. In contrast, this section addresses whether low-temperature geochemical processes can affect Ni isotopic compositions of silicate rocks, drawing on data from two sets of samples that have undergone alteration of different types.

4.5.1 Alteration of the oceanic crust

The oceanic crust regularly becomes altered by low- and high-temperature hydrothermal fluids circulating within cracks and vents in the ocean floor, particularly close to mid-ocean ridges. These hydrothermal vents are fed mostly by sea-water but may also contain fluids released by underlying magma. However, the chemistry of these fluids are important to understand how alteration of the oceanic crust contributes to the chemical as well as the isotopic composition of seawater.

Ocean Drilling Program (ODP) hole 504B is located 200 km south of the Costa Rica Rift Zone in the equatorial East Pacific. The ∼2 km section was drilled through sediments and into underlying igneous rocks, and is the deepest drill hole and the longest continuos section made within oceanic crust. As a result, it is now regarded as a reference section for petrology and geochemistry of the upper oceanic crust (e.g. Alt et al., 1989; Sharma et al., 2001; Laverne et al., 2001; Chan et al., 2002; Bach et al., 2003). Seven samples from this drill core were analysed to compare the Ni isotopic composition of hydrothermally altered oceanic crust with those determined for fresh MORB in Section 4.3. These samples are mostly taken from the sheeted dike complex section from the lower part of the oceanic crust and cover a variety of apparent alteration types (see Table 4.4).

The altered samples show consistently heavier δ^{60}Ni isotopic values (on average 0.08 ± 0.12 ‰) compared to unaltered basaltic glasses (-0.09 ± 0.15 ‰), even though these values are apparently within error of each other (Fig. 4.4). To

Sample	*Location*	Rock Type	*Alteration*	δ^{60}Ni (‰)	± 2 s.e.
81-1	*Hole 504B*	pillow rim	altered glass	0.14	0.06
104-2	*Hole 504B*	altered dyke	light grey halo	0.11	0.09
247R1	*Hole 504B*	altered dyke	light grey halo	0.00	0.10
150R1	*Hole 504B*	altered dyke	dark grey background	0.14	0.07
247R1	*Hole 504B*	altered dyke	dark grey background	0.00	0.03
251R1	*Hole 504B*	altered dyke	light green-grey patch	0.07	0.18
252R1	*Hole 504B*	altered dyke	light green-grey patch	0.10	0.10
			Altered basalts avg:	**0.08**	**± 0.12 ‰**

Table 4.4: *Summary of hydrothermally altered oceanic crust samples from ODP hole 504B.*

determine whether these two sample groups can be distinguished from one another the data was subjected to a student's t-test, which gave a result of $t = 4.00$ (or that the probability for the two data sets to be overlapping is as low as 0.15 percent) showing that the Ni isotopic composition for the MORB samples and the hydrothermally altered basalt samples are significantly different from each other.

However, a t-test does not take into account the full variation (2 s.d.) or each sample measurement, which is why also a probability density plot was made using the Excel program *isoplot* (Ludwig, 1999) (Fig. 4.5). Although the figure show some overlap of these two data sets, this plot confirms that there is a difference between the fresh and the altered oceanic crust samples. Together these results show that hydrothermal alteration of the oceanic crust may result in a small isotopic fractionation of Ni, leaving the remaining crustal reservoir ∼0.1 ‰ heavier in Ni isotopic composition.

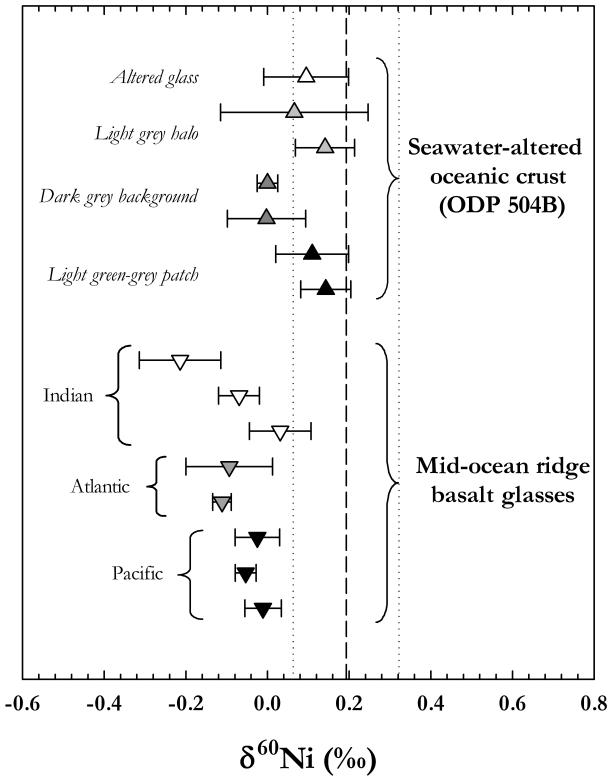

Figure 4.4: *Plot displaying the Ni isotopic composition of both fresh and hydrothermally altered oceanic crust. The dotted lines shows the estimated average mantle isotopic composition ($\delta^{60}Ni_{Mantle}$ = 0.19 ± 0.13 ‰) as a reference.*

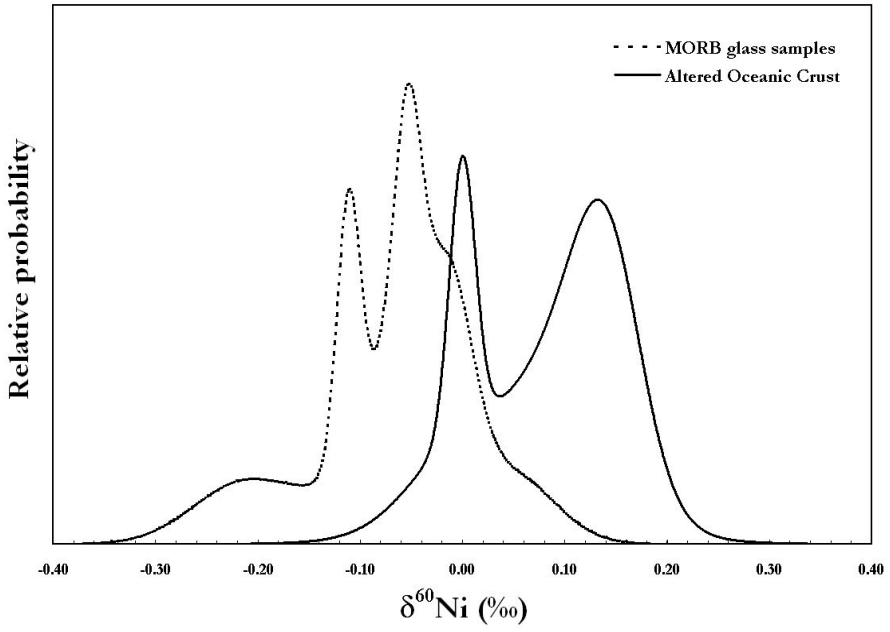

Figure 4.5: *Probability density plot made using isoplot showing that there is a significant difference in Ni isotopic composition between the fresh and the altered oceanic crust samples.*

4.5.2 Alteration of a peridotite protolith

Determining if, and how, sub-aerial weathering of silicate rocks fractionate Ni isotopes would provide an indication of the isotopic composition of the freshwater runoff from the continents into the ocean. This could in turn help constrain the Ni isotopic composition of the ocean. To investigate this, samples from the Cerro Matoso S. A. Ni-laterite deposit in northwestern Colombia have been analysed. The deposit is developed over a peridotite protolith thought to be part of the Cauca ophiolite complex (Bourgois et al., 1987). Further details of the deposit's geological setting can be found in Gleeson et al. (2004).

Three samples from this Ni-deposit were analysed for their Ni isotopic composition. The first sample is from the underlying weakly serpentinised peridotite (∼2500 μg/g Ni), whose δ^{60}Ni-value represents the "baseline" for the deposit. Material being leached from this protolith may be of heavier or lighter δ^{60}Ni-values than the protolith itself depending on the direction in which weathering causes Ni isotopes to fractionate. The second sample is taken from the weathered laterite, which consists of porous red and yellow Fe-(oxy)hydroxides, e.g. goethite, with high Ni content ($\leq$ 2 wt% Ni) from remaining Ni-containing peridotite minerals. The third sample is of the supergene enrichment zone, which is situated just above the peridotite and consisting of material leached form the overlying laterite and deposited further down the profile by percolating meteoritic water. This enrichment zone contains abundant silicate stockwork veins (*saprolite*) of the distinctive green minerals *pimelite* and *sepiolite*, which are talc and clay minerals with high

Sample	*Location*	Rock Type	*Alteration mineralogy*	δ^{60}Ni (‰)	± 2 s.e.
NHM04	*Cornwall, UK*	Peridotite	*Strongly serpentinised*	0.07	0.05
CM01	*Colombia*	Peridotite	*Weakly serpentinised*	0.08	0.06
CM03	*Colombia*	Laterite	*Fe,Ni-(oxy)hydroxides*	-0.11	0.09
CM02	*Colombia*	Supergene enr.	*Pimelite, sepiolite*	-0.30	0.08

Table 4.5: *Summary of the isotopic compositions of samples from the Cerro Matoso Ni-laterite mine, Colombia, and the Lizard complex, UK, analysed for this section on alteration.*

quantities of Ni substituted for Mg in the lattice structure. These silicate veins can contain as much as 30 to 40 wt% Ni.

The serpentinised peridotite from Cerro Matoso has a lighter δ^{60}Ni-value (0.08 ± 0.06 ‰) than the fresh peridotites analysed in section 5.2.1. A sample of the strongly serpentinised ophiolite from the Lizard Complex (Cornwall, UK) was also analysed and showing a similar value, indicating that these two samples may have been fractionated towards lighter δ^{60}Ni-values during the serpentinisation process. The laterite sample from Cerro Matoso has a lighter isotopic composition than the peridotite protolith (-0.11 ± 0.09 ‰), indicating that Ni-oxide minerals may prefer to take in the lighter Ni isotopes. The supergene enrichment zone, concentrating Ni bound in clay- and talc-type silicates, should then logically contain the heavier Ni isotopes. However, the analysis showed that instead this sample has an even lighter δ^{60}Ni-value than the Ni-oxide samples (-0.30 ± 0.08 ‰). Therefore, these data suggest that both oxides and clay silicates seem to prefer to take up the lighter Ni isotopes during weathering of a silicate rock body. This in turn implies that the heavier Ni isotopes from the protolith must have been leached and washed off in surface or ground water flows.

4.5.3 Primary conclusions for silicate alteration

Initially, these two weathering studies seem to contradict each other. The first section concludes that during seawater alteration the lower oceanic crust is shifted slightly toward heavier δ^{60}Ni-values, but during continental weathering the heavy Ni isotopes are extracted from the weathered rock. The main difference between these cases is the temperature, as the hydrothermal alteration would have occurred under much higher temperature than the weathering. One possibility is that the oceanic crust does not lose the light Ni, but gains heavy Ni isotopes from the (isotopically heavy) seawater during hydrothermal alteration. When comparing Ni concentration data of altered and unaltered oceanic crust in this drill core there is possible evidence for a Ni net gain in the lower crust samples analysed. To establish if this hypothesis is correct further studies of similar systems are needed.

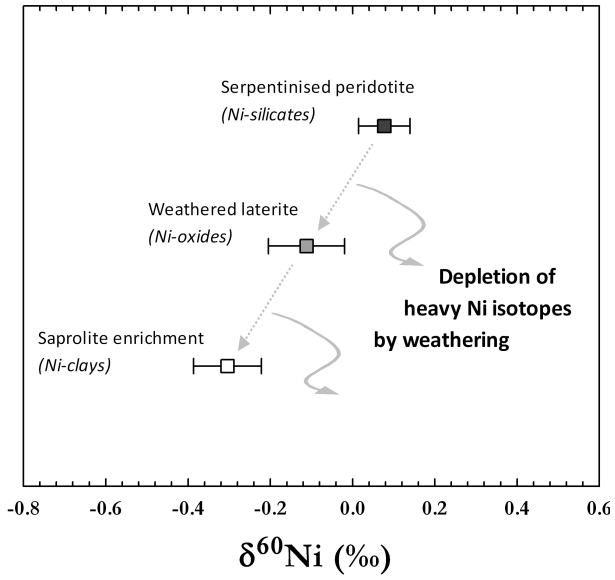

Figure 4.6: *Plot displaying the Ni isotopic composition of the weathered samples form Cerro Matoso laterite mine, showing how both Ni-oxides and Ni-clays contain a lighter Ni isotope composition than the underlying peridotite. This indicates that the heavier Ni isotopes must have been leached from the protolith and, ultimately, deposited in the ocean.*

4.6 The primitive Earth

The final section in this chapter deals with the larger scale geochemical problem of estimating the Ni isotopic composition of the silicate Earth and thereby also of the Earth's core. The core is believed to contain the large majority of the Earth's Ni in the form of a Fe-Ni-alloy, with minor (5-10%) contributions from other, lighter, elements (e.g. Si, S, C and O). It is theoretically possible that core-mantle differentiation during the earliest stages of the Earth's formation could have fractionated the pool of Ni originally present on Earth. To investigate this, the terrestrial samples described before in this chapter have been compared with Ni isotopic data for both differentiated and undifferentiated meteorites.

4.6.1 The Bulk Silicate Earth

Under mantle conditions Ni is a highly compatible element in mantle minerals, with the consequence that the Earth's silicate Ni is largely contained within the mantle. A good estimate of the Ni isotopic composition for the bulk silicate Earth (BSE) is therefore the same as the estimated value for the mantle, i.e. $\delta^{60}\mathrm{Ni}_{BSE}$ = 0.19 ± 0.13 ‰ (2 s.d.), as discussed in section 4.2.1.

4.6.2 Nickel isotopic composition of meteorites

Chondrites: These are undifferentiated meteorites formed during the earliest phase of solar system formation, making them the best materials available for estimating the chemical composition of the primitive Earth (Scott & Krot, 2003).

Chondrites are divided into three groups: carboneceous, ordinary, and enstatite.

Carbonaceous chondrites contain 1.5–6% carbon (mainly CI and CM) and are divided into eight well-resolved groups (CI, CM, CV, CR, CB, CK, CO, and CH, where the letters refers to individual meteorites) on the basis of refractory element abundances. For this thesis, samples from two groups (CV and CM) have been analysed for their Ni isotopic compositions, thus representing both high- and low-carbon chondrites. Compositionally, CI chondrites correspond best to the solar photosphere (Krot et al., 2003) and are considered to be the best representation of the primitive protoplanetary material from which the Earth accreted. Carbonaceous chondrites display considerable variation in both mass-independent and mass-dependent oxygen isotope compositions relative to other chondrite classes. The main body of subgroups plot below the terrestrial mass fractionation line, roughly following the fractionation line defined by carbonaceous chondrites anhydrous minerals, but CI chondrites plot on a fractionation line with similar slope, although slightly above, the terrestrial line (Clayton, 2003).

Ordinary chondrites do not have the same high carbon content as carbonaceous chondrites and are therefore separated from these. The group is subdivided into three groups depending on the bulk iron content, where H chondrites have high total iron, L chondrites have low total iron, and LL chondrites have low metallic iron relative to total iron as well as low total iron content (Krot et al., 2003). For this thesis only a sample of the L group has been analysed for its Ni isotopic composition. Oxygen isotopes analyses of ordinary chondrites show that all meteorites

in this group plot slightly above the terrestrial fractionation line (Clayton, 2003).

Enstatite chondrites are recognised as a group of their own due to their unique mineralogy, which indicates formation under extremely reducing conditions (Krot et al., 2003). The group is subdivided into two groups (EH and EL) on similar basis to ordinary chondrites and one sample of each group was analysed here. In terms of oxygen isotopes, enstatite chondrites are the only chondrite group that plot on the same mass fractionation line as the Earth, and it has therefore been argued that enstatite chondrites are the group of meteorites most chemically similar to the primitive Earth (Clayton, 2003).

The five chondrites analysed here vary within a narrow range of Ni isotopic composition, only between 0.20 to 0.31 ‰. The two carbonaceous chondrites showed the lightest and the one ordinary chondrite analysed presented the heaviest δ^{60}Ni-value, while the enstatite chondrites were of a Ni isotopic composition in between the other two groups (Table 4.6). On average, the chondrites analysed here have a δ^{60}Ni-value of 0.26 ± 0.11 ‰, which is in good agreement with published data (Cameron et al., 2009) showed an average chondrite value of δ^{60}Ni = 0.25 ± 0.11 ‰). These results suggest that carbonaceous chondrites are very similar to the bulk silicate Earth in Ni isotopic composition, which in turn implies that minimal Ni isotope fractionation took place during metal-silicate segregation and core formation. In this case, the primitive (undifferentiated) Earth may also have had a Ni isotope composition similar to that of chondrites.

Sample	Number	Type of meteorite	Class	Ni content	δ^{60}Ni (‰)	± 2 s.e.
Allende	BM1969.148	Carboneceous Ch.	CV3	10.8 wt%	0.21	0.08
Murchinson	BM197016	Carboneceous Ch.	CM2	12.0 wt%	0.20	0.08
Khaipur	BM1985.M144	Enstatite Ch.	EL6	12.9 wt%	0.28	0.09
Indarch	BM86948	Enstatite Ch.	EH4	18.3 wt%	0.27	0.10
Baratta	BM1925.1286	Ordinary Ch.	L3	12.0 wt%	0.31	0.04
Nahkla	BM1913.25	SNC *(Martian)*	ANAK	90 μg/g	0.20	0.09

Table 4.6: *Summary of the Ni isotopic compositions in all meteorites analysed for this thesis.*

Martian meteorites: Twenty-six meteorites believed to be of martian origin have been found on Earth. This group, named SNC (for Shergottites, Nahklites, Chassigny), are highly fractionated volcanic and plutonic rocks of unique oxygen isotopic compositions, indicating that they are derived from a large, planet-sized body other than the Earth of Moon (Krot et al., 2003). Oxygen isotope analyses of SNC meteorites show how these meteorites lie on a fractionation line with same slope as the terrestrial, although it is displaced above this line (McSween, 2003).

One sample of this group (Nahkla, a clinopyroxenite cumulate) was analysed for its Ni isotopic composition. The results show that this martian meteorite is indistinguishable from the bulk silicate Earth (0.20 ± 0.09 and 0.19 ± 0.13 ‰ respectively, Table 4.6). Mars does not seem to have ongoing plate tectonics, which should result in a less depleted martian mantle compared to the Earth (McSween, 2003). Therefore, the crust of Mars is likely to be more mafic than the Earth's crust and its Ni isotopic composition more similar to the Earth's upper mantle.

Although only one sample of a martian meteorite has been analysed so far, this one sample confirms this argument as its Ni isotopic composition is like that of Earth's mantle. Furthermore, this result shows that silicates of the inner solar

system may be homogeneous in Ni isotopic composition, which indicates that the planetary accretion itself did not significantly fractionate Ni isotopes.

4.6.3 Fractionation of Ni isotopes during core formation?

The Earth is believed to have undergone chemical differentiation, involving the physical separation of metal from silicate and the formation of a Fe-rich metal core. Core formation is considered to have been concomitant with planetary accretion, and essentially complete by the time of the Moon-forming giant impact (e.g. Kleine et al., 2002; Halliday, 2003; Walter & Tronnes, 2004). During core formation and segregation siderophile elements such as Ni D_{Ni} = 23-27, see equation 4.1) partitioned into the metal core generating characteristic depletions in the residual silicate Earth. High temperature and pressure experiments have shown Ni to be a moderately siderophile element, that becomes less siderophile with increasing pressure (e.g. Righter, 2003; Chabot et al., 2005; Kegler et al., 2008). Both Ni and Co (a siderophile element of similar volatility to Ni) are overabundant in the silicate Earth compared to their low pressure metal silicate partition coefficients, but experimental studies have revealed that both of these elements become less siderophile with increasing pressure such that their abundances in the silicate Earth can be explained by core segregation at high pressures at the base of a magma ocean (e.g. Wood et al., 2006).

$$D_{Ni} = \frac{[Ni]_{metal}}{[Ni]_{silicate}} \approx \frac{[Ni]_{core}}{[Ni]_{mantle}} \tag{4.1}$$

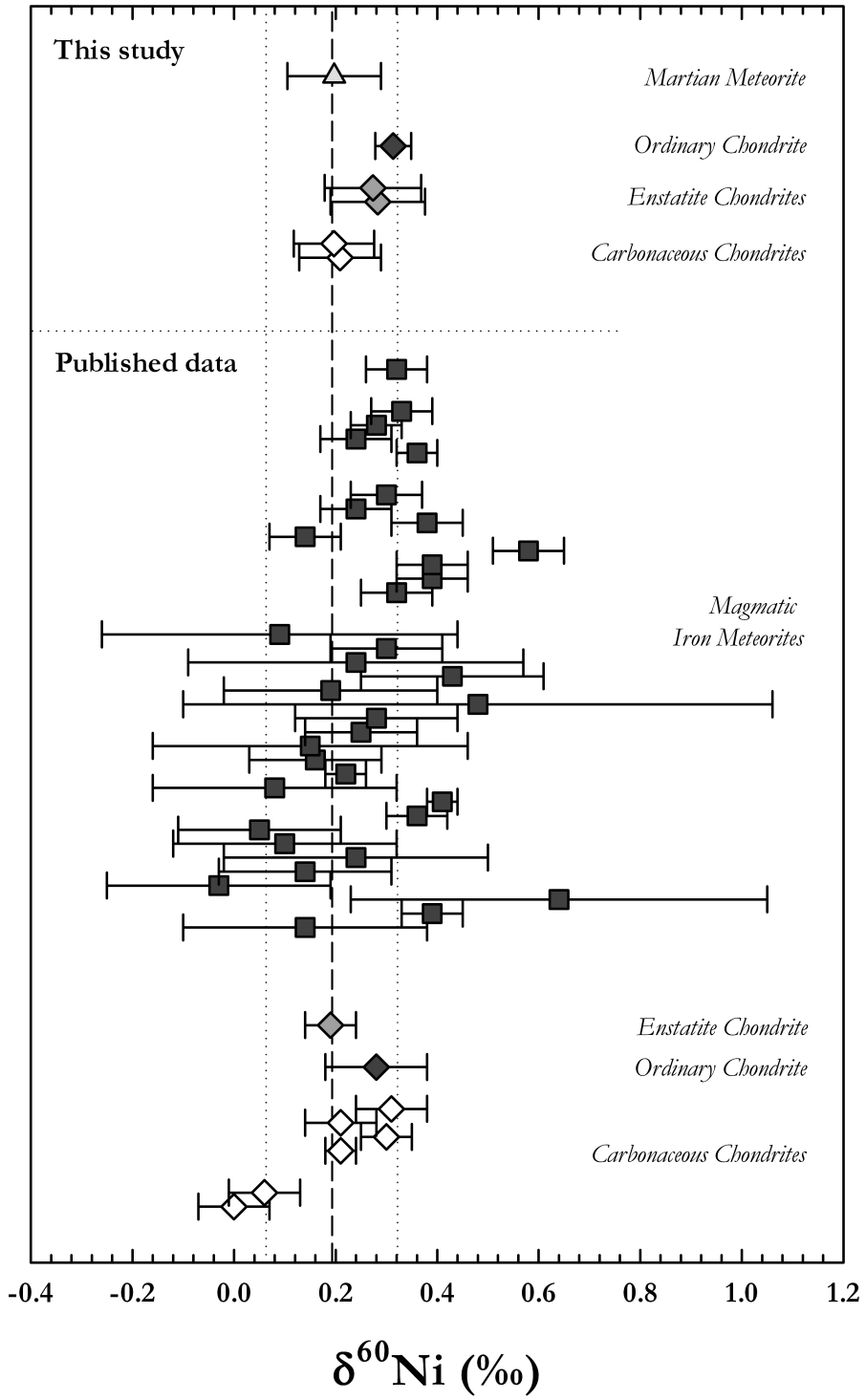

Figure 4.7: *Figure showing the Ni isotopic compositions in all meteorites analysed for this study (top), compared to all published data (from Cook et al. (2007); Moynier et al. (2007); Cameron et al. (2009) and Steele et al. (2011)), showing that the new data agree well with published data. The dotted lines shows the estimated isotopic composition for the silicate Earth as a reference.*

Futhermore, continuous oxidation of the Earth and partitioning of significant amounts of Si into the core (e.g. Wade & Wood, 2005) would also have made Ni more lithophile, substituting into silicates instead of the metal core. The Earth's core has been calculated to be of 1.93×10^{24} kg in mass and have an estimated Ni content of 50,200 μg/g (McDonough, 2003), making the core contain 9.7×10^{23} kg Ni or approximately 91.5% of the total Earth Ni (Allégre et al., 1995; McDonough & Sun, 1998).

Iron meteorites are considered to be remnants of the metallic core from disaggregated and differentiated planetary objects, broken up by asteriod collisions (Haack & McCoy, 2003). Although it is likely that the parent bodies of iron meteorites were smaller than the Earth, these meteorites are the only available samples of a planet's interior, which for a long time have enabled researchers to make estimations about the Earth's core. Iron meteorites are divided into several subgroups based on their petrology and chemical composition. Magmatic iron meteorites are believed to be samples of metal cores of planetesimals that formed by fractionation of the metal from the silicate followed by fractional crystallisation of the metallic melt, while non-magmatic iron meteorites are thought to have a more complex genetic history and to therefore not be representative of the Earth's core (e.g. Markl et al., 2006). A few high-precision studies partly, or wholly, concerning mass-dependent Ni isotopic compositions of iron meteorites have been published over the years. Using the most recent Ni isotope data (Cameron et al., 2009; Steele et al., 2011) suggests that magmatic iron meteorites have an average δ^{60}Ni

composition of 0.31 ‰ (± 0.09, 2 s.d.). If it is assumed that the Earth's core has a similar isotopic composition to magmatic iron meteorites, the magnitude of isotopic fractionation between the silicate Earth and the core ($\Delta^{60}\mathrm{Ni}_{core-BSE}$) can be calculated as 0.11 ‰ by $\delta^{60}\mathrm{Ni}_{core}$ – $\delta^{60}\mathrm{Ni}_{BSE}$ (alternatively, the fractionation factor, α, can be calculated to 0.999887) with the heavier Ni isotopes preferentially being sequestered into the Earth's core. Moreover, the Ni isotopic composition of the primitive Earth (PE) can be calculated from the isotopic compositions assumed for the BSE and mean magmatic iron meteorites by the simple mixing equation:

$$\delta^{60}Ni_{PE} \;=\; \delta^{60}Ni_{BSE} \cdot f \;+\; \delta^{60}Ni_{core} \cdot (1-f) \tag{4.2}$$

Where f is the part of the Earth's Ni present in silicates (from McDonough (2003)). The isotopic composition of the primitive Earth should thus be 0.30 ‰, which is within error of both carboneaceous chondrites and the bulk silicate Earth, as well as the δ^{60}Ni-value estimated for magmatic iron meteorites, due to the current analytical precision of these analyses. Interestingly though is this value closer to the isotopic composition measured for enstatite chondrites rather than carboneaceous chondrites, which, as previously stated, also have the same oxygen isotopic composition as the Earth. To determine whether the primitive Earth really is of enstatite chondritic value with regards to its Ni isotopic composition demands further high-precision analyses of both chondritic and iron meteorites as well as of high-pressure experiments that simulate the conditions of core formation on Earth.

4.7 Conclusions

This chapter presents the first detailed study of Ni isotopic variations in silicate materials. Although Ni is a relatively heavy element, high temperature processes, e.g. melting, seem to cause small variations in Ni isotopic composition in terrestrial igneous silicates. The total variation span over quite a narrow interval, between -0.2 to +0.3 ‰ (δ^{60}Ni), making high-precision analyses of Ni isotope ratios necessary for investigating these processes.

Data presented in this chapter conclude that the upper mantle most likely is of homogeneous Ni isotopic composition, as analyses of ultramafic xenoliths and komatiite rocks agree well with each other. Neither is there any significant difference in δ^{60}Ni between mantle rocks, intraplate basalts, and more acidic rocks, such as andesite or granitoids. This shows that larger scale melting and igenous differentiation is not accompanied by isotopic fractionation. On the other hand, data from Mid-Ocean Ridge basalts suggest that there may be differences in the Ni isotopic composition between the source ares for MORB and intraplate basalts.

Low-temperature processes seem to have a larger impact on the variation of Ni isotope ratios than high-temperature igneous processes. A small sample set analysed in this thesis show how surface weathering of a mafic rock body produce residual products (oxides and clay-silicates) of lighter δ^{60}Ni-values than the original protolith. This suggests that the heavier isotopes are leached from the continents and ultimately transported to the ocean. This heavy Ni may later be taken up by the oceanic crust during hydrothermal alteration.

The final section in this chapter concerns cosmochemistry and the Earth's core formation, comparing Ni isotope analyses of terrestrial igneous samples with analyses of chondrites and iron meteorites. The isotopic composition of the bulk silicate Earth was estimated as being similar to the mantle, which, compared to published values for the Ni isotopic composition of magmatic iron meteorites, suggests that the process of core formation was accompanied by an only very limited fractionation of Ni isotopes of $\sim$0.11 ‰. By using the same δ-values for the silicate Earth and the core, the Ni isotopic composition of the primitive Earth was estimated have similar isotopic composition as enstatite chondrites, implying that these chondrites may represent the isotopically best material for the precursor forming the primitive Earth.

CHAPTER

FIVE

VARIATIONS IN NI ISOTOPE COMPOSITIONS OF FERROMANGANESE CRUSTS

5.1 Introduction

Over the past decade there has been a rising interest in transition metal isotopic variations as a method for investigating ocean chemistry, biology, and element cycling. The first row transition metals are essential for primary productivity, and thereby may be bio-limiting. As such, these elements occupy a special place in ocean biogeochemical cycles. This chapter summarises the present understanding of the geochemistry of Ni in seawater and investigates its isotopic variability by determining whether ferromanganese crusts could be used as reliable archives.

5.1.1 Nickel in seawater

In the water column nickel exhibits a nutrient-type distribution pattern, with very low concentrations in the surface water, then increasing to around 1000 m depth, after which concentrations remain at a high level, or decrease somewhat, in the rest of the water column. This pattern is typical of elements involved in biological cycles, i.e. those necessary for primary productivity, where removal in surface waters is followed by oxidation and regeneration at depth as waste products sink through the water column.

The concentration of Ni in seawater has been measured in the Atlantic Ocean (e.g. Jickells, 1988; Saager et al., 1997; Bowie et al., 2002), the Southern Ocean (e.g. Löscher, 1999; Frew et al., 2001), the Indian Ocean (e.g. Saager et al., 1992), and the Pacific Ocean (e.g. Bruland, 1980; Noriki et al., 1998; Mackey et al., 2002). A comparison of the water column profiles of Ni concentrations for the different

ocean basins is shown in Fig. 5.1. Worldwide, the concentration of Ni in seawater varies between approximately 2–12 nmol/kg with a global average concentration of 8.2 nmol/kg (MBARI, 2011). The highest bottom water concentrations (∼12.1 nmol/kg) have been found in the northeast Pacific (Sclater et al., 1976), while the lowest bottom water concentrations (∼5 nmol) have been measured in the north Atlantic (Saager et al., 1997).

Early literature on the subject (e.g. Bruland, 1983; Brookins, 1988) suggested that the main speciation of Ni in seawater should be the free hydrated ion, Ni^{2+}. However, more recent models of this system have shown that the principal speciation ($> 50\%$) for Ni in seawater are complexes such as $NiCO_3^0$ followed by $NiCl^+$ (Calvert & Pedersen, 1993; Glasby & Schulz, 1999). Furthermore, Fujii et al. (2010) modelled how changes in Ni speciation in seawater should fractionate Ni isotopes. Their results suggested that the heaviest isotopes should preferentially be taken up into carbonate ($NiCO_3^0$), sulphate ($NiSO_4^0$), and bicarbonate ($NiHCO_3^+$) complexes, while the light isotopes would occur in hydroxide complexes (e.g. $NiOH^+$). Theoretically, this could cause fractionations of up to nearly 0.8 ‰ (δ^{60}Ni) between different speciations of Ni in seawater, and therefore also of sediments consisting of mainly one speciation (e.g. carbonates).

5.1.2 Biological utilisation of Ni in seawater

The marine geochemistry of Ni has previously been discussed in detail by Sclater et al. (1976), who showed that Ni concentrations in seawater are strongly corre-

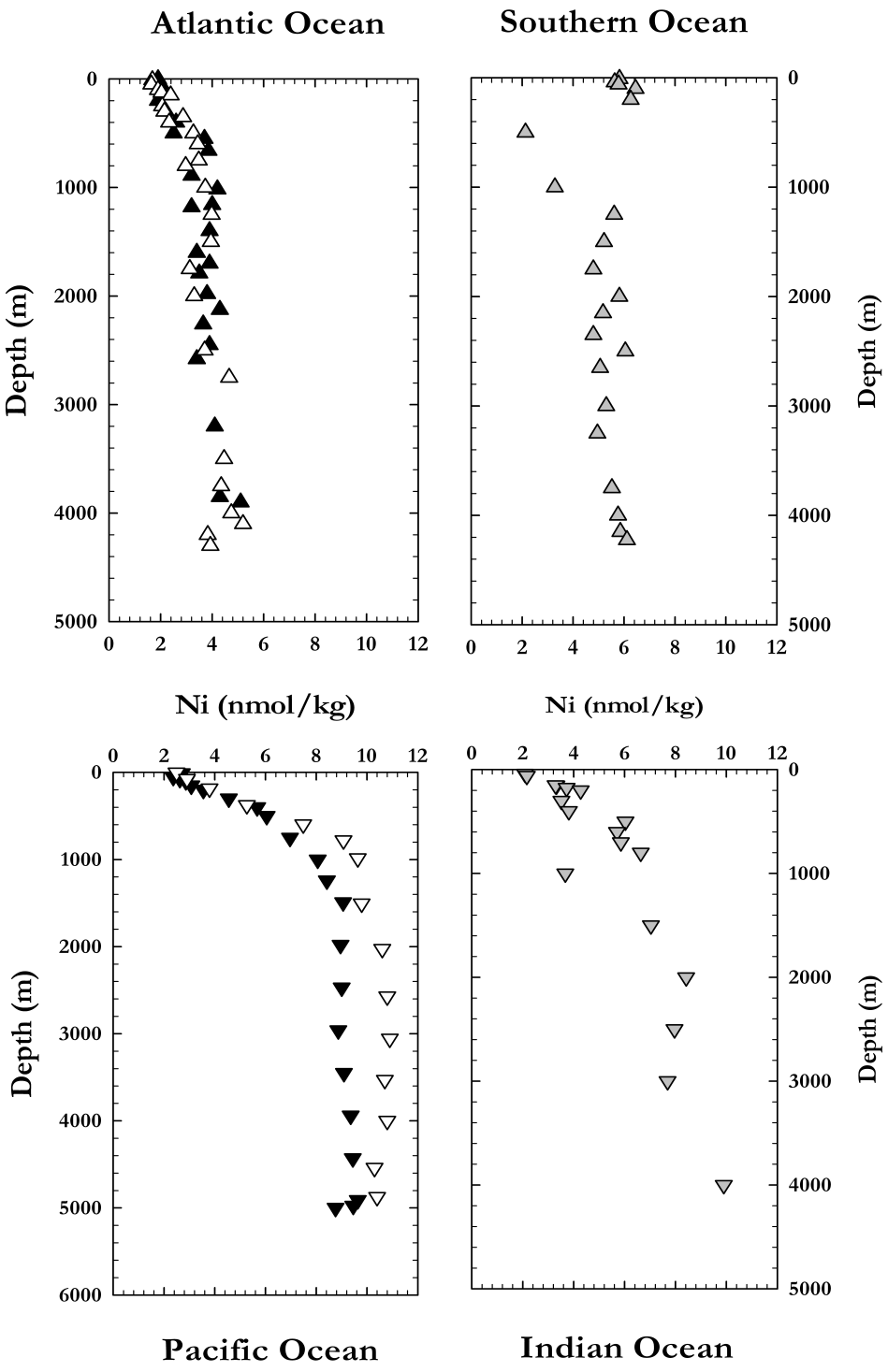

Figure 5.1: *Seawater concentration of Ni with depth in the Atlantic, Southern, Indian, and Pacific Ocean, showing how the dissolved Ni concentration varies between different ocean basins. In the top figures – black triangles are data NE Atlantic (British Isles, Jickells (1988)), white triangles data from NW Atlantic (Sargasso Sea, Saager et al. (1997)), and grey triangles data from the Southern Ocean (Atlantic side, Löscher (1999)). In the bottom figures – black triangles are data from NW Pacific Ocean (Southern China Sea, Norisuye et al. (2007)), white triangles data from NE Pacific Ocean (California–Hawaii, NE Pacific Bruland (1980)), and grey triangle data from the Indian Ocean (west of India, Saager et al. (1997)).*

lated with the major nutrients silicon and phosphorous. As a result, and because their measurements of Ni concentrations in the water column showed a typical nutrient profile, Sclater et al. (1976) were the first to suggest that Ni is a bio-essential element involved in primary productivity. Since then it has been recognised that Ni is incorporated in at least eight different enzymes (as described in Chapter 1). Assimilation of the various forms of nitrogen available to photoautotrophic plankton in seawater (mainly N_2, NH_4^+, and NO_3^-) usually requires complex enzymes containing transition metals, such as Fe, Mo or Cu to act as electron transporters (Morel, 2008). An alternative nitrogen source is the commonly available zooplankton waste product urea ($(NH_2)_2CO$). However, in order to use this nitrogen source, plankton need the Ni-containing enzyme *urease* to catalyse the reaction and break down urea to ammonia, which is a favourable nitrogen form for uptake by plankton (Glass et al., 2009) . Although theoretically enzymes should not be consumed during such reactions, in reality enzymes do get incorporated into the biological organism while catalysing biological reactions. Because of this, low concentrations of dissolved Ni in ocean surface waters can limit the growth of phytoplankton when the only nitrogen source is urea (Price & Morel, 1991), which has been shown for e.g. coastal diatoms (Oliviera & Antia, 1984, 1986b; Egleston & Morel, 2008) and marine cyanobacteria (Dupont et al., 2008). Surprisingly, however, the Ni concentration in surface waters are significantly higher than other micro-nutrients showing similar distribution patterns in the water column, such as Cd and Zn (Fig. 5.2). This relatively high Ni surface water concentration could potentially

be caused by the remaining ∼2 nmol/kg Ni being organically bound and therefore not bioavailable. Coale & Bruland (1988); Bruland (1989); Bruland et al. (1991); Rue & Bruland (1995) and Mackey et al. (2002) have shown that the majority of other transition metals in surface water are organically complexed. The organic complexes act as a buffer, as higher concentrations of free metal ions would be poisonous to phytoplankton. van den Berg et al. (1991); Xue et al. (2001) and Turner & Martino (2006) showed that the majority ($< 90\%$) of the available Ni could possibly be bound to organic ligands instead of as carbonate or chloride complexes, but Achterberg & van den Berg (1997) on the other hand reported only very small amounts (10–20% of measured concentration) of organically complexed Ni in surface seawater. More research on Ni speciation and bioactivity in surface seawater is therefore required in order to determine whether Ni may be a biolimiting factor in some areas.

5.2 Sources and sinks of Ni in the ocean

The residence time (τ) for an element in the oceans is calculated by $\tau = [A]/(dA/dt)$, where $[A]$ is the total amount of the element in the ocean reservoir and dA/dt is the rate at which the element is added to (or removed from) that reservoir (Bruland, 1980). The residence time of Ni in the ocean has previously been estimated to be around 10,000 years by Sclater et al. (1976), based on their calculations of sedimentation rates in the open ocean. As the total mixing cycle for the world's

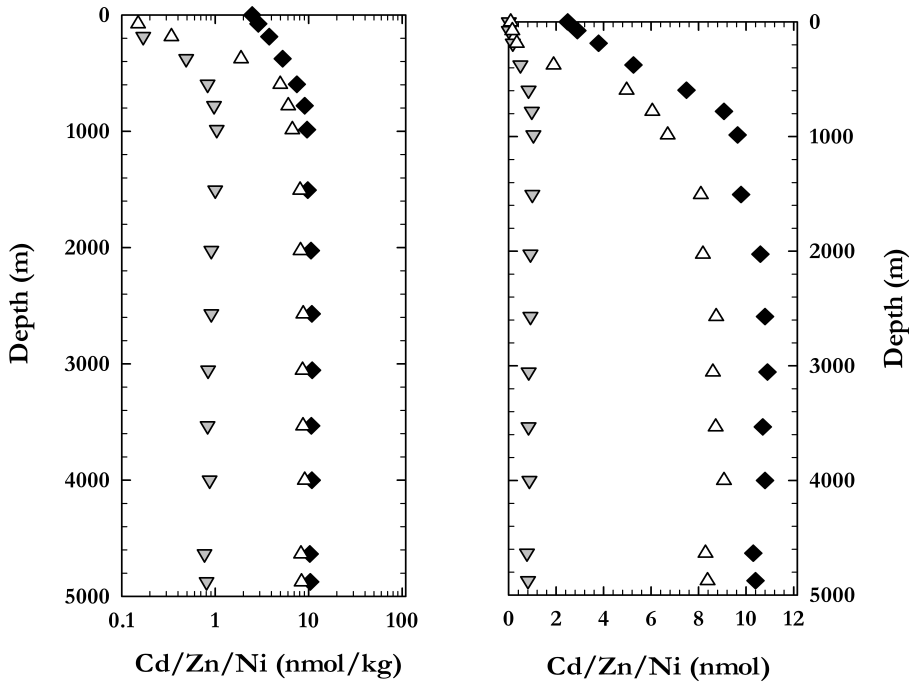

Figure 5.2: *Seawater concentration (nmol/kg) of micro-nutrients Cd (grey triangles), Zn (white triangles), and Ni (black diamonds) with depth (NE Pacific data from Bruland (1980)), plotted in both linear and logarithmic scale to clarify the difference in surface water concentrations. The figure shows that surface waters contain significantly higher concentrations of Ni than of Cd and Zn, but all elements show the same concentration pattern below 1000 m depth.*

oceans is estimated to be approximately 1000 years (Broecker, 1991; Morel & Price, 2003), a residence time of 10,000 years would be sufficiently long enough for Ni to have a homogenous isotopic distribution in the ocean.

5.2.1 Nickel sources

Dissolved Ni in the ocean mainly originates from the weathering products of oceanic and continental crust transported to the ocean by rivers (Li & Schoonmaker, 2003). The second largest source of Ni in the ocean is the atmosphere, which also contributes significantly to the yearly input. Though at first glance hydrothermal vents might also appear a likely candidate, they actually make a much

smaller contribution to the yearly Ni budget of the ocean (see section below).

5.2.1.1 Freshwater flux

River water: The highest Ni concentrations have been found in the Yukon River, NW Canada/USA (Alaska), where the average concentration is 10 ng/g. Other rivers draining the same area in the Canadian Rocky Mountains also showed remarkably high levels of Ni (e.g. Beaton River - 5 ng/g, Peel River - 3 ng/g, and Mackenzie River - 2 ng/g). Despite the high Ni load in these rivers, their overall significance as inputs of Ni to the ocean is small, as none of them (except the Mackenzie River) have a large flux of water to the ocean per year ($<$ 1,000 m^3/s). The Amazon is the dominant riverine source of freshwater to the ocean, alone supplying $>$ 40% of the annual input. The average Ni concentration in the Amazon River has been measured at 0.7 ng/g, very close to the global average river concentration. The second largest freshwater source area is South East Asia, whose rivers together provide the ocean with half the discharge of the Amazon River, but the measured Ni concentrations in these rivers are only between 0.15 and 0.6 ng/g, lower then the worldwide average.

According to a recent review on trace metals in river waters by Gaillardet et al. (2003), the global average Ni content in rivers is 0.8 ng/g (corresponding to 13.5 nmol/kg). Based on that value, the riverine water flux to the ocean would be between 36,000 and 38,000 km^3 per year (Gaillardet et al. (2003) estimate the total mass of Ni entering the ocean each year to be $\sim$30 kt (or $\sim 5.0 \times 10^8$ mol).

However, considering that the upper continental crust on average contains ∼55 μg/g Ni (Li & Schoonmaker, 2003), this estimate appears on the low side. If the Ni transported to the ocean by particulate matter were also taken into account, the amount of Ni entering the ocean every year could add up to far more than the estimated 30 kt.

Ground water: In an attempt to quantify the Earth's global cycle of several transition metals, including Ni, Rauch & Pacyna (2009) estimated the average Ni concentration in ground water to be 3 ng/g. This corresponds to 51 nmol/kg, which together with the average yearly ground water run off to the ocean of 2,400 km^3 (Zektser & Loaiciga, 1993) provides the ocean with yet another 7 kt (or 1.2 $\times$ 10^8 mol) Ni each year.

5.2.1.2 Atmospheric flux

Mineral dust: Studies on atmospheric inputs of Ni to the ocean have to date mainly been focussed on mineral dust particles, although the anthropogenic inputs of Ni are probably substantial due to metal production emissions and fossil fuel combustion. The yearly mass flux of mineral dust from natural sources has been estimated to be between 5,300 and 9,700 Mt (Rehkämper & Nielsen, 2004), adding between 3–57 kt Ni to the ocean each year. Additionally, Duce et al. (1991) calculated that up to 47% of the Ni in mineral dust dissolves in the ocean, which would result in an additional 0.2–4.6 $\times$ 10^8 mol Ni being dissolved in the ocean each year.

Volcanic emissions: The annual emission of volcanic gases is estimated to be between 1.2–2.5 $\times$ 10^{10} kg sulphur (S) per year (Rehkämper & Nielsen, 2004), and the ratio between Ni and S has been measured at 4.4 $\times$ 10^{-4} (Galindo et al., 1998). Using these figures, the total amount of Ni emitted from volcanoes every year is between 5–11 kt Ni (or 0.9–1.9 $\times$ 10^{8} mol) per year.

These two sources make the total atmospheric flux the second largest input of Ni to the ocean. However, the actual input could be significantly higher if anthropogenic emissions are also accounted for, as these are estimated to currently be at least twice the size of the natural emissions (Pacyna & Pacyna, 2001; Nriagu, 1989).

5.2.1.3 Hydrothermal flux

The flux from vents on or near the mid-ocean ridges are estimated to be between 1.5–15 $\times$ 10^{13} litres per year (Elderfield & Schultz, 1996). These fluids can contain up to 2.2 μmol/kg Ni (the value from ultra-mafic hosted hydrothermal vents, Gaillardet et al. (2003)), thereby inputting between 2 and 20 kt (or 0.3–3.3 $\times$ 10^{8} mol) Ni to the ocean each year. However, Ni should form sulphides and precipitate when hot hydrothermal fluids come in contact with seawater. Analysis of basal and ridge sediments confirms this theory, as these contain 430 μg/g Ni (Li & Schoonmaker, 2003), which is significantly more than the average for pelagic sediments (230 μg/g, Bruland & Lohan (2003)). On the other hand, it is possible that the Ni coming from vent fluids is complexed by organics (as has been shown

for Cu and Fe by Sander & Koschinsky (2011)), in which case the Ni could be mixing into the seawater instead of precipitating.

5.2.1.4 Other input sources

Benthic flux of dissolved Ni from sedimentary material may contribute to the oceanic Ni reservoir as sediments contain significant amounts of Ni (the average for pelagic sediments is 230 μg/g, Bruland & Lohan (2003)). In pelagic clays, most Ni is believed to be adsorbed by manganese oxides coatings on sedimentary grains. During diagenesis the MnO is reduced by oxidation of organic material, a reaction remobilising and releasing to the sediment pore water (Klinkhammer, 1980b). Analyses of bottom water close to the water-sediment interface have shown that even though Ni is released from sediments, not much escapes to the overlying seawater (Heggie et al., 1986). Therefore, the flux of Ni from sediments is estimated to only be in the range of 40–94 μmol/cm^2 per year (Klinkhammer et al., 1982). If these values of benthic flux are similar all over the globe, then this corresponds to a total maximum benthic mass flux of 3.4×10^6 mol Ni per year.

Cosmic dust input is yet another potential source of Ni in the ocean, albeit a small one. The average yearly mass flux of cosmic dust falling on the Earth has been estimated to be up to 5.0×10^7 kg by Peucker-Ehrenbrink (1996). If we assume that this incoming cosmic dust has an average Ni concentration of 19,000 μg/g (Rauch & Pacyna, 2009), the total mass flux of Ni to the earth from cosmic dust would be $\sim$1 kt per year. The oceans cover approximately 71% of the

Earth's surface so, assuming the cosmic dust fallout would be evenly distributed over the Earth's surface and that the dust is fully dissolved in the ocean, the total contribution to the ocean would be ∼70,000 kg (or approximately 1.2×10^7 mol).

5.2.2 Nickel sinks

The two processes which appear to dominate the removal of dissolved Ni from the oceans are the uptake by primary productivity and subsequent incorporation into pelagic clays, and the adsorption onto ferromanganese oxide particles.

5.2.2.1 Pelagic sediments

The average Ni concentration in pelagic clays is 230 μg/g, which is significantly higher than the average of 55 μg/g Ni measured in the upper crust (Li & Schoonmaker, 2003). The strongly elevated concentration in sediments is probably due to both the assimilation of Ni in phytoplankton, and the fact that Ni, as with many other transition metals, is adsorbed onto manganese oxide coatings on both detrital and biogenic sediment grains. If the area of pelagic sedimentation is 300 $\times 10^6$ km^2 (∼80% of the ocean), and the sedimentation rate of pelagic clays is 0.23 g/cm^3/year (Rehkämper & Nielsen, 2004), then the total amount of Ni being incorporated into pelagic sediments each year is 2.7×10^9 mol. This would make pelagic sediments the main sink of dissolved Ni in the ocean.

5.2.2.2 Ferromanganese crusts

Ferromanganese crusts, and partly also nodules, are a sink for most transition metals including Ni. Sclater et al. (1976) considered these precipitates to be the main sink for Ni. Kraemer & Schornick (1974) estimated the average accumulation rate of ferromanganese oxides in the Pacific Ocean to be approximately 2.5 $g/cm^2/10^6y$, which corresponds to a total deposition of 7.5 Mt of oxides worldwide per year, assuming that ferromanganese oxides only precipitate in the deep ocean (surface area 300×10^6 km^2). With an average concentration of ~4,000 $\mu g/g$ (Li & Schoonmaker, 2003) this adds up to a total of 30 kt (5.1×10^8 mol) Ni being removed from the ocean each year. This shows that ferromanganese crusts and nodules are a considerable sink for Ni in the ocean.

5.2.2.3 Other output sinks

Alteration of the oceanic crust could possibly result in removal of Ni and therefore act as an oceanic sink. The amount of oceanic crust hydrothermally altered by seawater has been estimated to be between 3.8 and 5.7 Gt per year. As discussed in chapter 4, alteration of oceanic crust may cause heavy Ni from seawater to be taken up by the oceanic crust. There are however no clear evidence for a change in Ni concentration during alteration of the oceanic crust present in current literature (Alt et al., 1989; Bach et al., 2003), which makes it impossible to estimate how much Ni could be removed from the ocean due to this process.

	Mass *(kg)*	*Ref.*	**Avg Ni conc.**	*Ref.*		**Tot Ni *(mol)***
Oceans	1.37×10^{21} (L)	*a*	8.2 nmol/kg	*a*		1.12×10^{13}
Inputs	**Mass flux *(yr)***	*Ref.*	**Avg Ni conc.**	*Ref.*	**Ni flux *(mol/yr)***	**Residence time**
River water	3.6–3.8 $\times$ 10^{16} kg	*a*	13.5 nmol/kg	*b*	4.9–5.2 $\times$ 10^{8}	
Ground water	12.4 $\times$ 10^{15} kg	*c*	51 nmol/kg	*d*	1.2 $\times$ 10^{8}	
Mineral dust	5.3–9.1 $\times$ 10^{11} kg	*e*		*f*	0.2–4.6 $\times$ 10^{8} *(1)*	
Volcanic emissions	1.2–2.5 $\times$ 10^{10} kg S	*e*	Ni:S = 4.4 $\times$ 10^{-4}	*g*	0.9–1.9 $\times$ 10^{8}	
Hydrothermal fluids	1.5–15 $\times$ 10^{13} kg	*h*	2.2 μg/g	*b*	0.3–3.3 $\times$ 10^{8}	
				Total:	0.8–1.6 $\times$ 10^{9}	**6,900 – 14,500 y**
Outputs	**Mass flux *(yr)***	*Ref.*	**Avg Ni conc.**	*Ref.*	**Ni flux *(mol/yr)***	**Residence time**
Pelagic sediments	2.2 g/m^2	*e*	230 μg/g	*b*	2.6 $\times$ 10^{9} *(2)*	
Ferromanganese crusts	0.025 g/m^2	*i*	4,000 μg/g	*b*	5.1 $\times$ 10^{8} *(2)*	
				Total:	2.6–3.1 $\times$ 10^{9} *(3)*	**3,600 – 4,300 y**

Table 5.1: *Estimated fluxes of inputs and outputs of mol Ni to the ocean over one year.*

References: *a) MBARI (2011), b) Li & Schoonmaker (2003); Gaillardet et al. (2003), c) Zektser & Loaiciga (1993), d) Rauch & Pacyna (2009) (and references therein), e) Rehkämper & Nielsen (2004) (and references therein), f) Nriagu (1989), g) Galindo et al. (1998), h) Elderfield & Schultz (1996), i) Kraemer & Schornick (1974) ; (1) Based on that only 0.47% of the Ni attached to aerosol particles is soluble in seawater (Duce et al., 1991) ; (2) Area for pelagic accumulation was estimated to 300 $\times$ 10^6 km^2 ; (3) higher total value includes the ferromanganese crusts.*

5.2.3 Oceanic residence time of Ni

Estimates for the oceanic residence time for Ni can be determined using either the estimated fluxes of inputs or those of outputs (Table 5.1), and the two give very different results. On the one hand, using the total amount of mol added to the ocean each year, which is 0.8–1.6 $\times$ 10^9 mol, the estimated residence time is 6,900 – 14,500 years. On the other hand, using the total amount of Ni taken out of the ocean each year, which according to this calculation is 3.1 $\times$ 10^9 mol, the resulting residence time is only 3,600 years. This calculation shows that the inputs and outputs of Ni are unbalanced, implying that the oceanic Ni budget is not in steady state. Most likely this is not true, either because the inputs are underestimated or because of some other, unknown input sources. As the conditions for outputs in general are better known than those for inputs to the ocean (Li, 1982), the results from the output calculation are likely to give a more accurate estimate. The calculated residence time is still twice the ocean mixing time, although Bruland (1980) states that the residence times of an element needs to be >5,000 years for mixing to achieve full homogeneity of elemental concentrations, and isotope ratios, in the deep ocean water.

5.3 Ferromanganese oxide crusts

Marine ferromanganese (FeMn) oxide crusts are formed by the inorganic precipitation of dissolved iron and manganese in oxidising seawater onto sediment-free

volcanic surfaces, such as sections of basaltic seamounts, ridges or plateaus. The growth of the crusts is extremely slow, adding on average only 1-10 mm/Ma and adsorbing dissolved metals in the seawater during the process (Koschinsky et al., 1996). Crusts are characterised according to the origin of their metal contents. *Hydrogenetic* FeMn crusts are pure precipitates of seawater and can acquire very high metal concentrations through their slow rate of accumulation. For example, the average Ni concentration in hydrogenetic crusts is ∼4,000 μg/g (Maynard, 2003). *Hydrothermal* FeMn-crusts grow in areas of intense hydrothermal activity and acquire most of their metal contents from vent fluids. In this setting, most metals have already been precipitated as sulphides in the sediments surrounding the vent, and hydrothermal crusts therefore have comparatively low Ni concentrations, with an average content of only ∼300 μg/g (Li & Schoonmaker, 2003). A third class of FeMn oxide precipitates are FeMn nodules. These grow within sediments or at the sediment-water interface by precipitation of oxides derived from overlying seawater or underlying sedimentary pore waters, making them partially hydrogenetic. The high Ni concentrations averaging ∼7,000 μg/g (Maynard, 2003) are thought to mainly originate from the reduction of oxide (MnO) coatings of pelagic sediment grains during diagenesis (Verlaan et al., 2004).

For the purpose of studying metal distribution in the ocean, hydrogenetic FeMn crusts are of the most interest, as these provide a record of changes in seawater metal chemistry over the past 10-100 Ma. These crusts consist of amorphous iron oxyhydroxides intergrown with the poorly crystalline manganese oxide *vernadite*,

together with carbonates and detrital silicate minerals. The relative proportions of the different phases in a crust control the nature and amount of metals sorbed onto the surface and incorporated into the crust mineral phases. As all these factors in their turn are dependent on physical conditions, such as water depth, currents, productivity and geographic location, the isotopic composition of the adsorbed metals could potentially provide clues about cycles of ocean chemistry and insights into past ocean circulation patterns.

5.3.1 Nickel adsorption to FeMn crusts

The current model for FeMn precipitation is summarized well by Koschinsky & Halbach (1995). This shows how Mn^{2+} is oxidised during mixing of the O_2-depleted water from the oxygen minimum zone (OMZ) and underlying O_2-rich bottom water, following precipitation of MnO (and FeOOH) colloids. Adsorption of Ni onto MnO particles most likely occurs because of coloumbic interaction forces between the cation and the negatively charged surface of MnO_2, without changing the speciation of Ni. This is supported by leaching experiments by Koschinsky & Halbach (1995), which show that in hydrogenetic crusts Ni is almost exclusively contained within the MnO-phase. Although there is no evidence for a change in speciation during Ni adsorption onto Mn oxide, the adsorption process may cause a measurable fractionation between seawater and hydrogenetic crusts.

In oxygen-rich water Mn is present in the form of oxyanions, e.g. MnO_4^{2-} or MnO_4^{3-}, in which Mn is also in a high oxidation state (+VI and +V respectively).

In waters where oxygen is scarce, Mn may be used as an oxidation agent during in-situ breakdown of organic matter, thereby reducing the manganate ions to free Mn^{2+}. Because of this, maximum dissolved Mn^{2+} in the ocean occurs at the oxygen minimum zone (OMZ), usually around 1000-1500 m depth in the water column (Halbach & Puteanus, 1984; Koschinsky & Halbach, 1995). The adsorption of Ni onto MnO occurs during the mixing of water from the OMZ with underlying bottom water. Therefore, if a crust has at times been growing within the OMZ then the formation of MnO_2 may have been suppressed, which in turn could affect the uptake of Ni and possibly the Ni isotopic fractionation factor.

5.4 Experimental study on Ni–MnO adsorption

Recently, several experimental studies have investigated Ni sorption onto MnO_2 of different origin, e.g. ferromanganese coatings on quartz (Manceau et al., 2007), synthetic hexagonal birnessite (Peacock & Sherman, 2007a,b), and biogenic hexagonal birnessite (Pena et al., 2010). These studies have shown that the hydrated divalent Ni ion is adsorbed by surface complexation over vacancy sites in the MnO_2 layer. Furthermore, Peacock (2009) found that at neutral pH (>7), or higher, the adsorbed Ni migrates into the vacancy sites to progressively become incorporated into the MnO lattice structure. Extended X-ray adsorption fine structure (EXAFS) fluorescence spectra performed by the authors on natural marine vernadite phases provided no evidence for surface adsorbed Ni, suggesting that all Ni in

natural FeMn deposits is fully structurally incorporated.

Both the sorption and the incorporation reaction could theoretically cause fractionation of Ni isotope ratios and explain the surprisingly heavy δ^{60}Ni-values found in FeMn crusts. To closely investigate if isotopic fractionation are accompanying these reactions, experiments using synthetically produced hexagonal birnessite ($\delta MnO_x \cdot nH_2O$) as an analog to natural vernadite were performed at the School of Earth and Environment, University of Leeds in collaboration with Dr. Caroline Peacock. Similar experimental isotope work have recently been published for MnO-adsorption of other transition metals – e.g. Cu (Sherman & Peacock, 2010), Zn (Pokrovsky et al., 2005), Mo (Barling & Anbar, 2004; Wasylenki et al., 2008), and Tl (Peacock et al., 2009) – using hexagonal birnessite as the MnO-phase. Of these metals, only Zn has been shown to, just like Ni, not take part in redox reactions during adsorption onto MnO. However, as Zn adsorption was found to be accompanied by significant, pH-dependent, isotope fractionation, adsorption may also cause Ni isotope fractionation.

5.4.1 Experimental procedure

Sorption experiments were designed to illustrate a situation where the dominant form of Ni in seawater is Ni^{2+} (although in reality the dominant form is most likely $NiCO_3^0$ or $NiCl^+$, see section 5.1.1.), and that wt% Ni sorbed were within natural values for FeMn crusts (0.3-0.9%). Stock solutions containing 100 μg/g Ni (from crystalline $Ni(NO_3)_2 \cdot 6H_2O$) and 0.1M $NaNO_3$ (used as background elec-

trolyte) were prepared before start of the experiments using 18.2 MΩ grade water and reagents of laboratory reagent grade from Fisher Scientific. Experiments were conducted at room temperature (25^{o}C) and under a normal atmosphere. The hexagonal birnessite (Hx-birnessite) was synthesised in-house prior to the experiments (following methods from Peacock (2009)). All sorption experiments were prepared by addition of 4.5 mL of Ni stock solution (experiment total Ni 450μg) to 25 mL of 0.1M $NaNO_3$ background electrolyte solution, together with 0.05 g Hx-birnessite. The total experimental volume was therefore 29.5 mL and the solid/solution ratio was 1.7 g/L.

The experiments were performed in 50 mL centrifuge tubes at four different pH levels – 1.5, 2, 3, and >7 respectively. All solutions were calibrated to within ±0.05 of required pH by adding drops of HNO_3/NaOH directly after adding the Hx-birnessite to the solution as well as after 1 h, to ensure that the suspension pH was kept at the chosen level. For pH levels 1.5, 2, and 3 experiments were performed for 48 hours, to allow for maximum adsorption of Ni possible at each pH level. For pH >7 three experiments lasting 4, 48, and >500 hours respectively were performed to, if possible, discern fractionation differences during Ni incorporation into the MnO-lattice with time. Sorption samples were continuously shaken for the chosen time of each experiment and were checked intermittently to ensure that pH level was kept the same for the entire duration of the experiment. Afterwards all samples were filtered, using 0.2 μm cellulose nitrate membrane filters, to separate the Ni adsorbed to the MnO and the Ni still left in solution.

At pH >7 all Ni in the solution should be adsorbed to the MnO (as shown by experimental work on Ni concentration adsorption edges, (e.g. Peacock & Sherman, 2007a), of which some Ni should have been incorporated into the MnO structure. Therefore, to separate the adsorbed and the incorporated Ni, the solids from these samples were transferred to new 50 mL centrifuge tubes filled with 18.2 MΩ grade water. Drops of HNO_3 were added to these vials until pH was stabilised at 0.5, after which the samples were shaken for 30 min. This procedure should result in desorption of any surface bound Ni without releasing the structurally incorporated Ni or dissolving the birnessite. Afterwards the samples were again filtered to separate the desorbed Ni from the lattice-incorporated Ni. To confirm that only Ni adsorbed to the surface had been removed during the desorption stage and no MnO, including incorporated Ni, had been dissolved, aliquots of the desorption solutions were analysed for Mn content by Quadrupole-ICPMS. These aliquots only showed minor Mn concentrations, therefore the samples were considered to contain only desorbed Ni. It is however fully possible that some adsorbed Ni may still be attached to the MnO-surfaces together with the incorporated MnO-Ni.

The total Ni blank for the entire experimental procedure was ∼50 ng/sample, which was mostly connected with the synthesised birnessite. However, considering that the total amount of Ni in each experiment was 450 μg, this is negligible. The total Ni recovery after filtration and separation was >95% for all samples but one, the Ni-$NaNO_3$-solution for sample no 3a, (pH 3.0) where some Ni appeared to have been lost. All results from the experiments are given in Table 5.2 and Fig. 5.4.

5.4.2 Preliminary results

All experimental samples were measured against the $NiNO_3$-solution used in the experiments, which by definition then is set to $\delta^{60}Ni_{NiNO_3} = 0.00$. This is done to facilitate calculation of fractionation factors between the three different phases.

The results from the low pH experiments (pH 1.5, 2, and 3) showed a large fractionation between the Ni left in the $NaNO_3$-solution and the Ni adsorbed onto the Hx-birnessite, with total difference in δ^{60}Ni between the two phases varying from to 1.7 ‰ to 2.2 ‰ for the different experiments (see Table 5.2). Given that the duration of the experiments was only 48 h, the fractionation is probably the result of preferential adsorption of lighter Ni isotopes due to kinetics. The increasing magnitude of the fractionation factor observed with higher pH is likely due to kinetic fractionation. As shown by model curves in Fig. 5.3 the observed fractionations can be explained by closed system Rayleigh fractionation assuming a fractionation factor for Ni adsorption onto birnessite between 0.9980 and 0.9983.

At pH >7 all Ni in the solution should have been adsorbed to the Hx-birnessite surface and the fractionation discussed here is instead between Ni desorbed (i.e. only weakly adsorbed to the MnO-surface) and the Ni still attached to the MnO (i.e. theoretically, incorporated into the MnO-lattice structure). The pH 7 experiments with exposure time of only 4 h and 48 h respectively gave similar results to the lower pH experiments, with the incorporated Ni being fractionated towards lighter δ^{60}Ni-values. However, the experiments with >500 h exposure time on the other hand showed fractionations in the opposite direction between the desorbed

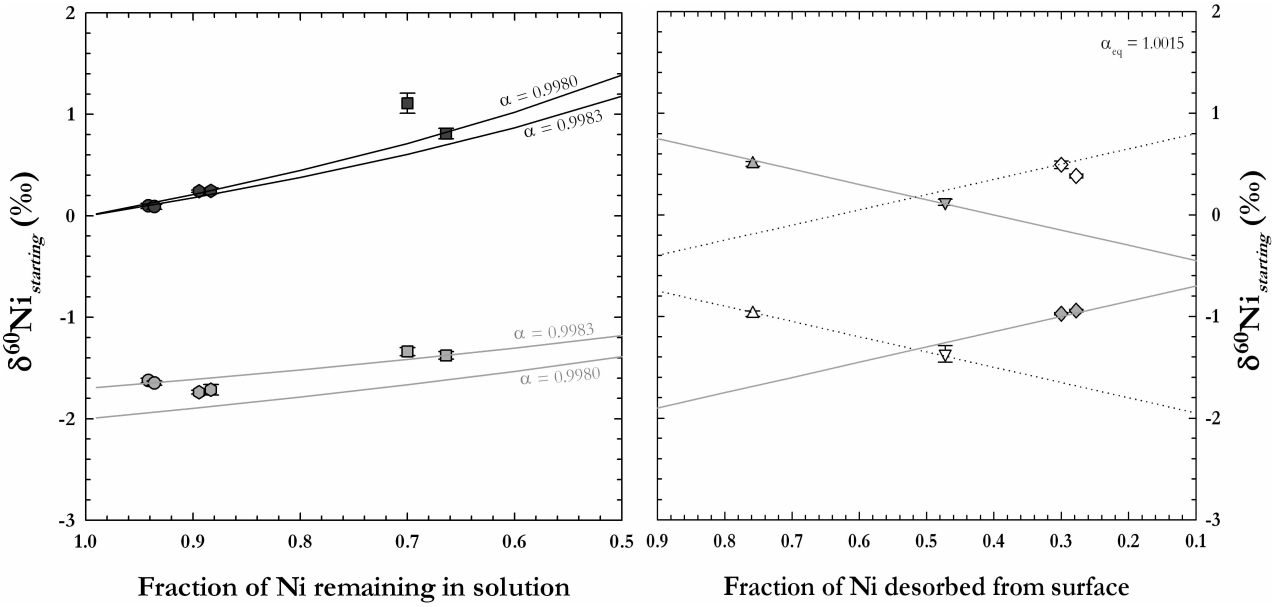

Figure 5.3: *Isotope data from the adsorption experiments plotted together with model fractionation curves. The low pH experiments (left) fit well with Rayleigh fractionation curves, while pH 7 experiments (right) seem to follow a constant, equilibrium, fractionation.*

Ni and the incorporated Ni (see Table 5.2). This suggests that incorporation of Ni into the MnO lattice structure starts of as a kinetic fractionation process with full isotopic equilibrium between these phases developing some time between 48 – 500 h (assuming that full equilibrium was reached in these experiments). As pictured in Fig. 5.3 the fractionation between the adsorbed and incorporated Ni-phase does not seem to follow a Rayleigh fractionation law as the lower pH experiments, but rather produces a constant fractionation of 1.5 ‰ ($\alpha = 0.9985$ or 1.0015 respectively) between these two phases (Fig. 5.3).

These experiments confirm that a possible cause for Ni isotope fractionation is Ni incorporation into vacancies in the vernadite lattice structure. Fractionation theory dictates that the heavier isotopes of an element are preferably situated in stronger (shorter or stiffer) bonds with other elements (e.g. Valley & Cole, 2001).

Sample	pH	Time (h)	Ni_{sol} (g)	$\delta^{60}Ni_{Soln}$	Ni_{ads} (g)	$\delta^{60}Ni_{ads}$	α^{sol}_{ads}
1a	1.5	48	424	0.10	26	-1.63	0.9983
1b	1.5	48	421	0.09	29	-1.65	0.9983
2a	2	48	403	0.24	48	-1.74	0.9980
2b	2	48	398	0.25	53	-1.71	0.9980
3a	3	48	315	1.11	135	-1.34	0.9976
3b	3	48	299	0.81	151	-1.38	0.9978

Sample	pH	Time (h)	Ni_{ads} (g)	$\delta^{60}Ni_{ads}$	Ni_{inc} (g)	$\delta^{60}Ni_{inc}$	α^{ads}_{inc}
4	>7	4	341	0.50	71	-0.97	0.9985
5	>7	48	213	0.13	203	-1.37	0.9985
6a	>7	>500	125	-0.94	290	0.38	1.0015
6b	>7	>500	135	-0.97	250	0.49	1.0015

Table 5.2: *Preliminary Ni isotope data for the experiments on Ni adsorption onto synthetic hexagonal birnessite. Errors on each sample measurement (2 s.e.) was 0.02-0.03 ‰.*

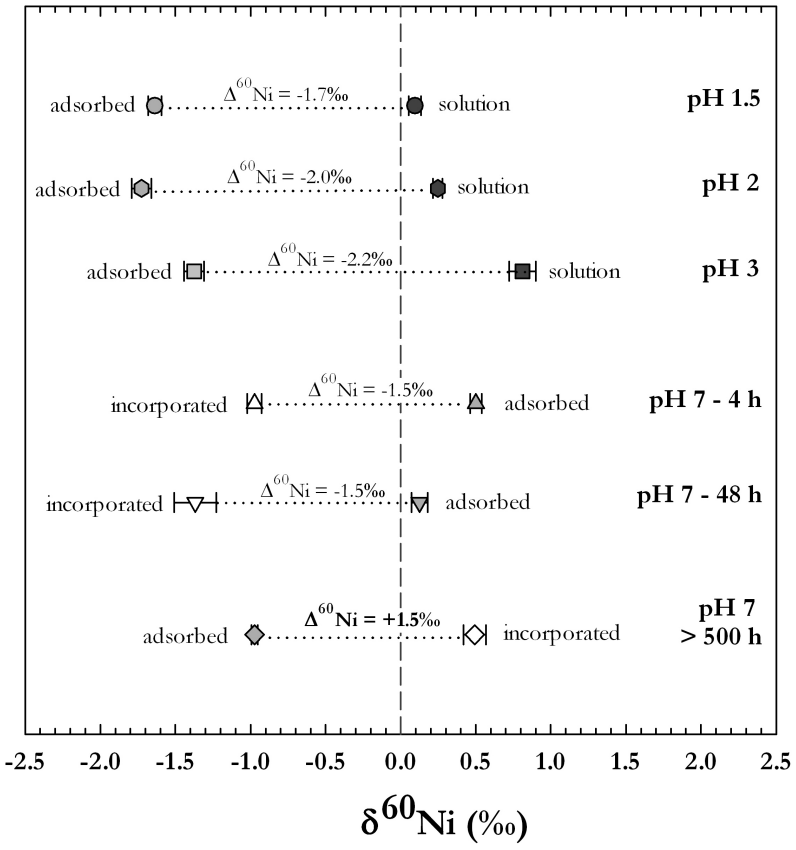

Figure 5.4: *Preliminary results showing Ni isotope fractionations (expressed as $\Delta^{60/58}Ni$) between $Ni_{solution}$ – $Ni_{adsorbed}$ (pH 1.5, 2, and 3) and $Ni_{adsorbed}$ – $Ni_{incorporated}$ (pH >7).*

As a Ni atom situated in a lattice would be tighter bound to the surrounding atoms then compared to either Ni adsorbed to the surface of a particle or to Ni dissolved (hydrated) in seawater, a large positive isotopic fractionation could most likely be caused by incorporating Ni into a lattice structure. This is consistent with both the experimental results above and with the observed variations in Ni isotope composition in natural FeMn crusts. However, further experiments are needed to confirm the exact magnitude of the equilibrium fractionation factor for Ni, as well as to determine other possible factors (e.g. variations in solution Ni concentration, pH or temperature) that can affect its magnitude.

5.5 Isotopic composition of surface scrapings

5.5.1 Sample selection

To investigate whether Ni isotopic variations in hydrogenetic FeMn crusts exist and could be used as an archive for deep water Ni isotopic compositions, the top surface of 23 globally distributed crusts were analysed. Sampling was performed by shaving off the top 0.5 mm of the crust using a scalpel, after identifying the most recent growth surface by way-up indicators (e.g. substrate rock). The hydrogenetic crusts analysed here were selected to include all the major ocean basins, and have previously characterised for other radiogenic and stable isotope systems. For comparison, one hydrothermal crust from the Southern Ocean and two powdered nodules (USGS reference materials Nod-A-1 and Nod-P-1) were also analysed.

Cruise	Sample	Location	Latitude	Longitude	Section	Depth (m)	Ni (μg/g)	δ^{60}Ni	2 s.d.
Ferromanganese crusts:									
S6-79-NP	D4-13A	NE Pacific	53°32' N	144°22' W	0-0.5	2100	7646	1.63	0.05
Challenger stn 253	M317	NE Pacific	38°09' N	156°25' W	0-0.5	5715	5645	1.41	0.11
GMAT	14D	E Pacific	13°59' N	96°08' W	0-0.5	4119	4729	2.47	0.30
SO-79	22KD	E Pacific	06°33' S	90°44' W	0-0.5	2313-2381	4552	1.82	0.13
SO-79	21KD	E Pacific	06°33' S	90°44' W	0-0.5	2643-2713	3211	1.70	0.05
F10-89-CP	D11-1	W Pacific	11°38' N	161°41' E	0-0.5	1690-1870	3294	1.69	0.20
F10-89-CP	D18-1	W Pacific	10°16' N	160°40' E	0-0.5	1800-1925	5714	1.89	0.16
SO-67-1	4KD	SW Pacific	10°18' S	161°28' W	0-0.5	1425	6125	1.68	0.05
SO-67-1	8KD	SW Pacific	10°15' S	161°26' W	0-0.5	2615	4600	2.00	0.05
Challenger stn 281	M353	SW Pacific	22°21' S	150°17' W	0-0.5	1789	4700	1.04	0.25
SO-36	63KD	SW Pacific	28°34' S	163°00' E	0-0.5	1700	3208	1.00	0.04
SO-27	70TKD	South China Sea	09°19' N	115°20' E	0-0.5	1589	5442	1.84	0.13
SO-49	42KD	South China Sea	15°40' N	116°06' E	0-0.5	2800	5708	2.27	0.15
SO-36	52KD	Southern Ocean	46°13' S	147°01' E	0-0.5	1600-1810	2666	1.93	0.06
MW8801	D18-1	Southern Ocean	50°02' S	126°44' E	0-0.5	3993	1330	1.47	0.11
HEMS Mabahiss	96626.E (6)	NW Indian Ocean	01°26' N	66°34' E	0-0.5	3385	1950	1.46	0.11
Antipode	145D-C	NW Indian Ocean	07°20' N	57°56' E	0-0.5	2094-2748	3881	1.58	0.22
DODO	232D	E Indian Ocean	05°23' S	97°29' E	0-0.5	4121	2563	1.73	0.08
Antipode	109D-C	S Indian Ocean	27°58' S	60°48' E	0-0.5	5178-5698	1263	1.56	0.11
Discovery II stn 5978	1966.0.69	NE Atlantic	42°54' N	20°13' W	0-0.5	3155-3338	2475	1.68	0.11
ALVIN	539; 2-1A	NW Atlantic	35°36' N	58°47' W	0-0.5	2665	8916	1.82	0.05
Hudson stn 54	1969.05	NW Atlantic	39°00' N	60°57' W	0-0.5	1830	2551	0.88	0.02
ArcI TR079	D-14	NW Atlantic	16°55' N	61°10' W	0-0.5	2000	2429	1.02	0.11
SO-84	43DS	SE Atlantic	15°09' S	08°21' W	0-0.5	1966-1990	2272	1.24	0.12
Ferromanganese nodules:									
USGS ref. mtrl.	Nod-A-1	NW Atlantic	31°02' N	78°22' W	bulk sample	788	6360	1.08	0.07
USGS ref. mtrl.	Nod-P-1	E Pacific	14°50' N	124°28' W	bulk sample	4300	13400	0.40	0.10

Table 5.3: *Summary of crust samples and results of Ni isotope analyses of the surface scrapings. The samples were provided by the US Geological Survey (Jim Hein), Menlo Park, USA; Scripps Inst. Oceanography, UC San Diego, USA; University Rhode Island, USA; National History Museum and British Museum, London, UK; Bundesanstalt für Geowissenschaften und Rohstoffe, Germany; and Universität Kiel, Germany.*

5.5.2 Results: isotopic variations in hydrogenetic crusts

The analysed surface scrapings from hydrogenetic crusts show a large spread in δ^{60}Ni-values, from 0.88 to 2.47 ‰, with a global average δ^{60}Ni-value of 1.6 ± 0.8 ‰(2 s.d.). These data are the heaviest Ni isotope ratios found during this project, indicating that low temperature fractionation produces large isotopic variations for the Ni system. Additionally, resampling of the surface scrapings displays variable reproducibilities between 0.02 and 0.30 ‰ (Table 5.3), indicating that some crusts may be heterogeneous in Ni isotope composition even in the same surface layer.

5.5.3 Results: isotopic composition of hydrothermal crusts

A few of the crusts analysed grew close to, or on, mid-ocean ridges and should therefore be described as hydrothermal crusts. These crusts display an average δ^{60}Ni-value of 1.51 ‰ (± 0.12, 2 s.d.), which lies within the range of the analysed hydrogenetic crusts. This similarity in the Ni isotope composition of hydrothermal and hydrogenetic samples contrasts with other metal stable isotope systems (e.g. Rehkämper et al., 2002). There are two possible interpretations for this; either the Ni isotope composition of hydrothermal fluids is similar to that of seawater, or the isotope compositions of both hydrothermal and hydrogenetic crusts are controlled by fractionation processes associated with precipitation and crust formation. However, more analyses of hydrothermal crusts, in addition to hydrothermal fluids, would probably be required in order to single out the correct option.

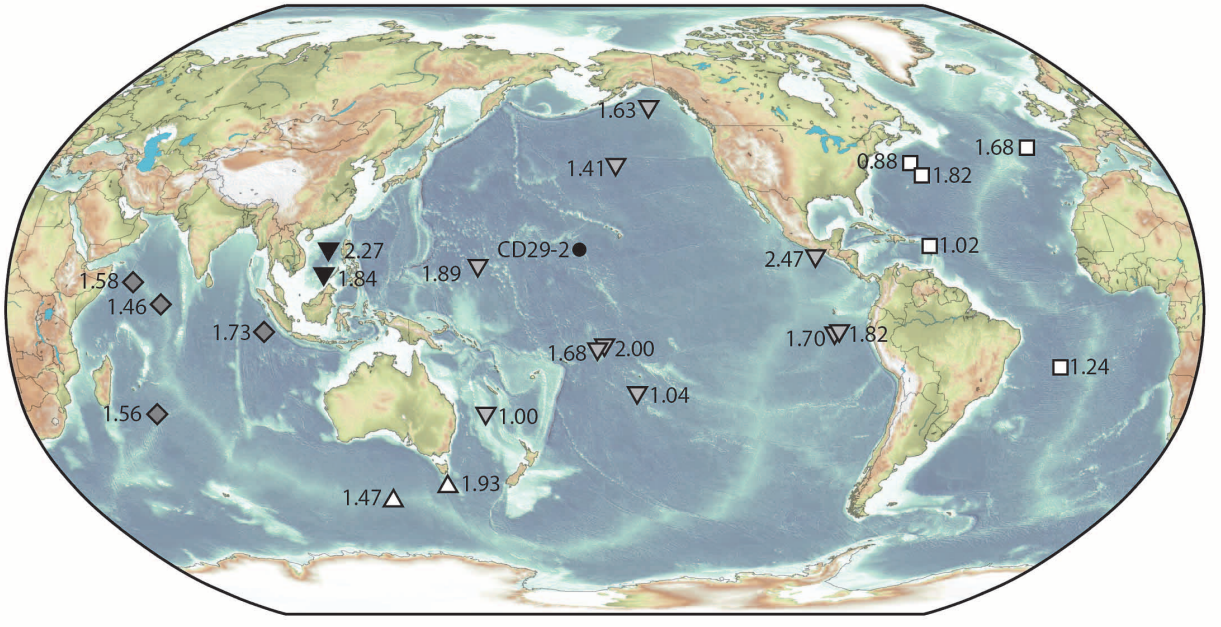

Figure 5.5: *Samples and results for all ferromanganese crust surface scrapings analysed for their Ni isotope composition plotted according to their location of growth. Also plotted is the location for the crust selected for an isotope depth profile study (CD29-2).*

5.5.4 Discussion

The global variation in δ^{60}Ni for FeMn crusts of >1.5 ‰ is remarkably large considering that igneous and sedimentary rocks only vary between -0.2 to 0.3 ‰ (see Chapter 4). It also distinguishes the Ni system from other "heavy" stable (metal) isotope systems, which show little variation among surface scrapings from the same type of samples (e.g. Mo, Tl and Cd; Siebert et al., 2003; Rehkämper et al., 2002; Horner et al., 2010). The lack of isotopic variation in these other metals lead to suggestions that FeMn crusts could provide a record of deep water isotope composition of the element, distorted by a possible steady fractionation between seawater and the oxide surface due to adsorption of the element.

At the moment, there are no available seawater Ni isotope data with which

to compare the results for FeMn crusts. Such data could be used to determine whether the spread in FeMn crust Ni isotope values reflects differences in seawater composition or varying degrees of fractionation during adsorption or incorporation into the manganese oxide lattice. The large Ni isotopic variation could conceivably be due to several factors, such as changes in the seawater isotopic composition or changes in the fractionation factor between seawater and FeMn crusts. Another possibility is that it could be controlled by crustal growth parameters.

5.5.4.1 Crustal growth location

In Fig. 5.5, all samples and results are plotted at the location (latitude/longitude) of their growth. At first, there does not seem to be any clear connection between the location of growth and the Ni isotope composition. In Fig. 5.6, the samples are plotted in groups according to which ocean basin they are from. Of all samples analysed, only crusts from the Indian Ocean show relatively consistent δ^{60}Ni-values throughout the basin. There is a hint that compositions may become progressively heavier from the Atlantic (0.88-1.82 ‰, $n = 6$) to the Indian (1.46-1.73 ‰, $n = 4$) to the Pacific (including the South China Sea) (1.00-2.47 ‰, $n = 13$). To investigate whether the difference in isotopic composition between the three different basins is statistically significant, a student's t-test was performed on the different data sets. When comparing the data from the Pacific with the data from the Atlantic the resulting t-value is $t = 2.4$ (probability of 2.7 %). This suggests that the data from these ocean basins are statistically distinct from each another.

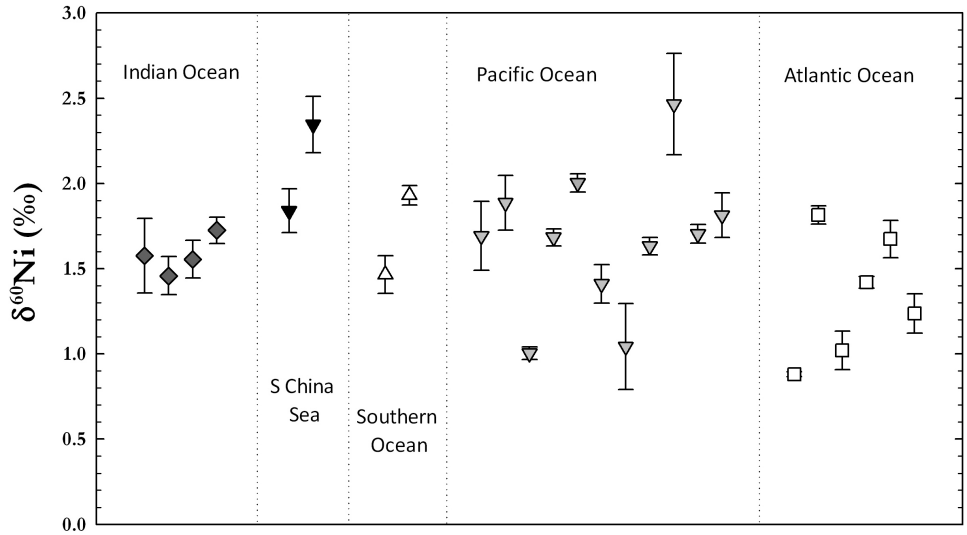

Figure 5.6: *Nickel isotope compositions of surface scrapings gathered by ocean basin of origin (Atlantic, Indian, Southern, and Pacific Ocean). No clear variation between the different ocean basins can be seen, although there is a hint of generally lighter δ^{60}Ni-values in the Atlantic than in the Pacific. Error bars are 2 s.d. of all measurements performed.*

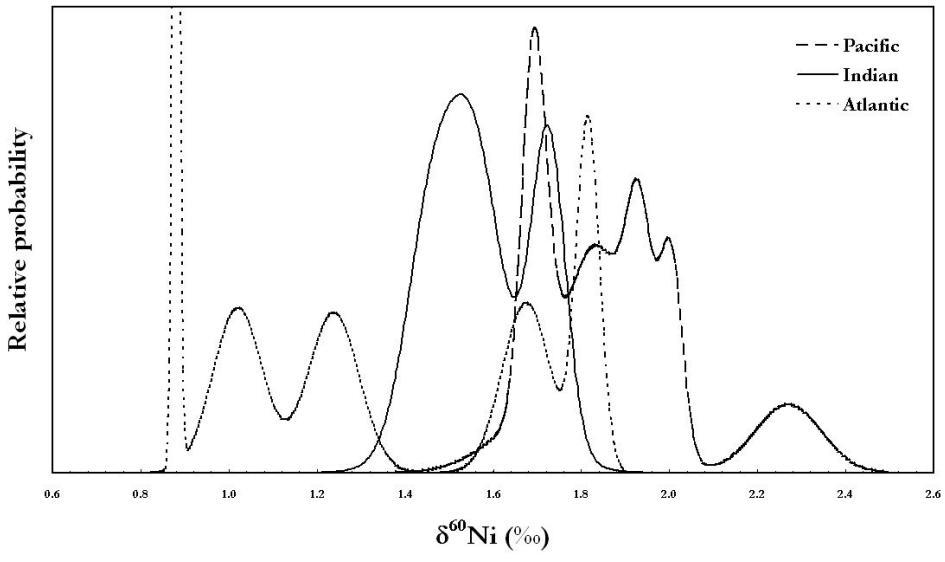

Figure 5.7: *Probability density plot comparing the Ni isotopic composition (including individual sample errors) of FeMn crust samples from the Atlantic, Indian, and Pacific Ocean. Although the curves are overlapping the mean of their respective curve are offset from each other, implying a statistical difference in the isotopic composition of FeMn crusts of the three ocean basins.*

However, a t-test does not take into account the full variation of each sample measurement (as is expressed in a sample's standard deviation). Because of this, a probability density plot of the whole data set was also created using the *Isoplot* program. This plot, shown in Fig. 5.7, reveals three curves (representing the Atlantic, Indian, and Pacific Ocean) which despite overlapping are clearly offset from one another. This confirms the findings from the t-tests that, statistically, there is a real difference in the isotopic composition of FeMn crusts between different ocean basins.

5.5.4.2 Crustal growth depth

The crusts were collected from a large variety of ocean depths, from 1400 m down to 5700 m depth. This difference in depth could potentially be a contributing factor to the variation in isotopic composition of the FeMn crusts. However, Fig. 5.8 shows that sample δ^{60}Ni-values are spread evenly with depth, providing no indication of a connection between the depth of growth and the Ni isotope composition.

5.5.4.3 Crustal Ni concentration

The Ni content of each FeMn crust sample was measured by Q-ICPMS before chemical separation and was found to vary between 1,200 and 8,900 μg/g, with the Pacific samples showing higher average concentrations relative to the samples from the Atlantic and Indian ocean. Although no information about the growth rate of the crust samples was available, there is no indication that the growth rate is related to differences in sample Ni content.

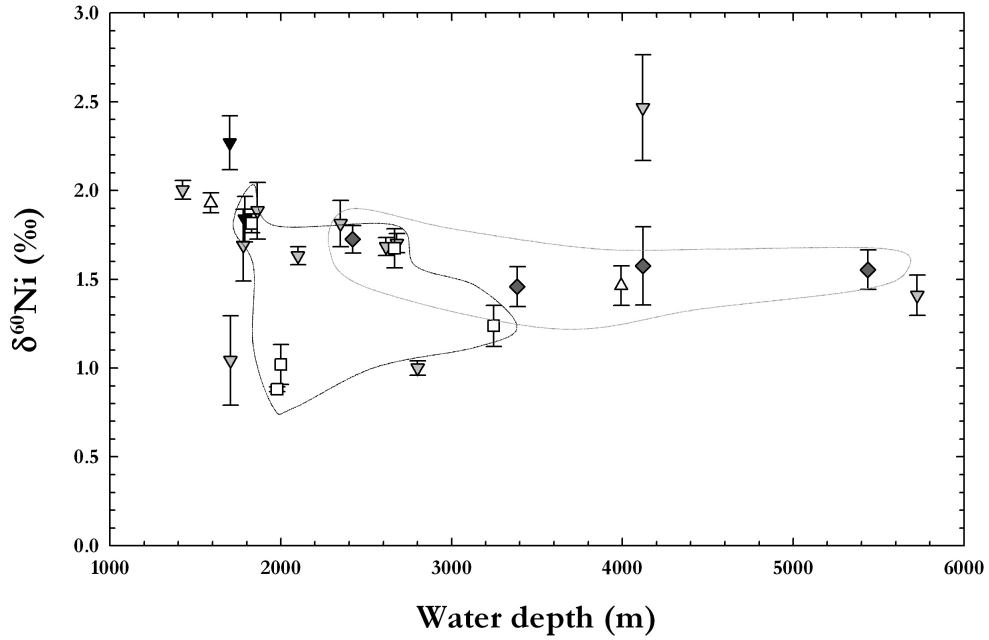

Figure 5.8: *Nickel isotope ratios of ferromanganese crusts plotted against the sample depth of growth. The samples are grouped by ocean basin for clarification (white squares = Atlantic; black diamonds = Indian; grey triangles = Pacific; black triangles = South China Sea; white triangles = Southern Ocean).*

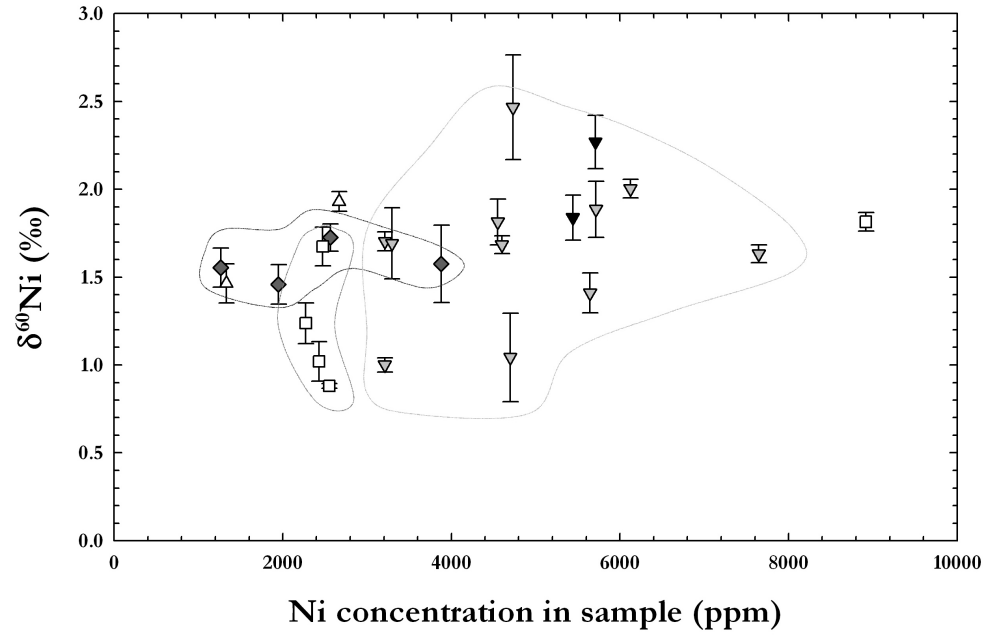

Figure 5.9: *Nickel isotope ratios of ferromanganese crusts plotted against the sample Ni concentrations. The samples are grouped by ocean basin for clarification (white squares = Atlantic; black diamonds = Indian; grey triangles = Pacific; black triangles = South China Sea; white triangles = Southern Ocean). The figure shows how the crust Ni concentration seem to increase from the Atlantic to the Pacific Ocean (except for one Atlantic outlier), but the same trend is not seen for Ni isotopic composition.*

However, as Fig. 5.1 (p. 133) shows, the bottom water concentrations increase from the Atlantic to the Pacific, and it is possible that the differences in Ni concentration of FeMn crusts may simply be a reflection of the abundance of Ni in the water column in each basin. Comparing the samples Ni concentrations with their Ni isotope compositions (Fig. 5.9), there is a hint of a correlation, although it is difficult to know whether these factors really influence each other. However, if FeMn crusts do reflect the composition of deep water, then it would suggest that Pacific seawater is of heavier Ni isotopic composition than Atlantic seawater.

5.5.4.4 Seawater composition

In a previous section, statistical tests suggested that there is a significant difference in the isotopic values between the samples from the Atlantic, Indian, and Pacific Oceans. If FeMn crusts reflect the deep water Ni isotopic composition this provides a hint that the deep water may be isotopically heterogeneous between different basins. The cause for this heterogeneity may be due to the new shorter residence time of ∼3,500 years calculated at the beginning of this chapter, as this may be too short a time for complete mixing between the ocean basins to occur. If this were the case, the variations in the Ni isotope data would then be consistent with isotopic fractionation during progressive removal of Ni from the deep water as it is advected via the conveyor belt defined by the ^{14}C age, which increases from the Atlantic to the Indian to the Pacific Ocean (Stuiver et al., 1983; Broecker, 1991).

Another possible reason for the deep water isotopic heterogeneity is differences

in speciation. As mentioned earlier, Fujii et al. (2010) discussed how changes of Ni speciation in seawater might fractionate Ni isotopes. Their model results suggest that the heaviest isotopes should preferentially be complexed by carbonate ions ($NiCO_3^0$), while the lightest isotopes would move into hydroxide complexes (e.g. $NiOH^+$). Theoretically, this could cause fractionations of up to nearly 0.8 ‰ (δ^{60}Ni) between different speciations of Ni in seawater. In areas with higher concentrations of some anion complexes, changes in speciation of Ni ions could possibly contribute to isotopic heterogeneity in the deep ocean water, which in turn may be linked to the variations in Ni isotope ratios of FeMn crusts.

Similarly, a difference in seawater composition, local or regional, could also affect variations in major element chemistry, and thereby mineralogy, of FeMn crusts, which could in turn affect the Ni isotope fractionation factor by changing the mechanism of adsorption or lattice-incorporation. Experiments have shown that Ni is mainly adsorbed onto the Mn oxide phase (Koschinsky & Halbach, 1995), so any variation in the Ni isotope fractionation factor between seawater and hydrogenetic crusts might be due to varying Mn concentration. Unfortunately, no major or trace element data are available for the crusts analysed, which would be needed to determine whether variations in crustal chemistry, and thus seawater chemistry, are the controlling factor for the Ni isotopic variations of FeMn crusts.

5.5.4.5 Biological input

In seawater, Ni is correlated with major nutrients such as silicon and phosphorous, suggesting that Ni is a micronutrient in the ocean (e.g. Sclater et al., 1976). This highlights another possible reason for the extent of Ni isotopic variability in ferromanganese crust samples that grew distant to both continents and mid-ocean ridges: local differences in seawater isotopic composition could be due to isotopic fractionation during biological uptake of Ni. Biological processes are generally thought to be accompanied by a kinetic isotope fractionation, where the lighter isotope is preferentially concentrated in the biomass, forcing the residual reservoir towards a heavier isotopic composition. The behaviour of Ni during biological uptake was demonstrated by Cameron et al. (2009) to be similar to that documented for other isotope systems. Since open-ocean seamounts produce obstruction upwelling, primary productively is increased locally compared to surrounding areas, this could drive the local ocean reservoir of dissolved Ni towards heavier Ni isotopic composition.

Of the other bioactive first-row transition metals, only for Fe do their exist published stable isotope compositions for surface scrapings of hydrogenetic FeMn crusts (Levasseur et al., 2004). However, a plot of the Fe isotope data against the Ni isotope data from the same crusts shows no clear correlation between the two isotope systems (Fig. 5.11). This implies that the isotopic variations in FeMn crusts are probably controlled by different processes for the Fe isotopic system than for Ni.

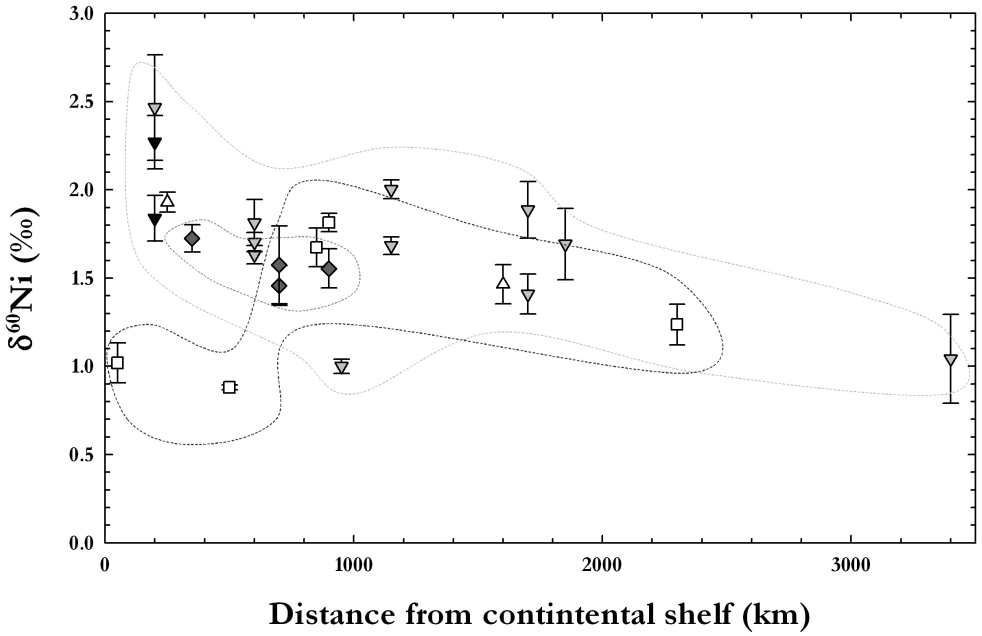

Figure 5.10: *Variation in Ni isotope composition of the ferromanganese crusts plotted against the distance from the closest continental shelf to the crust's place of growth. The samples are grouped by ocean basin for clarification (white squares = Atlantic; black diamonds = Indian; grey triangles = Pacific; black triangles = S. China Sea; white triangles = Southern Ocean). The figure shows how the heaviest Ni isotope compositions are found in crusts growing very close to a continental shelf.*

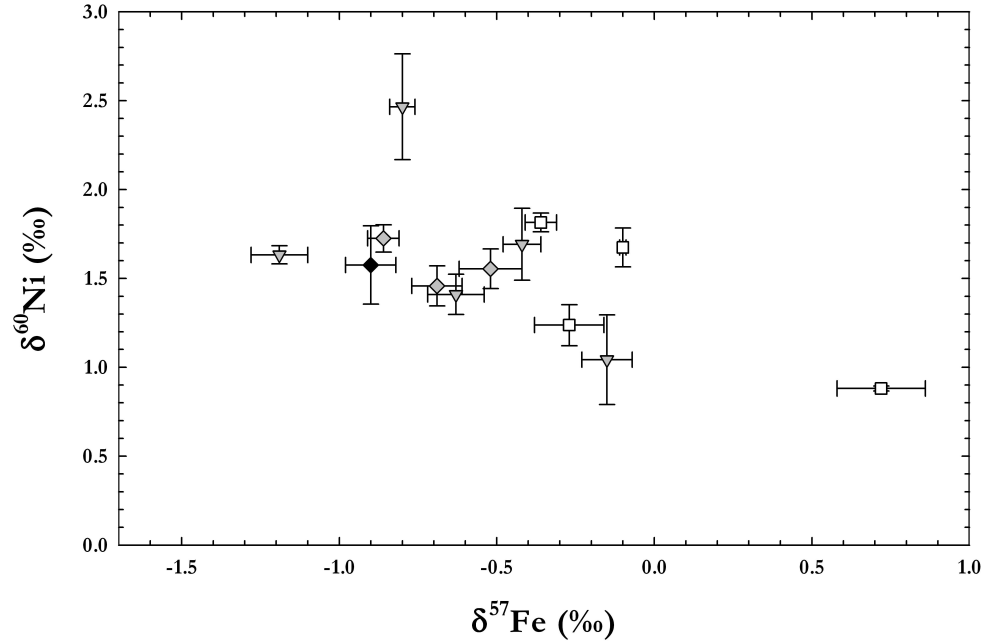

Figure 5.11: *Plot of the Ni isotope composition versus the sample Fe isotopic composition (data from Levasseur et al. (2004)). Legend for samples of the different ocean basins are the same as in Fig. 5.6.*

5.6 Depth profile through a hydrogenetic crust

To follow up the study of spatial Ni isotope variations in FeMn crusts, a detailed depth profile through a single hydrogenetic crust was also sampled and analysed. This provides a record of the temporal variations of Ni isotope ratios within a single crust growing at a particular geographical location, and could potentially help determine the causes of Ni isotopic fractionation in FeMn crusts, as well as provide insights into changes in seawater chemistry over the last 50-100 Myrs.

5.6.1 Sampling and analytical procedures

The crust chosen for depth profiling is identified as CD29-2 and was provided by Jim Hein, at the US Geological Survey. It is a hydrogenetic crust collected during cruise F7-86-HW from a seamount in the central Pacific Ocean (16^{o}42' N/168^{o}14' W, see Fig. 5.5) at a water depth between 1970-2390 m. The average growth rate for this crust is 2.1 mm/Myr (determined using ^{10}Be/^{9}Be ratios by Ling et al. (1997)) and the crust started growing at $>$ 70 Ma (determined with Os isotope stratigraphy by Klemm et al. (2005)). CD29-2 is also well characterised for radiogenic isotopes (e.g. Christensen et al., 1997; Lee et al., 1999) and has previously been used for similar profile studies (e.g. Rehkämper et al., 2004; Nielsen et al., 2009). A photograph of the crust section sampled for Ni depth profiling is shown in Fig. 5.12. The crust was sampled using a micro drill, enabling high-resolution profiling with intervals of 0.2 mm between samples. Some samples were processed for Tl and Fe separation before the Ni was extracted; to ensure that no

isotope fractionation occurred during these procedures the USGS nodules Nod-A-1 and Nod-P-1 were treated the same way and analysed alongside the crust samples.

Figure 5.12: *Photograph of the crust CD29-2 sampled for this depth profile isotope study.*

Section	δ^{60}Ni	2 s.e.	*cont.*	δ^{60}Ni	2 s.e.	*cont.*	δ^{60}Ni	2 s.e.
16-17	1.99	0.02	42.6	1.86	0.01	84-85	1.98	0.02
20-21	1.90	0.02	54.5	1.60	0.01	87-88	1.93	0.01
23.0	1.87	0.01	57.0	1.66	0.01	92-93	1.90	0.02
24.0	1.85	0.02	57.5	1.69	0.02	93-94	1.70	0.01
25.0	1.79	0.01	58.5	2.27	0.01	94-95	1.91	0.02
26.0	1.64	0.01	59.0	2.17	0.02	95-96	1.78	0.02
27.0	1.81	0.02	60.0	1.91	0.02	96.0	1.82	0.01
28.0	1.62	0.02	60.5	1.65	0.05	96-97	1.89	0.02
30.5	1.89	0.02	64.0	2.05	0.02	97-98	1.76	0.01
31.5	1.86	0.04	64.5	2.21	0.06	98-99	1.84	0.02
33.2	2.13	0.01	70.5	1.92	0.01	99-100	1.85	0.02
34.2	2.05	0.02	73.0	1.87	0.03	100-101	1.87	0.01
35.2	1.89	0.01	78.5	1.94	0.02	102.0	1.65	0.02
35.4	1.98	0.02	79.0	1.90	0.13	102-103	1.80	0.03
35.6	1.84	0.01	79-80	1.77	0.05	103-104	1.86	0.01
37.2	2.04	0.01	81-82	1.77	0.02	104-105	1.74	0.02
37.8	1.85	0.02	83-84	1.79	0.02			

Table 5.4: *Intervals (mm from top of crust) sampled and analysed for a Ni isotope ratio depth profile through ferromanganese crust CD29-2, from north central Pacific Ocean. Every sample aliquot was analysed three times, the errors given are 2 s.e. of these measurements.*

5.6.2 Results

A plot of Ni isotope ratio variations within the crust is shown in Fig. 5.13, while detailed results (labelled by distance in mm from the top of the crust) are given in Table 5.4. Throughout the crust, the total spread in δ^{60}Ni-values is 1.6-2.3 ‰. It is possible that the isotope data are biased due to diffusion (Henderson & Burton, 1999). However, this appears unlikely as this process should work towards erasing gradients in concentration or isotope ratios. Instead, the large fluctuation in Ni isotopic composition between different layers implies the contrary.

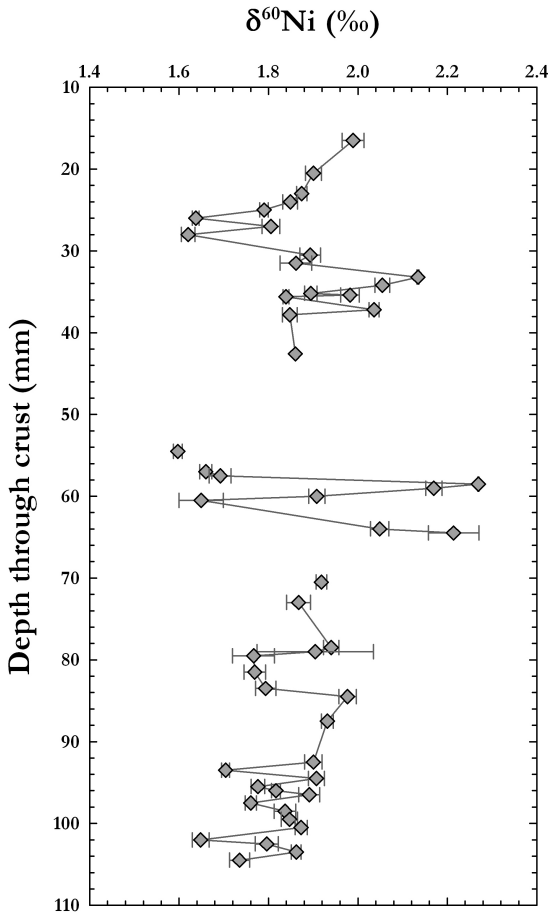

Figure 5.13: *Nickel isotopic depth profile through the crust CD29-2 from the north central Pacific Ocean. Section δ^{60}Ni-values are plotted according to their position in the crust, measured in mm from the most recent growth surface. The error bars shown are 2 s.e.*

5.6.3 Discussion

In total, the δ^{60}Ni-values measured in CD29-2 vary by over 0.7 ‰. Although this variation is large, all values fall within the range measured for surface scrapings from the Pacific Ocean basin (1.4–2.5 ‰). The fact that a crust growing at a particular geographical location shows a large isotopic fluctuation through time suggests that seawater heterogeneity is unlikely to be the cause of the global variations of Ni isotope ratios in FeMn crusts. Instead, it hints that changes in seawater composition is more likely to cause the observed isotopic variations.

5.6.3.1 Crustal mineralogy

In contrast with the surface scrapings samples, a piece of the crust CD29-2 was analysed for major elements on a microprobe (suppl. data, Frank et al., 1999). Fig. 5.15 shows some of these data, in the form of profiles of the major elements Fe, Mn, Ti, Ni, Ca and P, plotted according to their placement within the crust. There are clear connections between the concentrations of certain elements, mainly resulting from their preferential adsorption to either Fe- or Mn-oxides. The concentration profiles of Ti and Fe show similar trends, as do Ni and Mn, suggesting that Ti is almost exclusively adsorbed to Fe-oxides while Ni is mainly adsorbed by Mn-oxides. The close relationship between Mn and Ni is further demonstrated in Fig 5.14, which shows the clear correlation between the concentrations of the two elements. This relationship can be represented as an exponential growth equation, showing that higher concentrations of Mn (i.e. more MnO-surfaces available for

adsorption) lead to higher Ni concentrations.

Ling et al. (1997) noted that secondary phosphatization has affected the crust layers of CD29-2 at depths below 52 mm. The concentration profiles in Fig. 5.15 show that the P and Ca concentrations increase sharply below this point in the crust, probably due to the formation of apatite. It is possible that such phosphatization could have affected the Ni isotope ratios at this level, which could explain the very large fluctuations in δ^{60}Ni-values (1.6 – 2.3 ‰) at this depth in the crust. However, Fig. 5.16 shows that the Ca concentration does not correlate with Ni isotope ratios, nor does Fe or Mn concentrations, suggesting that crustal mineralogy is not the dominant factor controlling Ni isotope fractionation in FeMn crusts.

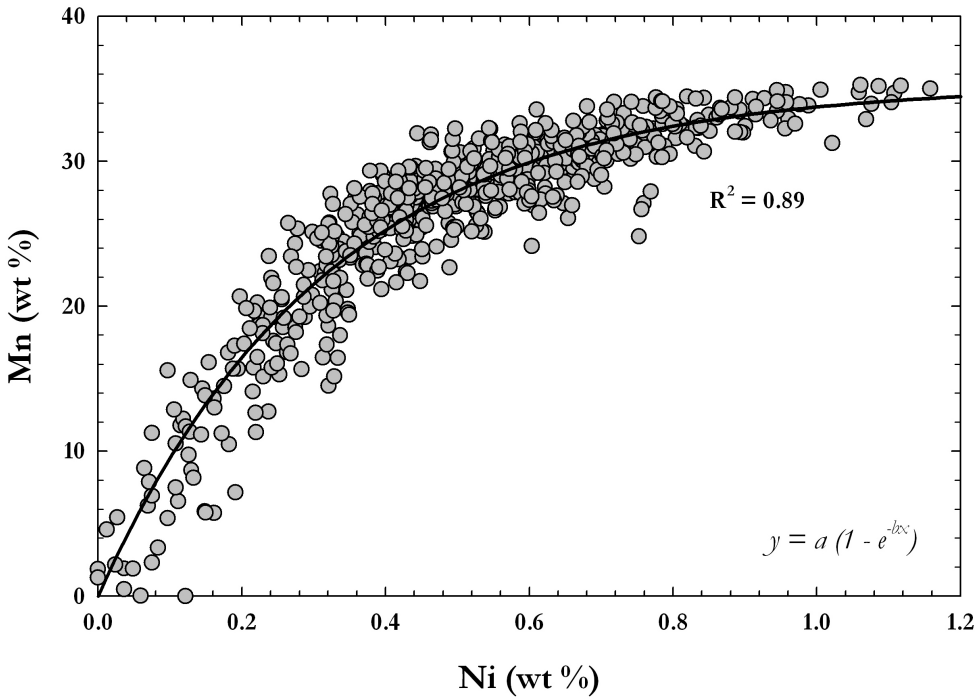

Figure 5.14: *Correlation between the concentrations of Mn and Ni in crust CD29-2. The regression shows how the relationship between the elements can be described by the exponential growth equation given in the figure, where a = 35.3, and b = 3.14.*

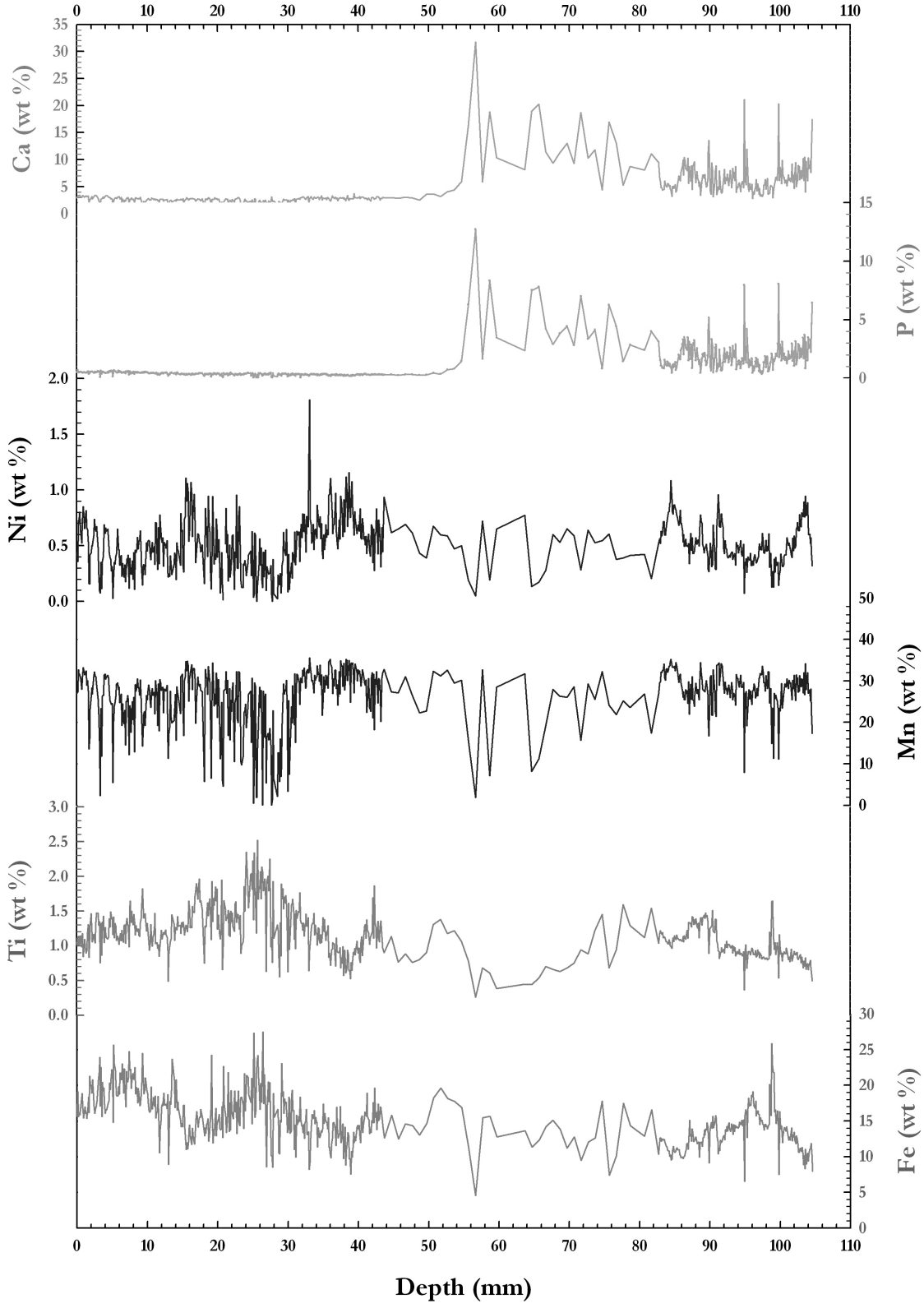

Figure 5.15: *Major element data profiles through CD29-2 analysed by electron microprobe byFrank et al. (1999) (the full dataset is yet unpublished). The data profiles shows that the concentrations of selected element pairs (Fe–Ti, Mn–Ni, and Ca–P) are related.*

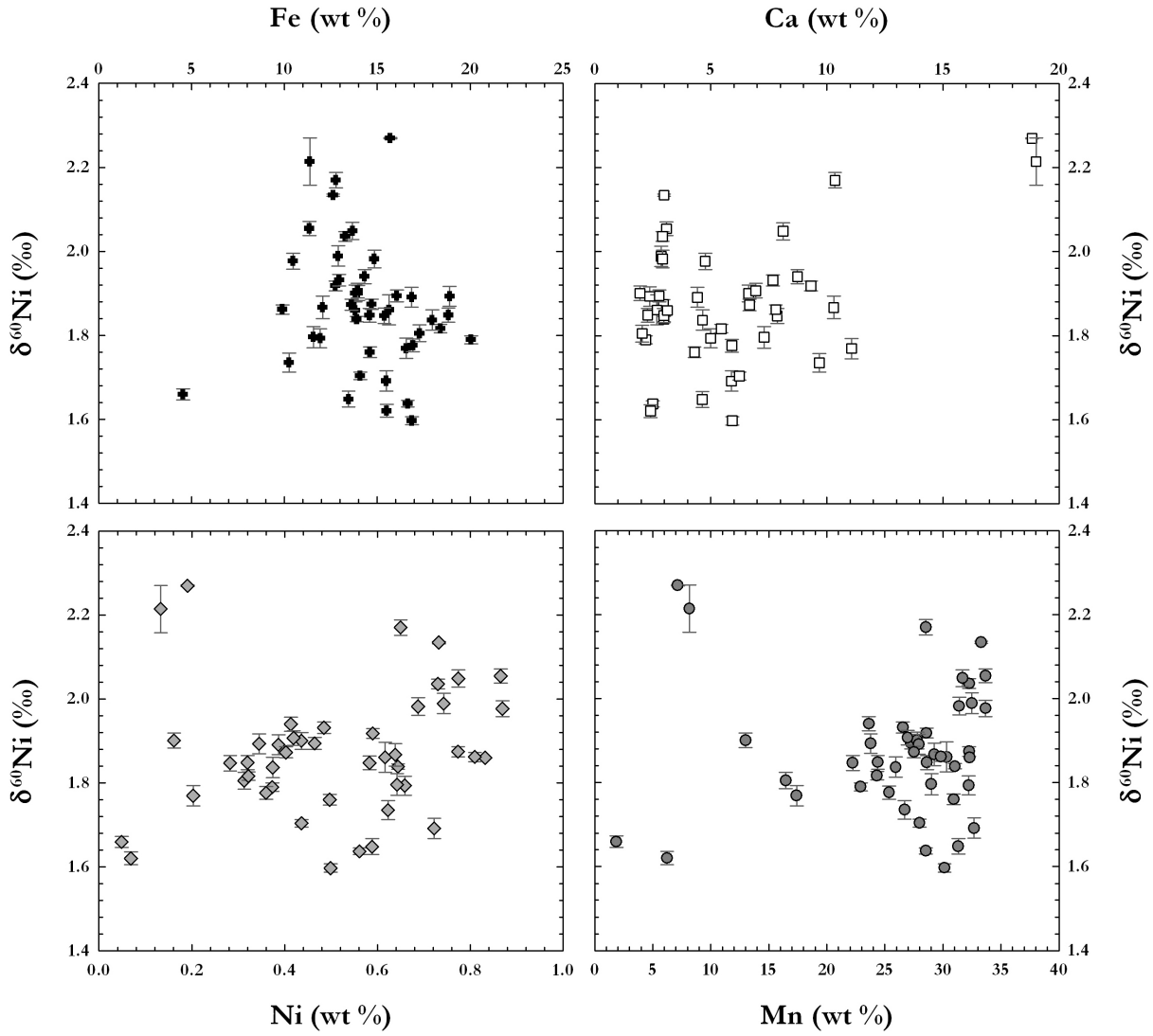

Figure 5.16: *δ^{60}Ni-values plotted against the concentration of major elements in crust CD29-2: Fe, Ca, Mn, and Ni. As no correlations with Ni isotope ratios are visible, the controlling factor for isotopic fractionation is probably not the crust's mineralogy.*

5.6.3.2 Comparison with Fe isotope ratios

Fe isotope ratios ($\delta^{57/54}$Fe) were determined for the same section aliquots as were analysed for Ni isotopes (data from Helen Williams, *pers. com.*). Fig. 5.17 shows profiles of both isotopes, plotted according to distance from the top of the crust. The two profiles show very different trends, with the Fe isotopes displaying heavier δ-values when Ni isotope ratios show lighter values. This supports the conclusions from the comparison of the surface scrapings study with data from Levasseur et al. (2004), namely that fractionation of Ni and Fe isotopes in FeMn crusts are unrelated and probably controlled by different processes.

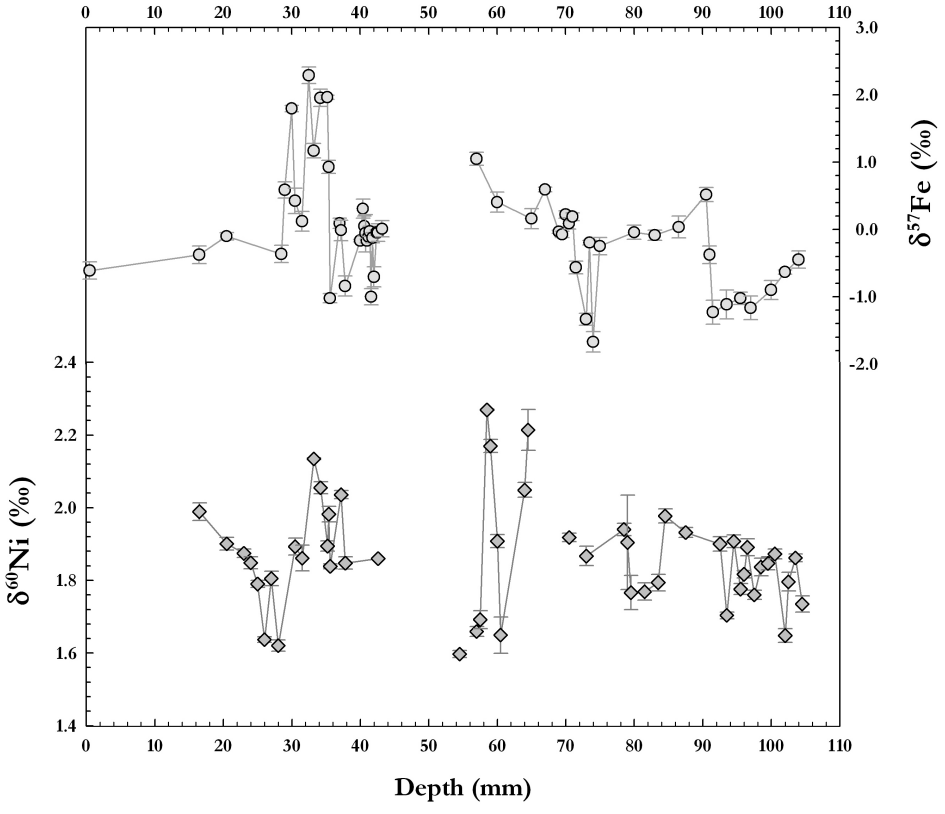

Figure 5.17: *Profiles of Ni isotope and Fe isotope ($\delta^{57/54}$Fe) data from CD29-2 plotted according to their position within the crust (mm from the top). The ratios were analysed on the same sample solutions. Iron isotope analyses were performed by Helen Williams (pers. com.).*

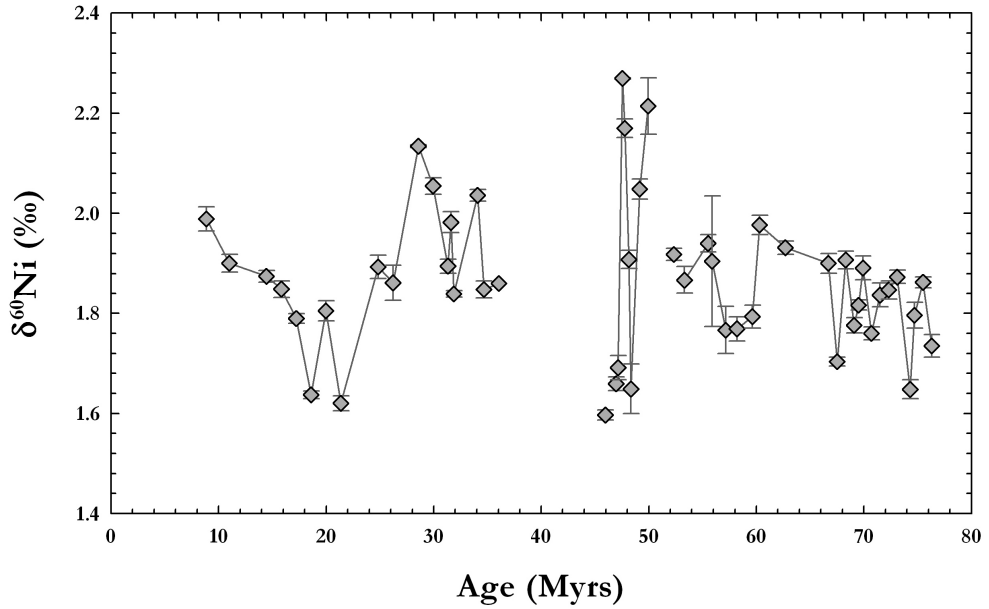

Figure 5.18: *Nickel isotope compositions of the depth profile through the crust CD29-2 plotted according to the sample model age (by Nielsen et al. (2009) based on Klemm et al. (2005)).*

5.6.3.3 Isotopic signature due to environmental change?

One reason that CD29-2 was chosen for the isotope profile study was the existence of a growth model for this crust, produced using Os isotope stratigraphy by Klemm et al. (2005). In Fig. 5.18, the Ni isotope compositions through the crust are plotted according to this age model. The Ni isotope ratios fluctuate, but there is a suggestion that they tend towards heavier values between 75–55 Ma. The largest fluctuation in isotope ratios then occurs between 50–45 Ma, although this may be due to secondary phosphatization of the crust. Thereafter the isotope ratios appear to be climbing towards a maximum of 2.1 ‰ at around 30 Ma, followed by a marked drop of 0.5 ‰ down to 1.6 ‰ at approximately 20 Ma. Finally, from 20 Ma until the youngest sample analysed, the isotopic composition steadily

rises, ending at a δ^{60}Ni-value of 2.0 ‰ at around 8 Ma. However, as this is the only Ni isotope profile through a FeMn crust currently available, it is difficult to ascertain whether the temporal variations in Ni isotope composition are due to environmental changes affecting seawater chemistry.

5.7 Conclusions

This study has shown that FeMn crusts could provide insight into the Ni isotopic composition of deep water. Assuming that the Ni inputs and outputs to the ocean are correctly calculated, a new, shorter, residence time of 3,500 years was estimated. This implies that the Ni isotopic composition of deep water may be isotopically heterogeneous, as 3,500 years is probably not long enough time to ensure complete isotopic mixing in the ocean. This could mean that as the deep water is transported via the conveyor belt from the Atlantic, via Indian, to the Pacific Ocean isotopic fractionation during progressive removal of Ni could result in isotopic heterogeneity in the ocean.

Sorption experiments aiming to determine the isotopic fractionation factor during adsorption of Ni onto synthetic Mn-oxide suggest that Ni incorporated into the MnO lattice are isotopically heavy compared to the original solution composition. However, further experiments are needed to confirm the exact magnitude of the equilibrium fractionation factor for Ni, as well as to determine other possible factors (e.g. variations in solution Ni concentration, pH or temperature) that can

affect its magnitude, and finally to determine the exposure time needed to reach isotopic equilibrium.

A detailed study of the Ni isotope ratios in natural samples of hydrogenetic ferromanganese crusts show that these chemical sediments are indeed both isotopically heavy and heterogeneous in isotopic composition. The global variation of crustal surface scrapings is ∼1.5 ‰, while a depth profile through one crust show a temporal variation of half that range (∼1.5 ‰). The cause of the isotopic heterogeneity is difficult to determine without knowing the Ni isotopic composition of seawater, but there are indications that this may be influenced by local, or regional, variations in biological cycling, as well as by variations in seawater chemistry affecting crustal mineralogy.

A time series study of Ni isotopic compositions in central north Pacific deep-water crust CD29-2 displays significant variability. Some of this may reflect redistribution during phosphatisation, however, the younger (<30 Ma) sections of the crust show systematic variations over time that cannot be explained by diagenesis. Notwithstanding possible phosphatisation effects, the deep part of the crust CD29-2 in no different on average from the younger, more shallow, part. Furthermore, these average Ni isotope compositions of this crust are identical to that of the Pacific surface samples. Therefore, overall there appear to have been no systematic change in the sources and fractionation mechanisms affecting Ni supplied to the Pacific over the Cenozoic, despite large changes in plate configurations, ocean circulation, climate, and weathering during this time.

CHAPTER

SIX

APPLICATIONS OF NICKEL ISOTOPES AS A TRACER IN ECONOMIC GEOLOGY

6.1 Introduction

This final chapter focuses on possible applications of Ni isotopes studies within economic geology. Nickel is used in a vast array of materials and products from stainless steels to batteries and is an important catalyst in the chemical industry. Approximately 1,000,000 tonnes of nickel metal are consumed in the world every year. As a trace element in crude oil Ni is also important for the hydrocarbon industry, aiding in estimating oil-well connection and causing corrosion problems during refining processes. Applications of Ni isotopes in these areas could be of great use for both mining and oil companies, as well as in shedding light on scientific questions, such as the origin of Ni in crude oil and the development of giant Ni ore deposits.

6.2 Nickel in petroleum geochemistry

Crude oils are complex natural fluids composed of both saturated and aromatic hydrocarbons mixed with emulsified water and minerals. Petroleum geochemists study crude oil and its components in order to assess critical aspects of the petroleum source rock, such as its age, lithology, depositional setting and thermal maturity before oil migration. The presence of transition metals in petroleum oils is of particular interest in this regard. Vanadium and nickel are the most abundant of these transition metals, usually present in concentrations of 10-1500 ppm for V and 1-300 ppm for Ni (e.g. Barwise, 1990). Contents of Fe, Co, Mn,

Cu, Zn, Mo, and Ti tend to be much lower, with concentrations of $<$ 10ppm. As concentrations of Ni and V are so much higher than other metals, the ratio of these elements is frequently used as a simple way of characterising crude oils and aiding oil-oil or oil-source rock correlations (e.g. Greibrokk et al., 1994; López et al., 1995)).

The ratio of Ni to V is thought to depend on the source of organic matter and the environmental conditions present during burial of oil-generating sediments. Principal factors affecting this proportionality are the redox potential and the hydrogen and sulphide activity in the depositional environment (Lewan & Maynard, 1982; Lewan, 1984). Based on these relations, the Ni/V ratio has been linked to simple petroleum classification schemes, with higher ratios occurring in oils derived from marine source rocks deposited under anoxic conditions, and lower ratios potentially indicating oxic to suboxic conditions or lacustrine deposition (Barwise, 1990).

6.2.1 Metal speciation

In crude oils, Ni and V are mainly found accommodated in free tetrapyrrole complexes belonging to a group named *porphyrins*. These complexes are organic compounds probably derived from chlorophyll or haeme molecules (Fig. 6.1), and are therefore direct evidence of the biotic origin of crude oils (Treibs, 1934; Keely et al., 1990; Keely, 2006). Elsewhere, significant quantities of transition metals are also found within the insoluble asphaltene fraction, which can constitute up to 25%

of the crude oil by weight. Here, the metals are thought to be incorporated into the asphaltene sheet structure through complexation by the heteroatoms nitrogen, sulphur or oxygen (Sheu & Mullins, 1996). However, others have argued that metalloporphyrins may also attach to asphaltene molecules (Pearson & Green, 1993), in which case Ni might only be present in the porphyrin form in crude oils. Ever since the first publications describing porphyrins in petroleum Treibs (1934, 1936), these complexes have been the focus of extensive research (Barwise & Roberts, 1984; Sundararaman et al., 1988; Sundararaman & Boreham, 1993; Sundararaman, 1993; Boreham et al., 1989, 1990)).

6.2.2 Origin of metals

Although porphyrins are well studied as organic complexes, there has been relatively little focus on the origin of metals situated inside these porphyrins, or on the timing of metallation. During primary diagenesis, insoluble macromolecular organic matter dispersed within sediments is forced together to form large molecules with long carbon chains, known by the collective name kerogen. It is from these basic polymeric organic molecules that petroleum can later be generated, as a consequence of the kerogen structure attempting to attain thermodynamic equilibrium as temperature and pressure increase (Vandenbroucke & Largeau, 2007). The predominance of Ni and V in petroleum porphyrins probably results from the higher stability of their metal-nitrogen bonds in porphyrin complexes (Fleischer, 1970), coupled with the high abundances of these metals in sediments (Lewan, 1984) (e.g.

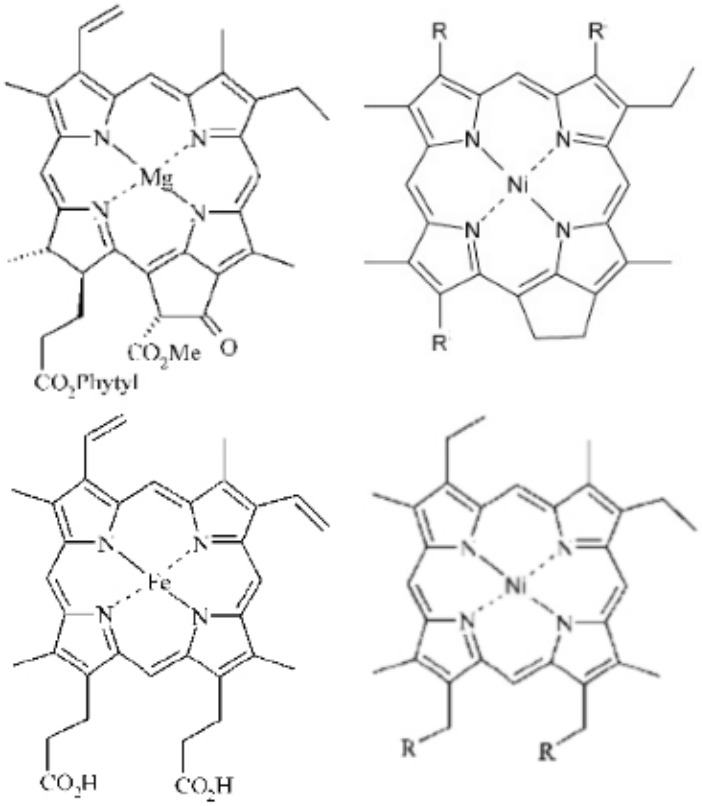

Figure 6.1: *Comparison of two common Ni-porphyrins and there probable precursor molecules. Top row shows a 'Chlorophyll a' (left) which during diagenesis could be transformed into a 'deoxophylloerythroetioporphyrin' (right), while the bottom row shows a 'Haeme' molecule (left) which breaks down to an 'etioporphyrin' (right) (figure adapted from Treibs, 1934; Czernuszewicz, 2000; Keely, 2006).*

concentration of Ni in pelagic clay is 230 μg/g Ni, Li & Schoonmaker (2003)), and possibly further aided in the metallation process by reactions with minerals and clay particles (Seewald, 2003; Vandenbroucke & Largeau, 2007). However, some of these metals are also likely to have been adsorbed into porphyrins during petroleum migration from source rock to reservoir rock (Callot & Ocampo, 2000).

Nickel present in petroleum oils could therefore have been incorporated at several stages. The most likely theory is that Ni present in crude oil (i) is a remnant of the original biological material, as Ni is frequently complexed by organic matter in

sediments, or that it has (ii) originated from seawater or sedimentary pore water. A less likely, but very possible, source is (iii) adsorption from detrital material dissolved during diagenesis, while (iv) incorporation from another aqueous or mineral phase during oil migration, or (v) leaching of Ni into the crude oil from the reservoir rock are the most unlikely scenarios. All sources mentioned are however potential contributors to a crude oil's Ni isotopic composition, requiring isotope analysis and consideration of each factor for determination of the origin of Ni in crude oil. As shown in previous chapters, the Ni isotopic compositions of igneous and sedimentary material (FeMn oxides) are significantly different. Therefore, Ni stable isotope ratios have the potential to provide a strong isotopic fingerprint for determining the origin of this metal in crude oil, assuming that Ni is not fractionated during transformation of the sedimentary organic material to oil-forming kerogen. In this way the Ni isotopic composition of crude oils and source rocks could help strengthen oil–source rock correlations and distinguish connections within an oil field. If, on the other hand, Ni is partly picked up during migration or from the reservoir, then its isotopic composition could potentially help unravel the migration path taken by a crude oil deposit.

6.2.3 Previous isotope studies on petroleum

Most previous isotopic studies conducted on petroleum materials have utilised the traditional stable isotopes of H, C, O, N, and S, investigating isotopic fractionation in relation to maturation and migration of oil and to the origin of porphyrins

(see (e.g. Park & Dunning, 1961; Boreham et al., 1989; Conrad et al., 1999). In addition, a few studies have used radiogenic isotopes, such as Pb, Nd, Sr (Dreyfus et al., 2007; Bing-Qian et al., 2001; Manning et al., 1991) and the Re-Os system (Selby & Creaser, 2005; Selby et al., 2007), to attempt to reconstruct the history of petroleum systems and constrain the age of kerogen deposition. Amongst non-traditional stable isotopes, only the V isotope system has so far been exploited in petroleum research. Premovic et al. (2000, 2002) analysed V isotopic compositions of asphaltenes and related kerogens from Venezuela, concluding that the observed fractionation of V in these petroleum-related materials must have originated from biological processing of V in seawater.

6.2.4 Nickel isotopic composition of crude oil

For this preliminary study of Ni isotopes in petroleum, 5 bulk crude oils were analysed for their Ni isotopic composition. One of these samples is a NIST reference material consisting of heavy Venezuelan crude oil (RM 8505), whilst the other four are unknown crude oils provided by the Brazilian oil company Petrobras (samples labelled Amostra 1–4). The crude oils display a range of trace metal contents, with the most viscous oils (RM 8505 and Amostra 3) having highest metal contents (45 and 30 μg/g Ni, respectively), while the remaining three crude oils have much lower Ni concentrations (see Table 6.1).

Crude oils are extremely difficult to digest due to their natural mixture of saturated and aromatic hydrocarbons together with large asphaltene hydrocarbon

Sample		Location	*Description*	Ni (μg/g)		δ^{60}Ni (‰)	*Error*
Crude Oils							*2 s.e.*
RM 8505	NIST	Venezuela	*viscous*	45		0.36	0.12
					repeat	0.53	0.23
Amostra 1	Petrobras	Brazil	*non-viscous*	4		0.40	0.03
					repeat	0.45	0.05
Amostra 2	Petrobras	Brazil	*non-viscous*	7		0.78	0.07
					repeat	0.72	0.02
Amostra 3	Petrobras	Brazil	*viscous*	30		0.39	0.001
					repeat	0.50	0.08
Amostra 4	Petrobras	Brazil	*non-viscous*	7		0.78	0.01
					repeat	0.47	0.03
Organic rich shales							*2 s.d.*
SGR-1	USGS	Colorado	*Eocene*	29 μg/g		0.57	0.15
SDO-1	USGS	Ohio	*Devonian*	100 μg/g		0.68	0.10

Table 6.1: *Summary of all crude oils and organic rich shales analysed for their Ni isotopic composition.*

complexes. The crude oils analysed here were therefore digested in a high-pressure microwave as described in Chapter 2. Even though this digestion procedure produces clear solutions, there is a high possibility that hydrocarbons are still present in the solution (as noted by Costa et al. (2001)). Furthermore, the complex nature of crude oils could possibly produce isotopic heterogeneity within one oil sample, as different hydrocarbon molecules may prefer complexing either light or heavy Ni isotopes. This could theoretically produce a fractionation between e.g. porphyrins and asphaltene complexes, thereby producing different analysis results dependent on the amount of different types of hydrocarbon complexes in each aliquot. To circumvent this problem the crude oil samples were dissolved in an organic solvent (dichloromethane) prior to microwave digestion, which should achieve a homogeneous mixture of hydrocarbon complexes and, therefore, reproducible isotope ratios. Because of this, the Ni isotope ratios presented here were only reproduced

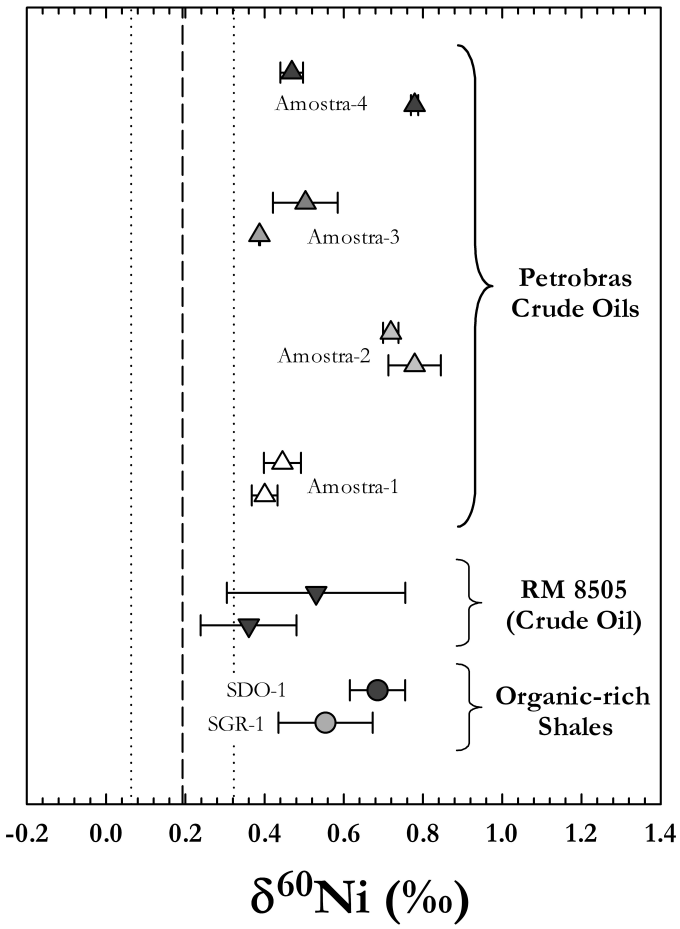

Figure 6.2: *Plot showing the Ni isotopic compositions of the five crude oil samples (NIST RM 8505, and Amostra 1-4) together with analysed isotopic compositions of two organic rich shales (USGS reference materials SDO-1 and SGR-1). The dotted lines show the estimated average isotopic composition of the mantle (see Chapter 4) as a reference.*

by reanalysing the dichloromethane dissolution of each sample, not by analysing a different aliquot of the original crude oil sample.

The preliminary results of the Ni isotope analyses suggest that the five crude oils have significantly heavier isotopic compositions than igneous rocks, varying from 0.36 to 0.78‰ (Table 6.1) compared with the mantle isotopic composition of 0.22 ± 0.10‰determined in chapter 4. The Venezuelan crude oil (NIST RM 8505) showed very large variations within one sample (2 s.d. = 0.17 and 0.32‰),

which might reflect remnant organic material left in the sample producing variable matrix effects in the plasma. Three of the four Brazilian crude oils (Amostra 1, 2, and 3) showed good reproducibility, but the fourth (Amostra 4) displayed a large difference between the two aliquots analysed (0.78 vs. 0.47‰). The different results from the two sample digestions are therefore probably a result of Ni isotopic heterogeneity within the sample due to incomplete dissolution of the bulk sample in dichloromethane before aliquots were taken for digestion.

As showed in Chapter 4, shales with low carbon contents exhibit δ^{60}Ni-values close to igneous rocks. To determine whether shales with high organic contents (i.e. possible petroleum source rocks) have different isotopic compositions, two organic-rich shales from the USGS were analysed. One is an organic- and sulphur-rich shale of Devonian age (SDO-1), the other an oil shale from the Eocene period (SGR-1). The results show that both organic-rich shales have significantly heavier isotopic compositions than shales of low organic content, suggesting that heavy Ni isotopes are incorporated into the sedimentary material as organic complexes. Furthermore, δ^{60}Ni-values of these shale samples are within error of those of all crude oils samples (Fig. 6.2), suggesting that the heavy Ni isotopic composition in crude oil may be inherited from the source rock. Therefore, Ni is probably incorporated into kerogen very early on in the source rock development, possibly originating from the sedimentary organic material itself.

Petroleum source rocks are thought to develop in sedimentary basins with high primary productivity and low oxygen content in the bottom water and uppermost

layer of sediment. These factors are likely to be coupled, as an area with high productivity is likely to cause suboxic to anoxic conditions at the water-sediment interface, as existing oxygen is used up in the decomposition of organic material. Higher rates of productivity also provide a faster sedimentation rate, which results in quicker burial of the sedimentary material and the preservation of a greater amount organic material without any biodegradation (Killops & Killops, 2005). The heavy Ni isotope ratios in organic rich shales and crude oils may therefore be the result of scavenging of Ni from the water column by complexation with organic matter and depositing this material in sedimentary anoxic conditions (Piper & Perkins, 2004).

6.3 Nickel in ore deposit geochemistry

6.3.1 Introduction

Global production of Ni is dominated by Ni sulphide deposits, which originate from sulphur-saturated silicate melts. A silicate melt can become saturated in sulphur through mixing with crustal rocks (e.g. S-rich sedimentary rocks) during emplacement. This causes sulphide-silicate segregation and leads to the concentration of sulphide droplets, with Ni partitioning into the sulphide melt (e.g. $D^{Ni}_{S-SiO_2}$ = 500-900 for coexisting sulphides and silicates in MORB glasses (Peach et al., 1990)). If the melt originally had a high Ni content, then Ni sulphides will precipitate in a cumulate layer (Naldrett, 1999). As ultramafic rocks have far higher Ni concentrations than crustal rocks (e.g. the average Ni content of mantle rocks is ∼2,000 μg/g (McDonough, 2003)), Ni deposits are generally associated with large ultramafic to mafic intrusions. Due to their emplacement, most Ni sulphide deposits are associated tectonically with rift zones (Naldrett, 2004), which can form suitable Ni-rich melts such as komatiite suites (e.g. *Kambalda*, Australia) or flood basalts (e.g. *Noril'sk*, Russia).

6.3.2 Chemistry of Ni sulphides

The most common Ni-sulphide in ore deposits is *pentlandite*, which has the chemical composition $(Fe,Ni)_9S_8$, but which can also accommodate large amounts of Ag, Co, Cu, Mn, Cd, Pb, and Se in alternative forms. Pentlandite is associated

with ultramafic rocks and is usually found in massive form or intergrown with pyrrhotite and chalcopyrite. In contrast, *millerite* is a low-temperature sulphide with the composition NiS, and is usually found in sedimentary rocks or as a metamorphic replacement for pentlandite. In addition, several iron sulphides frequently accommodate large amounts of Ni, particularly those associated with pentlandite. *Pyrrhotite* is a magnetic Fe-sulphide of variable composition with the general chemical formula $Fe_{1-x}S$, where $x \leq 0.2$. The resulting vacancies in the crystal structure produce a defect in the lattice, which causes the mineral to become magnetic. The copper sulphide *chalcopyrite*, $CuFeS_2$, is also associated with high-temperature magmatic deposits. This sulphide occurs both in ultramafic rocks, as a consequence of silicate-sulphide segregation, and in hydrothermal stockwork veins of andesitic porphyry copper deposits (Anthony et al., 2011).

In silicates, Ni is mainly situated in octahedral coordination, but in sulphides both octahedral and tetrahedral coordination occurs (Table 6.2). As discussed earlier in this thesis, this change in coordination of the Ni^{2+}-ion may be an important factor in causing Ni isotope fractionation.

6.3.3 Nickel ore deposits associated with komatiites

Nickel ore deposits found in connection with komatiite suites can generally be categorised in two groups (Naldrett, 1999); (i) small, high grade sulphide deposits occurring at the base of dunitic flows (in the case of *Kambalda*, (e.g. Gresham & Loftus-Hills, 1981; Groves et al., 1986; Keays, 1995) and (ii) large, low-grade de-

Sulphide	Chemical formula	Coordination of Ni	Packing	Crystal system
Pentlandite	$(Fe,Ni)_9S_8$	tetra- & octrahedral	ccp	cubic
Millerite	NiS	octrahedral	hcp	hexagonal
Pyrrothite	$Fe_{1-x}S$ ($x \leq 0.2$)	octrahedral	hcp	monoclinic
Chalcopyrite	$CuFeS_2$	tetrahedral	ccp	tetragonal
Pyrite	FeS_2	octrahedral	ccp	cubic

Table 6.2: *Structural and chemical information on Ni-sulphides (pentlandite and millerite) and important Ni-containing Fe and Cu sulphides (pyrrhotite, pyrite and chalcopyrite). Data from Makovicky (2006) and Anthony et al. (2011).*

posits of finely disseminated sulphides in channel-like lenses of cummulate dunite (*Mt. Keith* (Butt & Nickel, 1981), and *Scotia* (Stolz & Nesbitt, 1981)). Nickel sulphides in these deposits form by sulphide segregation following sulphur saturation of an ultramafic melt intruding into crustal rocks, and the subsequent partitioning of Ni into the sulphide liquid. The different Ni contents of the sulphide samples from these Ni deposits may result from different sulphur concentrations in the melts, or alternatively from variations in the amount of contact between the silicate and sulphide melt, as Ni will preferably enter sulphides if given the possibility.

6.3.4 The Sudbury Igneous Complex

One notable exception from the traditional model of Ni-ore formation is the world's largest Ni-sulphide deposit at Sudbury in Ontario, central Canada. This ore body contains on average 1.2% Ni with a total estimated resource of almost 20 Mt Ni (Naldrett, 2004). The Sudbury Igneous Complex is a ∼3 km thick, 60 × 27 km elliptical igneous rock body with the sulphide contact layer consisting of a

quatrz-gabbro (norite) intrusion, and has been dated at 1850 Ma (Faggart et al., 1985; Davis, 2008). Sudbury differs from traditional ore deposits in layered mafic intrusions in its average intermediate composition and its clear crustal isotopic signatures, which imply crustal contamination of the intrusion (Faggart et al., 1985; Walker et al., 1991; Darling et al., 2010). The currently accepted theory of the structure's origin, first proposed by Dietz (1964), is that it represents an impact crater. This theory is based on observed shatter cones, which point towards the proposed impact structure. The impactor had an estimated diameter of 10-15 km and formed a crater with an original diameter of $\leq$ 280 km (Deutsch et al., 1995; Grieve et al., 1991), making the Sudbury impact crater second in size only to the deeply eroded Vredefort impact structure in South Africa (Grieve & Therriault, 2000).

Impact models suggest that the upper crust was completely evaporated by the impactor and that melting occurred to depths of $\sim$30 km (Deutsch et al., 1995; Grieve et al., 1991; Mungall et al., 2004). This implies that the source of the impact sheet now hosting the giant Ni deposit was the lower crust, or possibly the upper mantle, a theory supported by the sulphide-carrying host rock being a mafic quartz-gabbro locally termed norite. Subsequently, the Ni (and Cu) in this structure must have originated from a sulphur undersatuarted mafic melt, forming and precipitating Ni-sulphide during mixing of the intruding mafic melt with surrounding crustal rocks of higher sulphur contents within the impact melt sheet (Lightfoot et al., 2001).

6.3.5 Nickel isotopic composition of sulphides

Sulphide formation can occur as both a high- and low-temperature geochemical process. Determining whether isotope fractionation accompanies Ni partitioning into sulphides is therefore an important aspect of Ni isotope geochemistry. To investigate this topic, samples of different sulphide compositions from different locations were analysed for their Ni isotopic composition. All the samples were provided by the Natural History Museum.

Three of the analysed samples were mixed Ni-sulphides from komatiite Ni-deposits. These samples are from the Australian Ni-mines Kambalda, Mt. Keith and Scotia, all of which are considered to be Archean in age (e.g. Chauvel et al., 1985; Compston et al., 1986). All three samples from the komatiite related deposits have very light Ni isotopic compositions compared with igneous rocks, with δ^{60}Ni-values varying from -0.40 to -0.93‰ (see Table 6.3 for details). The reason for the variation between these samples may be the same as for the differences in their Ni concentrations, although there does not seem to be a simple correlation between Ni concentration and isotopic composition. However, these analyses do show that Ni partitioning between silicates and sulphides is accompanied by a significant negative fractionation of Ni isotopes.

As a comparison with the komatiite sulphides, five whole rock samples of different compositions from the Sudbury Igneous Complex were also analysed. These samples are: (a) a massive sulphide of pentlandite only, (b) a massive sulphide of pentlandite and pyrrhotite, (c) a norite containing large amounts of pyrrhotite

Sample	Rock Type	Location	*Description*	Ni (μg/g)	δ^{60}Ni (‰)	± 2 s.d.
NHM-Sa	Pent	Sudbury, CA	*massive sulphide*	100,000	0.58	0.02
NHM-Sb	Pyrr + pent	Sudbury, CA	*massive sulphide*	45,000	-0.37	0.03
NHM-Sc	Norite + pyrr & cpy	Sudbury, CA	*host rock with high sulphide conc.*	6,500	-0.35	0.08
NHM-Sd	Norite + pent & cpy	Sudbury, CA	*host rock with diss. sulphides*	2,000	0.09	0.09
NHM-Se	Norite	Sudbury, CA	*host rock only*	200	0.19	0.03
NHM-Ka	Komatiite	Scotia, AU	*diss. sulphides*	22,000	-0.40	0.05
NHM-Kb	Komatiite	Mt. Keith, AU	*diss. sulphides*	5,000	-0.69	0.04
NHM-Kc	Komatiite	Kambalda, AU	*crystalline sulphides (pent/pyrr/cpy)*	100,000	-0.93	0.06

Table 6.3: *Summary of all sulphides analysed for their Ni isotopic composition. Pent = pentlandite, pyrr = pyrrhotite, cpy = chalcopyrite. All samples were provided by the Natural History Museum, London.*

and chalcopyrite, (*d*) a norite with disseminated pentlandite and chalcopyrite, and (*e*) a norite only. The sample of the silicate melt sheet (norite, or quatrz-gabbro) agrees well with other mantle rocks analysed (0.19 ± 0.03‰, compared to the mantle average of 0.22 ± 0.10‰), while the sample with only small amounts of disseminated sulphides (sample *d*) shows a slightly lighter δ^{60}Ni-value, most likely due to mixing of the isotopically lighter sulphides with the silicate. The two samples comprising mixtures of pentlandite, pyrrhotite and chalcopyrite, both have an isotopic composition similar to the lightest komatiite sample (-0.34 and -0.37‰ for sample *c* and *b* respectively). Surprisingly though, the massive pentlandite (sample *a*) displayed a considerably heavier isotopic composition of +0.58 ± 0.02‰, almost one permil heavier than the other sulphides samples (Table 6.3).

We can also compare these data with two published Ni isotope values for Ni-sulphides from Tanimizu & Hirata (2006), comprising one millerite sample from

Manitoba, Canada, and one pentlandite sample from the Sudbury Igneous Complex. The Tanimizu & Hirata (2006) analyses agree well with those performed here, with their millerite showing a negative δ^{60}Ni-value — similar to both one komatiite sample as well as the Sudbury samples containing sulphide mixtures (sample *b* and *c*) — and their pentlandite overlapping with the heavy isotopic composition of sample *a* (Fig. 6.3).

The large isotopic heterogeneity amongst sulphides from the same impact sheet could be explained in a number of ways. One possibility is that there may be distinct differences in the preference of heavy or light Ni isotopes between different sulphides, perhaps caused by their different crystal structures. As described in Table 6.2, pentlandite is the only sulphide analysed here that incorporate Ni into both its tetrahedral and octahedral vacancies. However, if this structural arrangement were the determining factor then it is surprising that no such effect is observed in sample *d*, which only contains disseminated pentlandite and chalcopyrite (where Ni is only situated in tetrahedral coordination), as this sample is lighter than the norite host rock instead of heavier as it then should be.

A second possibility is that the impact melt sheet was exposed to high temperatures for a time period long enough for the Ni isotopes to homogenise within the sheet, after which sulphide crystallisation occurred in the order chalcopyrite → pyrrhotite → pentlandite. The heavy Ni isotopes may have been left within the sulphide melt, forcing the pentlandite in the middle of the sheet to accommodate the remaining heavy isotopes. This theory requires the crystallisation of magmatic

sulphides to have occurred in this order. However, according to Prichard et al. (2004) sulphide crystallisation is more likely to proceed in the opposite order, with pentlandite and pyrrhotite being the first minerals to crystallise from a magmatic sulphide melt.

A third explanation for the heavy pentlandite sample is that the heavy Ni may have been inherited from the impacting meteorite. As discussed in both the introduction chapter and Chapter 4, heavy Ni isotopic compositions of similar values have previously been measured in iron meteorites. Assuming the impacting meteorite had a diameter of 10 km (the minimum value estimated by Deutsch et al. (1995)), then between 150 Mt and over 300 Gt Ni (depending on the meteorite's composition) could have been added to the impact melt sheet. It may therefore be possible for an inherited Ni isotopic composition to be visible in Ni sulphides formed as a consequence of the impact. However, further analyses of Ni-sulphides from different deposits are necessary before this theory can be either confirmed or ruled out.

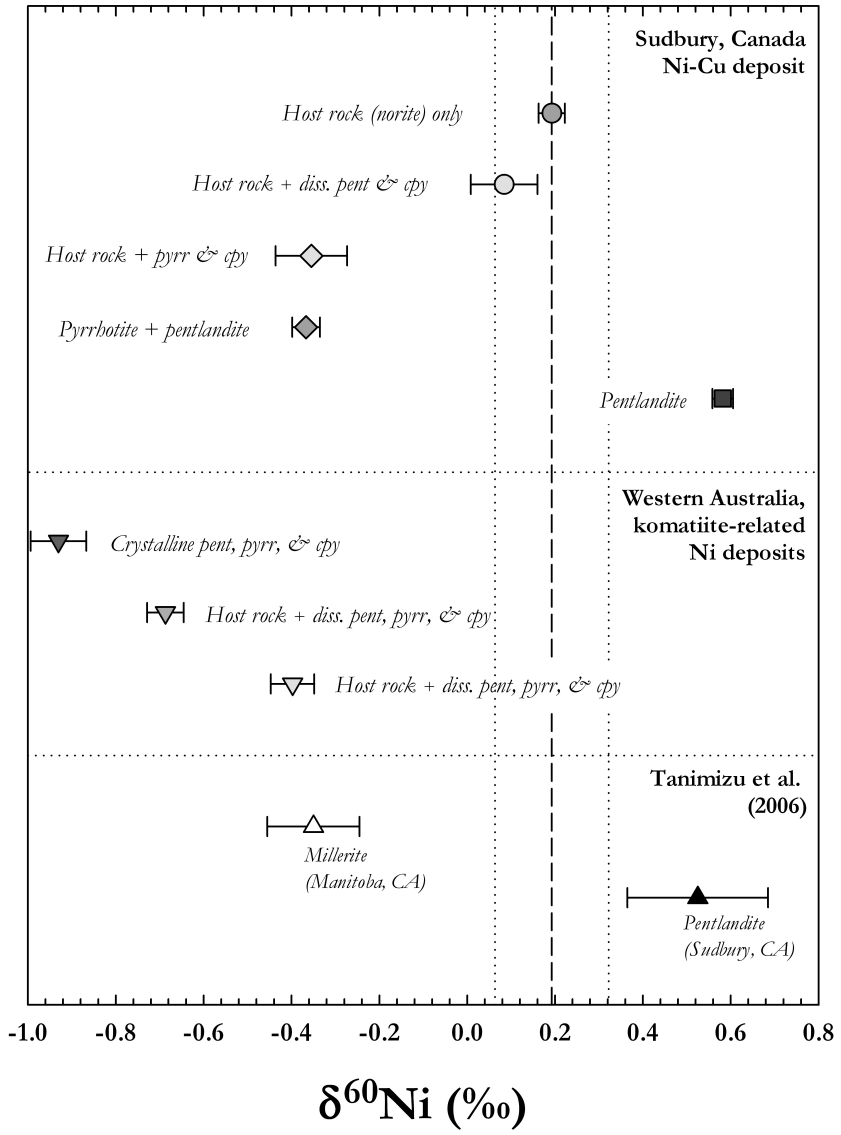

Figure 6.3: *Plot showing the Ni isotopic compositions of all analysed sulphide samples. Also plotted are the two sulphide samples analysed by Tanimizu & Hirata (2006), which agrees well with the samples analysed here. The dotted lines show the estimated average isotopic composition of the mantle (see Chapter 4) as a reference.*

6.4 Conclusions

This chapter demonstrates that Ni isotopes can be successfully applied to research within what traditionally has been termed economic geology. Analyses of crude oils show that their Ni isotopic composition may be a remnant of their source rocks, as organic-rich shales exhibit similar δ^{60}Ni-values. These results show that the heavy Ni isotopes (compared to igneous rocks) correlate with the organic matter in sedimentary rocks. This implies either that the Ni taken up during primary productivity is originally heavy (hinting that the ocean may also be isotopically heavy), or that Ni is fractionated towards heavier isotopic composition during biological uptake.

The formation of Ni-sulphides plays an important role in the Ni geochemical cycle, taking part in reactions in both low- and high-temperature processes. Analyses of a variety of Ni-sulphide minerals from different types of Ni ore deposits show how the partitioning into sulphides fractionate Ni isotopes towards lighter compositions than magmatic systems. The only exception is a sample of massive pentlandite from the Sudbury Igneous Complex, a world class Ni ore deposit originating from a large meteorite impact. One possibility is that the heavy Ni isotopic composition of this sample is a signature from the impacting meteorite, although more analyses of other Ni-sulphides samples are needed to confirm or reject this hypothesis.

CHAPTER

SEVEN

CONCLUSIONS AND OUTLOOK

7.1 Conclusions of thesis project

In this thesis I demonstrate how a new, low blank, separation technique was developed for producing clean Ni solutions from geological samples. The purified solutions are of high yield and contain no interfering matrix elements, making them suitable for isotope analysis by MC-ICPMS. In addition, I have established an analysis procedure for the accurate and precise measurement of Ni isotope ratios, drawing on a double-spike technique to correct both for instrumental fractionation effects and for possible isotope fractionation during the chemical separation.

After outlining these new methods, the thesis goes on to present the first detailed study of Ni isotopic variations in geological materials. Results presented here suggest that the mantle is probably of homogeneous Ni isotopic composition, although data from Mid-Ocean Ridge basalts hint that there may be differences in Ni isotopic composition between the source areas for MORB and those for intraplate basalts. As the mantle contains almost all silicate Ni, the isotopic composition of the bulk silicate Earth was estimated to be similar to that of the mantle. In light of published Ni isotope data for magmatic iron meteorites, these results suggest that the mantle-core differentiation process on Earth may have been accompanied by small fractionation of Ni isotopes, and further imply that the Ni isotopic composition of the primitive Earth is 0.29‰.

Low-temperature processes appear to have a greater impact in fractionating Ni isotopes than high-temperature igneous processes. The sample set of weathered rocks analysed in this thesis, though limited in size, shows that surface weathering

of a mafic rock body produces residual products (oxides and clay-silicates) with lighter Ni isotopic compositions than the original protolith. This indicates that the heavier isotopes in silicate material are leached from the continents during weathering and ultimately transported to the ocean, which by consequence then should be of a heavier Ni isotope composition

A detailed study of the Ni isotope ratios in hydrogenetic ferromanganese crusts show that these chemical sediments are heterogeneous in isotopic composition. The global variation of crustal surface scrapings is $\sim$1.5‰, while a depth profile through one crust show a temporal variation of half that range ($\sim$1.5‰). The cause of the isotopic heterogeneity is difficult to determine without knowing the Ni isotopic composition of seawater, but there are indications that this may be influenced by local, or regional, variations in biological cycling, as well as by variations in seawater chemistry affecting crustal mineralogy. Alternatively, the variations could reflect isotopic fractionation during progressive removal of Ni from the deep water as this is transported via the conveyor belt from the Atlantic, via Indian, to the Pacific Ocean, as suggested by new estimations of the Ni residence time in the ocean. Sorption experiments aiming to determine the isotopic fractionation factor during adsorption of Ni onto synthetic Mn-oxide suggest that Ni incorporated into the MnO lattice are isotopically heavy compared to the original solution composition. However, further experiments are needed to confirm the exact magnitude of the equilibrium fractionation factor for Ni, as well as to determine other possible factors that can affect its magnitude (e.g. variations in solution Ni concentration),

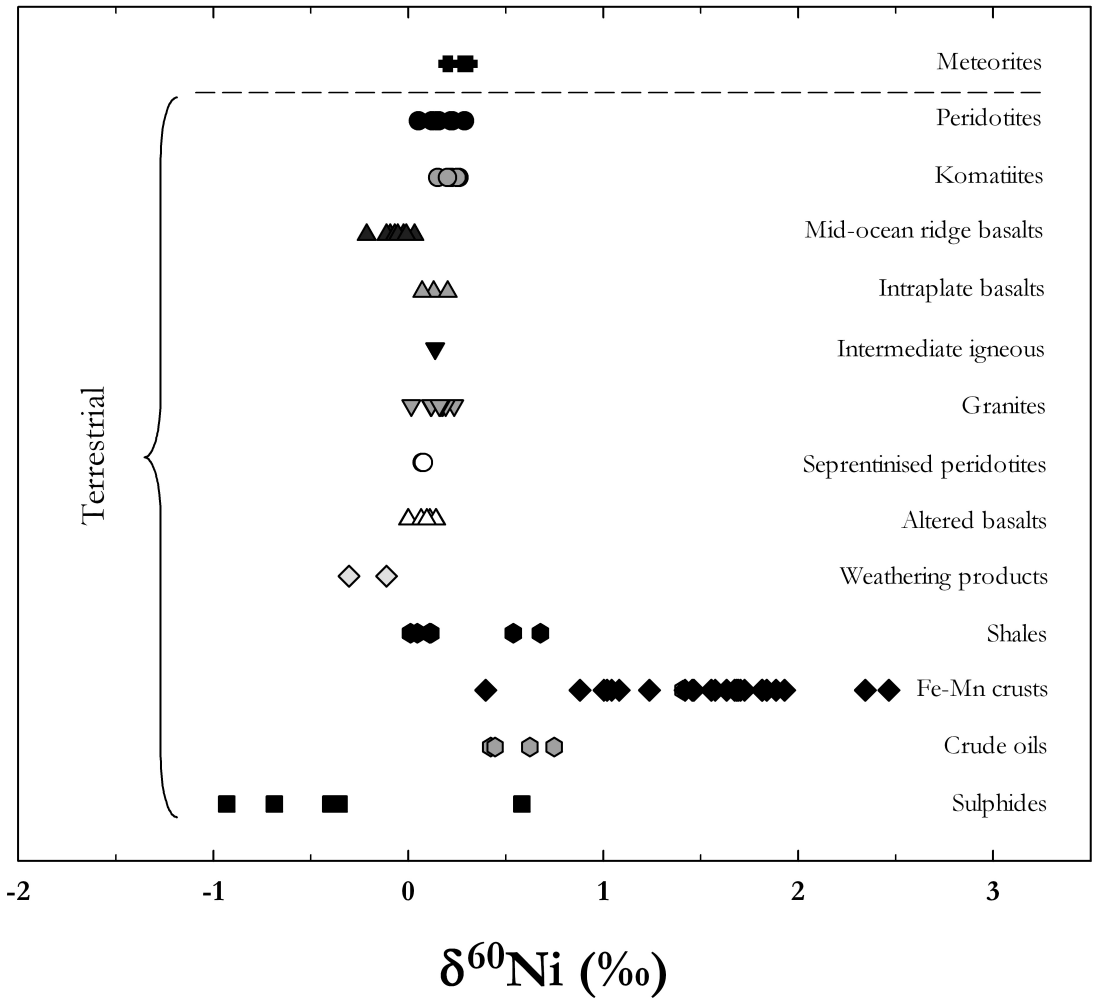

Figure 7.1: *Summary of the Ni isotope compositions of all samples discussed in this thesis.*

and finally to determine the exposure time needed to reach isotopic equilibrium.

Lastly, the Ni isotopic composition of crude oil was established as being heavier than that of igneous rocks, lighter than that of ferromanganese crusts, and similar to that of organic-rich shales. This suggests that the Ni isotope ratio of a crude oil may be an inherited signature from the oil-forming source rock, and that the Ni incorporated into the oil's organic complexes was originally derived from the organic matter in sediments.

The only reservoir of a lighter isotopic composition than igneous rocks found here are sulphides from magmatic systems. However, as the formation of Ni-sulphides plays an important role in the Ni geochemical cycle, this reservoir of light Ni may be enough to complete the mass balance of Ni isotopes on Earth.

7.2 Future work on nickel isotope geochemistry

This thesis introduces a framework for future research into the Ni isotope system, by determining the range of variation in isotope ratios present in several major Ni reservoirs. As shown here, the isotopic fractionations accompanying several processes are relatively large for a transition metal isotope system ($< 3‰$), demonstrating great promise for future use of this isotope system in both low and high temperature applications.

7.2.1 The role of Ni in biogeochemical reactions

One area where Ni isotopes may have a considerable impact is our understanding of biological processes and biogeochemical reactions. Nickel was long considered a biologically inactive element, but research in the past two to three decades has shown the opposite to be the case. Nickel occupies the active site in several microbial enzymes that are crucial to a diverse set of biological processes (Hausinger, 1987; Ragsdale, 1998; Watt & Ludden, 1999; Ragsdale, 2007; Evans, 2005; Siegel et al., 2006), some of which are very interesting from a biogeochemical perspective.

For example, as discussed in Chapter 1, Cameron et al. (2009) investigated

whether cultured cells of methanogens fractionate Ni isotopes. The cultured methanogens in their experiment were shown to preferentially incorporate lighter Ni isotopes, yielding on average δ^{60}Ni-values of -0.9‰. This lead the authors to suggest that Ni isotopes could be used as a signature for the presence of methanogens in ancient sediments. However, as described in Chapter 1, there are several Ni-containing enzymes, that could theoretically fractionate Ni isotopes. Before this methanogen "signature" can be utilised in further research, the fractionations accompanying all these enzyme reactions must be established in order to ensure that the correct isotopic signature is determined.

7.2.2 Decline of Ni before oxygenation of the atmosphere?

Studies published during the last decade have shown how oxygenation of the atmosphere started at ∼2.4 Ga (Farquhar et al., 2000; Holland, 2002; Canfield, 2005; Anbar et al., 2007; Scott et al., 2008), but the reasons behind the start of this process remain poorly understood. One theory, proposed by Zahnle et al. (2006), is that a decrease of atmospheric methane caused the progressive rise of oxygen in the atmosphere. Recently, Konhauser et al. (2009) showed how this decline of atmospheric methane may be linked to a more general decline in dissolved Ni in the ocean. Based on elemental analyses of Banded Iron Formations (BIF), these authors calculated that the Ni concentration in the Archean ocean may have been as high as 400 nmol/L (compared to an average of ∼8 nmol/L in the present ocean). This huge reduction in available Ni may well have had a devastating

effect on methane-producing Archaea, causing a decline in methanogens and an opportunity for oxygen producing bacteria to take over. Therefore, if the fractionations accompanying the different Ni-enzyme reactions can be established, then Ni isotope analyses of Archean sediments, such as BIFs (Frost et al., 2007) or well preserved Archean shales (Wille et al., 2007), could conceivably help determine whether the decline in Ni was accompanied by a decrease in atmospheric methane.

7.2.3 Chemical evolution of the mantle

If Ni is directly linked to the oxygenation of the atmosphere, as suggested by Konhauser et al. (2009), this event could possibly also be connected to the chemical evolution of the mantle. As discussed briefly in Chapter 4, the mantle was considerably hotter in the Archean and Paleoproterozoic than it is today (Berry et al., 2008), which resulted in Ni-rich komatiite and basalt eruptions at the Earth's surface (Arndt, 1991). Data presented in Chapter 4 show that the Ni isotopic composition of basalts appears to depend on their source, with MORB being somewhat lighter in composition than intraplate basalts. These data indicate that the Ni isotopic composition of the mantle may have been affected by the evolution of the mantle due to extraction of partial melts and subduction of oceanic lithosphere and sediments (Halliday et al., 1995). Through additional analyses of mafic rocks (e.g. komatiites) of different ages, Ni isotopes could therefore provide constraints on the condition of the mantle during the Archean, as well as shed further light on the timing and nature of the chemical evolution of the mantle.

BIBLIOGRAPHY

Achterberg, E. & van den Berg, C., 1997. Chemical speciation of chromium and nickel in the western mediterranean, *Deep-Sea Research II*, **44**, 693–720.

Aitkem, B. & Echeverria, L., 1984. Petrology and geochemistry of komatiites and tholeiites from Gorgona Island, Colombia, *Contributions to Mineralogy and Petrology*, **86**, 94–105.

Allégre, C., Poirier, J.-P., Humler, E., & Hofmann, A., 1995. The chemical composition of the Earth, *Earth and Planetary Science Letters*, **134**, 515–526.

Alt, J., Anderson, T., Bonnell, L., & Muehlenbachs, K., 1989. Mineralogy, chemistry, and stable isotopic compositions of hydrothermally altered sheeted dikes: ODP, hole 504B, leg 111, *Proc. Ocean Drilling Program, Scientific Results*, **111**, 27–40.

Anbar, A., Duan, Y., Lyons, T., Arnold, G., Kendall, B., Creaser, R., Kaufman, A., Gordon, G., Scott, C., Garvin, J., & Buick, R., 2007. A whiff of oxygen before the great oxidation event?, *Science*, **317**, 1903–1906.

Anthony, J., Bideaux, R., Bladh, K., & Nicols, M., 2011. *Handbook of Mineralogy, Mineralogical Society of America*, url: http://www.handbookofmineralogy.org/.

Archer, C. & Vance, D., 2004. Mass discrimination correction in multiple-collector plasma source mass spectrometry: an example using Cu and Zn isotopes, *J. Analytical Atomic Spectrometry*, **19**, 656–665.

Arndt, N., 1991. High Ni in Archean tholeiites, *Tectonophysics*, **187**, 411–419.

Arndt, N., Ginibre, C., Chauvel, C., Albarède, F., Cheadle, M., Herzberg, C., Jenner, G., & Lahaye, Y., 1998. Were komatiites wet?, *Geology*, **26**, 739–742.

Aston, F., 1935. The isotopic constitution and atomic weights of hafnium, thorium, rhodium, titanium, zirconium, calcium, gallium, silver, carbon, nickel, cadmium, iron and indium, *Proc. Royal Soc. of London*, **149**, 396–405.

Bach, W., Peucker-Ehrenbrink, B., Hart, S., & Blusztajn, J., 2003. Geochemistry of hydrothermally altered ocenic crust: DSDP/ODP hole 504B - implications for seawater-crust exchange budgets and sr-and pb-isotopic evolution of the mantle, *Geochemistry, Geophysics, Geosystems*, **4**.

Barling, J. & Anbar, A., 2004. Molybdenum isotope fractionation during adsorption by manganese oxides, *Earth and Planetary Science Letters*, **217**, 315–329.

Barwise, A., 1990. Role of nickel and vanadium in petroleum classification, *Energy & Fuels*, **4**, 647–652.

Barwise, A. & Roberts, I., 1984. Diagenetic and catagenetic pathways for porphyrins in sediments, *Organic Geochemistry*, **6**, 167–176.

Beard, B., Johnson, C., Cox, L., Sun, H., Nealson, K., & Aguilar, C., 1999. Iron isotope biosignatures, *Science*, **285**, 1889.

Becker, J., 1996. Mass spectrometric and theoretical investigations into the formation of argon molecular ions in plasma mass spectrometry, *J. Analytical Atomic Spectrometry*, **11**, 643–648.

Becker, J., 2007. *Inorganic Mass Spectrometry*, Wiley.

Berry, A., Danyushevsky, L., O'Neill, H., Newville, M., & Sutton, S., 2008. Oxidation state of iron in komatiitic melt inclusions indicates hot Archean mantle, *Nature*, **455**, 960–963.

Bing-Qian, Z., Jing-Lian, Z., Xiang-Yang, C., Cai-Yuan, F. adn Ying, L., & Ju-Ying, L., 2001. Pb, Sr, and Nd isotopic features in organic matter from China and their implications for petroleum generation and migration, *Geochimica et Cosmochimica Acta*, **65**, 2555–2570.

Birck, J., 2004. An overview of isotopic anomalies in extraterrestrial materials and their nucleosynthetic heritage, *Reviews in Mineralogy & Geochemistry*, **55**, 25–64.

Birck, J. & Lugmair, G., 1988. Nickel and chromium isotopes in Allende incusions, *Earth and Planetary Science Letters*, **90**, 131–143.

Boreham, C., Fookes, C., Popp, B., & Haynes, J., 1989. Origins of etioporphyrins in sediments: Evidence from stable carbon isotopes, *Geochimica et Cosmochimica Acta*, **53**, 2451–2455.

Boreham, C., Fookes, C., Popp, B., & Haynes, J., 1990. Origin of petroporphyrins 2: evidence from stable carbon isotopes, *Energy & Fuels*, **4**, 658–661.

Bourgois, J., Toussaint, J.-F., Gonzalez, H., Azema, J., Calle, B., Desmer, A., Murcia, L., Acevedo, A., Parra, E., & Tournon, J., 1987. Geological history of the Cretaceous ophiolitic complexes of northwestern South America (Colombian Andes), *Tectonophysics*, **143**, 307–327.

Bowie, A., Whitworth, D., Achterberg, E., Mantoura, R., & Worsfold, P., 2002. Biochemistry of Fe and other trace elements (Al, Co, Ni) in the upper Atlantic Ocean, *Deep-Sea Research I*, **49**, 605–636.

Broecker, W., 1991. The great ocean conveyor, *Oceanography*, **4**, 79–89.

Brookins, D., 1988. *Eh, pH diagrams for geochemistry*, Springer-Verlag, Berlin.

Bruland, K., 1980. Oceanographic distributions of cadmium, zinc, nickel, and copper in the North Pacific, *Earth and Planetary Science Letters*, **47**, 176–198.

Bruland, K., 1983. *Chemical Oceanography*, vol. 8, chap. Trace metals in sea-water, pp. 157–220, Academic Press, London.

Bruland, K., 1989. Complexation of zinc by natural organic ligands in the Central North Pacific, *Limnology and Oceanography*, **34**, 269–285.

Bruland, K. & Lohan, M., 2003. Controls of trace metals in seawater, *Treatise on Geochemistry, vol. 6 (The Oceans and Marine Geochemistry)*, pp. 23–47.

Bruland, K., Donat, J., & Hutchins, D., 1991. Interactive influences of bioactive trace metals on biological production in ocean waters, *Limnology and Oceanography*, **36**, 1555–1577.

Burton, K., Schiano, P., Birck, J., Allégre, C., Rehkämper, M., Halliday, A., & Dawson, J., 2000. The distribution and behavious of rhenium and osmium amongst mantle minerals and

the age of the lithospheric mantle beneath Tanzania, *Earth and Planetary Science Letters*, **183**, 93–106.

Butt, C. & Nickel, E., 1981. Mineralogy and geochemistry of the weathering of the disseminated nickel sulfide deposit as Mt. Keith, Western Australia, *Economic Geology*, **76**, 173601751.

Callot, H. & Ocampo, R., 2000. *The Porphyrin Handbook*, vol. 1, Synthesis and Organic Chemistry, chap. Geochemistry of porphyrins, Academic Press.

Calvert, S. & Pedersen, T., 1993. Geochemistry of recent oxic and anoxic marine sedimentsl implications for the geological record, *Marine Geology*, **113**, 67–88.

Cameron, V., Vance, D., Archer, C., & House, C., 2009. A biomarker based on the stable isotopes of nickel, *PNAS*, **106**, 10944–10948.

Canfield, D., 2005. The early history of atmospheric oxygen, *Annual Reviews in Earth and Planetary Sciences*, **33**, 1–36.

Carswell, D. & Dawson, J., 1970. Garnet peridotite xenoliths in South African kimberlite pipes and their petrogenesis, *Contributions to Mineralogy and Petrology*, **25**, 163–184.

Chabot, N., Drper, D., & Agee, C., 2005. Conditions of core formation in the Earth: constraints from nickel and coblat partitioning, *Geochimica et Cosmochimica Acta*, **69**, 2141–2151.

Chan, L.-H., Alt, J., & Teagle, D., 2002. Lithium and lithium isotope profiles through the upper oceanic crust: a study of seawater-basalt exchange at ODP sites 504B and 896A, *Earth and Planetary Science Letters*, **201**, 187–201.

Chappell, B. & Simpson, P., 1984. Source rocks of I- and S-type granites in the Lachland Fold Belt, Southeastern Australia, *Philosophical Transactions of the Royal Society of London, Series A: Mathematical and Physical Sciences*, **310**, 693–707.

Chappell, B., White, A., Williams, I., Wyborn, D., & Wyborn, L., 2000. Lachlan Fold Belt granites revisited: high- and low-temperature granites and their implications, *Australian J. Earth Sciences*, **47**, 123–138.

Chauvel, C., Dupre, B., & Jenner, G., 1985. The Sm-Nd age of Kambalda volcanics is 500 Ma too old!, *Earth and Planetary Science Letters*, **74**, 315–324.

Chen, J., Papanastassiou, D., & Wasserburg, G., 2009. A search for nickel isotopic anomalies in iron meteorites and chondrites, *Geochimica et Cosmochimica Acta*, **73**, 1461–1471.

Christensen, J., Halliday, A., Godfrey, L., Hein, J., & Rea, D., 1997. Climate and ocean dynamics and the lead isotopic records in Pacific ferromanganese crusts, *Science*, **277**, 913.

Clayton, R., 2003. Oxygen isotopes in meteorites, *Treatise on Geochemistry, vol. 1 (Meteorites, comets, and planets)*, pp. 129–142.

Coale, K. & Bruland, K., 1988. Copper complexation in the northeast Pacific, *Limnology and Oceanography*, **33**, 1084–1101.

Cohen, R., O'Nions, R., & Dawson, J., 1984. Isotope geochemistry of xenoliths from East Africa: implications for development of mantel reserviorsand their interaction, *Earth and Planetary Science Letters*, **68**, 209–220.

Compston, W., Williams, I., Campbell, I., & Gresham, J., 1986. Zircon xenocryst from teh Kambalda volcanics: age constrains and direct evidence for older continental crust below the Kambalda-Norseman greenstones, *Earth and Planetary Science Letters*, **76**, 299–311.

Conrad, M., Templeton, A., Daley, P., & Alvarez-Cohen, L., 1999. Isotopic evidence for biological controls on migration of petroleum hydrocarbons, *Organic Geochemistry*, **30**, 843–859.

Cook, D., Wadhwa, M., Janney, P., Dauphas, N., Clayton, R., & Davis, A., 2006. High precision measurements of non-mass-dependent effects in nickel isotopes in meteoritic metal via multicollector ICPMS, *Analytical Chemistry*, **78**, 8477–8484.

Cook, D., Wadhwa, M., Clayton, R., Dauphas, N., Janney, P., & Davis, A., 2007. Mass-dependent fractionation of nickel isotopes in meteoritic metal, *Meteoritics & Planetary Science*, **42**, 2067–2077.

Coplen, T., 2011. Guidelines and recommended terms for expression of stable-isotope-ratio and gas-ratio measurement results, *Rapid Commun. Mass Spectrom.*, **25**, 2538–2560.

Costa, L., Silva, F., Gouveia, S., Nogueria, A., & Nobrega, J., 2001. Focused microwave-assisted acid digestion of oils: an evaluation of the residual carbon content, *Spectrochemica Acta Part B*, **56**, 1981–1985.

Cumming, G., 1973. Propagation of experimental errors in lead isotope ratio measurements using the double spike method, *Chemical Geology*, **11**, 157–165.

Czernuszewicz, R., 2000. Geochemistry of porphyrins: Biological, industrial and environmental aspects, *J. Porphyrins and Phthalocyanines*, **4**, 426–431.

Darling, J., Hawkesworth, C., Storey, C., & Lightfoot, P., 2010. Shallow impact: isotopic insights into crustal contributions to the Sudbury impact melt sheet, *Geochimica et Cosmochimica Acta*, **74**, 5680–5696.

Dauphas, N., Teng, F.-Z., & Arndt, N., 2010. Magnesium and iron isotopes in 2.7 Ga Alexo komatiites: mantle signatures, no evidence for Soret diffustion, and identification of diffusive transport in zoned olivine, *Geochimica et Cosmochimica Acta*, **74**, 3274–3291.

Davis, D., 2008. Sub-million year age resolution of Precambrian igenous events by thermal extraction (TE-TIMS) Pb dating of zirconl application to crystallization of the Sudbury impact melt sheet, *Geology*, **36**, 383–386.

Dawson, J., Powell, D., & Reid, A., 1970. Ultrabasic xenoliths and lava from the Lashine volcano, nothern Tanzania, *J. Petrology*, **11**, 519–548.

Dawson, J., James, D., Paslick, C., & Halliday, A., 1997. Ultrabasic potassic low-volumn magmatism and continental rifitng in North central Tanzania: association with enhanced heat flow, *Russ. Geol. Geophys. (in: Proc. 7th Int. Kimberlite Conf.)*, **38**, 69–81.

Deer, W., Howie, R., & Zussman, J., 1982. *Rock Forming Minerals*, vol. Vol. 1A and 2A, Longman, 2nd edn.

Dempster, A., 1936. The isotopic constitution of iron and nickel, *Physical Review*, **50**, 98.

Deutsch, A., Grieve, R., Avermann, M., Bischoff, L., Brockmeyer, P., Buhl, D., Lakomy, R., Müller-Mohr, V., Ostermann, M., & Stöffler, D., 1995. The Sudbury Structure (Ontario, Canada): a tectonically deformed multi-ring impact basin, *Geol. Rundsch.*, **84**, 697–709.

Dietz, R., 1964. Sudbury Structure as an astrobleme, *J. Geology*, **72**, 412.

Dodson, M., 1963. A theoretical study of the use of internal standards for precise isotopic analysis by the surface ionization technique: Part i, General first-order algebraic solutions, *J. Scientific Instrumentation*, **40**, 289.

Dodson, M., 1970. Simplified equations for double-spiked isotopic analyses, *Geochimica et Cosmochimica Acta*, **34**, 1241–1244.

Dreyfus, S., Pecheyran, C., Lienemann, C., Magnier, C., Prinzhofer, A., & Donard, O., 2007. Determination of lead isotope ratios in crude oils with Q-ICP/MS, *J. Analytical Atomic Spectrometry*, **22**, 351–360.

Duce, R., Liss, P., Merrill, J., Atlas, E., Buat-Menard, P., Hicks, B., Miller, J., Prospero, J., Arimoto, R., Church, T., Ellis, W., Galloway, J., Hansen, L., Jickells, T., Knap, A., Reinhardt, K., Schneider, B., Soudine, A., Tokos, J., Tsunogai, S., Wollast, R., & Zhoul, M., 1991. Atmospheric input of trace species to oceans, *Global Biogeochemical Cylces*, **5**, 193–259.

Dupont, C., Barbeau, K., & Palenik, B., 2008. Ni uptake and limitation in Marine *Synechoccus* strains, *Applied and Environmental Microbiiology*, **74**, 23–31.

Echeverria, L., 1980. Tertiary of Mesozoic komatiites from Gorgona Island, Colombia: field relations and geochemistry, *Contributions to Mineralogy and Petrology*, **73**, 253–266.

Egleston, E. & Morel, F., 2008. Nickel limitation and zinc toxicity in a urea-grown diatom, *Limnology and Oceanography*, **53**, 2462–2471.

Elderfield, H. & Schultz, A., 1996. Mid-ocean ridge hydrothermal fluxes and the chemical composition of the ocean, *Annual Reviews in Earth and Planetary Sciences*, **24**, 191–224.

Evans, D., 2005. Chemistry relating to the nickel enzymes CODH and ACS, *Coordination Chemistry Reviews*, **249**, 1582–1595.

Ewald, H., 1944. Photometrische Bestimmung seltener isotope. Reletive Isotopenhaufigkeiten und Atomgewicht von Nickel., *Z. Phys.*, **122**, 689–696.

Faggart, B.E., J., Basu, A., & Tatsumoto, M., 1985. Origin of the Sudbury Complex by meteorite impact: neodynium isotopic evidence, *Science*, **230**, 436–439.

Farquhar, J., Bao, H., & Thiemens, M., 2000. Atmospheric influences of Earth's earliest sulfur cycle, *Science*, **289**, 756.

Fleischer, E., 1970. The structure of porphyrins and metalloporphyrins, *Accounts of Chemical Research*, **3**, 105–112.

Foster, D. & Gray, D., 2000. Evolution and structure of the Lachlan Fold Belt (orogen) of Eastern Australia, *Annual Reviews in Earth and Planetary Sciences*, **28**, 47–80.

Frank, M., O'Nions, R., Hein, J., & Banakar, V., 1999. 60 Myr records of major elements and Pb-Nd isotopes from hydrogeous ferromanganese crusts: reconstruction of seawater paleochemistry, *Geochimica et Cosmochimica Acta*, **63**, 1689–1708.

Frew, R., Bowie, A., Croot, P., & Pickmere, S., 2001. Macronutrient and trace-metal geochemistry of an in situ iron-induced Southern Ocean bloom, *Deep-Sea Research II*, **48**, 2467–2481.

Fritz, J. & Rettig, T., 1962. Separation of metals by cation exchange in acetone-water-hydrochloric acid, *Analytical Chemistry*, **34**, 1562–1566.

Fritz, J., Garralda, B., & Karraker, S., 1961. Cation exchange separation of metal ions by elution with hydrofluoric acid, *Analytical Chemistry*, **33**, 882.

Frost, C., Blanckenburg, von, F., Schoenberg, R., Frost, B., & Swapp, S., 2007. Preservation of Fe isotope heterogeneitites during diagenesis and metamorphism of banded iron formation, *Contributions to Mineralogy and Petrology*, **153**, 211–235.

Fujii, T., Moynier, F., Telouk, P., & Abe, M., 2010. Experimental and theoretical investigation of isotope fractionation of zinc aqua, chloro, and macrocyclic complexes, *J. Physical Chemistry*, **114**, 2545–2552.

Gaillardet, J., Viers, J., & Dupre, B., 2003. Trace elements in river waters, *Treatise on Geochemistry, vol. 5 (Surface and Ground Water, Weathering, and Soils)*, pp. 225–272.

Galer, S., 1999. Optimal double and triple spiking for high precision lead isotopic measurements, *Chemical Geology*, **157**, 255–274.

Galindo, I., Ivlev, L., Gonzalez, A., & Ayla, R., 1998. Airborne measurements of particle and gas emissions from December 1994 - January 1995 eruption of popocatepetl volcano (Mexico), *J. Volcanology and Geothermal Research*, **83**, 197–217.

Gannoun, A., Burton, K., Parkinson, I., Alard, O., Schiano, P., & Thomas, L., 2007. The scale and origin of the osmium isotope variations in mid-ocean ridge basalts, *Earth and Planetary Science Letters*, **259**, 541–556.

GERM, 2011. *Geochemical Earth Reference Model*, url: http://earthref.org/germ/.

Glasby, G. & Schulz, H., 1999. Eh, pH diagrams for Mn, Fe, Co, Ni, Cu and As under seawater conditions: applications of two new tyrpes of Eh, pH diagrams to the study of specific problems in marine geochemistry, *Aquatic Geochemistry*, **5**, 227–248.

Glass, J., Wolfe-Simon, F., & Anbar, A., 2009. Coevolution of metal availability and nitrogen assimilation cyanobacteria and algae, *Geobiology*, **7**, 100–123.

Gleeson, S., Herrington, R., Durango, J., Velásquez, C., & Koll, G., 2004. The mineralogy and geochemistry of the Cerro Matoso S.A. Ni laterite deposit, Montelíbano, Colombia, *Economic Geology*, **99**, 1197–1213.

Glen, R., Walshe, J., Barron, L., & Watkins, J., 1998. Ordovician convergent-margin volcanism and tectonism in the Lachlan sector of east Godwana, *Geology*, **26**, 751–754.

Gramlish, J., Machlan, L., Barnes, I., & Paulsen, P., 1989a. Absolute isotopic abundance ratios and atomic weight of a reference sample of nickel, *J. Res. of the Natl. Inst. of Stand. and Tech.*, **94**, 347–356.

Greibrokk, T., Lundanes, E., Norli, H., Dyrstad, K., & Olsen, S., 1994. Experimental simulation of oil migration - distribution effects on organic compound groups and on metal/metal ratios, *Chemical Geology*, **116**, 281–299.

Gresham, J. & Loftus-Hills, G., 1981. The geology of the Kambalda nickel field, Western Australia, *Economic Geology*, **76**, 1373–1416.

Grieve, R. & Therriault, A., 2000. Vredefort, Sudbury, Chicxulub: three of a kind?, *Annual Reviews in Earth and Planetary Sciences*, **28**, 305–338.

Grieve, R., Stoffler, D., & Deutsch, A., 1991. The Sudbury Structure - controversial or misunderstood?, *J. Geophysical Research*, **96**, 22753–22764.

Groves, D., Korkiakoski, E., McNaughton, N., Lesher, C., & Cowden, A., 1986. Thermal erosion by komatiites at Kambalda, Western Australia and the genesis of nickel ores, *Nature*, **319**, 136–139.

Guan, Y., Huss, G., & Leshin, L., 2007. ^{60}Fe–^{60}Ni and ^{53}Mn–^{53}Cr isotopic systems in sulfides from unequilibrated enstatite chondrites, *Geochimica et Cosmochimica Acta*, **71**, 4082–4091.

Haack, H. & McCoy, T., 2003. Iron and stony-iron meteorites, *Treatise on Geochemistry, vol. 1 (Meteorites, comets, and planets)*, pp. 325–345.

Halbach, P. & Puteanus, D., 1984. The influence of the carbonate dissolution rate on the growth and composition of Co-rich ferromanganese crusts form Central Pacific seamount areas, *Earth and Planetary Science Letters*, **68**, 73–87.

Halliday, A., 2003. The origins and earliest history of the Earth, *Treatise on Geochemistry, vol. 1 (Meteorites, comets, and planets)*, pp. 509–557.

Halliday, A., Lee, D.-C., Tommasini, S., Davies, G., Paslick, C., Fitton, J., & James, D., 1995. Incompatible trace elements in OIB and MORB and source enrichment in the sub-oceanic mantle, *Earth and Planetary Science Letters*, **133**, 379–395.

Hausinger, R., 1987. Nickel utilization by microorganisms, *Microbioligical Reviews*, **51**, 22–42.

Heggie, D., Kahn, D., & Fischer, K., 1986. Trace metals in metalliferous sediments, MANOP site M: interfacial pore water profiles, *Earth and Planetary Science Letters*, **80**, 106–116.

Henderson, G. & Burton, K., 1999. Using (^{234}U/^{238}U) to assess diffusion rates of isotope tracers in ferromanganese crusts, *Earth and Planetary Science Letters*, **170**, 169–179.

Hofmann, A., 1971. Fractionation corrections for mixed-isotope spikes of Sr, K, and Pb, *Earth and Planetary Science Letters*, **10**, 397–402.

Hofmann, A., 1997. Mantle geochemistry: the message from oceanic volcanism, *Nature*, **385**, 219–229.

Holland, H., 2002. Volcanic gases, black smokers, and the Great Oxidation Event, *Geochimica et Cosmochimica Acta*, **66**, 3811–3826.

Horner, T., Schöbächler, M., Rehkämper, M., Nielsen, S., Williams, H., Halliday, A., Xue, Z., & Hein, J., 2010. Ferromanganese crusts as archines of deep water Cd isotope compositions, *Geochemistry, Geophysics, Geosystems*, **11**.

Huppert, H., Sparks, R., Turner, J., & Arndt, N., 1984. Emplacement and cooloing of komatiite lavas, *Nature*, **309**, 19–22.

Jickells, T., 1988. Cobalt, copper, manganese and nickel in the Sagasso Sea, *Marine Chemistry*, **23**, 131–144.

Johnson, C. & Beard, B., 1999. Correction of instrumentally produced mass fractionation during isotopic analysis of Fe by thermal ionization mass spectrometry, *Int. J. Mass Spectrometry*, **193**, 87–99.

Johnson, C., Beard, B., & Albarède, F., 2004. *Reviews in Mineralogy & Geochemistry: Geochemistry of Non-Traditional Stable Isotopes*, vol. 55, Mineralogical Society of America.

Keays, R., 1995. The role of komatiitic and picritic magamatism and S-saturation in the formation of ore deposits, *Lithos*, **34**, 1–18.

Keely, B., 2006. *Chlorophylls and Bacteriochlorophylls: Biochemistry, Biophysics, Functions and Applications*, chap. Geochemistry of chlorophylls, pp. 531–561, Springer.

Keely, B., Prowse, W., & Maxwell, J., 1990. The Treibs Hypothesis: An evaluation based on structural studies, *Energy & Fuels*, **4**, 628–634.

Kegler, P., Holzheid, A., Frost, D., Rubie, D., Dohmen, R., & Palme, H., 2008. New Ni and Co metal-silicate partitioning data and their relevance for an early terrestrial magma ocean, *Earth and Planetary Science Letters*, **268**, 28–40.

Kerr, A., 2005. La Isla de Gorgona, Colombia: a petrological enigma?, *Lithos*, **84**, 77–101.

Killops, S. & Killops, V., 2005. *Introduction to organic geochemistry*, Blackwell Publishing, 2nd edn.

Kleine, T., Münker, C., Mezger, K., & Palme, H., 2002. Rapid accretion and early core formation on asteroid and terrestrial planets from Hf-W chronometry, *Nature*, **418**, 952–955.

Klemm, V., Levasseur, S., Frank, M., Hein, J., & Halliday, A., 2005. Osmium isotope stratigraphy of a marine ferromanganese crust, *Earth and Planetary Science Letters*, **238**, 42–48.

Klinkhammer, G., 1980b. Early diagenesis in sediments from the eastern equatorial Pacific, ii. pore water metal results, *Earth and Planetary Science Letters*, **49**, 81–101.

Klinkhammer, G., Heggie, D., & Graham, D., 1982. Metal diagenesis in oxic marine sediments, *Earth and Planetary Science Letters*, **61**, 211–219.

Konhauser, K., Pecoits, E., Lalonde, S., Papineau, D., Nisbet, E., Barley, M., Arndt, N., Zahnle, K., & Kamber, B., 2009. Oceanic nickel depletion and a methanogen famine before the Great Oxidation Event, *Nature*, **458**, 750–754.

Koschinsky, A. & Halbach, P., 1995. Sequential leaching of marine ferromanganese precipitates: Genetic implications, *Geochimica et Cosmochimica Acta*, **59**, 5113–5132.

Koschinsky, A., Halbach, P., Hein, J., & Mangini, A., 1996. Ferromanganese crusts as indicators for paleoceanographic events in the NE Atlantic, *Geol. Rundsch.*, **85**, 567–576.

Kraemer, T. & Schornick, J., 1974. Comparison of elemental accumulation rates between ferromanganese deposits and sediments in the south pacific ocean, *Chemical Geology*, **13**, 187–196.

Krot, A., Keil, K., Goodrich, C., Scott, E., & Weisberg, M., 2003. Classification of meteorites, *Treatise on Geochemistry, vol. 1 (Meteorites, comets, and planets)*, pp. 83–128.

Laverne, C., Agrinier, P., Hermitte, D., & Bohn, M., 2001. Chemical fluxes during hydrothermal alteration of a 1200-m long section of dikes in the oceanic crust, DSDP/ODP hole 504B, *Chemical Geology*, **181**, 73–98.

Lee, D., Halliday, A., Hein, J., Burton, K., Christensen, J., & Günther, D., 1999. Hafnium isotope stratigraphy of ferromanganese crusts, *Science*, **285**, 1052–1054.

Levasseur, S., Frank, M., Hein, J., & Halliday, A., 2004. The global variation in the iron isotope composition of marine hydrogenetic ferromanganese deposits: implications for seawater chemistry?, *Earth and Planetary Science Letters*, **224**, 91–105.

Lewan, M., 1984. Factors controlling the proportionality of vanadium and nickel in crude oils, *Geochimica et Cosmochimica Acta*, **48**, 2231–2238.

Lewan, M. & Maynard, J., 1982. Factors controlling enrichment of vanadium and nickel in the bitumen of organic sedimentary rocks, *Geochimica et Cosmochimica Acta*, **46**, 2547–2560.

Li, H.-Y. & Schoonmaker, J., 2003. Chemical composition and mineralogy of marine sediments, *Treatise on Geochemistry, vol. 7 (Sediments, Diagenesis, and Sedimentary rocks)*, pp. 1–35.

Li, W., Jackson, S., Pearson, N., Alard, O., & Chappell, B., 2009. The Cu isotopic signature of granites from the Lachlan Fold Belt, SE Australia, *Chemical Geology*, **258**, 38–49.

Li, W.-Y., Teng, F.-Z., Ke, S., Rudnick, R., Gao, S., Wu, F.-Y., & Chappell, B., 2010. Heterogeneous magnesium isotopic composition of the upper continental crust, *Geochimica et Cosmochimica Acta*.

Li, Y.-H., 1982. A brief discussion on the mean oceanic residence time of elements, *Geochimica et Cosmochimica Acta*, **46**, 2671–2675.

Lightfoot, P., Keays, R., & Doherty, W., 2001. Chemical evolution and origin of nickel sulfide mineralization in the Sudbury Igneous Complex, Ontario, Canada, *Economic Geology*, **96**, 1855–1875.

Ling, H., Burton, K., O'Nions, R., Kamber, B., Blanckenburg, von, F., Gibb, A., & Hein, J., 1997. Evolution of Nd and Pb isotopes in Central Pacific seawater from ferromanganese crusts, *Earth and Planetary Science Letters*, **146**, 1–12.

López, L., S., L., Galarraga, F., Lira, A., & Cruz, C., 1995. V/Ni ratio in maltene and asphaltene fractions of crude oils from the west Venezuelan basin: correlation studies, *Chemical Geology*, **119**, 255–262.

Löscher, B., 1999. Relationships among Ni, Cu, Zn, and major nutritiens in the Southern Ocean, *Marine Chemistry*, **67**, 67–102.

Lub, W., 1939. The isotopic constitution of nickel and chromium, *Proc. Acad. Sci. Amsterdam*, **42**, 253–256.

Ludwig, K., 1999. Isoplot/Ex: a geochronological toolkit for Microsoft Excel, Tech. rep., Berkley Geochronology Center.

Mackey, D., O'Sullivan, J., Watson, R., & Dal Pont, G., 2002. Trace metals in the Western Pacific: temporal and spatial variability in the concentrations of Cd, Cu, Mn and Ni, *Deep-Sea Research I*, **49**, 2241–2259.

Makovicky, E., 2006. Crystal structures of sulfides and other chalcogenides, *Reviews in Mineralogy & Geochemistry*, **61**, 7–125.

Manceau, A., Kersten, M., Marcus, M., Geoffroy, N., & Granina, L., 2007. Ba and Ni speciation in a nodule of binary Mn oxide phase composition from Lake Baikal, *Geochimica et Cosmochimica Acta*, **71**, 1967–1981.

Manning, L., Frost, C., & Branthaver, J., 1991. A neodynium isotopic study of crude oils and soruce rocks: potential applications for petroleum exploration, *Chemical Geology*, **91**, 125–138.

Maréchal, C., Télouk, P., & Albarède, F., 1999. Precise analysis of copper and zinc isotope compositions by plasma-source mass spectrometry, *Chemical Geology*, **156**, 251–273.

Markl, G., Blanckenburg, von, F., & Wagner, T., 2006. Iron isotope fractionation during hydrothermal ore deposition and alteration, *Geochimica et Cosmochimica Acta*, **70**, 3011–3030.

Maynard, J., 2003. Manganiferous sediments, rocks, and ores, *Treatise on Geochemistry, vol. 7 (Sediments, Diagenesis, and Sedimentary rocks)*, pp. 289–309.

MBARI, 2011. The MBARI chemical sensor program: *Periodic Table of Elements in the Ocean*, url: http://www.mbari.org/chemsensor/pteo.htm.

McDonough, W., 2003. Compositional model for the Earth's core, *Treatise on Geochemistry, vol. 2 (The mantle and core)*, pp. 547–568.

McDonough, W. & Sun, S.-S., 1998. The composition of the Earth, *Chemical Geology*, **120**, 223–253.

McSween, H.Y., J., 2003. Mars, *Treatise on Geochemistry, vol. 1 (Meteorites, comets, and planets)*, pp. 601–621.

Morand, P. & Albarède, F., 1983. Nickel isotope studies in meteorites, *Earth and Planetary Science Letters*, **63**, 167–176.

Morel, F., 2008. The co-evolution of phytoplankton and trace element cycles in the ocean, *Geobiology*, **6**, 318–324.

Morel, F. & Price, N., 2003. The biogeochemical cycles of trace metals in the oceans, *Science*, **300**, 944.

Mostefaoui, S., Lugmair, G., & Hoppe, P., 2005. ^{60}Fe: A heat source for planetary differentiation from a nearby supernova explosion, *The Astrophysical Journal*, **625**, 271–277.

Moynier, F., Blichert-Toft, J., Télouk, P., Luck, J.-M., & Albarède, F., 2007. Comparative stable isotope geochemistry of Ni, Cu, Zn, and Fe in chondrites and iron meteorites, *Geochimica et Cosmochimica Acta*, **71**, 4365–4379.

Mungall, J., Ames, D., & Henley, J., 2004. Geochemical evidence form the Sudbury Structure for crustal redistribution by large bolide impacts, *Nature*, **429**, 546–548.

Naldrett, A., 1999. World-class Ni-Cu-PGE deposits: key factors in their genesis, *Mineralium Deposita*, **34**, 227–240.

Naldrett, A., 2004. *Magmatic sulfide deposits: geology, geochemistry, and exploration*, Springer-Verlag, Berlin.

Nielsen, S., Mar-Gerrison, S., Gannoun, A., LaRowe, D., Klemm, V., Halliday, A., Burton, K., & Hein, J., 2009. Thallium isotope evidence for a permanent increase in marine organic carbon export in the early Eocene, *Earth and Planetary Science Letters*, **278**, 297–307.

Noriki, S., Arashitani, Y., Minakawa, M., Harada, K., & Tsunogai, S., 1998. Vertical cycling of Cu and Ni in the Western, North, and Equatorial Pacific, *Marine Chemistry*, **59**, 211–218.

Norisuye, K., Ezoe, M., Nakatsuka, S., Umetani, S., & Sohrin, Y., 2007. Distribution od bioactive trace metals (Fe, Co, Ni, Cu, Zn and Cd) in the Sulu Sea and its adjacent seas, *Deep-Sea Research II*, **54**, 14–37.

Nriagu, J., 1989. A global assessment of natural sources of atmospheric trace metals, *Nature*, **338**, 47–49.

Oliviera, L. & Antia, N., 1984. Evidence of nickel ion requrement for autotrophic growth of marine diatom with urea serving as nitrogen source, *European J. Phycology*, **19**, 125–134.

Oliviera, L. & Antia, N., 1986b. Some observations on the urea-degrading enzyme of the diatom *Cyclotella cryptica* and the role of nickel in its production, *J. Plankton Research*, **8**, 235–242.

Pacyna, E. & Pacyna, J., 2001. An assessment of global and regional emissions of trace metals to the atmosphere from anthropogenic sources worldwide, *Environmental Reviews*, **9**, 269–298.

Park, R. & Dunning, H., 1961. Stable carbon isotope studies of crude oils and their porphyrin aggregates, *Geochimica et Cosmochimica Acta*, **22**, 99–105.

Peach, C., Mathez, E., & Keays, R., 1990. Sulfide melt-silicate melt distribution coefficients for noble metals and other chalcophile elements as deduced from MORB: implications for partial melting, *Geochimica et Cosmochimica Acta*, **54**, 3379–3389.

Peacock, C., 2009. Physiochemical controls on the crystal-chemistry of Ni in birnessite: Genetic implications for ferromanganese precipitates, *Geochimica et Cosmochimica Acta*, **73**, 3568–3578.

Peacock, C. & Sherman, D., 2007a. Sorption of Ni by birnesite: Equilibrium controls on Ni in seawater, *Chemical Geology*, **238**, 94–106.

Peacock, C. & Sherman, D., 2007b. Crystal-chemistry of Ni in marine ferromanganese crusts and nodules, *American Mineralogist*, **92**, 1087–1092.

Peacock, C., Moon, E., Nielsen, S., & Halliday, A., 2009. Oxidative scavenging of Tl by Mn oxide birnessite: sorption and stable isotope fractionation, *Geochimica et Cosmochimica Acta*, p. A1003.

Pearson, C. & Green, J., 1993. Vanadium and nickel complexes inpetroleum recid acid, base, and neutral fractions, *Energy & Fuels*, **7**, 338–346.

Pena, J., Kwon, K., Refson, K., Bargar, J., & Sposito, G., 2010. Mechanisms of nickel sorption by a bacteriogenic birnessite, *Geochimica et Cosmochimica Acta*, **74**, 3076–3089.

Peucker-Ehrenbrink, B., 1996. Accreation of extraterrestrial material during the last 80 million years and its effect on the marine osmium isotope record, *Geochimica et Cosmochimica Acta*, **60**, 3187–3196.

Piper, D. & Perkins, R., 2004. A moders vs. Permian black shale - the hydrography, primary productivity, and water-column chemistry of deposition, *Chemical Geology*, **206**, 177–197.

Pokrovsky, O., Viers, J., & Freydier, R., 2005. Zinc stable isotope fractionation during its adsorption on oxides and hydroxides, *J. Colloid and Interface Science*, **291**, 192–200.

Premovic, P., Tonsa, I., Lopez, L., Pavlovic, M., Neskovic, O., LoMonaco, S., Dordevic, D., & Veljkovic, M., 2000. The vanadium isotopic comstitution of petroleum asphaltenes: La Luna Formation (Venezuela), *J. Inorganic Biochemistry*, **80**, 153–155.

Premovic, P., Dordevic, D., & Pavlovic, M., 2002. Vanadium of petroleum asphaltenes and source kerogens (La Luna Formation, Venezuela): isotopic study and origin, *Fuel*, **81**, 2009–2016.

Price, N. & Morel, F., 1991. Colimitation of phytoplankton growth by nickel and nitrogen, *Limnology and Oceanography*, **36**, 1071–1077.

Prichard, H., Hutchinson, D., & Fisher, P., 2004. Petrology and crystallization history of multiphase sulfide droplets in a mafic dike from Uruguay: implications for the origin of Cu-Ni-PGE sulfide deposits, *Economic Geology*, **99**, 365–376.

Quitte, G. & Oberli, F., 2006. Quantitative extraction and high precision isotope measurements of nickel by MC-ICPMS, *J. Analytical Atomic Spectrometry*, **21**, 1249–1255.

Quitte, G., Meier, M., Latkoczy, C., Halliday, A., & Günther, D., 2006. Nickel isotopes in iron-meteorites – nucleosynthetic anomalies in sulphides with no effects in metals and no trace of ^{60}Fe, *Earth and Planetary Science Letters*, **242**, 16–25.

Quitte, G., Halliday, A., Meyer, B., Markowski, A., Latkoczy, C., & Günther, D., 2007. Correlated iron 60, nickel 62 and zirconium 96 in refractory inclusions and the origin of the solar system, *The Astrophysical Journal*, **655**, 678–684.

Ragsdale, S., 1998. Nickel biochemistry, *Chemical Biology*, **2**, 208–215.

Ragsdale, S., 2007. Nickel and the carbon cycle, *J. Inorganic Biochemistry*, **101**, 1657–1666.

Rauch, J. & Pacyna, J., 2009. Earth's global Ag, Al, Cr, Cu, Fe, Ni, Pb, and Zn cycles, *Global Biogeochemical Cylces*, **23**.

Regelous, M., Elliott, T., & Coath, C., 2008. Nickel isotope heterogeneity in the early solar system, *Earth and Planetary Science Letters*, **272**, 330–338.

Rehkämper, M. & Nielsen, S., 2004. The mass balance of dissolved thallium in the oceans, *Marine Chemistry*, **85**, 125–139.

Rehkämper, M., Frank, M., Hein, J., Porcelli, D., Halliday, A., Ingri, J., & Liebetrau, V., 2002. Thallium isotope variations in seawater and hydrogenetic, diagenetic, and hydrothermal ferromanganese deposits, *Earth and Planetary Science Letters*, **197**, 65–81.

Rehkämper, M., Frank, M., Hein, J., & Halliday, A., 2004. Cenozoic marine geochemistry of thallium deduced from isotopic studies of ferromanganese crusts and pelagic sediments, *Earth and Planetary Science Letters*, **219**, 77–91.

Righter, K., 2003. Metal-silicate partitioning of siderophile elements and core formation in the early Earth, *Annual Reviews in Earth and Planetary Sciences*, **31**, 135–174.

Rudge, J., Reynolds, B., & Bourdon, B., 2009. The double spike toolbox, *Chemical Geology*, **265**, 420–431.

Rudnick, R., McDonough, W., & Orpin, A., 1992. Northern Tanzanian peridotite xenoliths: a comparison with Kaapvaal peridotites and interferences on metasomatic interactions, *Kimberlites, related rocks and mantle xenoliths (in: Proc. 5th Int. Kimberlite Conf.)*, **1**, 336–353.

Rue, E. & Bruland, K., 1995. Complexation of iron(iii) by natural organic ligands in the Central North Pacific as determined by new competitive ligand equilibration/adsorptive cathodic stripping voltametric method, *Marine Chemistry*, **50**, 117–138.

Russell, W., Papantastassiou, D., & Tombrello, T., 1978. Ca isotope fractionation on the earth and other solar system materials, *Geochimica et Cosmochimica Acta*, **42**, 1075–1090.

Saager, P., de Baar, H., & Howland, R., 1992. Cd, Zn, Ni and Cu in the Indian Ocean, *Deep-Sea Research*, **39**, 9–35.

Saager, P., de Baar, H., de Jong, J., Nolting, R., & Schijf, J., 1997. Hydrography and local sources of dissolved trace metals Mn, Ni, Cu and Cd in the northeast Atlantic Ocean, *Marine Chemistry*, **57**, 195–216.

Saito, H., 1977. Nickel content of basaltic magmas: identification of primary magmas and a measure of the degree of olivine fractionation, *Lithos*, **10**, 113–120.

Saito, N., 1984. Selected data on ion exchange separations in radioanalytical chemistry, *Pure and Applied Chemistry*, **56**, 523–539.

Sander, S. & Koschinsky, A., 2011. Metal flux from hydrothermal vents increased by organic complexation, *Nature Geoscience*, **4**, 145.

Savage, P., Georg, R., Williams, H., Burton, K., Halliday, A., & Chappell, B., 2010. The silicon isotopic composition of I- and S-type granites, *American Geophysical Union, Fall Meeting*.

Schoenberg, R. & Blanckenburg, von, F., 2006. Modes of planetary-scale Fe isotope fractionation, *Earth and Planetary Science Letters*, **252**, 342–359.

Sclater, F., Boyle, E., & Edmond, J., 1976. On the marine geochemistry of nickel, *Earth and Planetary Science Letters*, **31**, 119–128.

Scott, C., Lyons, T., Bekker, A., Shen, Y., Poulton, S., Chu, X., & Anbar, A., 2008. Tracing the stepwise oxygenation of the Proterozoic ocean, *Nature*, **452**, 456–459.

Scott, E. & Krot, A., 2003. Chondrites and their components, *Treatise on Geochemistry, vol. 1 (Meteorites, comets, and planets)*, pp. 143–199.

Seewald, J., 2003. Organic-inorganic interactions in petroleum-producing sedimentary basins, *Nature*, **426**, 327–333.

Selby, D. & Creaser, R., 2005. Direct radiometric dating of hydrocarbon deposits using rhenium-osmium isotopes, *Science*, **308**, 1293–1295.

Selby, D., Creaser, R., & Fowler, M., 2007. Re-Os elemental and isotopic systematics in crude oils, *Geochimica et Cosmochimica Acta*, **71**, 378–386.

Sharma, M., Polizzotto, M., & Anbar, A., 2001. Iron isotopes in hot springs along the Juan de Fuca Ridge, *Earth and Planetary Science Letters*, **194**, 39–51.

Sherman, D. & Peacock, C., 2010. Surface complxation of Cu on birnessite (δMnO_2): Controls on Cu in the deep ocean, *Geochimica et Cosmochimica Acta*, **74**, 6721–6730.

Sheu, E. & Mullins, O., eds., 1996. *Asphaltenes: fundamentals and applications*, Springer.

Shima, M., 1965. The geochemical studies of stable isotopes on iron and nickel, *J. Jap. Ass. Min. Petr. Econ. Geol. (in Japanese)*, **53**, 228–233.

Shimamura, T. & Lugmair, G., 1983. Ni isotopic composition in Allende and other meteorites, *Earth and Planetary Science Letters*, **63**, 177–188.

Siebert, C., Nägler, T., & Kramers, J., 2001. Determination of molybdenum isotope fractionation by double-spike multicollector inductively coupled plasma mass spectrometry, *Geochemistry, Geophysics, Geosystems*, **2**, 1032.

Siebert, C., Nägler, T., von Blanckenburg, F., & Kramers, J., 2003. Molybdenum isotope records as a potential new proxy for paleoceanography, *Earth and Planetary Science Letters*, **211**, 159–171.

Siegel, A., Siegel, H., & Siegel, R., eds., 2006. *Nickel and its surprising impact in nature*, vol. 2 of **Metal ions in lift sciences**, Wiley.

Sobolev, A., Hofmann, A., Sobolev, S., & Nikogosian, I., 2005. An olivine-free mantle source of Hawaiian shield basalts, *Nature*.

Steele, R., Elliott, T., Coath, C., & Regelous, M., 2011. Confirmation of mass-independent ni isotopic variability in iron meteorites, *Geochimica et Cosmochimica Acta*.

Stolz, G. & Nesbitt, R., 1981. The komatiite nickel sulfide association at Scotia; a petrochemical investigation of the ore environment, *Economic Geology*, **76**, 1480–1502.

Strelow, F., 1960. An ion exchange selectivity scale of cations based on equilibrium distribution coefficients, *Analytical Chemistry*, **32**, 1185.

Strelow, F., 1990. Distribution coefficient and cation-exchange behaviour of some amines and aquo complexes of metallic elements in ammonium nitrate solution, *Analytica Chimica Acta*, **233**, 129–134.

Strelow, F. & Bothma, C., 1967. Anion exchange and a selectivity scales for elements in sulfuric acid media with a strong basic resin, *Analytical Chemistry*, **39**, 595.

Strelow, F. & Victor, A., 1972. Selective separation of copper from other elements by cation-exchange chromatography in hydrocholoric acid-acetone media, *Analytica Chimica Acta*, **59**, 389–396.

Strelow, F., Rethemeyer, R., & Bothma, C., 1965. Ion exchange selectivity scales for cations in nitric acid and sulfuric acid media with a sulfonated polystyrene resin, *Analytical Chemistry*, **37**, 106.

Strelow, F., Weinert, C., & Eloff, C., 1972. Distribution coefficients and anion exchange behaviour of elements in oxalic acid-hydrochloric acid mixtures, *Analytical Chemistry*, **44**, 2352.

Stueber, A., 1969. Abundances of K, Rb, Sr and Sr isotopes in ultramafic rocks and mineral from western North Carolina, *Geochimica et Cosmochimica Acta*, **33**, 543–553.

Stuiver, M., Quay, P., & Ostlund, H., 1983. Abbyssal water carbon-14 distribution and the age of the worlds oceans, *Science*, **219**, 849–851.

Sundararaman, P., 1993. On th emechanism of change in DPEP/ETIO ratio with maturity, *Geochimica et Cosmochimica Acta*, **57**, 4517–4520.

Sundararaman, P. & Boreham, C., 1993. Comparison of nickel and vanadyl porphyrin distribution of sediments, *Geochimica et Cosmochimica Acta*, **57**, 1367–1377.

Sundararaman, P., Biggs, W., Reynolds, J., & Fetzer, J., 1988. Vanadylporphyrins, indicators of kerogen breakdown and generation of petroleum, *Geochimica et Cosmochimica Acta*, **52**, 2337–2341.

Suzuki, M. & Matsuo, S., 1967. Measurements of the isotopic ratios of nickel in iron meteorites using nickel carbonyl, *Geochemical Journal (Japan)*, **1**, 55–60.

Tachibana, S., Huss, G., Kita, N., Shimoda, G., & Morishita, Y., 2006. ^{60}Fe in chondrites: debris from a nearby supernova in the early solar system?, *The Astrophysical Journal*, **639**, L87–L90.

Tanimizu, M. & Hirata, T., 2006. Determination of natural isotopic variation in nickel using inductively coupled plasma mass spectrometry, *J. Analytical Atomic Spectrometry*, **21**, 1423–1426.

Teng, F.-Z., McDonough, W., Rudnick, R., Dalpe, C., Tomascak, P., Chappell, B., & Gao, S., 2004. Lithium isotopic composition and concentration of the upper continental crust, *Geochimica et Cosmochimica Acta*, **68**, 4167–4178.

Treibs, A., 1934. Chlorophyll- un Häminderivate in bituminösen Gesteinen, Erdölen, Erdwaschen in Asphalten - ein Beitrag zur Entstehung des Erdöls, *Justus Liebigs Annalen der Chemie*, **510**, 42–62.

Treibs, A., 1936. Chlorophyll- un Häminderivate in organischen Mineralstoffen, *Angewandte Chemie*, **49**, 682–686.

Turner, A. & Martino, M., 2006. Modelling the equilibrium speciation of nickel in the Tweed Esturay, UK: voltametric determination and simulations using WHAM, *Marine Chemistry*, **102**, 198–207.

Turner, S., Blundy, J., Wood, B., & Hole, M., 2000. Large ^{230}Th-excess in baslats produced by partial melting of spinel lherzolite, *Chemical Geology*, **162**, 127–136.

Valley, J. & Cole, D., 2001. *Reviews in Mineralogy & Geochemistry: Stable Isotope Geochemistry*, vol. 43, Mineralogical Society of America.

van den Berg, C., Kahn, S., Daly, P., Riley, J., & Turner, D., 1991. An electromchemical study of Ni, Sb, Se, Sn, U and V in the estuary of the Tamar, *Estuarine, Coastal and Shelf Science*, **33**, 309–322.

Vandenbroucke, M. & Largeau, C., 2007. Kegogen, origin, evolution and structure, *Organic Geochemistry*, **38**, 719–833.

Verlaan, P., Cronan, D., & Morgan, C., 2004. A comparative analysis of compositional variations in and between marine ferromanganese nodules and crusts in the South Pacific and their environmental controls, *Progress in Oceanography*, **63**, 125–158.

Victor, A., 1986. Separation of nickel from other elements by cation-exchange chromatography in dimethylglyoxime/hydrochloric acid/acetone media, *Analytica Chimica Acta*, **183**, 155–161.

Wade, J. & Wood, B., 2005. Core formation and the oxidation state of the Earth, *Earth and Planetary Science Letters*, **236**, 78–95.

Walker, R., Morgan, J., Naldrett, A., Li, C., & Fassett, J., 1991. Re-Os isotope systematics of Ni-Cu sulfide ores, Sudbury Igneous Complex, Ontario: evidence for a major crustal component, *Earth and Planetary Science Letters*, **105**, 416–429.

Walker, R., Storey, M., Kerr, A., Tarney, J., & Arndt, N., 1999. Implications of ^{187}Os isotopic heterogenities in a mantle plume: evidence form Gorgona Island and Curacao, *Geochimica et Cosmochimica Acta*, **63**, 713–728.

Walter, M. & Tronnes, R., 2004. Early Earth differentiation, *Earth and Planetary Science Letters*, **225**, 253–269.

Wasylenki, L., Rolfe, B., Weeks, C., Spiro, T., & Anbar, A., 2008. Experimental investigation of the effects of temperature and ionic strengh on Mo isotope fractionation during adsorption to manganese oxides, *Geochimica et Cosmochimica Acta*, **72**, 5997–6005.

Watt, R. & Ludden, P., 1999. Nickel-binding proteins, *Cell. Mol. Life Sci.*, **56**, 604–625.

Weyer, S. & Ionov, D., 2007. Partial metling and melt percolation in the mantle: the message from Fe isotopes, *Earth and Planetary Science Letters*, **259**, 119–133.

White, J. & Cameron, A., 1948. The natural abundance of isotopes of stable elements, *The Physical Review*, **74**, 991–1000.

Wille, M., Kramers, J., Nägler, T., Beukes, N., Schröder, S., Meisel, T., Lacassie, J., & Voegelin, A., 2007. Evidence for a gradual rise of oxygen between 2.6 and 2.5 Ga from Mo isotopes and Re-PGE signatures in shales, *Geochimica et Cosmochimica Acta*, **71**, 2417–2435.

Williams, H., Peslier, A., McCammon, C., Halliday, A., Levasseur, S., Teutsch, N., & Burg, J.-P., 2005. Systematic iron irotope variations in the mantle rocks and minerals: the effects of partial melting and oxygen fugacity, *Earth and Planetary Science Letters*, **235**, 435–452.

Wood, B., Walter, M., & Wade, J., 2006. Accretion of the Earth and segregation of its core, *Nature*, **441**, 825–833.

Xue, H., Jansen, S., A., P., & L., S., 2001. Nickel speciation and complexation kinetics in freshwater by ligand exchange and DPCSV, *Environmental Science & Technology*, **35**, 539–546.

Young, E., Galy, A., & H., N., 2002. Kinetic and equilibrium mass-dependent isotope fractionation laws in nature and their geochemical and cosmochemical significance, *Geochimica et Cosmochimica Acta*, **66**, 1095–1104.

Zahnle, K., Claire, M., & D.C., C., 2006. The loss of mass-independent fractionation of sulfur due to a Paleoproterozoic collapse of atmospheric methane, *Geobiology*, **4**, 271–283.

Zektser, I. & Loaiciga, H., 1993. Groundwater fluxes in the global hydrological cycle: past, present and future, *J. Hydrology*, **144**, 405–427.

APPENDIX

A

DOUBLE-SPIKE CALCULATIONS: MATHEMATICAL DESCRIPTIONS

A.1 The angle (θ) in between two planes

To calculate the angle in between to planes in a three isotope space the isotopic ratios of the double-spike (S), the natural standard (N), and the spike-standard mixture (M) are all thought to be lying on a unique line in isotope-space (line $N - M - S$ in Fig. A.1). As the instrumental mass fractionation shifts the N^{true} and M^{true} to the points N^{meas} and M^{meas} respectively the exponential mass fractionation law (described above) can be used to calculate N^{meas} and M^{meas}:

$$R_N^{meas} = R_N^{true} \cdot \left(\frac{m_n}{m_{58}}\right)^{\beta} \tag{A.1}$$

$$R_M^{meas} = R_M^{true} \cdot \left(\frac{m_n}{m_{58}}\right)^{\beta} \tag{A.2}$$

With the help of these equations and the true standard and spike compositions the vectors X_1 and X_2 (for the isotope pair of 60/58), X_1 and Y_2 (for 61/58), and Z_1 and Z_2 (for 62/58) describing the corresponding planes n (through N^{true}, N^{meas}, S) and m (through M^{true}, M^{meas}, S) are calculated:

$$nX_1 = R_N^{true} - R_S^{true} \tag{A.3}$$

$$nX_2 = R_N^{meas} - R_S^{true} \tag{A.4}$$

$$mX_1 = R_M^{true} - R_S^{true} \tag{A.5}$$

$$mX_2 = R_M^{meas} - R_S^{true} \tag{A.6}$$

With these six vectors for each plane (nX_1, nX_2, nY_1, nY_1, nZ_1, nZ_1, and mX_1, mX_2, mY_1, mY_1, mZ_1, mZ_1) the planes n and m can be calculated and normalised to the length of each plane ($m_{1\ (norm)}$, $m_{2\ (norm)}$, and $m_{3\ (norm)}$ are calculated in the same way as for n)

$$n_1 = (nY_1 \cdot nZ_2) - (nY_2 \cdot nZ_1) \tag{A.7}$$

$$n_2 = (nX_2 \cdot nZ_2) - (nX_1 \cdot nY_2) \tag{A.8}$$

$$n_3 = (nX_1 \cdot nY_2) - (nX_2 \cdot nY_1) \tag{A.9}$$

$$n_{1\ (norm)} = \frac{n_1}{\sqrt{n_1^2 + n_2^2 + n_3^2}} \tag{A.10}$$

$$n_{2\ (norm)} = \frac{n_2}{\sqrt{n_1^2 + n_2^2 + n_3^2}} \tag{A.11}$$

$$n_{3\ (norm)} = \frac{n_3}{\sqrt{n_1^2 + n_2^2 + n_3^2}} \tag{A.12}$$

As we now know the planes positions the line $N - M - S$ – the intersection between the two planes – and the intersection angle (θ) can be determined:

$$cos(\theta) = n_{1(norm)} \cdot m_{1(norm)} + n_{2(norm)} \cdot m_{2(norm)} + n_{3(norm)} \cdot m_{3(norm)} \tag{A.13}$$

The optimum double-spike composition is given by the spike combination producing a large θ, as the angle is a measure of how well the planes can be resolved from each other. A larger θ should therefore give a more exact determination of the $N - M - S$ line and consequently give a low error on the calculation of N_{true} (Galer, 1999; Siebert et al., 2001).

A.2 Optimal spike by geometrical projection

This method – taken from Siebert et al. (2001) – was used in calculation of the optimum double-spike composition, and has also been used for data reduction and calculation of sample isotope ratios. The method attacks the problem from a geometrical viewpoint and considers the isotope ratios of the spike, standard and sample as being actual points in in a three isotope space geometrical projection. It also assumes the exponential fractionation law is valid for Ni, and calculates α and β by adopting a starting value of each fractionation factor (here 0.1 and 2 respectively). The calculations are then reiterated until conversion of these factors, after which the sample's actual isotope ratios are calculated. Assuming that the sample is a fractionated standard the exponential fractionation law gives:

$$\frac{R^{\,measured}}{R^{\,true}} = \left(\frac{m_{isotope\ 1}}{m_{isotope\ 2}}\right)^{\beta} \qquad \Longrightarrow \qquad R_{Ni}^{\,sample} = R_{Ni}^{\,std} \cdot \left(\frac{m_n}{m_{58}}\right)^{\alpha} \tag{A.14}$$

The true isotope ratios of the standard, sample and spike are assumed to lie in the same plane (z), isotope ratios are denoted Rx ($^{60/58}$Ni), Ry ($^{61/58}$Ni), Rz ($^{62/58}$Ni), and st (standard), sa (sample), sp (spike). The plane p is calculated by the equation $p = ax + by + c$, where the parameters a, b, and c are defined by:

$$a = \frac{Ry_{st}(Rz_{sa} - Rz_{sp}) + Ry_{sa}(Rz_{sp} - Rz_{st}) + Ry_{sp}(Rzst - Rz_{sa})}{Ry_{st}(Rx_{sa} - Rx_{sp}) + Ry_{sa}(Rx_{sp} - Rx_{st}) + Ry_{sp}(Rxst - Rx_{sa})} \tag{A.15}$$

$$b = \frac{Ry_{st}(Rz_{sa} - Rz_{sp}) + Ry_{sa}(Rz_{sp} - Rz_{st}) + Ry_{sp}(Rzst - Rz_{sa})}{Ry_{st}(Rx_{sa} - Rx_{sp}) + Ry_{sa}(Rx_{sp} - Rx_{st}) + Ry_{sp}(Rxst - Rx_{sa})} \tag{A.16}$$

$$c = Rz_{st} - aRx_{st} - bRy_{st} \tag{A.17}$$

The exponential fractionation law also gives (*true* ratio = *corrected* ratio):

$$\frac{R^{\,measured}}{R^{\,true}} = \left(\frac{m_{isotope\ 1}}{m_{isotope\ 2}}\right)^{\beta} \qquad \Longrightarrow \qquad R_{Ni}^{corr} = \frac{R_{Ni}^{meas}}{(m_n/m_{58})^{\beta}} \tag{A.18}$$

The sample's isotope ratios of the measured (*meas*) values and the corrected mass bias corrected values (*corr*) define a line, which should intercept the plane z at the same point as the true exponential fractionation curve if the values assumed for α and β are correct. This line is defined by the two equations $l_1 = dx + e$ and $l_2 = fy + g$ with the parameters *d, e, f, g* as defined as follows:

$$d = \frac{Rz_{meas} - Rz_{corr}}{Rx_{meas} - Rx_{corr}} \qquad f = \frac{Rz_{meas} - Rz_{corr}}{Ry_{meas} - Ry_{corr}} \tag{A.19}$$

$$e = Rz_{meas} - dRx_{meas} \qquad g = Rz_{meas} - dRy_{meas} \tag{A.20}$$

The intersection between this line ($l_1 = dx + e$ and $l_2 = fy + g$) and the plane ($p = ax + by + c$) are in turn defined by the coordinates X_{int}, Y_{int}, and Z_{int}, which are found trough the other parameters (*a, b, c, d, e, f, g*) by:

$$X_{int} = \frac{bg - be + ef - cf}{af + bd - df} \qquad Y_{int} = \frac{bg - be + ef - cf}{af + bd - df} \qquad Z_{int} = aX_{int} + bY_{int} + c \tag{A.21}$$

The intercept values are now set as the new values for Rx_{corr}, Ry_{corr}, and Rz_{corr} (instead of the values calculated using only the exponential fractionation law) and a new value for β and α can be calculated and used instead of the assumed values. The calculations are reiterated until conversion of the parameters β and α.

$$\beta = ln\left(\frac{R_{Ni}^{corr}/R_{Ni}^{meas}}{m_n/m_{58}}\right) \qquad \alpha = ln\left(\frac{R_{Ni}^{\,sample}/R_{Ni}^{std}}{m_n/m_{58}}\right) \tag{A.22}$$

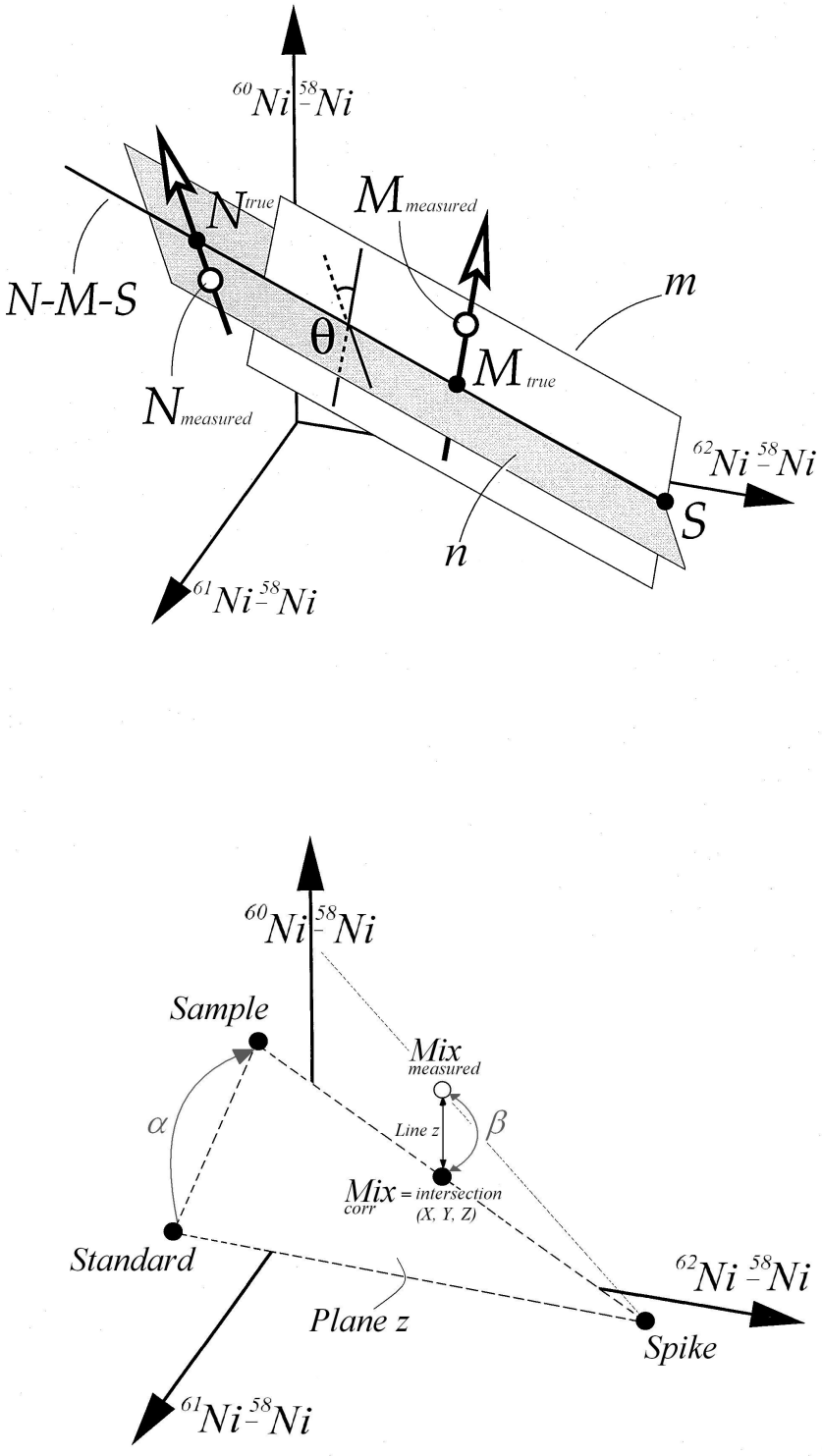

Figure A.1: *Figures describing the notations used in the geometrical calculations. Top – illustration of the line N-M-S and angle θ; Bottom – illustration of the plane (z), line (z), and intersection point of the line on the plane (X, Y, Z) for finding β and α*

A.3 Optimal spike by algebraic inversion

This way of calculating the optimal double-spike composition is based on the relative amounts of four isotopes, which are expressed in terms of vectors of three isotopic ratios with a common denominator. For the calculation of the optimal double-spike for Ni we have used $^{60/58}$Ni, $^{61/58}$Ni, and $^{62/58}$Ni and followed the descriptions in Rudge et al. (2009). The inversion is based on the exponential fractionation law and all notations are explained in Fig. A.2.

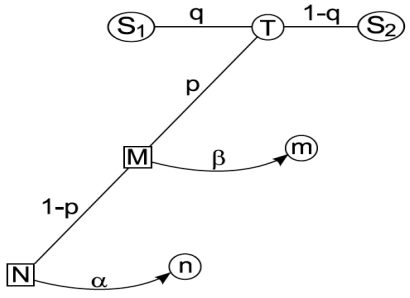

Figure A.2: *From Rudge et al. (2009)*

$$n_i = N_i \left(\frac{mass^i}{mass^{58}} \right)^{\alpha} \tag{A.23}$$

$$m_i = M_i \left(\frac{mass^i}{mass^{58}} \right)^{\beta} \tag{A.24}$$

$$N_i = \frac{{}^{i}Ni}{{}^{58}Ni_{\,sample}} \qquad T_i = \frac{{}^{i}Ni}{{}^{58}Ni_{\,spike}} \tag{A.25}$$

Further is M_i related to N_i and T_i following A.24 (left eq.), and λ therefrom is related to the proportion (p, right eq.) double-spike in the sample-spike mixture.

$$M_i = \frac{{}^{i}Ni}{{}^{58}Ni_{\,mix}} = \lambda T_i + (1-\lambda)\, N_i \qquad p = \left(1 + \frac{1-\lambda}{\lambda} \left(\frac{1+\Sigma N}{1+\Sigma T} \right) \right)^{-1} \tag{A.26}$$

where ΣN and ΣT are the total sum of the moles of Ni from all isotopes in the sample and spike respectively. Combining all equations above gives:

$$F_i = \lambda T_i + (1-\lambda)\, n_i \left(\frac{mass^i}{mass^{58}} \right)^{-\alpha} - m_i \left(\frac{mass^i}{mass^{58}} \right)^{-\beta} = 0 \tag{A.27}$$

These three equations can be solved for λ, β, and α by iteration in e.g. MATLAB.

ACKNOWLEDGEMENTS

First of all, I'd like to thank my supervisor Alex Halliday for giving me the opportunity to come to Oxford and work on this project, and for all the advice and support he's offered me over the years (when we had the chance to meet!) Despite his assurances that any numbers will do, I do hope I have produced the right ones. I'm of course, as well, indebted to my other supervisors, Helen Williams and Chris Siebert, who I thank for all their support and suggestions over the past four years, with extra thanks to Helen for helping me by reading and commenting on nearly my entire thesis on her own! I would also like to thank my two examiners, Gideon Henderson and Friedhelm von Blanckenburg, for all their insightful comments on my thesis – especially on chapter five.

Caroline Peacock (University of Leeds) and Brendan Keely (University of York) are both thanked for their input and collaboration on different subjects during my project, and Helen Williams, Kevin Burton, Bruce Chappell, Jim Hein (USGS), Richard Herrington (NHM), and Petrobras are all thanked for providing me with the samples and accompanying information necessary for writing this thesis. For

the financial support which made this research possible are the following funding sources acknowledged: Petrobras, the Science and Technology Research Council (STFC), the European Research Council (ERC), and the Burdett Coutts fund.

Furthermore, I am very grateful to Nick Belshaw and Theo Krastev for swiftly fixing errant mass spectrometers at times of need, to Fatima Mokadem for help with lab issues and ordering equipment and chemicals, and to the everyone in the workshop who has helped make or repair necessary equipment. I'd also like to thank the academic administration staff at the department for helping me with the Oxford University bureaucracy. More generally, I'd like to thank all the other geochemists and PhD students at the Earth Sciences department for their company over the years, particularly during late night mass spec sessions when it is always reassuring to know that you are not the only student working late (again).

Lastly I'd like to thank my friends, here and at home, for their support, with especially large thanks to the City of Oxford Rowing Club and the University of Oxford Women's Rugby Club for helping me overcome the frustrations of non-functioning mass spectrometers. My final thanks goes to my boyfriend Ed for his love and endless support, to my sister and brothers (and aunts, uncles and grandfathers) back in Sweden for their encouragement and for providing packages of Swedish goodies to cheer me up, and to two furry four-legged friends, Hebe and Panda, for tirelessly keeping me company during many long hours of writing.